Proceeding of JSPS-CAS Core-University Program (CUP) on Superconducting Key Technology for Advanced Fusion Device

October 18-21, 2010, Xi'an, P.R . China

Edited by
FU Peng, SONG Yuntao, MITO Toshiyuki and YAMADA Shuichi

Abstract

The JSPS-CAS Core University Program (CUP) seminar on "Superconducting Key Technology for Advanced Fusion Device" was held in Xi'an, China from October 18 to 21, 2010. This seminar was organized in the framework of the CUP in the field of plasma and nuclear fusion.

This seminar honored by NIFS and ASIPP is aim to have a wide discussion on the new application and achievements on superconducting technology of nuclear fusion reactor. The superconducting technology on fusion reactor involves the fields on high current superconductor and magnet, quench protection, current control, cooling of the magnet, and reliability of large scale refrigerator. The technology on ITER high temperature superconductor current leads and the conductor test of JT-60SA are discussed in this seminar.

Thirty-four oral talks and two summary talks were presented in this seminar. Total number of the participants was 34, including 12 Japanese participants.

Key Words: Superconducting Key Technology, Advanced Fusion Reactor, ITER related technology, LTS superconductor, HTS Applications, Cryogenic system, EAST, LHD, JT-60SA.

Organization:

Representatives:

Peng Fu (IPP, CAS) Chairperson
Toshiyuki Mito (NIFS) Chairperson

Program Committee:

Yanfang Bi (IPP, CAS), Lijian Ding (North China Electric Univ.), Peng Fu (IPP, CAS), Laifeng Li (TIPC, CAS), Xianghong Liu(WST, NIN), Yanzhong Li (Xi'an Jiaotong Univ.), Yuntao Song (IPP, CAS)), Youping Tu (North China Electric Univ.), Jiefeng Wu (IPP, CAS), Qiuliang Wang (IEE, CAS), Weiyue Wu (IPP, CAS), Yu Wu (IPP, CAS), Liuwei Xu (IPP, CAS), Qiyong Zhang (IPP, CAS)

Takatarou Hamajima (Tohoku Univ.), Toshiyuki Mito (NIFS), Takao Takeuchi (NIMS), Shuichi Yamada (NIFS).

Local Organization Committee:

Yanfang Bi (IPP, CAS), Peng Fu (IPP, CAS),Yuntao Song (IPP, CAS), Jiefeng Wu (IPP, CAS), Weiyue Wu (IPP, CAS), Yu Wu (IPP, CAS), Liuwei Xu (IPP, CAS), Qiyong Zhang (IPP, CAS)

Preface

The 2010 JSPS-CAS Core-University Program Seminar titled "Superconducting Key Technology for Advanced Fusion Device" was held at the JinYuanFuRun Hotel in Xi'an, P. R. China during 18 – 21 October 2010. 33 researchers and students (21 from China and 12 from Japan) participated in theseminar..

In this seminar, it had aimed to take up the superconducting technology necessary for an advanced fusion reactor, and to discuss study results recently at the time of related. The advanced superconducting conductors such as Nb_3Al and MgB_2, the superconducting magnet technologies, the cooling technologies, the high-reliability technologyof a large-scale superconducting system and the cryogenic systems were discussed based on latest research developments, the result of operation.The status report concerning a construction situation and a detailed design of ITER and JT-60SA and the discussion were done.Moreover, the latest study results in another field such as the superconducting magnets for space and the electric power application were presented, and the active discussionswere done aimingto integrate the common technology necessary for an advanced fusion reactor.

The superconducting technology is crucial for realization of an advances nuclear fusion reactor. It is also expected that the realizationof the nuclear fusion power generation in the near future is the most effective for the suppressionof the heat-trapping gas.A fruitful researcher exchange was able to be attempted though deeper bonds were constructed among researchers in Chinaand Japan.

We wish to express our sincere gratitude to the program committee and the local organization committee of this JSPS-CAP seminar. They made animpressive program in a short term and prepared the book of abstracts and agenda. We also wish to express our gratitude for local staffs' hospitality.

Yuntao Song (ASIPP)
Toshiyuki Mito (NIFS)
Chair of the 2010 JSPS-CAS Core-University Program Seminar
"Superconducting Key Technology for Advanced Fusion Device"

Contents

JSPS-CAS Core-University Program (CUP) on Superconducting Key Technology for Advanced Fusion Device

October 18-21, 2010, Xi'an, P. R. China

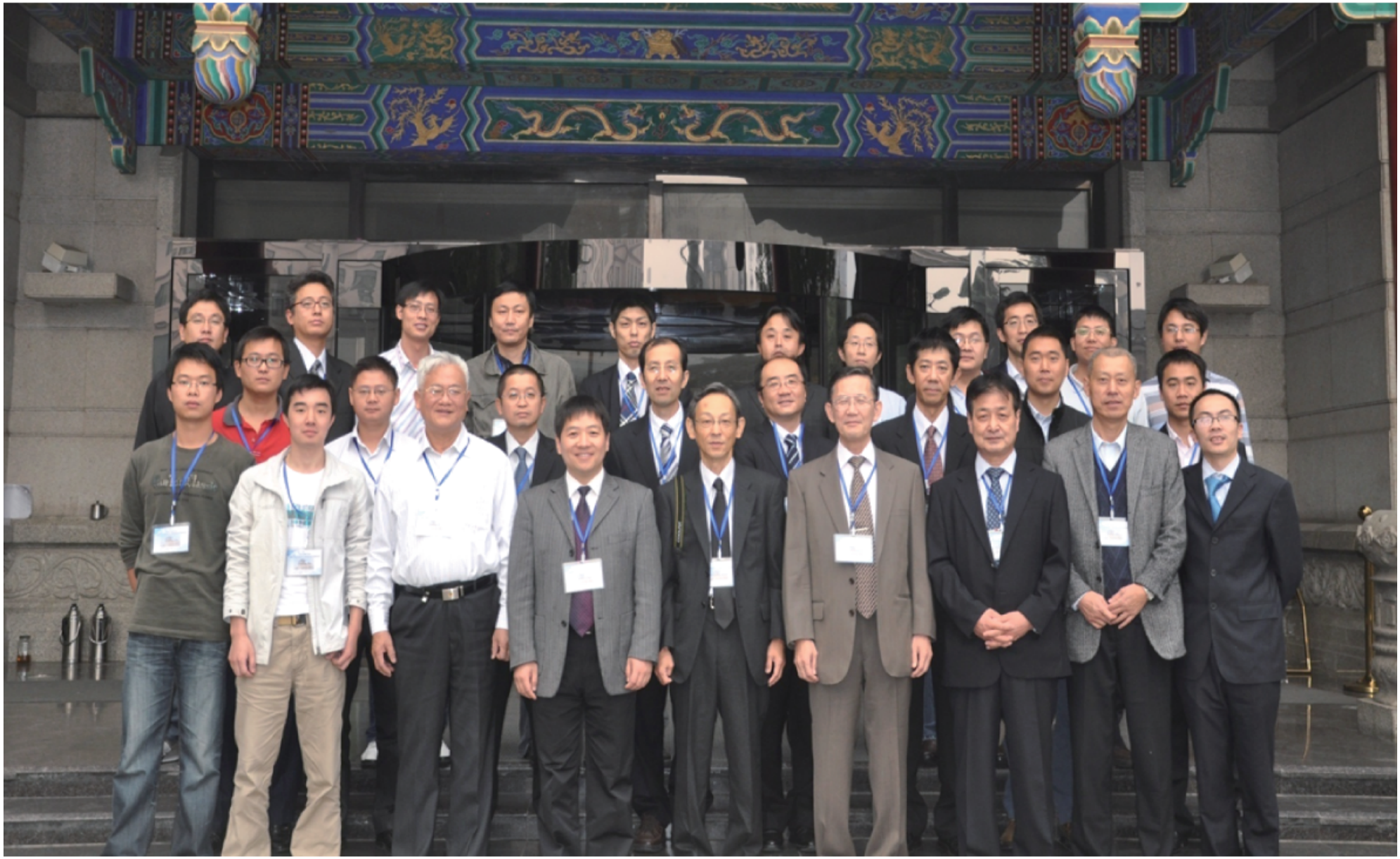

Coaxial Multi-Layer CIC Conductor for Large-Scale Superconducting Magnet

Takataro Hamajima
Tohoku University, Graduate School of Engineering, Sendai, 980-8579, Japan
hamajima@ecei.tohoku.ac.jp

Abstract

An unbalanced current distribution is often observed in cable-in-conduit (CIC) superconductors which are composed of triplet type multi-staged sub-cables, and hence deteriorates the performance of the coils. Since it is very difficult to control homogeneous current distribution in the triplet type CIC, we propose a coaxial multi-layer type CIC to obtain the homogeneous current distribution. We use a circuit model to analyze the current distribution in the coaxial multi-layer CIC. After calculating inductances between adjacent layers in the coaxial multilayer cable, we can derive a generalized formula governing the current distribution as explicit functions of the superconducting cable construction parameters, such as twist pitch, twist direction, layer radius and SC and Cu strands number. We apply the formula to design the coaxial multi-layer CIC for SC magnet of International Thermonuclear Experimental Reactor (ITER). We can design the coaxial multi-layer CIC with the homogeneous current distribution, and investigate several SC strand arrangements in the CIC, and optimize the superconducting strand volume.

1. Introduction

A Cable-in-Conduit (CIC) conductor, which is made of many strands of less than 1 mm in diameter, is mainly used for a forced-cooled coil, because it has many advantages such as high stability, reduced AC loss and high mechanical strength. Generally, a triplet type CIC conductor consists of 3×n×m, where n and m are integers 3 to 6, since it is imagined that every strand could be geometrically arranged in uniform. However, the cable is squeezed and compressed to about 60% in the conduit, and thereby the strands are slightly deviated from the original positions. These deviations cause different inductances among strands, and hence a current distribution in the conductor is no longer homogeneous during excitation. The imbalanced current can restrict the ramp rate of the current in a large coil, and also enhanced AC loss in large superconducting machines due to long decay time constants of loops between strands.

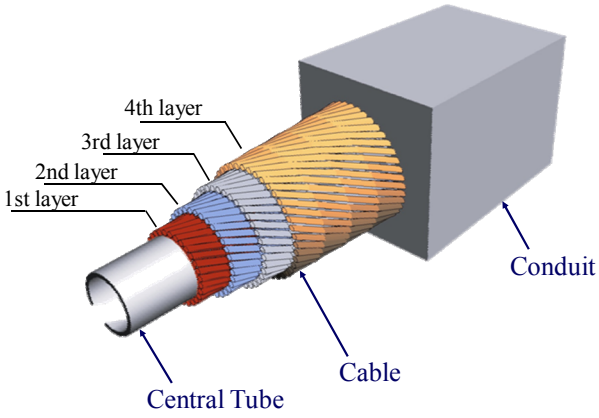

Fig. 1. Cross section of a coaxial multilayer CIC.

We propose a new coaxial multi-layer type CIC conductor as shown in Fig. 1, in order to suppress the imbalance current distribution. The coaxial multilayer CIC conductor is composed of several layers wound on around the central tube for cooling, while each layer has its own pitch. Since all strands are tightly fixed by the winding, they cannot move during the fabrication. All strands in each layer have also the same performance and cannot deviate from the original positions during cable fabrication process. Consequently the strand arrangement can be kept as designed and controlled [1-3].

Parameters governing the current distribution in the multi-layer type CIC conductor are layer radius, twist pitch and twist direction, which are controllable in fabrication of the conductor. The twist pitch is the most changeable parameter in them, and we can control it to obtain the homogeneous current distribution.

In this paper, we derive generalized equation which describes layer current distribution as functions of cable parameters such as layer twist pitch, twist direction, layer radius and superconducting strands number (SC strands) and segregated copper strands (Cu strands). Secondly we apply the equation to design a homogeneous current distribution in the CIC conductor, which is composed of SC strands and Cu strands, for a Central Solenoid (CS) Coil of International Thermonuclear Experimental Reactor (ITER), and investigate several typical superconducting strand arrangements with homogeneous current distribution in the CIC cross section and optimize the superconducting strand volume.

2. Fundamental Equation between Multi-Layer Current Distribution and Twist Pitches

2.1 Magnetic flux linkage between adjacent layers

The layer number is assigned from inner most layer as shown in Fig.1, and the multi-layer CIC is composed of n layers. In this paper since we treat superconducting state of the SC strand, we can neglect the resistance of each layer.

Generally speaking, in the case that each layer is wound with the same pitch, the current concentrates on the most outer layer because of its smallest reactance [1-5]. In order to suppress the layer current imbalance, we adjust reactance of all layers as a function of layer twist pitches, so as to obtain equal voltage drops of all layers, as following equation.

$$v_k - v_{k+1} = \frac{d\Phi_k}{dt} = 0 \tag{1}$$

Where, v_k is k-th layer voltage, Φ_k is flux between k-th and (k+1)-th layer. The flux should be kept constant as follows.

$$\Phi_k = \sum_{i=1}^{n} (M_{k,i} - M_{k+1,i}) I_i = \text{const.} \tag{2}$$

$$M_{k,i} = L_s \left(\frac{\mu_0}{2\pi} \left(\ln \frac{2L_s}{r_k} - 1 \right) + \mu_0 \pi r_i^2 \frac{1}{p_k p_i} \right) \text{ for } r_k \geq r_i \tag{3}$$

Where I_i is layer current, $M_{k,i}$ is mutual inductance between i-th and k-th layers, μ_0 is permeability in vacuum, L_s is conductor length, r_k is radius of k-th layer, p_k is twist pitch of k-th layer, z is distance along the conductor.

2.2 Generalized formula

Since the initial fluxes between layers are usually zero, we can obtain the following layer current distribution equation as explicit functions of layer twist pitches.

$$\frac{\mu_0}{2\pi} \left(\ln \frac{r_{k+1}}{r_k} \right) \sum_{i=1}^{k} I_i + \mu_0 \left(\frac{1}{p_k} - \frac{1}{p_{k+1}} \right) \sum_{i=1}^{k} \pi r_i^2 \frac{I_i}{p_i} + \mu_0 \left(\frac{\pi r_k^2}{p_k} - \frac{\pi r_{k+1}^2}{p_{k+1}} \right) \sum_{i=k+1}^{n} \frac{I_i}{p_i} = 0 \quad (k = 1, \cdots, n-1) \tag{4}$$

The twist pitch direction is given by sign of the pitch.

3. Model of Multi-Layer CIC Conductor

3.1 CIC conductor for ITER-CS coil

We treat a multi-layer type CIC conductor, which has the same specification of ITER-CS coil conductor, as listed in Table 1 [6]. The triplet is composed of 2 SC strands and 1 Cu strand with 0.83 mm in diameter, total number of SC strands and Cu strands in the CIC are 576 and 288, respectively. The CIC can supply about 40 kA at 13 T to the coil.

Table 1. Main specifications of triplet type CIC conductor for ITER-CS coil.

Operating current [kA]	40.0
Peak field [T]	13.0
SC and Cu strand diameter [mm]	0.83
Cabling pattern	(2SC+1Cu)×3×4×4×6
SC strand number	576
Cu strand number	288
Cable diameter [mm]	32.6
Central spiral outer diameter [mm]	9
Local void fraction [%]	33.2
Conductor outer dimension [mm]	49×49

3.2 Analysis of the Multi-Layer CIC conductor

Since the coaxial multi-layer CIC is homogeneously subject to the high field, the critical currents of all SC strands should be almost equal. As far as all strands are equal in operation currents, they have almost equal stability margin, and thereby the CIC conductor has the largest stability margin.

The strand number of the k-th layer is discrete as follows.

$$n_k = \left[\left(\frac{2\pi r_k}{d_s} \right) \Big/ \sqrt{1 + \left(\frac{2\pi r_k}{p_k} \right)^2} \right] \tag{5}$$

Where d_s is strand diameter, and symbol $[a]$ represents the maximum integer less than a. The layer current is proportional to the discrete number of SC strands. We calculate all twist pitches after inserting all layer currents and total strand number into equation (4). This process is repeated until the required layer current distribution and the number of layer strand converge. In this paper, we introduce the coaxial multi-layer type for the above conductor with keeping the total number of strands constant and arranging the SC strands distribution in the cross section. Since the mechanical strength is very high, thickness of conduit is fixed, that is, the outer diameter of the cable 32.6 mm is not changed.

4. Various Strand Arrangements of Multi-Layer Type Conductor

4.1 Typical two cases of SC strand arrangements

Since the copper is used for suppression of strand temperature rise in the case of coil quench, various arrangements of Cu and SC strands are proposed. In this section, we treat the following two typical cases.

Case (a) ; SC: Cu = 2 : 1 arrangement in each layer.

Case (b) ; Segregated SC and Cu strands layers arrangement which lead to the minimum SC strand number.

The SC and Cu strand number distributions for the above two cases are shown in Fig. 2. The layer current is proportional to the SC strand number. The calculated twist pitches for both cases are also

shown in Fig. 3, in the case that the twist pitch of inner most layer is 500 mm for case (a), and that of 5-th layer 500 mm for case (b), because the SC strands are distributed at lager layer number than the 5-th layer.

It is found from Fig. 2 that the layer strand number increases with layer number, because outer layer has larger strand numbers due to larger radius. However, the layer strand number decreases near the most outer layer. This is explained that since outer layers have shorter twist pitches as shown in Fig. 3, the strand numbers are restricted. The maximum layer SC numbers are 72 from 9-th to 11-th layer for case (a), and 94 at 9-th layer for case (b).

It is shown that twist pitches decrease monotonically with layer number. This stems from that since the first term in equation (4) is always positive, the summation of the second and third terms should be negative, and hence the twist pitch of outer layer should decrease. Consequently in the case that the outer layer twist pitch decrease rapidly compared with layer radius, the strand number of outer layer can decrease.

It is shown from Fig. 3 that since layer pitches of other SC layers than 1-st SC layer for the case (b) are larger than those for the case (a), the case (b) has larger layer strand number than the case (a), and hence the case (b) is composed of 11 layers while the case (a) is composed of 14 layers. SC strand volume of the case (b) is reduced to 89 % from that of the case (a), since all segregated copper strand are arranged in inner layers.

4.2 SC strand volume as a function of twist pitch

We investigate the strand volume as a function of layer twist pitches and obtain the volumes from 300 mm to 800 mm of the 1-st layer in the case (b), as shown in Fig. 4. The volumes normalized by the SC strand volume of the twist pitch of 500 mm.

It is fond from Fig. 4 that the strand volume decreases according to longer twist pitch of the most

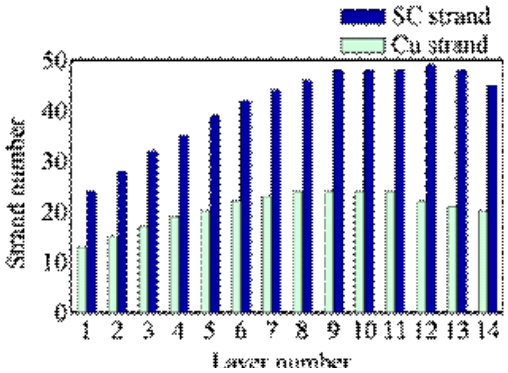

(a) SC / Cu strands ≈ 2 in each layer.

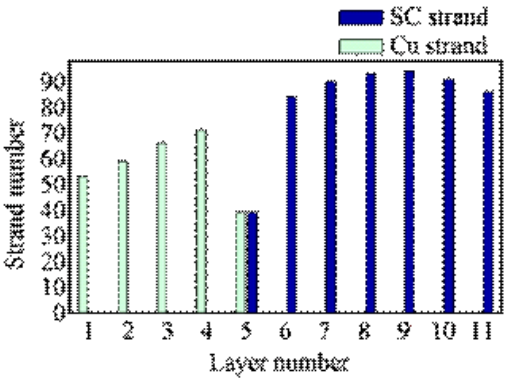

(b) SC strand volume is optimized.

Fig. 2. SC and Cu strand distribution for 2 cases.

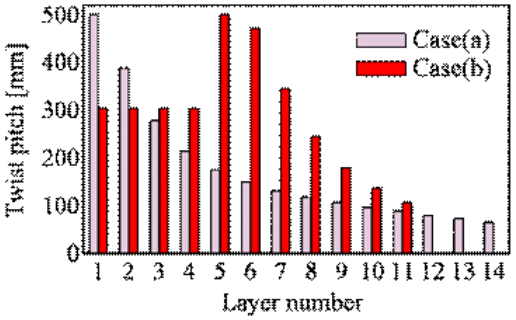

Fig. 3. Twist pitches distribution for 2 cases.

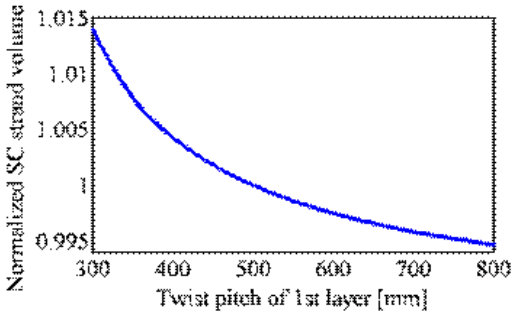

Fig. 4. The relationship between twist pitch of 1st layer and normalized SC strand volume.

inner layer, since longer twist pitch of the most inner layer leads to longer twist pitches of outer layers.

4.3 SC strand volume as a function of strand diameter

We investigate the strand volume as a function of strand diameter from 0.7 mm to 0.96 mm at an interval of 0.01 mm, with keeping SC strand cross section constant. Fig. 5 shows the strand volume of the case (b) as a function of strand diameters. The volume is normalized by that of 0.83 mm in diameter. The SC and Cu strand numbers as a function of strand diameter are shown in Fig. 6.

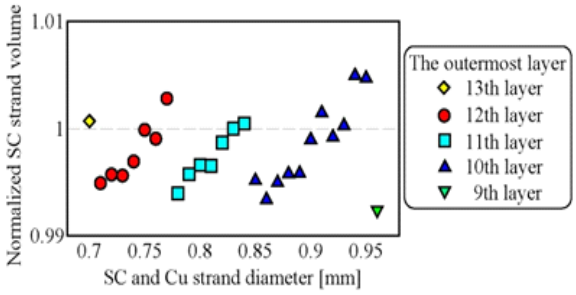

Fig. 5. The relationship between strand diameter and normalized SC strand volume.

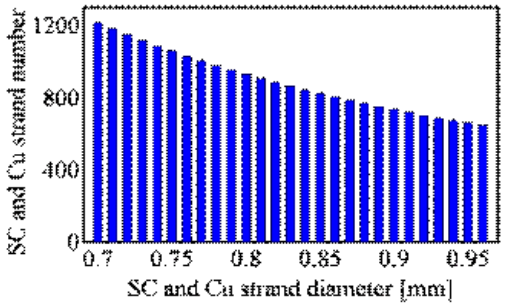

Fig. 6. SC and Cu strand number changing with strand diameter.

It is found from Figs. 5 and 6 that strand number becomes smaller due to larger strand diameter, and hence the conductor has smaller layer number. It is also found in the case of the same layer number, that the required strand number decreases when the maximum layer strands can be arranged. This is a reason that twist pitches of all layers become larger according to larger total strand number in the case of arrangement of the same total strand number in the same layer number. It is shown that smaller layer number slightly requires the smaller strand volume, since the twist pitches near most outer layer becomes longer twist pitches.

4.4 Reduction of strand volume

We investigate the strand volumes of various multi-layer type CIC in the same condition of CIC conductor for ITER-CS coil. The calculated minimum volume is the following case (c).

Case (c) ; pitch of the most inner layer is 800 mm, strand diameter is 1.22 mm, and layer number is 7.

The layer strand numbers of above case (c) is shown as a function of layer number in Fig. 7, and the layer twist pitches in Fig. 8. This arrangement suppresses reduction of twist pitches due to smaller layer currents at inner layers, as the

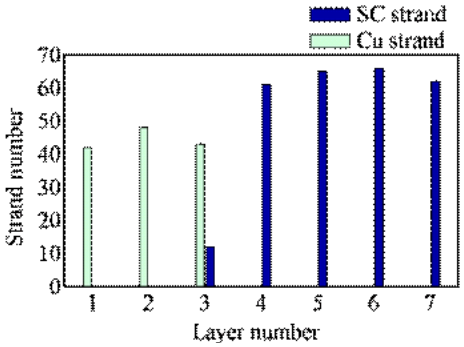

Fig. 7. SC and Cu strand distribution in Case(c).

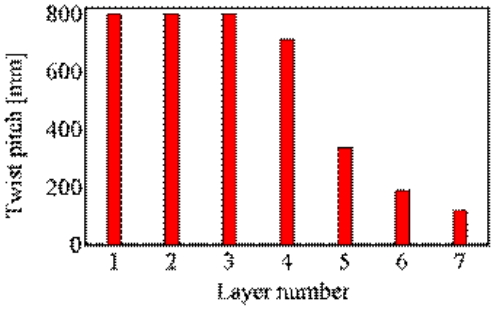

Fig. 8. Twist pitches distribution in Case(c).

same reason of the case (b).

Table 2 lists the comparison of 3 cases in terms of inner radius outer radius and void fraction and normalized strand volume. Since the multi-layer cable can have smaller size and more compact compared with triplet-type cable, it has potential to be high current density. It is possible for the multi-layer type conductor to reduce SC strand volume by making the twist pitch longer.

Table 2. Comparison of parameters.

	Case(a)	Case(b)	Case(c)
Inner radius [mm]	4.52	6.79	7.71
Outer radius [mm]	16.14	15.92	16.25
Void fraction [%]	22.1	22.1	22.4
Normalized SC strand volume	1	0.89	0.87

5. Conclusion

We proposed the multi-layer type CIC conductor with homogeneous current distribution to suppress the unbalanced current distribution caused in the triplet type CIC conductor. Since strands of the multi-layer CIC are orderly arranged, it is possible that we can precisely control the current distribution and hence it sufficiently satisfy cryogenic stability at the stage of conductor design.

We formulate the equation of twist pitch to satisfy the homogeneous current distribution, and then apply it to the CIC conductor for ITER-CS coil under the conditions of the same outer radius and strand number. We investigate several typical SC and Cu strands arrangements with homogeneous current distributions, and compared SC strand volumes for the arrangements. It is possible to reduce the strand volume by arranging the SC and Cu strands. It is demonstrated that the multi-layer type CIC conductor for ITER-CS coil is constructed with the same order of strand volume.

References

[1] Takataro Hamajima, A.K.M. Alamgir, Naoyuki Harada, Makoto Tsuda, Michitaka Ono, Hirohisa Takano, “Analysisi of current distribution in a large superconductor,” Cryogenics 40 (2000) 729-736.

[2] T. Hamajima, M. Tsuda, T. Yagai, K. Takahata and S. Imagawa, “Fundamental Design Based on Current Distribution in Coaxial Multi-Layer Cable-in-Conduit Conductor”, IEEJ, Transaction B, Vol. 129,(2009) pp.1299-1304.

[3] T. Hamajima, S. Teshima, Y. Shibata, T. Yagai, M. Tsuda, K. Takahata, S. Imagawa and T. Mito, “Conceptual Design of Coaxial Multi-Layer Type CIC for SC Magnet of FFHR”, IEEE Transactions on Applied Superconductivity, Vol.20, N0.3, (2010) pp. 560-563.

[4] H. Noji, T. Shibata, S. Isono, J. Fujikami, K. Sat, “AC Loss of a Coonductor withMultilayer, SpiralStructure for High-Tc Superconducting Power Cable”, TEION KOGAKU, Vol.33, (1998) pp.114-120.

[5] S. Kruger Olsen, C. Traeholt, A. Kuhle, O. Tonnesen, M. Daumling and J. Ostergaard : “Loss and Inductance Investigations in a 4-layer Superconducting Prototype Cable Conductor”, IEEE Transactions on Applied Superconductivity, Vol.9 (1999) pp.833-836.

[6] Y. Takahashi, K. Yoshida, Y. Nabara, M. Edaya and N. Mitchell : “Simulation of Quench Tests of the Central Solenoid Insert Coil in the ITER Central Solenoid Model Coil”, IEEE Transactions on Applied Superconductivity, Vol.16 (2006) pp.783-786.

Development of Rapid-Heating, Quenching and Transformation Processed Nb_3Al Superconducting Wires for Nuclear Fusion Devices

T. Takeuchi[(1)], A. Kikuchi[(1)], N. Banno[(1)], Y. Iijima[(1)], K. Tsuchiya[(2)], N. Koizumi[(3)], K. Matsui[(3)]

1) National Institute for Materials Science (NIMS), Tsukuba, Ibaraki 305-0047, Japan
2) High Energy Accelerator Research Organization (KEK), Tsukuba, Ibaraki 305-0801, Japan
3) Japan Atomic Energy Agency (JAEA), Naka, Ibaraki, 311-0193, Japan

E-mail: TAKEUCHI.Takao@nims.go.jp

Abstract

We have developed a Nb_3Al multifilamentary superconductor, which is based on a Jelly roll Nb/Al composite and fabricated by rapid-heating and quenching (RHQ) of such a composites wire with subsequent transformation annealing (T) to form Nb_3Al phase. In contrast to the conventional diffusion processed Nb_3Al conductors, the transformation from supersaturated bcc-solid-solution $Nb(Al)_{ss}$ enables the highly stoichiometric A15-Nb_3Al to form with fine grains, and the J_c characteristics are significantly improved over the whole range of magnetic fields. The resulting substantially improved high-field performance is compatible with the excellent strain tolerance. Thus, the RHQT processed Nb_3Al conductor is promising as a realistic alternative to Nb_3Sn for the fusion reactor use. The present study describes a result of a trial manufacture of a miniature cable-in-conduit conductor (CICC) consisting of RHQT Nb_3Al round strands that have a Ta filament-barrier to suppress low-magnetic-field instabilities and Cu stabilized by ion plating/electroplating techniques. The stabilities of CIC conductor at 15 T was tested under a forced flow cooled condition.

1. Introduction

The Japan Atomic Energy Agency has developed the low-temperature diffusion (LTD) processed Nb_3Al conductor for nuclear fusion devices, because it exhibits better tolerance to strain than Nb_3Sn conductor does. The starting material was a jelly roll (JR) composite in which alternate sheets of Nb and Al were wound onto a Cu rod, and they were stacked into a Cu tube, extruded and drawn down to a Cu-matrix mutifilamentary JR Nb_3Al strands that were used for a trial manufactured cable-in-conduit conductor [1]. Since the good strain tolerance allows the bending strain up to +- 0.4 % after heat treatment, they produced the Nb_3Al insert coil by the react-and-wind technique, and successfully energized in a bore of ITER central solenoid model coil which generated a background field up to 13T [2]. However, the non-Cu J_c of LTD-Nb_3Al is rather lower than that of bronze-route Nb_3Sn in a strain-free condition (figure 1 (a)). On the other hand, another conductor termed the rapid-heating, quenching and transformation (RHQT) processed Nb_3Al [3]-[5] exhibits significantly improved non-Cu J_c performance over the whole range of magnetic fields which

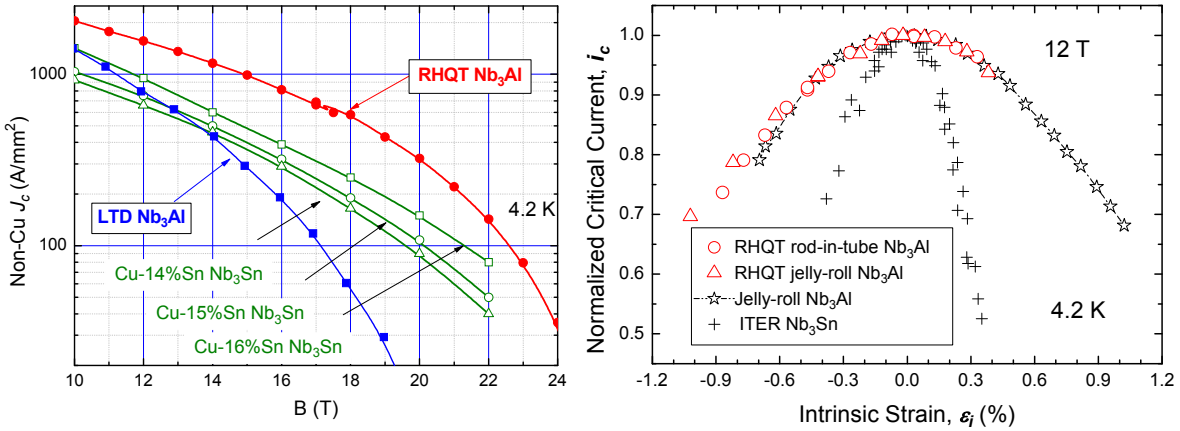

Figure 1 Comparison of superconducting properties of RHQT processed Nb_3Al to LTD Nb_3Al and bronze route Nb_3Sn wires.

are compatible with original excellent strain tolerance (Figure 1 (b)) [6],[7]. In the present article, the recent progress of RHQT Nb_3Al conductor for nuclear fusion device is reviewed.

2. RHQT-process

Figure 2 shows an overview of RHQT process to produce an improved Nb_3Al wire. The starting material is also the above-mentioned JR Nb/Al composite, but the matrix material is the high melting-point metal which acts as a mechanical support during RHQ treatment, in

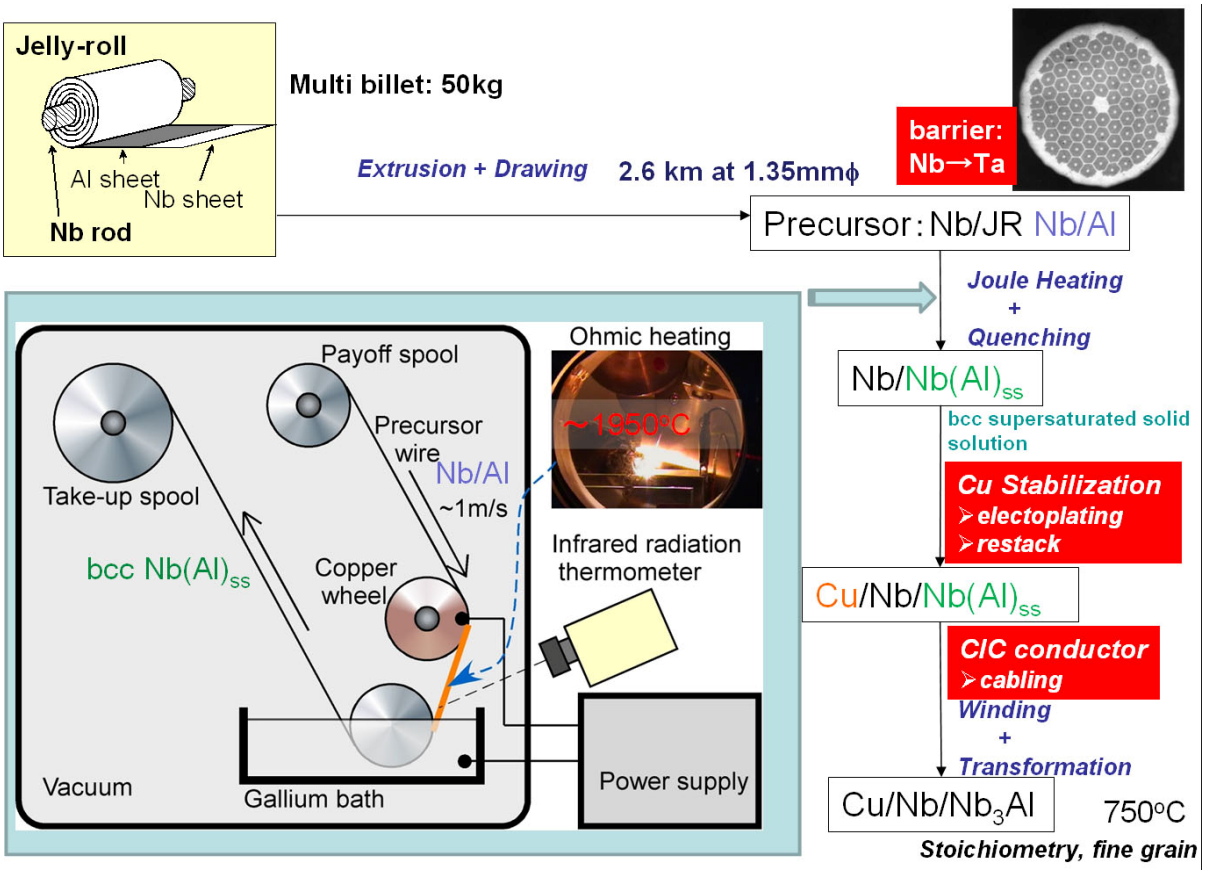

Figure 2 Overview of the rapid-heating, quenching and transformation annealing process for the multifilamentary Nb_3Al wire for nuclear fusion device uses.

contrast to the conventional Cu matrix JR wires. As explained latter, the filament barrier needs to be changed from the conventional Nb to Ta for nuclear fusion device uses. Such a multifilamentary precursor wire is fed from this payoff spool, around a Cu electrode wheel, into a liquid Ga bath which acts as electrode and also coolant, and onto a take-up spool. Joule heating is carried out by passing a current though the section of wire between the Cu wheel and the Ga. After quenching of wire, each JR Nb/Al filament is converted to a bcc supersaturated-solid-solution filament, and then Cu stabilizer is incorporated by electroplating or restacking method using a ductile nature of bcc supersaturated solid solution. Such a ductile nature also allows the cabling and winding. The winding would be finally subjected to transformation heat treatment at 750°C for 50 h to obtain a stoichiometric and fine grain A15 Nb_3Al filament.

3. Ta filament barrier

The RHQT-processed Nb_3Al conductor had been originally developed for a high-filed nuclear magnetic resonance magnet so that the filament barrier species of precursor was Nb which facilitated the superconducting joint technology [8]. However, Nb was still superconductive in a field up to 1 T at 4.2 K so that the Nb filament-barrier caused the electromagnetic coupling of Nb_3Al filament and hence frequently large flux jumps in a low magnetic field as shown in figure 3 (a) [9]. Such low magnetic field instability is undesirable when loading a coil, in particular for large scale applications like a nuclear fusion device. Thus, we have recently developed the Ta filament-barrier wire to suppress the low magnetic field instability. Although the critical temperature of Ta is 4.5 K, the Ta, at least at 4.4 K, became normal conductive in small fields. Figure 3 (b) shows the magnetizations of the Ta-filament-barrier sample. The magnetization curve at 4.4 K is very smooth and no flux jump is observed. Small flux jumps are, however, observed below a field-strength of 0.2 T at 2 K, of which temperature is much lower than the forced-cooled helium temperature.

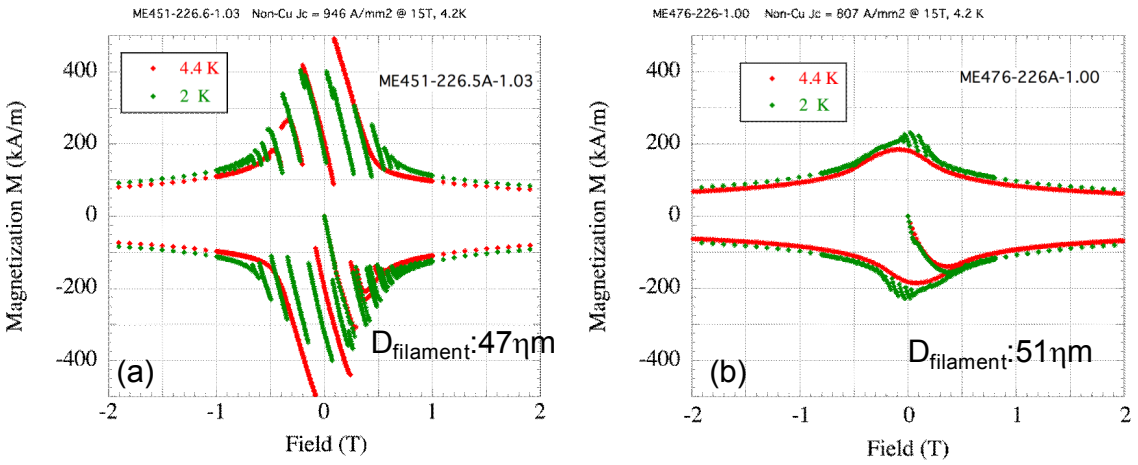

Figure 3 Magnetization curves at 4.4 K and 2 K for (a) Nb filament-barrier and (b) Ta filament-barrier RHQT Nb_3Al strands of that filament diameters are around 50 μm.

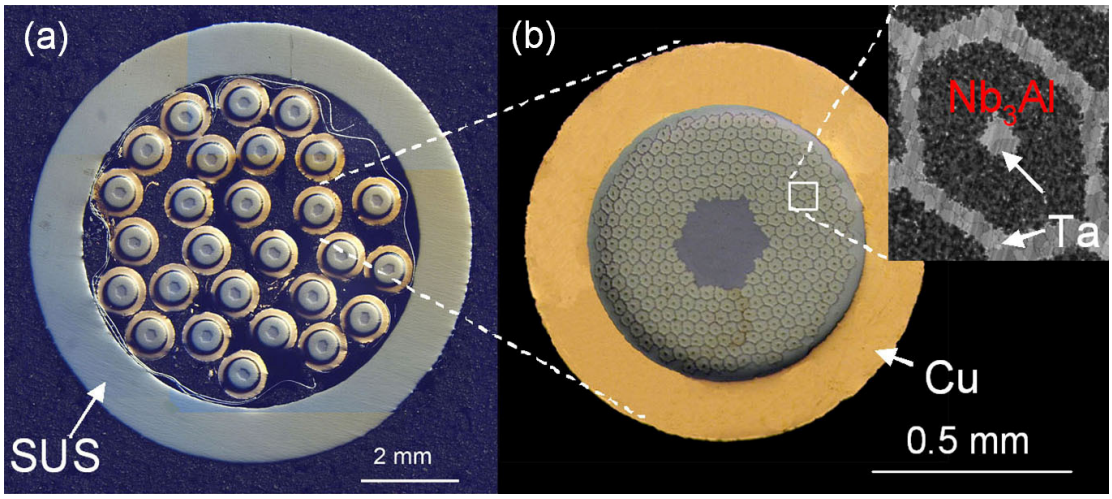

Figure 4 Cross sectional view of 27-strand RHQT-Nb3Al cable-in-conduit conductor; (a) overall, (b) strand.

4. Cu stabilization

The Cu stabilizer has been incorporated into a round-wire after RHQ treatment by a Cu ion-plating/electroplating technique; a reel-to-reel Cu ion-bombardment treatment followed by depositing thin (1 μm) Cu film on a surface of RHQed wire is effective in making a clean interface so as to improve the mechanical and electrical bonding between Cu and Nb [10]. We have succeeded in increasing a reel-to-reel moving speed of wire up to 240 m/h by optimizing the parameters of apparatus. After this pretreatment, a thick layer of Cu (volume ratio: 1.0) was put on the wire by the conventional reel-to-reel chemical electroplating with a

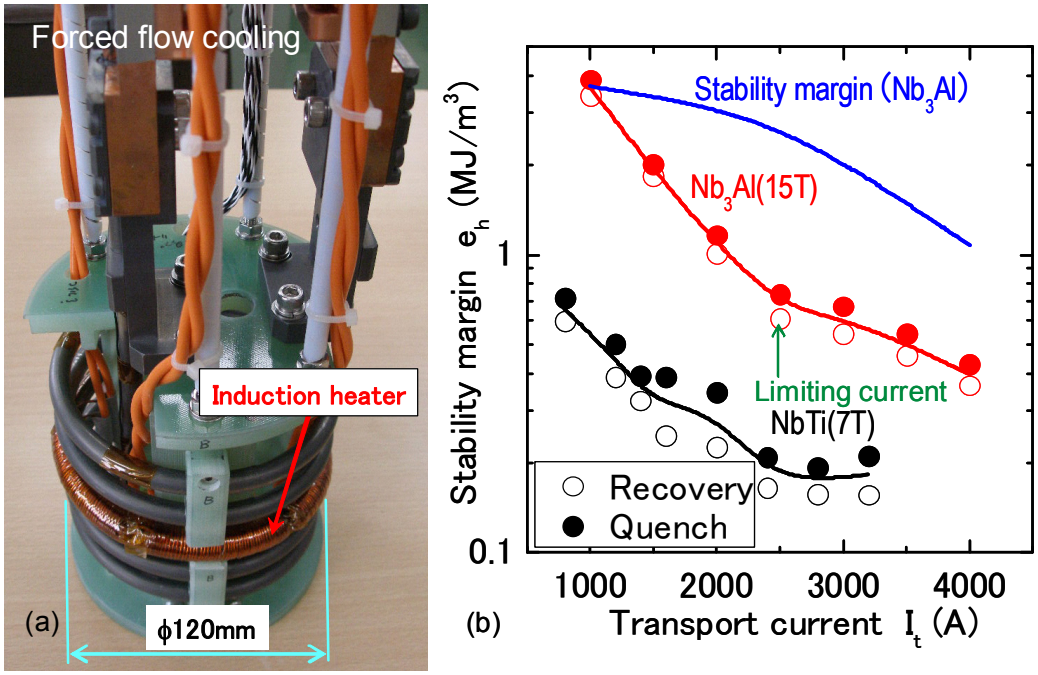

Figure 5 Evaluation of stability margin of RHQT Nb_3Al CIC conductor; (a) experimental setup, (b) stability margin as a function of transport current.

speed of 7 m/h. A typical cross section of Cu stabilized RHQT Nb_3Al strand is shown in figure 4 (b).

5. Cable-in-conduit conductor

We have trial manufactured a miniature cable-in-conduit (CIC) conductor using the above mentioned Cu-stabilized Ta-filament-barrier Nb_3Al round-wire (figure 4) [11]. The finished third stage cable of 3×3×3 was wrapped with a SUS316 tape and then drawn inside a SUS316 conduit to a void fraction of 36 %. The first, second and third cabling pitches are 56, 106 and 162 mm, respectively. The outer and inner diameters of conduit are 9.6 and 6.8 mm, respectively. A critical current (I_c) of strand at 16 T and 4.2 K was 245 A and thus the expected I_c (16T, 4.2 K) of CIC conductor became as large as 6.6 kA. Figure 5 shows an experimental setup for the stability margin evaluation, in which the CIC conductor is forced flow cooled. In this experiment, while flowing the transport current up to 4 kA at 15 T, thermal disturbance was given to the conductor by an induction heating for a short time, and we checked whether the normal zone propagates or not. The limiting current of RHQT Nb_3Al CIC conductor is about 2.5 kA, which is comparable to that of Nb-Ti CIC conductor. This clearly indicates that the RHQT Nb_3Al CIC conductor has a sufficient stability margin despite that a thick Cu layer has been incorporated by the electroplating technique.

Acknowledgment

This work was partly supported by the JSPS-CAS Core-University Program in the field of "Plasma and Nuclear Fusion".

References

[1] Yamada, Y., et al Development of Nb_3Al superconductors for international thermonuclear experimental reactor (ITER), *Cryogenics* 39 (1999) 115-22.

[2] Koizumi, N., et al., Evaluation of strain applied to strands in a 13T-46 kA Nb_3Al cable-in-conduit conductor, *Supercond. Sci. Technol.* 16 (2003) 1092–6.

[3] Takeuchi, T., Nb_3Al conductors for high field applications, *Supercond. Sci. Technol.* 13 (2000) R101–19.

[4] Takeuchi, T., et al., RHQT JR Nb_3Al conductors developed for nuclear fusion devices, *Fusion Engineering and Design*, 81 (2006) 2443-8.

[5] Takeuchi, T., et al., Status and perspective of the Nb_3Al development, *Cryogenics* 48 (2008) 371-80.

[6] Takeuchi, T., et al., Strain effects in Nb_3Al multifilamentary conductors prepared by phase transformation from bcc supersaturated-solid-solution, *Appl. Phys. Lett.* 71 (1997) 122-4.

[7] Banno, N., et al., Strain dependence of superconducting characteristics in technical Nb_3Al superconductors, *Supercond. Sci. Technol*. 18 (2005) 284-8.

[8] Fukuzaki, T., et al., Development of a superconducting joint for high field NMR, IEEE Trans. Appl. Supercond. 16 (2006) 1547-9.

[9] Tsuchiya, K., et al., Development of Ta matrix Nb_3Al wire for next generation accelerator magnet, IEEE Trans. Appl. Supercond. 19 (2009) 2674-7.

[10] Kikuchi, A., et al., Cu stabilized Nb_3Al strands for high field accelerator magnet, IEEE Trans. Appl. Supercond. 18 (2008) 1026-30.

[11] Koizumi, N., et al., Stability test results of RHQT Nb_3Al CIC conductor, Abstracts of CSJ Conf. 82 (2010) 1D-a09.

R&D on HTS Current Leads for Fusion Magnets

Yanfang BI
Institute of Plasma Physics, Chinese Academy of Sciences, P.O.Box 1126, Hefei China 230031
yfbi@ipp.ac.cn

Abstract: HTS current leads (HTSCL) can reduce cooling power consumption about two thirds comparison to conventional leads, the heat loads of which occupy near a half of a tokamak fusion magnet total. R&D on HTSCL at ASIPP started in 2003, five pairs of 15 kA HTSCL were used for EAST tokamak commissioning in 2006 due to the capacity of EAST cryoplant shortage. In 2008 the rest 8 pair leads were added HTS modules. The 68/52/10 kA HTSCL for ITER toroidal/poloidal field magnets and correction coils have been developed at ASIPP since 2007. Major achievements are as follows: the high-efficiency foil-stack heat exchangers (HEX) and transition between HEX and HTS modules, the low temperature SC (LTS) linker design with low enough contact resistance and inner water cooled room temperature terminal design. The test results show that the quench current of an EAST toroidal field magnet lead, which consists of 250 CryoBlock tapes, was 27.6 kA; the 68 kA trial lead containing 1080 tapes was ramped to 90 kA for 4 min without quench under the normal operating condition. The trial lead has the temperature margin near 20 K, heat load of 14 W at 5 K end, LOFA time of 373 s, burnout time of 22 s, contact resistances of 3.2 nΩ for 65 K end and 0.51 nΩ for 5K end, the twin-box type joint resistance of 0.9 nΩ, and HEX specific mass flow rate of 0.061 g/s/kA for the 10 kA lead cooled with 50 K helium inlet, which is equivalent efficiency of 98.4 %.

1. Introduction

Fusion can provide human being permanent and clear energy source. The fusion energy is generated by deuterium plasma under very high temperature condition. Superconducting (SC) magnets are the best way to confine plasma for fusion reactors because they create very large volume and quite high magnetic fields without Joule loss. But now all the SC magnets are made of low critical temperature SC conductors (LTS), such as NbTi or Nb3Sn, their operating temperature around liquid helium. The cryoplant spends a large amount power for LTS magnets, and almost ~50% of refrigeration is dissipated for magnets current leads if the conventional leads are used. The high temperature superconductor current leads (HTSCL) can reduce 2/3 of the cooling power consumption. So HTSCL is the most benefit and successful application of HTS technology in power engineering.

Based on HTSCL success of JAEA 60 kA [1] and KIT 70 kA leads [2] the LHC collider has been equipped more than one thousand HTSCL [3]; ITER Organization decided to accept HTSCL instead of original conventional lead design. Found on past three years R&D on 68/52/10 kA HTSCL the most of key technologies of ITER leads have been solved at ASIPP. The HTSCLs will also be used for the fusion experiment devices of W7-X and JT-60SA under construction. Therefore HTSCLs will service for all the fusion magnets, which become the absolutely necessary components for future fusion device.

2. Major components of HTS leads

A gas-cooled HTSCL usually consists of six components (see Fig.1): 1) a room temperature copper terminal connected to busbars from power supply, 2) a resistive HEX, 3) a HTS module, 4) a LTS linker connected to a SC busbar of the magnet, 5) insulation and flange for connection to the cryostat, 6) instrumentation to monitor the lead temperature and voltage. In this paper the component designs are described.

3. R&D at ASIPP

EAST cryoplant capacity of 2.3 kW/4.5K based on original design the central solenoid (CS) and poloidal field (PF) coils with symmetric current configuration, total amount is 7 pairs of 15 kA lead only. But the plasma controlled was quite difficult. Then the power supplies of PF

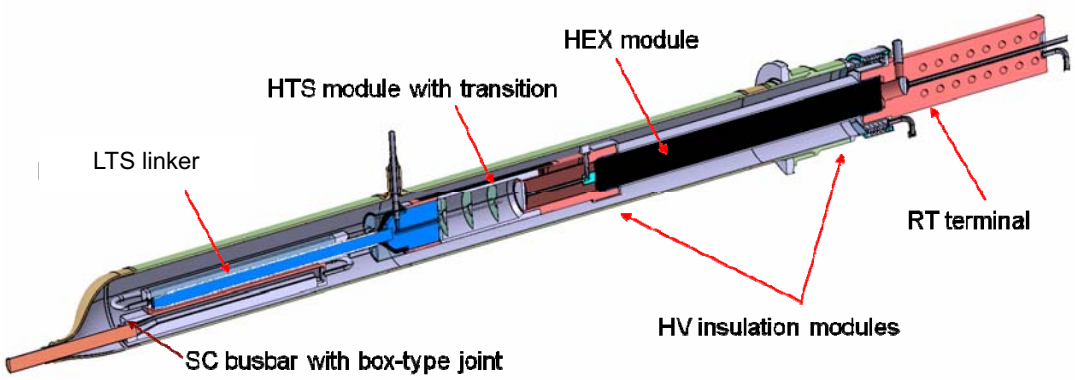

Fig.1 68 kA HTSCL design

and CS coils were increased up to 12 and the current lead amount also was raised to 13 pairs. It led to EAST cryoplant capacity shortage. Comparison to enlarging cryoplant capacity applying HTS current leads is a much economy way to avoid larger invest to add cryogenic equipment and to save operating cost. The 13 pairs of 15 kA conventional leads consume more than 13 g/s liquid helium, which is equivalent heat load of ~1.3 kW/4.5 K; however the total heat load of 13 pairs of 15 kA HTSCL is less than 50 W/4.5 K. Thus it results in the EAST cryoplant with enough cooling capacity to service the cryopumps and so on. All the HTSCL performed very stable during the latest three campaigns of EAST tokamak operation. There was no any trouble met.

R&D on HTS leads at ASIPP started in 2003. Five pairs of HTSCL were put into operation during EAST tokamak commissioning in 2006. The rest 8 pairs of copper leads were added a HTS section in 2008. Procurement Package of ITER magnet feeders (including current leads) was distributed to China. Based on successful EAST HTSCL ASIPP has taken charge of R&D for ITER leads since 2007. Three trial leads with rated currents 68/ 52/10 kA were designed, manufactured and tested in the past 3.5 years. The details are as follows.

3.1 HTSCL for EAST

The HEXs of the HTSCL are cooled with nitrogen gas from the tokamak thermal shields and only the transition between the HTS module and HEX must be cooled with liquid nitrogen. EAST lead contain 50 HTS stacks, each one consists of 5 layer AMSC/InnoST tapes (see Fig.2). Heat loads at 5K are < 2 W for PF leads and < 10 W for TF leads. The quench current of the TF lead reached 27.6 kA.

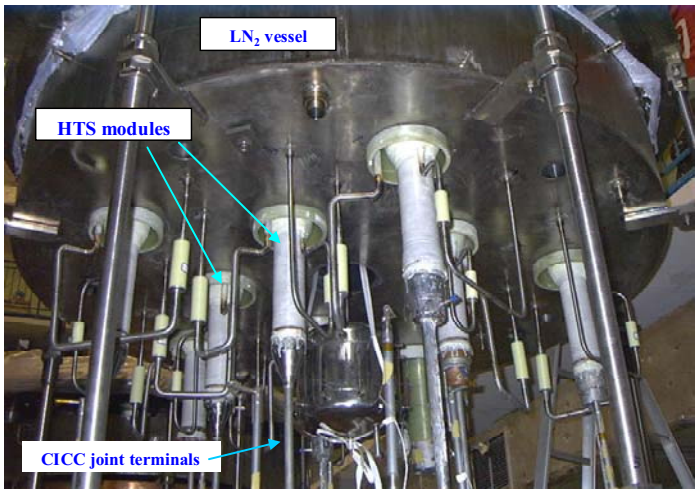

HTSCL in the cryostat

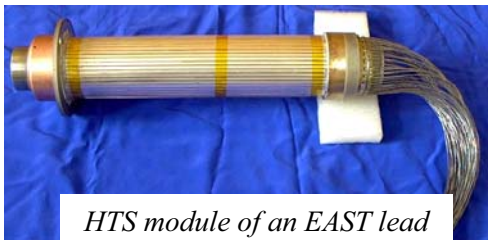

HTS module of an EAST lead

Fig.2 HTSCL for EAST tokamak

3.2 &D on HTSCL for ITERR

Based on R&D of 68/52/10 kA HTSCL following main points are recognized: 1) The temperature margin relates with average field inside HTS stacks rather than the maximum field; 2) HTSCL safety depends on the HTS temperature margin and HEX current density; 3) The mass flow rate required to cool HEX relates not only to dimension optimization but also to copper grade, contact resistance and HEX efficiency; 4) Foil-stack type HEX has much higher efficiency than the fin type HEX; 5) The transition between HTS and HEX modules should be cooled with helium directly; 6) Inner water cooling/heating for lead terminals is the better way to protect over-heated or icing comparison with electrical heaters.

3.2.1. HTS module

The HTS module consists of HTS stacks, a shunt-support cylinder and two copper caps. The critical current of each HTS tape is sensitive to magnetic field perpendicular to tape surface. To reduce lead self-field effect the more than several hundred to more than one thousand HTS tapes are arranged on a support cylinder surface and parallel connected in electric, and every tape critical current depends on the local perpendicular magnetic field. To estimate the critical current of a HTS module the average field is used rather than the maximum. According to the average perpendicular field load line (see Fig.3) the current carrying capacity of the 68 kA trial lead is about 110 kA in the test set-up, so the lead could ramped at 90 kA without quench, which exceeds the critical current very much for the maximum field load line (see Fig. 4).

The HTS lead design must consider loss of flow accident (LOFA) for safety. The TF magnets require HTSCL with a long LOFA time to avoid strong eddy current heating in their thick cases caused by a fast discharge. Fig.5 shows the profiles of HTS temperature and voltage along HTS stacks of the 68 kA trial lead. The LOFA time starts at coolant flow loss until HTS module quench, so it depends on two factors: 1) the temperature margin of HTS module, the lower operating temperature and the more HTS tape amount will lead a longer LOFA time; 2) current density and heat sink of the HEX, the lower current density and the larger heat sink will result in longer LOFA time. The LOFA time is 373 s if the LOFA starts at the initial temperature of 65 K at the HTS warm end (100% HTS) instead of 66.2 K, which is close to IO expected value of 400 s.

The temperature margin is defined a difference between the HTS current sharing and operating temperatures. The 68 kA trial lead has the temperature margin near 20 K at self field from its cold test (see Fig. 6). A large margin is necessary for a long LOFA time and benefits to stable operating.

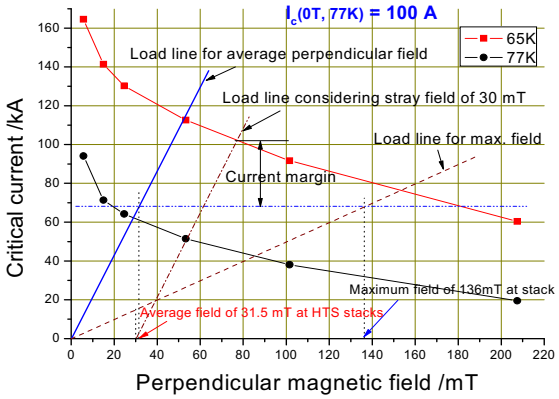

Fig.3 HTS load lines of the 68 kA lead

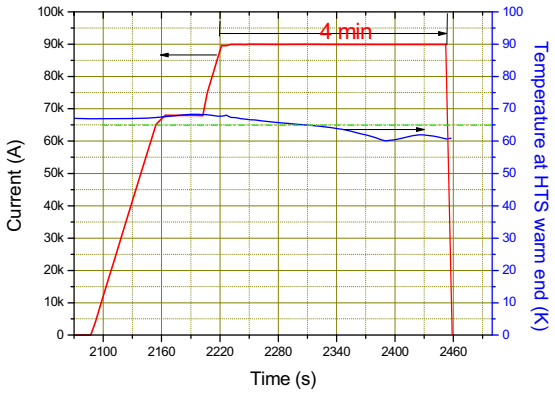

Fig.4 The 68 kA lead was held 90 kA for 4 min under warm end temperature at 65 K.

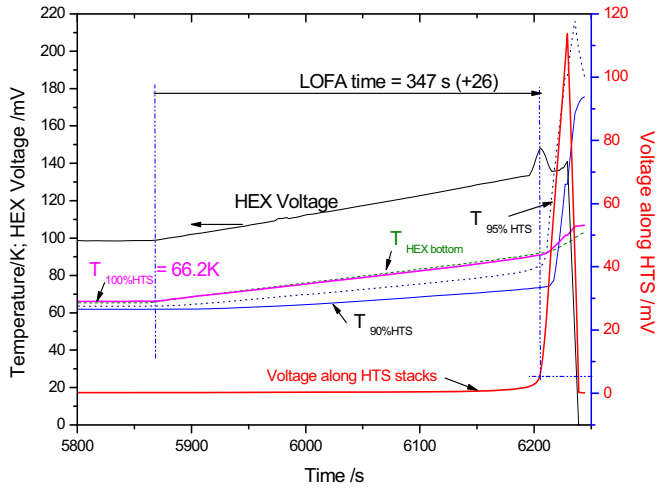

Fig.5 Temperature and voltage profiles of the HTS module after the 68 kA HEX flow loss

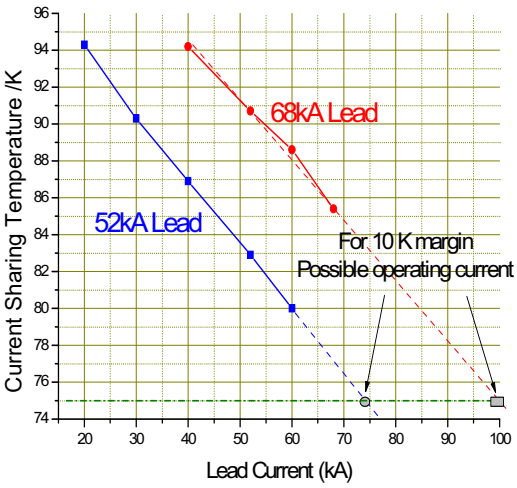

Fig.6. Current sharing temperature vs operating current

3.2.2. HEX module

HEX cooling is major power consumption for HTSCL, so HEX efficiency is one of the important factors. The HEX can be divided two basic types: 1) current carriers are made of fine wires or foils and have a large wet perimeter; 2) current carrier is made of a rod or tube with fins, which have a short wet perimeter. The two HEX types for 68 kA current leads are illustrated in Fig.7.

Fig.8 shows the relation between the HEX efficiency and mass flow required vs $\boldsymbol{hP_w}$ product value for a 68 kA lead with 65-300K operating temperature, 50 K inlet helium cooling and made of RRR 40 copper. A foil-type 68kA HEX is easier to reach $\boldsymbol{hP_w}$ value larger than 15,000 W/K-m and the efficiency higher than 99%; but a zigzag-fins HEX is hardly to reach over 1,500 W/K-m and its efficiency lower than 91%. Here $\boldsymbol{h}$ is heat transfer coefficient, which relates to cooling gas conductivity $\boldsymbol{k}$ and equivalent hydraulic diameter $\boldsymbol{de}$ for laminar flow

$$h = \frac{3.8k}{de}. \tag{1}$$

The $\boldsymbol{de}$ can be expressed

$$de = \frac{4A}{P_w} \tag{2}$$

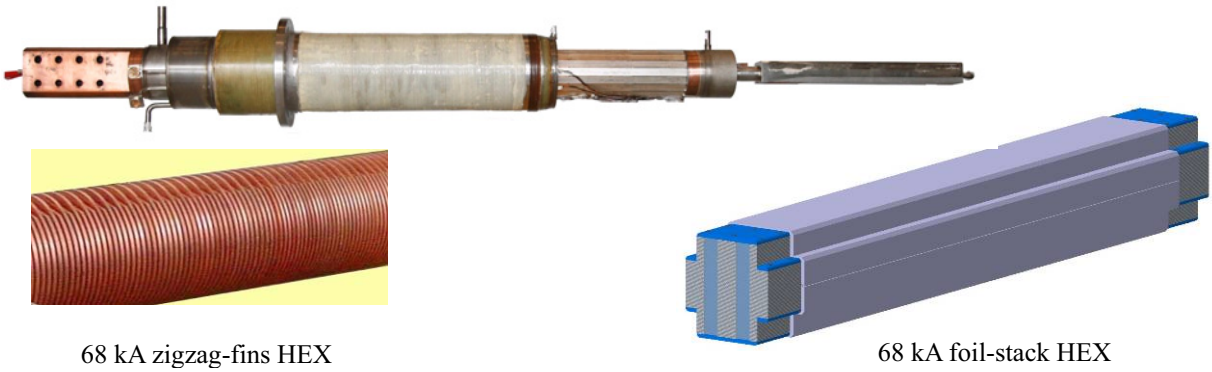

68 kA zigzag-fins HEX

68 kA foil-stack HEX

Fig.7 68 kA trial lead and the two type HEX

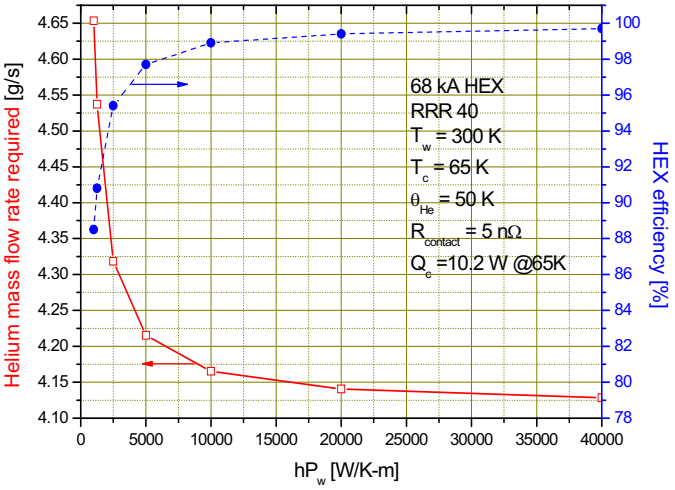

Fig.8 The minimum helium mass flow and efficiency relate to hP_w

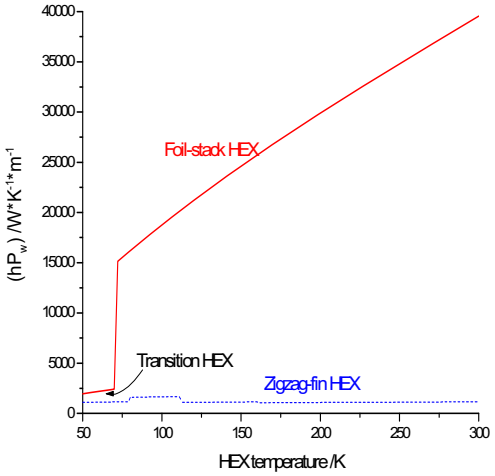

Fig. 9 (hPw) values comparison for the 68 kA lead with different HEX

where A is area of coolant flow channel and U is its perimeter. The ***de*** can reach quite small value (~0.5 mm) if the 0.25 mm gaps between two foils, it leads to higher ***h*** value (~500-1300 W/K*m^2). For a 68 kA foil-stack HEX $\boldsymbol{P_w}$ value is ~31 m if selecting the foil thickness of 0.4 mm and the current density of 11 A/mm^2. But a zigzag-fins 68 kA HEX has much short wet perimeter (3.5-4.6 m) and a larger ***de*** value (> 6 mm) because the gaps between two fins are greater than 2.5-3 mm.

Fig.9 shows a comparison of the hP_w values for the two types HEX. The $\boldsymbol{hP_w}$ values of the most left sections of the profiles are contributed by the transition HEX rather than the main HEX. The $\boldsymbol{hP_w}$ value difference of the other section is very obvious. Lower HEX efficiency not only requires more cooling power, but also leads to the outlet helium with lower temperature, which results in the lead terminal icing or dewing. To protect RT terminals from HV breaking they must be heated by electrical power or water flow. So the foil-stack HEX should be preferred. The helium mass flow rate measured is 0.486 g/s when the 10 kA HTS lead with a foil-stack HEX operated at the optimum current of 8 kA, HTS warm end temperature at 65 K and the inlet helium flow temperature of 50 K. The specific mass flow rate is 0.061 g/s/kA; the efficiency reaches 98.4 %

HEX cooling mass flow rate is also affected by HEX dimension optimum, copper RRR value and contact resistance from HTS stacks to the HEX cold end. The HEX should be made of OFHC copper with RRR > 50. The HEX current density option depends on safety requirement. It should be <= 11 A/mm^2 if the LOFA time > 300 s and there is a transition with current density < 3.5 A/mm^2. The HEX length is the result from optimization simulation [4].

3.2.3. Transition HEX

The 13 kA LHC current lead has a massive transition without cooling flow between the HEX and HTS module, which provides a large heat sink but also requires more mass flow rate for the HEX. We developed a transition HEX for 52 kA and 10 kA leads, which guides 50 K helium flow to cool the copper cap first at the HTS module warmer end then to the main HEX inlet. The current density of the transition HEX can be lower than 3.5 A/mm^2. So it not only improves HTS warmer end cooling but also provides large sink to increase LOFA time. Fig.9 shows the transition structure for a 10 kA lead.

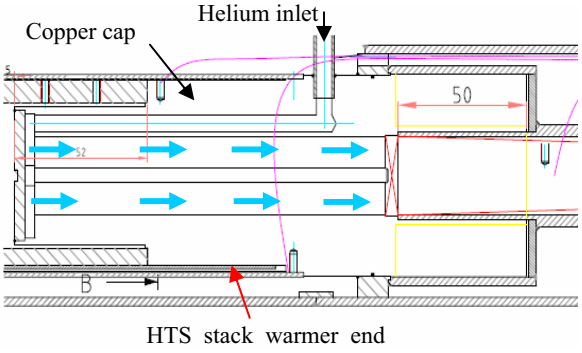

Fig.10 Transition HEX structure for a 10 kA lead

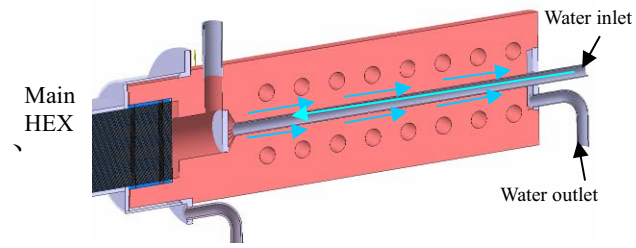

Fig.11 RT terminal with water cooler

3.2.4. RT terminal

The room temperature (RT) terminals of current leads suffer icing or dewing when they operating at lower or zero current. Inserting electrical heaters is a usual way. We found that an inner-cooling/heating water flow inside RT terminal is much more effective than heater cartridges due to very high heat transfer coefficient of water flow and larger wet surface. It makes RT terminal temperature very stable. Fig.11 shows the water cooler/heater design for a 68 kA current lead.

4. Conclusion

HTSCL can save refrigeration power consumption, so it is one of key technologies for fusion reactors. R&D on HTSCL at ASIPP started for EAST in 2003 and continues for ITER magnets. In past 3.5 years the 68/52/10 kA pre-prototype leads have been design, manufacture and tested at ASIPP. From test results following achievements have been obtained:

- ✧ The HTS temperature margin refers to LOFA time requirement; applying an average field for HTS module load line is more reasonable than the maximum.
- ✧ The HEX efficiency can reach >98% if foil-stack type HEX is accepted.
- ✧ Following ITER HTSCL requirements can be met: LOFA time > 350 s, burnout time >16 s, heat leak < 15 W, contact resistance between the HTS stack and copper cap < 10 nΩ at 65 K; < 1 nΩ at 5K (for 68/55/46 kA leads), the joint resistance between LTS module and LTS busbar < 2 nΩ at 5K.
- ✧ Insulator-flange insulating intensity > 30 kV in atmosphere.
- ✧ HTSCL test setup for 10~68 kA leads has been established.

References

[1] ISONO, T. et al., “Test results of 60-kA HTS current lead for fusion application”, Physica C 392-396 (2003), 1219-1224.
[2] HELLER, R. et al., “Experimental Results of a 70 kA High Temperature Superconductor Current Lead Demonstrator for the ITER Magnet System”, IEEE Trans. On Appl. Supercond., vol.15, no.2, pp. 1496-1499, June 2005.
[3] BALLARINO, A. et al., “13000 A HTS Current Leads for the LHC Accelerator: from Conceptual Design to Prototype Validation”, European Organization for Nuclear Research, 2003, Geneva
[4] SEEBER, B ed., Handbook of Applied Superconductivity, Université de Genève, Switzerland, Jan 1998.

Manufacturing Progress of ITER TF Coil in Japan

K. Matsui
Japan Atomic Energy Agency, 801-1 Mukoyama, Naka-shi, Ibaraki, 311-0193, Japan
Corresponding author: matsui.kunihiro@jaea.go.jp

Japan Atomic Energy Agency (JAEA) has a responsibility of the procurement of 25% of TF conductor, 9 TF winding packs and 19 TF coil cases as Japanese Domestic Agency (JADA). The TF conductor is a circular shaped cable-in-conduit conductor, which is composed of a cable and a stainless steel jacket, and its maximum length is 760 m. JAEA started to produce strands, cables, jackets and to contract a jacketing facility from 2008, and a jacketing facility, dummy cable, jacket sections and procedures have been prepared in December 2009. After the preparation, JAEA fabricated the 760-m Cu dummy conductor as a process qualification. Furthermore, JAEA has contracted companies for fabrication trials of a full-scale RP and winding trials of a one-third scale double pancake to verify feasibility of the required tolerances from an industrial view point. Prior to these trials, JAEA developed a preliminary manufacturing plan, and industry is carrying out small-scale trials to demonstrate applicability of the manufacturing plan. The progress of the TF conductor procurement, results of the small-scale trials and progress on the reduced and full-scale trials are presented.

1. Introduction

The magnet system for ITER as shown in Fig. 1 comprises 18 toroidal field (TF) coils, using a Nb3Sn cable-in-conduit conductor [1] as shown in Fig. 2, which is cooled through the forced flow of 4.5 K supercritical helium. The TF coil (TFC) consists of a winding pack (WP) and a coil case, and the WP consists of 7 double pancakes (DP) that come in two types, a regular DP (rDP) and a side DP (sDP) [2], as shown in Fig. 3.

The Japan Atomic Energy Agency (JAEA) has the responsibility to procure 25% of TF conductors, 9 TF WPs and 19 TFC cases including one case for the spare, as the Japanese Domestic Agency (JADA). JAEA signed the Procurement Agreement (PA) of TF conductor on November 2007, and has started the process qualification. After that, the series production of TF conductor has been started from April 2010. JAEA also signed the PAs to procure TF WP and TFC case on November 2008, and has started several mock-up trials for the solution of technical issues for the manufacturing process from April 2009. In this paper, the progress of TF conductor manufacture and mock-up trials for the manufacturing TF WP and TFC case are described.

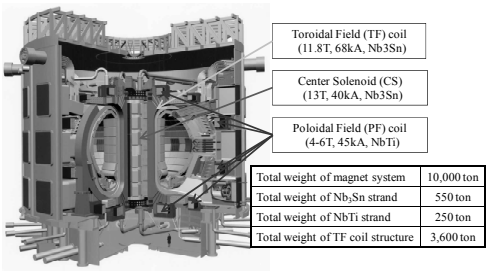

Fig. 1 ITER magnet system

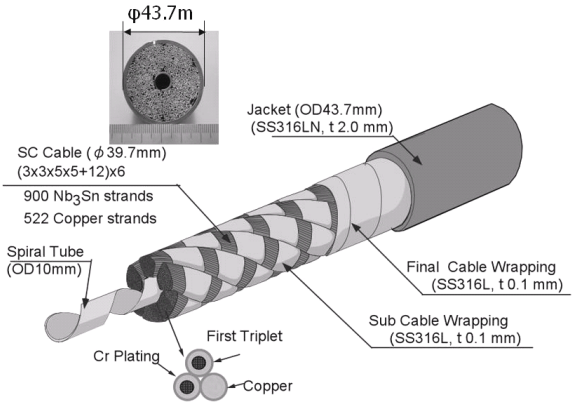

Fig. 2 ITER TF conductor

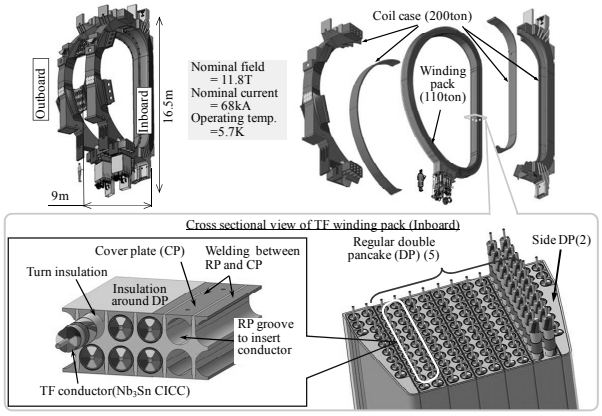

Fig. 3 Composition of TF coil

2. Manufacture of TF conductor [3]

The procurement activities of the TF conductor proceed sequentially through four phases; Phase I: Pre-production and contract singing with industries, Phase II: Preparation of procedures and process qualification, Phase III: Pre-production, and Phase IV: Series production. Phase I activities had completed by the signature of the PA, and the Phase II activities have started after the signature. Results in Phase II activities are described below.

2.1 Jacketing process and facility

The jacketing process that manufactures a TF conductor is summarized as shown in Fig. 4, and is as follows; 1) Fabrication of jacket sections and assembly of jackets by Gas Tungsten Arc Welding without filler to make a 760-m or 430-m long tube, 2) NDT of each welding joint by a radio graphic test (RT), dye penetrant test (PT), a local helium leak test and visual inspection, 3) Cable insertion through a long jacket, 4) Compaction of the jacket with cable, 5) Spool of the compacted conductor on a mandrel with a 4 m diameter, 6) NDT of conductor by a global helium leak test, PT, a pressure proof test, a flow test and a dimensional measurement.

JAEA constructed a jacketing facility for the manufacture of the TF conductor as shown

in Fig. 5. The facility has a long straight line for the cable insertion through a welded long jacket, and two large building for the jacket welding, the inspections, the compaction and the conductor spool. There are two assembly lines to manufacture two conductors in parallel in the facility.

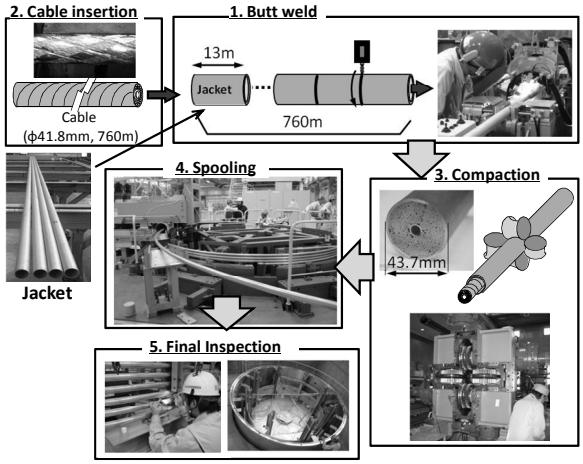

Fig. 4 Jacketing process of TF conductor

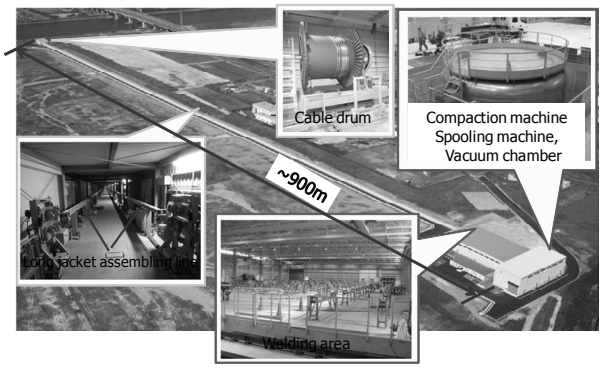

Fig. 5 Jacketing facility

2.2 Qualification of jacketing process

Before the fabrication of a conductor, manufacturing and inspection procedures are prepared. And a 760-m Cu dummy conductor is manufactured based on these procedures for the qualification of the jacketing process.

2.2.1 Welding of jacket sections

One path GTAW without filler is applied for full penetration of jacket sections using an automatic orbital machine, and its qualification is performed based on ASME Section VIII Div.2 and IX. The process qualification includes the RT, PT, a bend test and a full size tensile test at room temperature, a visual inspection o weld bead, go-gauge test and the local helium leak test at 3 MPa. The weld joint samples for the qualification test were manufactured, and all of samples have been passed above inspections. After that, four tensile test specimens were cut from them and tested at 4.2 K. As results of tensile tests, 0.2% offset yield strength (0.2%YS) and elongation at 4 K satisfied the requirements of more than 950 MPa and 30%.

2.2.2 Cable insertion

The biggest concern in the jacketing is a force to pull cable through the jacket. To reduce the pulling force as low as possible. The cleaning of the jacket inner surface, the control of protrusion of weld bead and the shrinkage, and the straightening of the cable before the cable insertion has been taken. The supplied cable is straightened by a set of rollers, and inserted in the jacket with the speed with 2 m/min. The pulling force as a function of cable length is shown in Fig. 6, and the maximum force is 32 kN. The pulling force per unit length is 42 N/m, and is similar value to 40 kN/m of 200-m long ITER TF model coil jacketing [4].

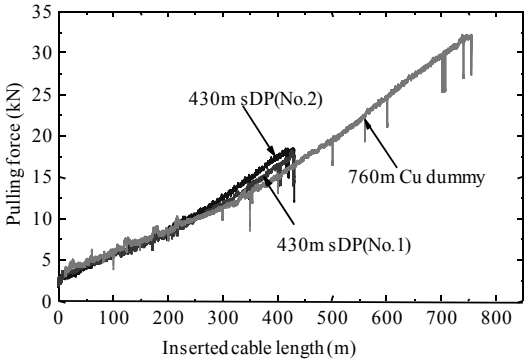

Fig. 6 Cable pulling force

2.2.3 Compaction, spooling and final inspection

After the cable insertion, the jacket and cable is compacted by the compaction machine, and the compacted conductor is spooled by the mandrel. The compaction and spooling speed is 2 m/min. The outer diameter of the Cu dummy conductor was measured after spooling, and satisfied the target value of 43.7 mm +/-0.3 mm. Furthermore, the global helium leak test at the inner pressure of 3 MPa and dye penetrant test are performed. No leak is detected with a background leak signal of 4 x 10-9 mbar liter/s, and no indication of PT is also detected.

From these qualification test results, the 760-m long Cu dummy conductor has been manufactured, and the qualification of TF conductor jacketing has successfully been completed.

2.3 Production of TF conductor

JAEA has manufactured the 100-m and 430-m long TF conductors as the process qualification of TF conductor jacketing. The 760-m long Cu dummy and 430-m long TF conductors are shown in Fig. 7. The conductors have successfully been manufactured, after that JAEA has manufactured two 430-m long TF conductors as the pre-production.

760-m Cu dummy conductor　　430-m TF conductor (for sDP)

Fig. 7 760-m Cu dummy and 430-m TF conductors

3. Trials for manufacture of TF WP [5]

The procurement activities of the TF WP proceed through four phases; Phase I: Contract winging with industries, Phase II: Process qualification, Phase III: Manufacturing of tooling and fabrication of the first TF coil, and Phase IV: Series production.

The TF coil manufacturing process is illustrated in Fig. 8 [2]. In the Phase II activity, JAEA and industry initially developed a preliminary TF coil manufacturing plan (TFMP) and are performing several small-scale trials to demonstrate the applicability of TFMP. The targets of these trials are as follows; 1) Demonstration of RP manufacturing techniques which achieve the required tolerances of ±1 mm in flatness, a few mm in in-plate deformation and groove length within ±0.01%, 2) optimization of manufacturing procedures for the cover plate (CP) by cold-drawing and bending to reduce manufacturing costs, 3) accuracy in winding to achieve the target conductor length of the order of 0.01%, 4) measurement of conductor elongation as a result of heat treatment, 5) demonstration of the feasibility of laser welding between the RP and CP and evaluation of the deformation from CP welding, and 6) insulation and impregnation [6] to sustain 19 kV DC and 2.5 kV AC while subjected to a total radiation dose of $1x10^{22}$ fast n/m. From end of 2009 until mid-2010, the winding trials of 1/3 scale DP and the machining trials of the RPs constitute the chief items of above focus because of their critical importance in the fabrication process [2]. Results are described below.

3.1 Conductor winding

For the winding trial, the winding system for 1/3 scale DP was constructed. The winding system is shown in Fig. 9, and consists of a conductor mandrel, benders, a winding head with a system for measuring the entire length of the conductor [7] and a winding table for the wound conductor. A conductor with a curvature of 2 m wound around a mandrel is stretched to a curvature of 4.5 m by the first bender, and is straightened by the straight bender. The straightened conductor is inserted into the winding head and its length is measured with a high accurate measurement system consisting of a laser marker and CCD cameras [7]. After that, the conductor is wound to the target curvature using 3-point bending rollers in the winding head, and subsequently inserted into the groove of the winding table.

In the commissioning of the winding head, a bending test using a dummy conductor was performed. The conditions of the bending rollers are determined based on the S-S curve obtained by the tensile test using a dummy conductor. In the first bending test, the measured curvature of the bent conductor differed by 5~10% from expected results as shown in Fig. 10. Therefore, an adjusted S-S curve is used to obtain better agreement. The relationship between the position of the bending roller and the bending curvature is shown in Fig. 10. The measured curvature is in good agreement with the expected curvature. These results demonstrate that highly accurate winding procedure has been developed. After the commissioning of this system, the winding trials of the 1/3 scale DP using a dummy conductor were performed. In this winding trials, two pancakes which were the upper and lower pancakes of the 1/3 scale DP were fabricated, and were inserted in the groove of the

winding table as shown in Fig. 11. As the results of the trial, it was confirmed that it was able to control the conductor length with the sufficient accuracy, and to bend the conductor to the expected curvature.

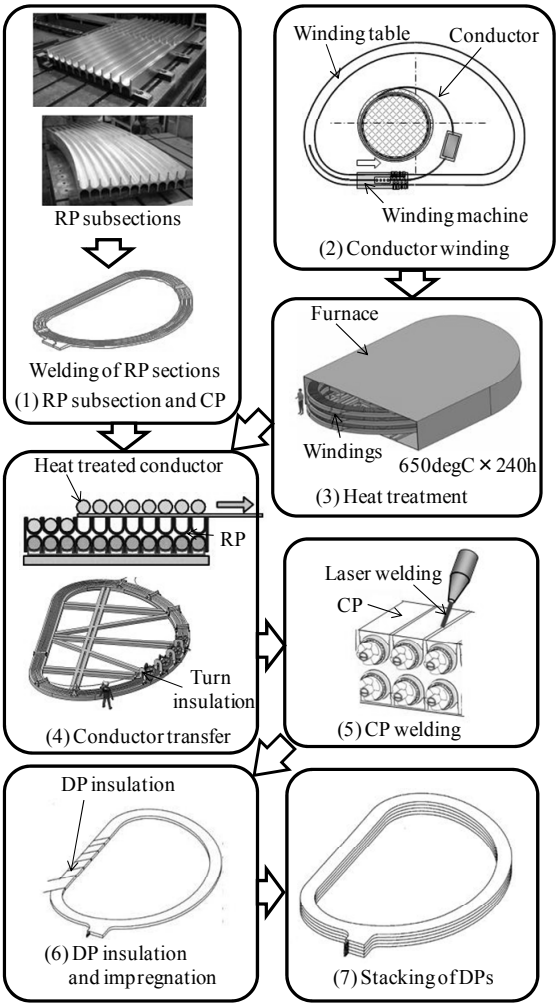

Fig. 8 TF coil manufacturing process

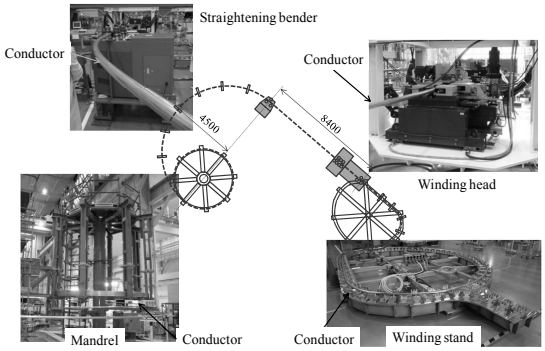

Fig. 9 Winding system for 1/3 scale DP

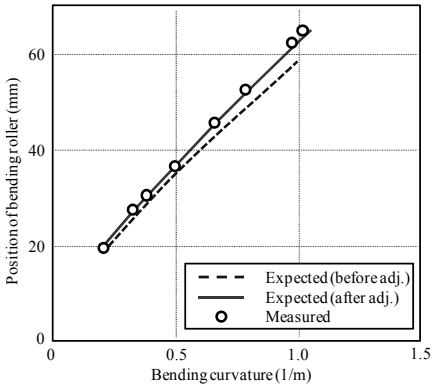

Fig. 10 Relationship between the position of the bending roller and the expected and measured curvature

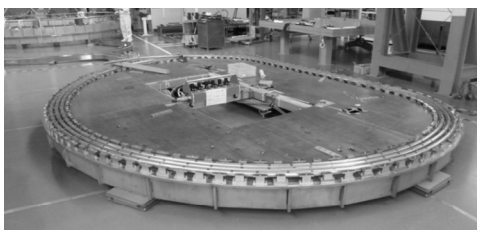

Fig. 11 Lower pancake inserted in the groove of the winding table

3.2 Radial plate machining

For the verification of the RP machining process, machining trials of two RP mock-ups which were for a terminal and inboard regions of the WP as shown in Fig. 12 were performed. The machining process has four steps, 1) surface machining to be flat the RP plate, 2) rough machining to make the groove roughly, 3) pre-finish machining to make the bottom of the groove roughly, and 4) final machining to complete the groove. The RP plate was clamped with the jigs to prevent the distortion during the machining. The completed RP mock-up for the terminal region is shown in Fig. 12. The flatness of the completed RP mock-ups was less than 1 mm and satisfies the required tolerances of ±1 mm.

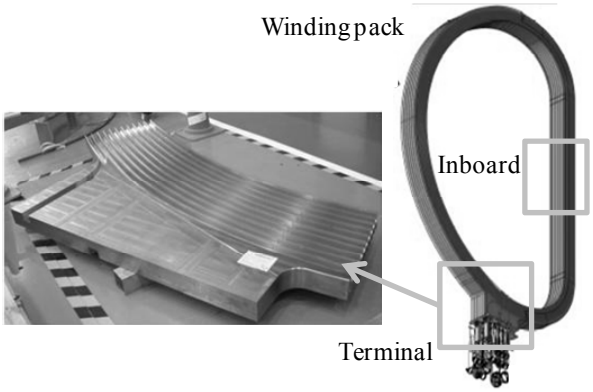

Fig. 12 Machined RP mock-up for terminal region

4. Trials for manufacture of TFC case [8]

The procurement activities of the TFC case proceed though four phases as same as that of the TF WP. The fabrication procedure of TFC case is illustrated in Fig. 13 [9]. The material planned to be used for the TFC case are fully austenitic stainless steel having high strength and high toughness properties, specified in four classes (FMJJ1, FM316LNH, FM316LNM, and FM316LNL) by JSME (The Japan Society of Mechanical Engineering) Code [10]. In the Phase II activity, JAEA and industries perform qualification tests of the material and trial fabrications with mock-ups. In the qualification tests of the material, the chemical composition and Yield strength (YS) of fabricated materials are evaluated to satisfy the each requirement of four class materials. In the trial fabrication with mock-ups, a 1m-long mock-up of the inboard straight part is fabricated in order to investigate the weldability and welding deformation. After that, the trial fabrication of the A1 and B3 segments which have several kinds of parts are fabricated. In this section, results of trial fabrication of the A1 segment are described.

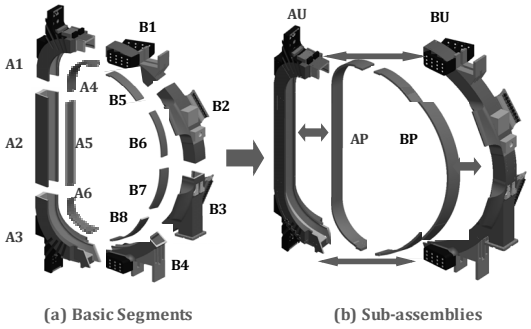

Fig. 13 Fabrication procedure of TFC case

4.1 Trial fabrication of A1 segment

The A1 segment has the complicated shape including PCR (Pre-Compression Ring) flanges and ribs. Several kinds of parts were forged during trial fabrication are shown in Fig. 14. Before starting A1 trial fabrication, preliminary tests shown in Fig. 15 were performed to confirm the following critical procedures; 1) joints between outer plate and side plate (welding position changes from vertical-up to flat), 2) joint between PCR side ribs and coil case outer plate (welding position changes along the curved welding line), and 3) welding procedure of the between PCR flange and coil case outer plate (welding depth is 260 mm with one-side welding). No problems were found as results of preliminary tests and appropriate welding parameters obtained during preliminary tests are used for the trial fabrication of the A1 segment.

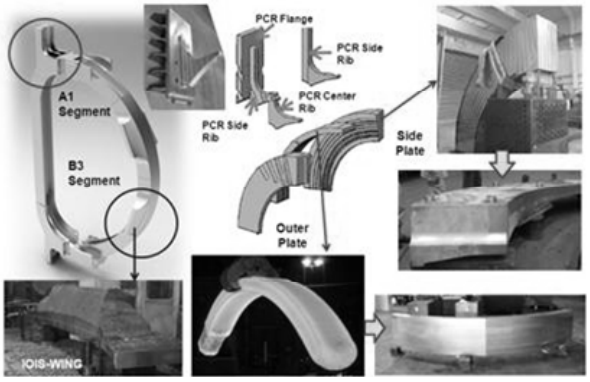

Fig. 14 Trial fabrication of forged parts

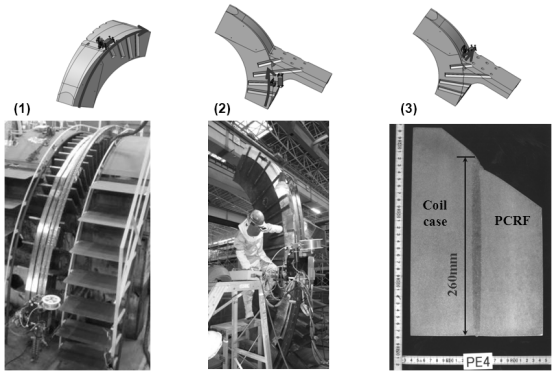

Fig. 15 Preliminary test before A1 segment trial fabrication

5. Summary

JAEA has started the procurement of the TF conductor and several trials for the manufacturing of the TF coil. The progress of these activities is summarized below:

(1) The qualification of fabrication process of the TF conductor and the fabrication of 760-m dummy and two SC conductors has already completed.

(2) Five 430-m and two 760-m TF conductors are fabricated by the end of October 2010.

(3) JAEA has contracted with TOSHIBA as the main contractor for developing a suitable manufacturing technique for the TF winding pack and TFC case.

(4) The several mock-up trials were performed as the process qualification, and several manufacturing techniques for manufacture the TF winding pack and TFC case are obtained.

References

[1] N. Mitchell, et al., “Status of the ITER magnets”, *Fus. Eng. Des.*, 84 (2009) 113-121

[2] N. Koizumi, et al., “Study of the Manufacturing Process of the ITER TF Coil Winding Pack” *Fus. Eng. Des.*, 84 (2009)210-213

[3] K. Hamada, et al., “First Qualification of ITER Toroidal Field Coil Conductor Jacketing”, Presented in 26th Symposium on Fusion Technology.

[4] A. della Corte, et al., "Successful completion of the conductor manufacture for the ITER TF model coil", Proc. 20th SOFT (1998)841-844

[5] K. Matsui, et at., “Progress of mock-up trials for ITR TF coil procurement in Japan”, Presented in 26th Symposium on Fusion Technology.

[6] T. Hemmi, et al., “Development of Insulation Technology with Cyanate Ester Resin for ITER TF Coils”, *Fus. Eng. Des.*, 84(2009)923-927

[7] N. Koizumi, et al., “Results of R&D on ITER-TF Winding Critical Issues”, *IEEE Trans. ASC*, 18(2008)475-478

[8] Y. Chida, et al., “Validation of Welding Technology for ITER TF Coil Structures”, Presented in 26th Symposium on Fusion Technology.

[9] M. Nakahira, et al., JSME Construction Standard for Superconducting Magnet of Fusion Facility “Fabrication, Installation, NDE and Testing”, ASME PVP2009-77639 Prague.

[10] JSME (The Japan Society of Mechanical Engineers) , Codes of Fusion Facilities – Rules on Superconducting Magnet Structure -, JSME S KA 1-2008, Maruzen (2008) (in Japanese).

Preparation and Cryogenic Properties of Radiation Stable Epoxy Composite

Z. X. Wu 1) 3), H. Zhang 1) 3), H. H. Yang 1) 3), X. X. Chu 1) 3),
Y. T. Song 2), W. Y. Wu 2), H. J. Liu 2), L. F. Li 1)

1) The Key Laboratory of Cryogenics, Technical Institute of Physics and Chemistry, Chinese Academy of Sciences, China
2) Institute of Plasma Physics, Chinese Academy of Sciences, China
3) Graduate University of Chinese Academy of Sciences, China

E-mail: zxwu@mail.ipc.ac.cn

Abstract. Impregnating resins in fusion magnet technology are required to be radiation stable, low viscosity, long usable life and high toughness. To meet these objectives, we developed a new epoxy based composite which consists of triglycidyl–p-aminophenol (TGPAP) epoxy resin and isopropylidenebisphenol bis[(2-glycidyloxy-3-n-butoxy)-1-propylether] (IPBE). The ratio of TGPAP to IPBE can be varied to achieve desired viscosity and working time. The boron free glass fiber reinforced composites were prepared by vacuum pressure impregnation. The radiation resistance was evaluated by ^{60}Co γ–ray irradiation of 1 MGy at ambient temperature. The mechanical properties of the composites have been measured at room temperature and at 77 K.

1. Introduction

Glass fiber reinforced plastics (GFRPs) consisting of boron-free glass fibers and organic matrix materials, especially epoxy resin based composite, have been widely used as insulating materials in cryogenic engineering fields because of their low cost, ease of processing, excellent mechanical, thermal and electrical properties [1]. In superconducting magnet systems, the insulation systems are subjected to a critical situation caused by the radiation environment at cryogenic temperatures. However, the organic matrix materials are sensitive to the high radiation dose level and may be damaged resulting in degrading mechanical and electrical insulation performance and affecting the performance of the entire magnet system. Therefore, it is important and necessary to develop the insulation materials which exhibit good mechanical strength and radiation resistance at cryogenic temperatures.

Recently, there have been a number of studies on developing high-quality fiber reinforced composites as electrical insulation at cryogenic temperatures [1-6]. With regards to epoxy systems, radiation tolerance increases with resin functionality. Unfortunately multifunctional epoxies tend to have relatively high viscosities and short working time that do not permit their application for vacuum pressure impregnation (VPI). In addition, some high functionality resins are known to be brittle and therefore have an increased probability of cracking when cooled to low temperatures.

Impregnating resins in fusion magnet technology are required to be stable for radiation, and have low viscosity, long usable life and high toughness. To meet these objectives, a blend of a

low viscosity tri-functional resin triglycidyl–p-aminophenol (TGPAP) and an aromatic flexible resin isopropylidenebisphenol bis[(2-glycidyloxy-3-n-butoxy)-1-propylether] (IPBE) was used in this study. All resins were hardened with a liquid aromatic amine diethyl toluene diamine (DETD) and reinforced by boron-free glass fibers. The properties of the composite materials were investigated at ambient temperature and 77 K before and after irradiation.

2. Experiment

2.1. Materials

The base resin, TGPAP (AFG-90 from the Institute of Synthetic Resin, Shanghai), is a low viscosity tri-functional resin, known for its radiation stability. The aromatic flexible resin, isopropylidenebisphenol bis[(2-glycidyloxy-3-n-butoxy)-1-propylether] (IPBE or PY 4122 from Huntsman), is a DGEBA type resin with substituted butoxy groups which creates an internally flexibilized resin that fully reacts into the structure when blended with other resins. The hardener, diethyl toluene diamine (DETD typically Huntsman HY 5200), is a liquid aromatic amine. The glass cloth is boron free, silane treated, 240 g/m^2 plain weave, with 18±1 threads per centimeter in the warp (length) direction and 14±1 threads per centimeter in the fill (width) direction (RW220-90, Sinoma Science and Technology Co., China). The thickness of the cloth is quoted as 0.2±0.022 mm.

2.2. Specimen preparation

The composition and processing details are listed in table Ⅰ and table Ⅱ, respectively. Composite panels were prepared at 4 mm, 10 mm and 20 mm thickness using 20 layers, 50 layers and 100 layers of glass cloth, respectively. Prior to the impregnation process, the metal mould tool filled with the required number of glass fiber layers need a heat treatment at 45°C for 10 hours. In addition, the release agent was rubbed into the surface of the metal mould tool to enable easy detachment of the laminate after the vacuum pressure impregnation (VPI) process. Glass, resin and void content was determined for each formulation and these are shown in table Ⅰ. These data are derived from the measured density of resin, glass and composite and from the determination of the weight fraction of glass in the composite.

Table□ Formulation of resin systems (pbw = parts by weight)

Resin System	TGPAP pbw	IPBE pbw	DETD pbw	Glass Content Vol. %	Resin Content Vol. %	Void Content Vol. %
1	100	0	44	42.5	57.0	<0.5
2	85	15	39	41.8	56.7	<0.5
3	75	25	36	41.9	56.6	<0.5
4	60	40	31	42.4	57.1	<0.5

Table □ Resin processing schedule

Processing temperature	45 ^{o}C
Gel temperature and time	80 ^{o}C ±3 ^{o}C for 10 h
Cure temperature and time	120 ^{o}C ±3 ^{o}C for 10 h

2.3. Irradiation and test procedures

In order to investigate the influence of irradiation on the properties of the TGPAP system, half of the samples were irradiated at ambient temperature by ^{60}Co γ-ray irradiations. The reactor is operating at a γ-dose rate of 100 Gy/min. The total absorbed dose was up to the dose of 1×10^{6} Gy.

The viscosity was measured for the resin system using a Brookfield DV 2 viscometer which is equipped with a thermostatically controlled water bath for temperature control.

The short beam shear (SBS) tests, the flexure tests and the compression tests were carried out at 300 K and 77 K using a MTS-SANS 100 kN microcomputer control electronic universal testing machine in combination with a cryostat. The apparent interlaminar shear strength (ILSS) was determined by short-beam bending test according to the ASTM D2344. A cross-head speed of 1 mm/min, and a sample thickness of 10 mm were used. The flexure tests was carried out according to the ASTM D2344. A cross-head speed of 1 mm/min, and samples with outer dimensions of 60 mm × 10 mm × 4 mm (length × width × thickness) were used. Through-thickness compression strength was assessed on small specimens with outer dimensions of 7 mm × 7 mm × 20 mm (length × width × thickness) according to ASTM D695.

3. Results and discussions

3.1. Processing characteristic

Impregnating resins are required to have low viscosity and long usable life. In generally, the epoxy systems with aromatic amine curing agents have shorter usable lives than that with anhydride curing agents. In order to determine the useful working life of these formulations, we have measured the viscosity for several ratios of TGPAP to IPBE at 45°C. The viscosity of these formulations as a function of time are shown in figure 1. The results indicate that IPBE can reduce the initial mixed viscosity of TGPAP-based epoxy resins and also slow the reaction rate with the hardener resulting in extending the effective working life and improving the processing characteristic. If the ‘end point’ for vacuum impregnation is taken as 500 mPa·s, the usable life for this system is around 17 hours at 45 °C for the base resin/hardener alone and around 24 hours when 30 pbw (pbw = parts by weight) of resin IPBE is added.

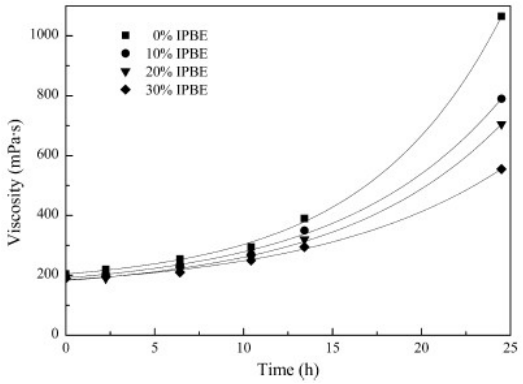

Figure 1. Viscosity versus time for TGPAP/DETD/IPBE resin system at 45 ^{o}C

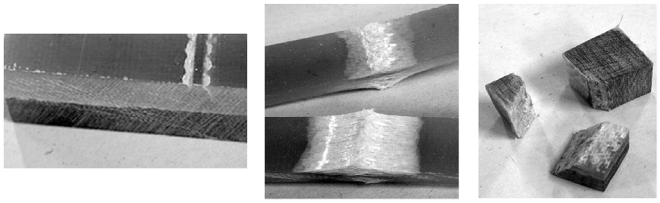

Figure 2. Broken style of interlaminar shearing specimen(a), flexure specimen(b) and compression specimen(c)

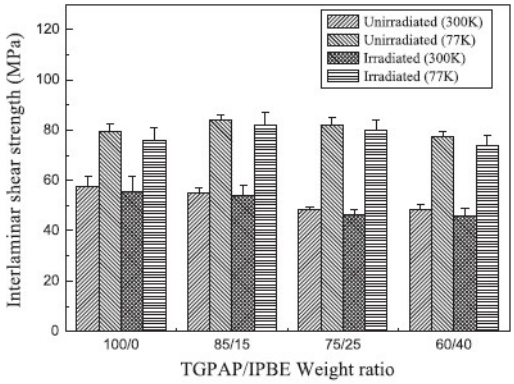

Figure 3. Results of interlaminar shear strength tests

3.2. Mechanical properties

3.2.1 Interlaminar shear strength

In the fusion superconducting magnets, the insulating materials are usually subjected to high mechanical stresses, such as the compressive stress and the flexural stress. The combination of these stresses induce interlaminar shear stress which results in the large deformation or local failure at the interlaminar area. The interlaminar shear strength (ILSS) may be defined as the resistance of a layered composite to internal forces that tend to induce relative motion parallel to, and between, the layers. Since it critically depends on the matrix-reinforcement interface, ILSS is the most sensitive indicator and has been widely used to estimate the change in composite properties with radiation dose. Recently, the short-beam shear test (ASTM D2344) has become a widely used method for characterizing the interlaminar failure

resistance of fiber-reinforced composites. Since the increase in shear strength may be larger than that in tensile strength when a specimen is cooled to low temperatures, a value of the span-to-thickness ratio less than 5 may be necessary to produce shear failure. In this work, to ensure interlaminar shear failure mode, a span-to-thickness ratio of 5:1 and 4:1 were used for room-temperature testing and for low-temperature testing, respectively. As shown in figure 2(a), all specimens failed with a single interlaminar shear failure along the centre line of the specimen. The apparent interlaminar shear strength was calculated from $3\times P_f/(4\times b\times h)$, where P_f is the applied load, b is the specimen width, and h is the specimen thickness. The test results are presented in figure 3. These results indicate that additions of IPBE resin do not significantly change the ILSS of materials tested at 300 K or 77 K. In the unirradiated state, the ILSS lies between 48 and 57 MPa at room-temperature and between 77 and 84 MPa at low-temperature. After ^{60}Co γ-ray irradiation up to the dose of 1×10^6 Gy, no distinct changes of the material performance were observed.

3.2.2 Flexure strength

It is well known that stresses that are caused by bending vary through the thickness in the composites. These flexural stresses are the maximum at the outer surfaces and zero in the middle at the neutral axis. For pure bending, if the composite is stronger in compression than in tension, the composite failure would initiate on the tensile side. Typical failure mode is shown in figure 2(b). In this work, the specimens showed tensile failure. As loading progressed, cracking developed on the tensile side and progressed towards compression side.
Figure 4 shows flexural strength obtained in three point flexural test both at 300 K and 77 K before and after irradiation. The flexural strength increases with decreasing temperature. For the unirradiated state, the flexural strength at 77 K is higher than that of room temperature. The test results show that irradiation affected scarcely to the flexure properties.

3.2.3 Compressive strength

The results of through thickness compression test are showed in figure 5. The compressive strength increases with decreasing temperature. For the unirradiated state, the through-thickness strength at 77 K is about 55% higher than that of room temperature. The measured failure strength is in the range from 418 to 458 MPa at room-temperature and from 645 to 813 MPa at low-temperature, which was found to be similar to that measured for G10 and G11 [7]. Similarly to the SBS test results, no significant degradation of the compressive strength at room temperature or at 77 K is observed after irradiation. For through thickness compression tests, a 45° failure mode was observed in all specimens and the typical photo of actual failure mode is illustrated in figure 2(c). The angular splitting was caused by both the matrix cracking and fiber breakage, while the horizontal splitting was caused by the delamination between the plies.

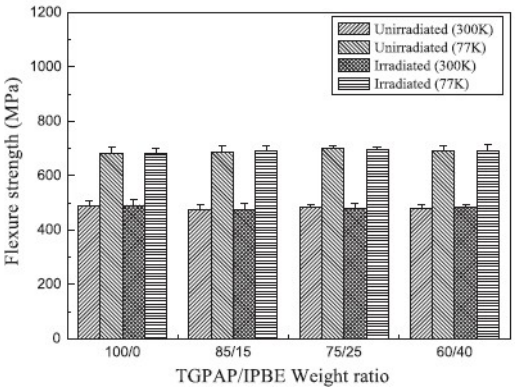

Figure 4. Results of flexure strength tests

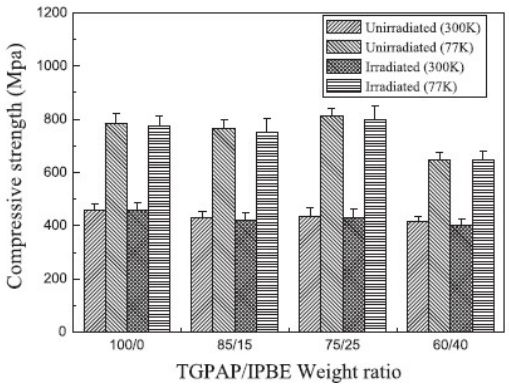

Figure 5. Results of compressive strength tests

4. Conclusion

A new radiation stable epoxy resin system has been developed which might be suitable for VPI process. IPBE improves the processing characteristic. The boron free glass fiber reinforced composites were prepared by VPI process and irradiated at ambient temperature by ^{60}Co γ-ray irradiations up to the dose of 1×10^{6} Gy. The mechanical properties of the composites are as following:

(a) The ILSS and the flexure strength at room temperature and low temperature were equivalent to other, less radiation stable resins.

(b) The through thickness compressive strength was showed to be similar to that of G10 and G11.

(c) Irradiation does not have significant influences on the mechanical properties.

From this work, the composites appear to be radiation resistant to a dose of 1 MGy but further work is required to determine the behavior at the larger radiation dose.

References

[1] Bittner-Rohrhofer K., et al., “Mechanical behavior of the ITER TF model coil ground insulation system after reactor irradiation”, Cryogenics, 2002;42(11):697-704.

[2] Zhang H., et al., “Properties of some toughened ,radiation stable epoxy resins”, Advances in Cryogenic Engineering, 2008;54:174-181.

[3] Schutz J.B., et al., “Radiation resistant epoxy for resin transfer molding fabrication of cryogenic electrical insulation”, Advances in Cryogenic Engineering, 2000;46A:197-204.

[4] Fabian P.E., et al., “Novel radiation-resistant insulation systems for fusion magnets”, Fusion Engineering and Design, 2002;61-62:795-799.

[5] Prokopec R., et al., “Mechanical strength of various cyanate ester/epoxy insulation systems after fast neutron irradiation to the ITER design fluence and beyond”, Fusion Engineering and Design, 2007;82:1508-1512.

[6] Prokopec R., et al., “Influence of various catalysts on the radiation resistance and the mechanical properties of cyanate ester/epoxy insulation systems”, Fusion Engineering and Design, 2009;84:1544-1547.

[7] Kasen M.B., et al., “Mechanical, electrical and thermal characterization of G-10CR and G-11CR glass cloth/epoxy laminates between room temperature and 4K”, Advances in Cryogenic Engineering, 1980;26:235-243.

Force-Balanced Helical Coil for Superconducting Magnetic Energy Storage

S. Nomura
Meiji University
1-1-1 Higashimita Tama-ku, Kawasaki-shi, Kanagawa 214-8571 Japan
nomuras@meiji.ac.jp

Abstract

Superconducting coils require special considerations for induced electromagnetic forces to limit allowable tensile stresses, especially in large scale superconducting magnetic energy storage (SMES). To overcome this problem, the author developed the concept of the force-balanced coil (FBC) which is a helically wound hybrid coil of toroidal field coils (TFCs) and a solenoid. The FBC can significantly reduce the required mass of the structure for induced electromagnetic forces. By exploiting this feature, the FBC can become one of the feasible options as a superconducting coil configuration for SMES. In order to demonstrate the feasibility of the FBC concept, a superconducting model coil was developed. From the excitation test results, the model FBC could be successfully excited up to 6.3 T without reinforcing materials for the NbTi/Cu strand. Additionally, in this paper, the author also summarized the concluding results of a road map of large scale SMES based on the progress of large superconducting coils which have been applied to particle detectors for high energy physics and magnetic confined nuclear fusion experimental devices. From the results, the technical status is already established to develop the several MWh class SMES for frequency controller and power compensator.

1. Demonstration Model Development of the Force-Balanced Coil

The FBC is a helically wound hybrid coil of a solenoid and TFCs. By selecting an optimal winding configuration, the FBC can balance the electromagnetic forces of a solenoid and TFCs, and control the distribution of the mechanical stress in the superconducting coil. Theoretically, the FBC can reduce the required mass of the structure for the same magnetic energy to a quarter of that in the TFCs case and less than half of that in the solenoid case [1].

Figure 1 shows a photograph and a schematic illustration of the superconducting model coil using NbTi/Cu composite superconductors. The hand-made winding was finished with 10584 poloidal turns after four months. The critical coil current and the critical magnetic field are 552 A and 7.1 T with a cooling temperature of 4.2 K, respectively. This FBC will have 270 kJ of the maximum magnetic energy.

Based on the virial theorem, the maximum mechanical stress of the FBC winding was designed within the elastic limit of the Cu matrix [2]. Therefore the hand-made windings of the model FBC are neither impregnated with epoxy resin nor reinforced with stainless steel wires. This means that the electromagnetic forces of the model FBC are mainly supported by the tensile stresses in the NbTi/Cu strand itself.

Four test runs were conducted at intervals of several months with liquid helium cooling, including supercooled liquid helium based on the saturated vapor pressure. Each test run was started by cooling down from room temperature. In the quench tests, the model FBC was

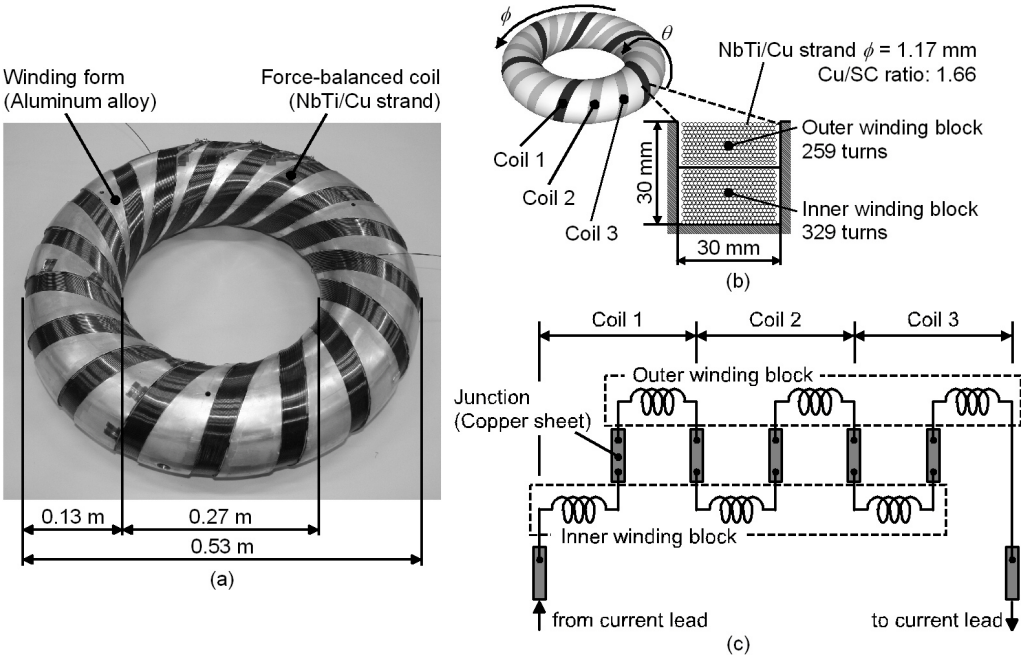

Figure 1: Photograph (a), schematic illustration (b), and equivalent circuit (c) of the model coil based on the FBC design. The darker hatch in the schematic illustration of the model FBC indicates one complete helical winding. The model FBC is composed of three helical coils. Each helical coil has 6 poloidal (θ direction) turns per toroidal (ϕ direction) turn, and consists of two winding blocks. These helical windings are connected in series.

usually excited with a rump rate of 1 A/s.

Figure 2 summarizes the training history of the model FBC. The maximum quench current reached 492 A with a cooling temperature of 4.2 K. This quench current is corresponding to 89% of the critical coil current. The model FBC could be successfully excited up to 6.3 T without reinforcing materials for the NbTi/Cu strand. Additionally, the model FBC maintained the training phenomena even after the coil was warmed up to room temperature. This property is one of the remarkable coil performances for SMES.

However, the model FBC required over 100 quenches in order to be excited up to 6.3 T. From the results in Figure 2, even when the model FBC was cooled with the supercooled liquid helium, the quench currents were not significantly improved. Since the windings of the FBC have a three-dimensional complex shape, the strong winding tension could not be directly applied to the NbTi/Cu strand. Due to this, it can be considered that the strand motion events, which induced the quenches, might occur in the helical windings. The author also investigated the relationship between the quench properties and the helical winding conditions of the model FBC based on the acoustic emission (AE) monitoring [3], [4]. As a further step of this work, the FBC winding configuration should be optimized in order to improve the coil performance.

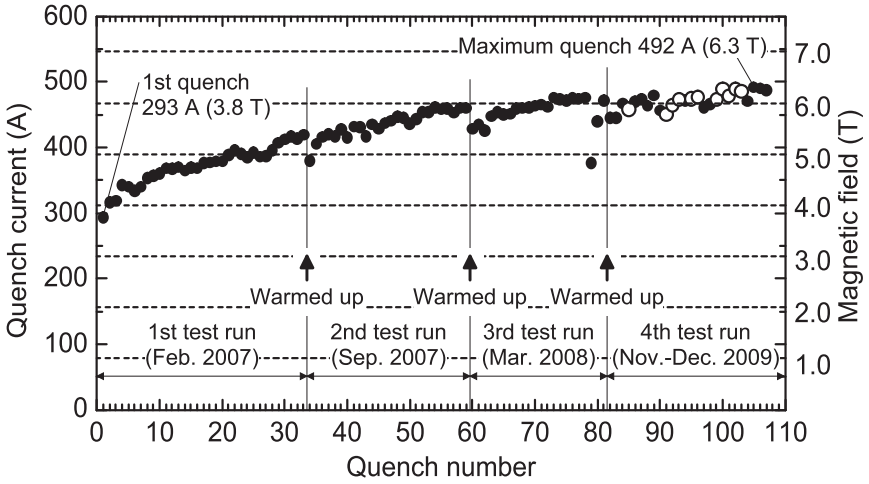

Figure 2: Training history of the model FBC. Each test run was started by cooling down from room temperature. 107 quench tests, including 11 supercooling tests, were conducted in total. Black circles indicate the quench currents with a cooling temperature of 4.2 K. White circles show supercooling test results based on the saturated vapor pressure curve of liquid helium. The cooling temperature of the supercooling tests was less than 2.7 K. From 100th to 103rd tests, although the cooling temperature was less than 2.2 K, superfluid helium could not be uniformly confirmed.

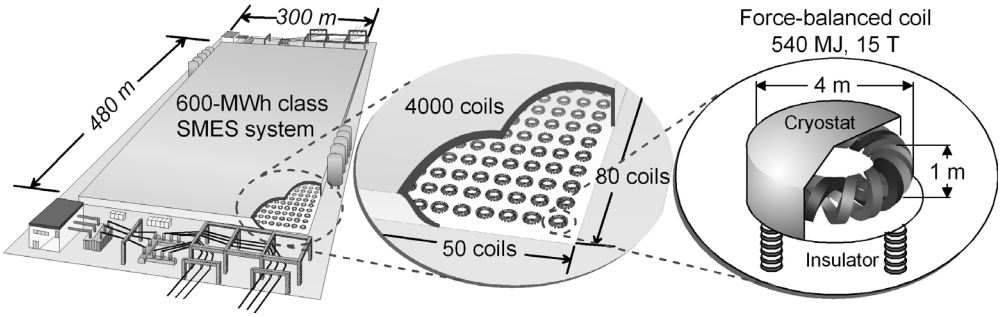

Figure 3: Schematic illustration of the 600-MWh SMES based on the FBC design.

2. Conceptual Design of 600-MWh SMES Coils based on the FBC Configuration

Figure 3 shows a schematic illustration of the 600-MWh SMES based on the FBC design. This SMES is composed of 4000 superconducting coils. The stored energy of each coil is 540 MJ (150 kWh). When several SMES coils have been constructed, these coils will be put into operation immediately. Then the stored energy can be continuously enlarged. Additionally, when the SMES coil is divided into a number of superconducting coils, the leakage magnetic fields can be reduced. Especially, in the case of the adjacent coils arranged in alternative magnetic moment directions, the leakage magnetic fields decrease drastically [5].

3. Road Map of Large Scale SMES toward 2050

IEA (International Energy Agency) is developing future scenarios for CO_2 reduction toward 2050, and remarks the importance of large scale energy storage systems for renewable energy systems. By request of IEA, RASMES (Research Association of Superconducting Magnetic

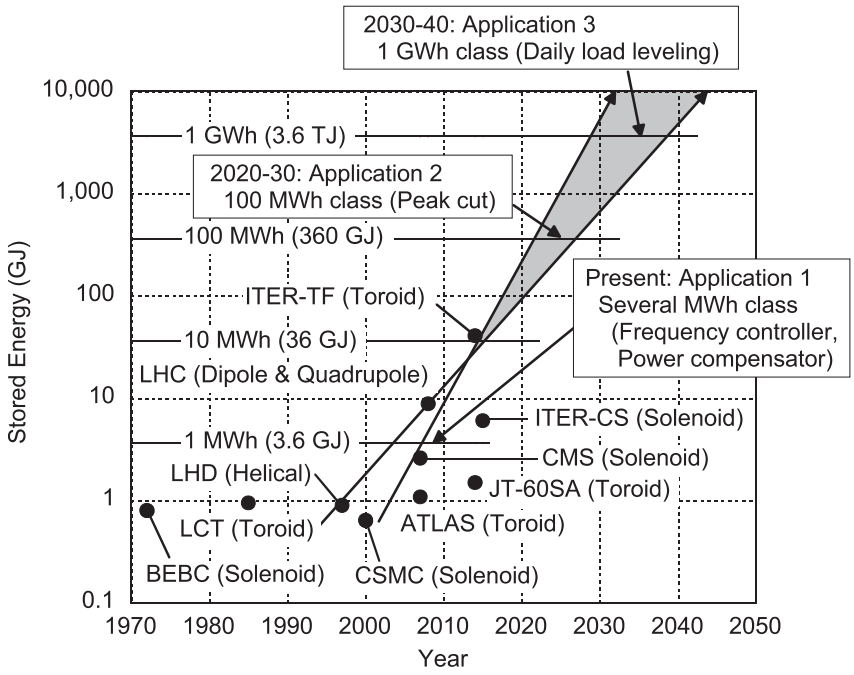

Figure 4: Road map of SMES based on the achievement and status of large superconducting coils. The black circles show the achievement and development plans of large superconducting coils which have been applied to particle detectors for high energy physics and magnetic confined nuclear fusion experimental devices. The darker hatch indicates the estimated installation periods of SMES systems.

Energy Storage) in Japan investigated the technical status of SMES, and developed a road map of SMES toward 2050. As a member of technical committee of RASMES, the author summarized the concluding results of the road map based on the progress of large superconducting coils and the cost estimation of SMES system [6]. The concluding results of the road map were also published in the 2009 IEA working paper (S. Inage, "Prospects for Large-Scale Energy Storage in Decarbonised Power Grids," IEA Working Paper (http://www.iea.org/papers/2009/energy_storage.pdf), pp. 72-78, 2009).

3.1 Installation Periods of Large Scale SMES Systems

Figure 4 summaries the status of large superconducting coils and shows the estimated installation period of SMES systems. At present, the 1 GJ class large superconducting coils have been enough developed in the field of the particle detectors for high energy physics experiments and magnetic confined nuclear fusion. This progress shows that the technical status of the 100 kWh (360 MJ) to 1 MWh (3.6 GJ) class superconducting coils is already established. Therefore it is possible at present to introduce the several MWh class SMES for application 1 that is for the frequency control, the load fluctuation compensation, and the generation fluctuation compensation.

The ITER magnet system will be constructed by 2015 [7], meaning that the refrigeration and power conversion systems for 10 MWh (36 GJ) class superconducting coils will be also

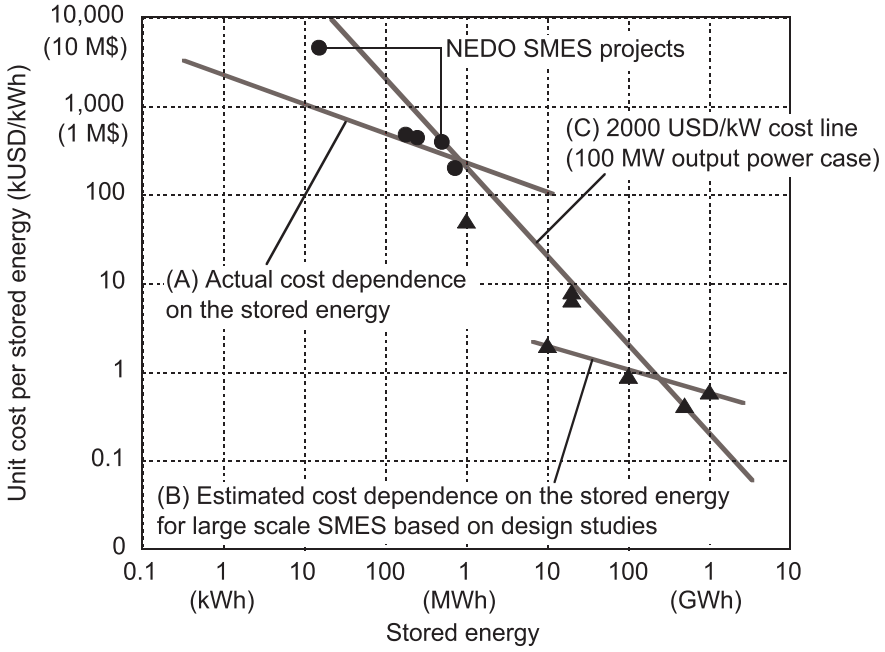

Figure 5: Cost estimation of SMES as a function of stored energy. The black circles indicate the concluding results of the NEDO projects, and the actual cost of the experimental device developments. The black triangles indicate the estimated cost based on the SMES design studies. The lines (A) and (B) show the unit cost per stored energy (USD/kWh) lines. The line (A) is the actual cost dependence based on the actual coil data of particle detector magnets (solenoid type). The line (B) is the estimated cost dependence based on the results of the SMES design study with toroid configurations. The line (C) shows 2000 USD/kW of the unit cost per output power line in the 100 MW output power case.

established. With integrated operations of several dispersed SMES systems, it is expected that the 100 MWh class SMES for application 2 that is for load fluctuation leveling (peak cut) can be introduced in the period of 2020-30.

After sufficient experience with the operation of the ITER magnet system has been gained, the development of 100 MWh class SMES for application 2 will be enough achieved. Therefore, it is expected that the first 1 GWh class SMES for application 3 that is for daily load leveling can be installed in the period of 2030-40.

3.2 Target Cost Evaluation of SMES Systems

As a Japanese national project from 1999 to 2003, the New Energy and Industrial Technology Development Organization (NEDO) estimated target costs of SMES systems for the commercialization, and carried out economical design studies of 100 MW/15 kWh SMES for power system stabilization and 100 MW/500 kWh SMES for load fluctuation compensation and frequency control, including model coil developments [8]. The concluding results of the SMES cost estimation, including capital cost and operating cost for 30 years, were 690 USD/kW in the 100 MW/15 kWh SMES case, and 1970 USD/kW in the 100

MW/500 kWh SMES case.

Figure 5 summarizes the unit cost per stored energy (the unit cost per kWh) estimated from the results of the prototype SMES systems of the NEDO projects, the experimental device developments and the SMES design studies.

Green summarized the actual cost data of particle detector magnets (solenoid type) and introduced the cost equation [9]. Based on the Green's equation, the actual cost dependence on the stored energy is also shown in Figure 5. Since most of detector magnets were developed for a specific purpose, in the case of SMES use, this cost dependence will be decreased by the effect of mass production.

From the results in Figure 5, if the output power of SMES is 100 MW, the target cost of SMES can be estimated with 2000 USD/kW of the unit cost per output power (the unit cost per kW). The prospects in the target cost achievement were successfully verified by the field tests of a 10 MVA/20 MJ prototype which is a successive stage of the NEDO project during 2004 to 2007. However, in the case of large scale SMES, the cost estimation of more than 1 MWh class SMES is based on the conceptual design studies. Therefore, the unit cost per stored energy (the unit cost per kWh) should also be evaluated. In this case, the life cycle cost of SMES system should be estimated by including its features such as site limitation, efficiency and lifetime.

References

[1] TSUTSUI, H., NOMURA, S., SHIMADA, R., "Optimization of SMES Coils by Using Virial Theorem," IEEE Trans, Appl. Supercond. 12 (2002) 800-803.

[2] NOMURA, S., et al., "Feasibility Study on High Field Magnets Using Stress-Minimized Helical Coils," Fusion Eng. Design 81 (2006) 2535-2539.

[3] NOMURA, S., et al., "Quench Properties of a 7-T Force-Balanced Helical Coil for Large-Scale SMES," IEEE Trans. Appl. Supercond. 19 (2009) 2004-2007.

[4] NOMURA, S., et al., "Acoustic Emission in a Superconducting Force-Balanced Helical Coil," presented at ASC 2010 (to be published in IEEE Trans. Appl. Supercond.).

[5] NOMURA, S., et al., "Flexible Power Interconnection With SMES," IEEE Trans. Appl. Supercond. 16 (2006) 616-619.

[6] NOMURA, S., et al., "Technical and Cost Evaluation on SMES for Electric Power Compensation," IEEE Trans. Appl. Supercond. 20 (2010) 1373-1378.

[7] MITCHELL, N., et al., "The ITER Magnet System," IEEE Trans. Appl. Supercond. 18 (2008) 435-440.

[8] TATSUTA, Y., et al., "Development of SMES for Power System Control," IEEE Trans. Appl. Supercond. 14 (2004) 693-698.

[9] GREEN, M. A., STRAUSS, B. P., "The Cost of Superconducting Magnets as a Function of Stored Energy and Design Magnetic Induction Times the Field Volume," IEEE Trans. Appl. Supercond. 18 (2008) 248-251.

Status of ITER Feeder System

Song Yuntao, ASIPP ITER Feeder Team
Institute of Plasma Physics, Chinese Academy of Sciences
P.O.BOX 1126, Hefei Anhui, China, 230031
Songyt@ipp.ac.cn

Abstract

International Thermonuclear Experimental Reactor (ITER) feeders are the systems convey the cryogenic cooling and electrical power to the coils and house the instrumentation wires. In total there are 31 such feeders for the ITER magnet system. This paper presents the latest feeder status in ASIPP, includes the R&D of ITER HTS current lead, design and analysis of feeder components and R&D on key technologies. For the R&D of ITER HTS current lead, the 68 kA (for TF feeder) and the 10 kA (for CC feeder) trial leads have been developed and tested successfully from 2008 to 2010, different HEX structures have been researched, the LOFA time, the joint resistances can meet the ITER requirements. The design and analysis of TF, PF, CS and CC feeder components was finished in 2010 and the issues of feeder assembly is discussed. The R&D of key technologies of feeder are also described in this paper, such as the bending and VPI of S-bend busbar, the ultrasonic and high voltage test of insulation, the design of the superconducting joint and insulator, the soldering and critical current test of HTS stacks, the experimental test of the thermal shield and the Paschen test of insulation sample and S-bend busbar.

1. Introduction

ITER Feeders conduct great current and supply supercritical helium for the large superconducting coils in the ITER Tokamak. There are also a number of instrumentation cables inside the Feeders. The total 31 Feeders are divided by the coils they connect, 9 Toroidal Field Coil Feeders, 6 Poloidal Field Coil Feeders, 6 Central Solenoid Feeders, 5 Correction Coil Feeders, 3 Structure Cooling Feeders and 2 Instrumentation Feeders. All these Feeders distribute around the Tokamak, each one is a system with ~50 ton weight and ~30 m length. From the center of the machine to outboard, a typical Feeder consists of four components: Inside Cryostat Feeder (ICF), Cryostat Feed-Through (CFT), S-Bend Box (SBB), Coil Terminal Box (CTB) and Dry Box (DB). Figure 1 shows the Feeder system and main components of the Feeder.

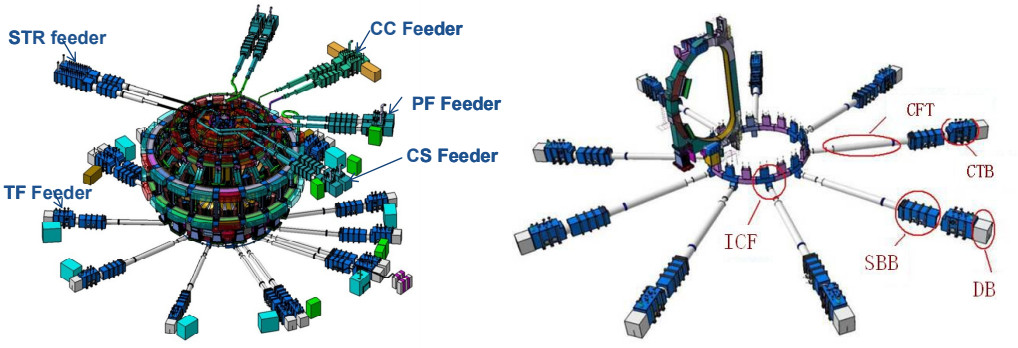

Figure 1: ITER Feeder system and its configuration

2. HTS current lead

High Temperature Superconducting Current Lead (HTS-CL) is applied on ITER current leads because it can reduce heat loads at 4.5 K and cooling power consumption by 1/3 comparison with conventional current leads. There are 4 types of HTS-CLs for the Feeder, separated by the current they carry: 68 kA, 57 kA, 45 kA and 10 kA. The performance of the HTS-CL is critical to the Feeders, including the LOFA and burnout time, supercritical joint resistance, insulation performance, heat exchanger efficiency and HTS stack performance, the manufacturing of the leads is also researched. Figure 2 presents the 68 kA HTS-CL.

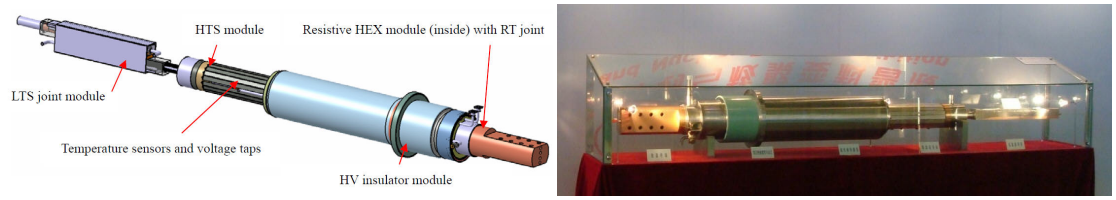

Figure 2: Configuration and prototype of the 68 kA HTS current lead

All the prototype current leads are tested and all critical parameters achieve the design target, for instance, the 68 kA HTS-CL has operated at 90 kA for 5 minutes and 65 minutes at 85 kA, 400 s LOFA time and 13 s burnout time, 2 $n\Omega$ contact resistance at 5 K. Figure 3 shows the superconducting joint manufacture and assembly details.

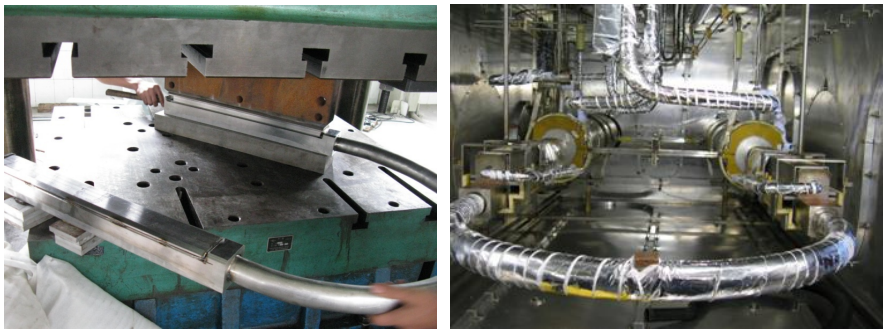

Figure 3: Superconducting joint welding and assembly

3. Feeder design and analysis

The Feeder design needs to consider electrical, mechanical and cryogenic requirements, because the Feeder has to work in an environment of strong magnetic field (~4 T) and supercritical helium temperature (~4 K), then the design should resist high Lorentz force (~13 ton/m) and compensate huge thermal shrinkage (~100 mm), meanwhile the heat load to the 4 K cryogenic system must be minimized; thus the mechanical structure of the Feeder must be strong and flexible enough, and all possible thermal insulation methods should be taken, such as 80 K thermal shield with Multi-layer Insulation (MLI), low conductivity composite material, optimized support configuration and dimension. A lot of analyses are performed to support the design optimization.

Figure 4 shows one Feeder magnetic and mechanical analysis result, the Lorentz force applied on the Feeder busbars are determined by the magnetic field of the coils, which have many working and accidental scenarios, therefore, a magnetic analysis is performed with the worst scenario to find out the peak Lorentz force distribution. Then other loads like gravity, low temperature and interface loads from neighboring components, then the mechanical strength and heat load of the Feeder is checked and optimized, to find the balance between them.

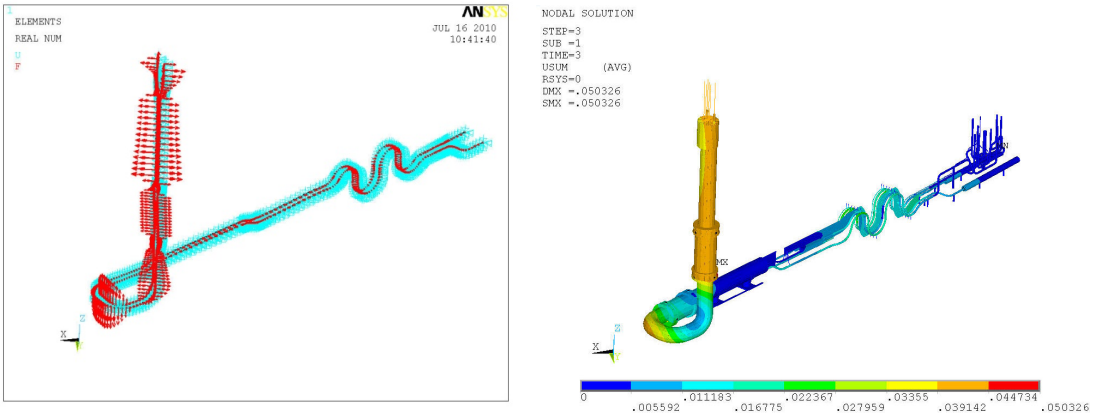

Figure 4: Typical Feeder Lorentz force distribution and displacement in worst scenario

Figure 5 is the 80 K thermal shield design and analysis, which covers the CTB, SBB and CFT, the temperature gradient and pressure drop are the design targets, dense pipe routing is helpful to reduce the former parameter, but will increase the pressure drop, thus different designs have been tried, then the temperature gradient along all thermal shield is within 20 K and the pressure drop is 0.2 bar, both meet the design requirement.

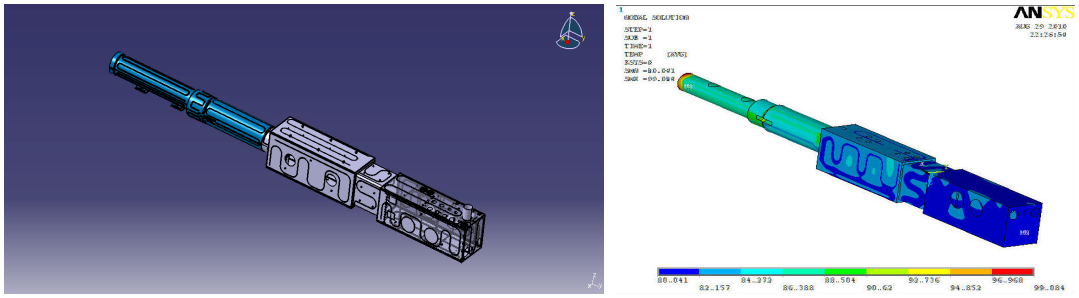

Figure 5: Feeder 80 K thermal shield design and temperature distribution

4. Other R&D programs

There are many other R&D programs for the Feeder, such as the insulator, busbar insulation and shaping progress, thermal shield, magnetic shield.

The insulator for the busbar is critical for the electrical insulation system, it's also playing the role of separating the CTB/SBB vacuum from the Tokamak vacuum, meanwhile, it should withstand the force from the busbar and the vacuum barrier, so both electrical and mechanical

performance should be researched, the 56 kV HV test, mechanical tests under 4 MPa/1000 Nm bending moment/100 Nm torque/2000 N tensile are performed in cryogenic environment. All results pass the design requirement. The prototype insulator and 56 kV HV test curve is shown in Figure 6.

Figure 6: Insulator prototype and 56 kV HV test result

Busbar insulation is surely critical to the Feeders, a number of HV tests are done for the insulation samples. Under DC 30 kV and 10^2 helium, the resistance is over 750 $M\Omega$, which has achieved the requirement.

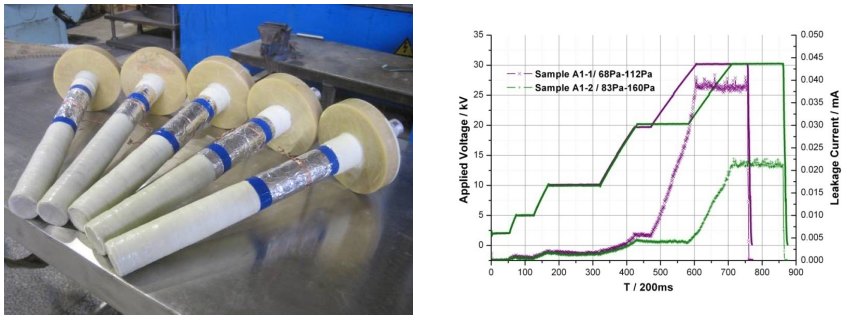

Figure 7: Insulation sample and HV test results

The insulation has to be wrapped and solidified on the outer surface of the busbar jacket, this work is difficult for the S-bend region, and meanwhile it has to hold the electrical insulation performance during the cool down tensile process. In the S-bend busbar manufacture, at first, the busbar jacket (with cables inside) is bended to the design shape, then the preimpregnated or VPI insulation solidification techniques are both tried. Then the preimpregnated S-bend sample is picked out to do the paschen test, as Figure 8 presents; in this test, not only the S-bend without deformation are tested, but also the sample experiences tensile process by 700 cycles. The resistance is over 3 $G\Omega$ in 1 Pa to 500 Pa helium environments, and the insulation performance keeps well even after the tensile cycles.

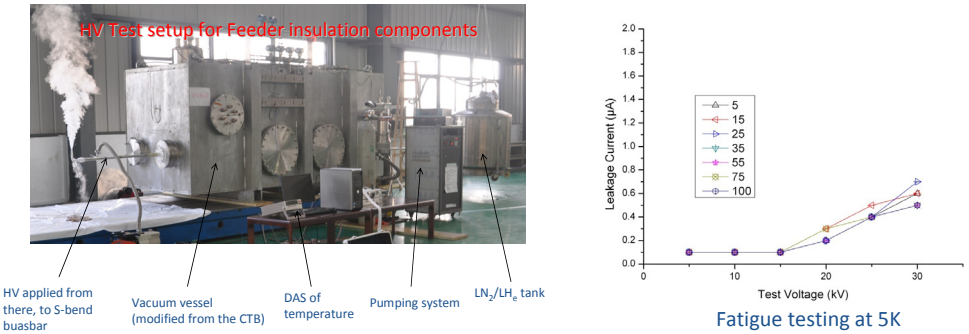

Figure 8: S-bend busbar sample Paschen test

The 80 K thermal shield can greatly reduce the heat load to the 4.5 K system, the connection ratio between the GHe pipe and the plate is important to the cooling effect, so different manufacture techniques are researched to find the balance between easy machining and good heat transfer, including clamp, clamp + Cu tape, clamp + Al tape, soldering. Figure 9 shows the tape between the pipe and the plate, as well as the clips on the pipe. The results indicate that even the pipe is clamped on the plate, dense pipe routing can provide enough cooling power to the thermal shield.

Figure 9: Details of the thermal shield pipe & plate connection

The Feeders contains many control components, which may be disturbed by the strong magnetic field around, thus an magnetic shield is researched, this shield aims at protecting the sensitive components inside from a static field of 30 mT, the peak field inside the shield is 5 mT. In this test, the field inside the shield (with/without hole) is measured, it's proved that even the background field rises to 60 mT, the internal field is lower than 0.5 mT.

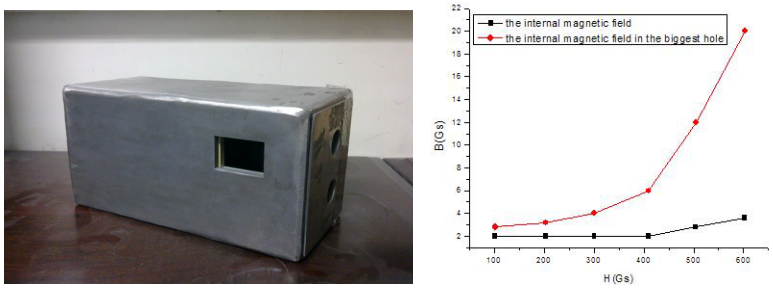

Figure 10: Magnetic shield mock-up and field measurement results

5. Conclusions

The ITER Feeder system is huge and needs many considerations over electric, magnetic, cryogenic and mechanical fields, meanwhile there is not such experience in the world to be referred to, therefore the design should be thoughtful, and meanwhile a lot of analyses and R&D work will be performed. All these efforts will increase the system performance and reliability.

Reference:

[1] DDD11-6__Feeders,_CTBs_and_Current_Leads, 2009
[2] Thermal_analysis_of_the_Feeder_CFT&ICF_containment_duct, 2010
[3] Analysis_of_the_Feeder_Thermal_Shield, 2010
[4] Song. Y. T, Status of ITER Feeder System, 2010
[5] Design report of 68 kA Trial Lead, 2008

Development of MgB_2 Tapes with High Aspect Ratios

A. Kawagoe, S. Kawabata, F. Sumiyoshi, N. Yanagi*, T. Mito*, M. Kiuchi**, T. Matsushita**, T. Tanaka*** and T. Wakuda***

Kagoshima University , Kagoshima, 890-0065, Japan

**National Institute for Fusion Science, Toki, Gifu, 509-5292, Japan*

***Kyushu Institute of Technology, 680-4, Kawazu, Iizuka, Fukuoka, 820-8502, Japan.*

****Hitachi Research Laboratory, Hitachi, Ltd., Ohmika-cho, Hitachi, Ibaraki, 319-1221, Japan*

kawagoe@eee.kagoshima-u.ac.jp

Abstract

MgB_2 has high critical temperature, about 39 K. Therefore, the extremely stable MgB_2 conductors are expected to be developed. Additionally, MgB_2 conductors may be cheaper to make. Recently, the technology to create wire from MgB_2 has developed and the performance of MgB_2 wires has been improved. Some coils have been wound and tested. The expectations for superconducting devices that employ MgB_2 coils are rising. However, many of these studies on MgB_2 conductors are about critical current densities, fabrication and tests on the MgB_2 coils for dc use. So these are not sufficient for development of pulse coils. In order to widely use MgB_2 conductors for superconducting pulse coils, both an increase in critical current densities and a decrease in ac losses is needed.

In order to develop the new conductors for superconducting pulse coils, the performance of the MgB_2 wires was improved. To achieve both increase in critical currents and decrease in ac losses of MgB_2 wires fabricated using the in-situ method, MgB_2 tapes with a high aspect ratio of cross-section have been proposed. We showed that deformation into tapes from round wires caused an increase in critical current densities and a decrease in ac losses. Then, in order to confirm that a coil wound with the tape has high performance, a test coil has been wound with a parallel conductor composed of two tapes insulated each other, and then the excitation tests on the coil has been carried out.

1. Introduction

Low temperature superconducting (LTS) conductors, NbTi and Nb_3Sn, have been widely used as windings for superconducting coils, for superconducting devices, superconducting magnetic energy storage (SMES), Fusion devices, and so on. The fabrication and operation of NbTi coils are particularly well known. However, the critical temperature of LTS conductors is very low, so coils wound with these conductors are operated near the temperature of liquid helium (4.2 K). At such low temperature, the specific heat of materials in the coils is very small, so the small heat generation in the windings of the coils produces a serious temperature rise. Therefore, the stability of the coils is low.

In general, coupling losses in superconducting coils wound with LTS conductors with plural strands increase when the stability of the coils is increased, i.e. the relationship between low coupling losses and high stability is the essential dilemma for almost all superconducting coils. Consequently, it is difficult to develop superconducting coils with both low ac losses and high stability.

MgB_2 has high critical temperature, about 39 K. Therefore, the extremely stable MgB_2 conductors are expected to be more effective than NbTi conductors. Additionally, MgB_2 conductors may be cheaper to make. Recently, the technology to create wire from MgB_2 has developed and the performance of MgB_2 wires has been improved[1-3]. Some coils have been wound and tested [4-6]. The expectations for superconducting devices that employ MgB_2 coils are rising.

However, many of these studies on MgB_2 conductors are about critical current densities,

fabrication and tests on the MgB_2 coils for dc use. So these are not sufficient for development of pulse coils. In order to widely use MgB_2 conductors for superconducting pulse coils, both an increase in critical current densities and a decrease in ac losses are needed.

In order to develop the new conductors for superconducting pulse coils, the performance of the MgB_2 wires was improved. To achieve both increase in critical currents and decrease in ac losses of MgB_2 wires fabricated using the in-situ method, MgB_2 tapes with a high aspect ratio of cross-section have been proposed. Our previous study showed that deformation into tapes from round wires caused an increase in critical current densities and a great decrease in ac losses [7, 8].

In order to improve the electromagnetic properties of MgB_2 conductors or coils, structures of conductors and coils which are composed of our tapes have been studied. In this paper, a parallel conductor composed of insulated tapes is proposed and the small coil wound with this conductor are designed, fabricated and tested.

2. Parallel conductor composed of insulated tapes

In case of large-scale superconducting conductors which are composed of low temperature superconducting wires, such as NbTi or Nb_3Sn, between wires as strands is not insulated to maintain the stability of the conductor. In contrast, in case using MgB_2 wires which have high critical temperature, the stability of the wire is expected to be sufficiently high. Therefore, electrical contact between strands might be not necessary in MgB_2 conductors. Inter-strand coupling losses in such a conductor are not produced.

For uniform current distributions, strands must be transposed in the conductor. In this study, transposition is one time in the test coil.

3. Winding MgB_2 Tape for the test coil

The winding tapes for test coil are non-doped MgB_2 tapes with aspect ratio of 2. Parameters of the MgB_2 tape are listed in Table 1. The test coil has been designed with the parallel conductor composed of the two tapes insulated from each other. In order to design the test coil, the critical currents have been measured on this tape and round wires before rolling process.

The critical currents of the short straight samples have been measured by the four-probe method in liquid helium. Four samples which are connected in series are mounted in the superconducting magnet. These samples are arranged in parallel with space of 10mm. The length of each sample is 60 mm and voltage taps are soldered to each sample. The distances between voltage taps are 10 mm[8].

The critical currents of the samples under the external transverse magnetic fields of 2T-7.5T were measured. Measurements of tapes for two cases, i.e., the edge-on (EO) and the flat-on (FO) transverse magnetic fields cases, are carried out, where the directions of EO and FO are parallel and perpendicular to the flat face of the tapes, respectively. When direction of magnetic fields is changed, each sample is turned around their axis by 90 degree.

The electrical fields along the axes of the sample have been measured by voltage taps. The average critical currents of samples were calculated. The voltage criterion has been defined as 1μV/cm.

From measured values of critical currents, the critical current densities, J_c of MgB_2 filaments in each sample are calculated. The magnetic field dependencies of J_c are shown in Fig. 1. In the figure,

Table 1 Parameters of MgB_2 tapes

dimension [mm]	1.05×0.504
filament dimension [mm]	0.712×0.233
filament aspect ratio	3.1

circle plots represent J_c of round wires. Square plots represent J_c of tapes. Open and solid symbols represent data for EO-fields and FO-fields, respectively. J_c of MgB_2 tapes are larger than that of round wires. J_c of MgB_2 tapes for EO-fields are about 3 times as large as that of round wires. Anisotropy of J_c is observed in high fields.

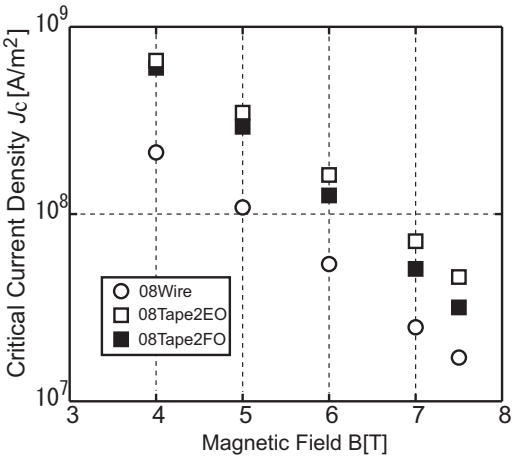

Fig. 1. Critical current densities of MgB_2 tapes and wires.

3. Design and fabrication of the test coil

A test coil has been designed. This coil wound with the parallel conductor composed of two MgB_2 tapes, which are mentioned above. The test coil is composed of two coils which are arranged coaxially and connected in series as shown by Fig. 2. The winding conductor for the test coil is composed of two insulated tapes from each other. The two tapes are transposed at joint point between the two coils for uniform current distribution between two tapes.

Parameters of the test coil are listed in Table 2. Inner and outer diameters of the coil are 65 mm and 107mm. Total turn of the test coil is 540 turn (270 turn x 2).

A load line of the test coil is shown in Fig. 3. The designed critical current of the coil is 340A which is about twice as large as one of the coil wound with a conductor with round wires. The designed value is based on the result of measured values on short samples. The designed value of a center magnetic field produced in the coil is 1.31T at 200A.

Table 2 Parameters of the test coil

inner diameter [mm]	64.6
outer diameter [mm]	107.4
length [mm]	56.0
inductance [mH]	16.8
conductor length [m]	140
layer	15
number of turns	540
distance between coils [mm]	10.0

The test coil has been wound & reacted. Firstly, the wires were wound around a coil bobbin with stainless steel, and then the coil were heat treated. Secondly, the test coil set into another coil bobbin with GFRP for measurements. In this procedure, the diameters of both coil bobbins were the same to avoid the degradation of critical currents of the windings due to bending strain.

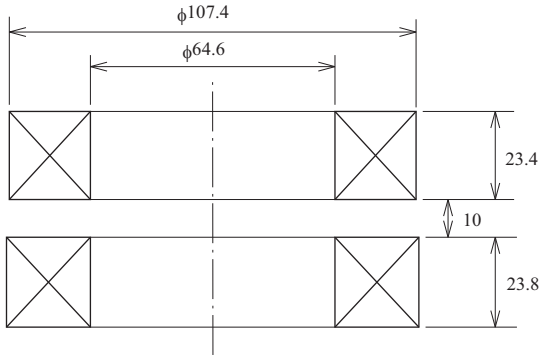

Fig. 2 Configuration of the test coil

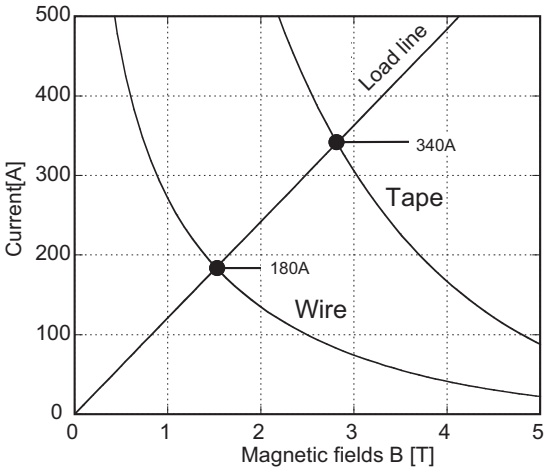

Fig. 3 Load line of the test coil

4. Experiments

Firstly, critical current of the test coil has been measured at 4.2 K. The voltage criterion has been defined as 1.4mV which is a coil voltage when an electric field of 0.1μV/cm is generated whole length of the conductor in the coil. The sweep rate was about 60A/min. Measured data is shown by Fig. 4. Horizontal and vertical axes represent a coil current and a voltage, respectively. The test coil has been stably excited up to 370 A. It was found that the critical current was 360 A. n value was about 10. Measured critical current is closely to value which is predicted from experimental data on short samples. It indicates our coil is fabricated without degradation. We found as follows: our tape is very effective to improve the performance of MgB_2 coil; MgB_2 conductor composed of insulated strands is not problem in case of slow sweep.

Next, ac losses in the test coil have been measured at 4.2K. The results of ac loss measurement are explained. The transport current is ac current superimposed on dc bias current. Dc bias currents are 100 A. Amplitude and frequency of ac current are 1–30 $A_{r.m.s}$ and 1-20 Hz, respectively. Experimental circuit is shown in Fig. 5. AC loss measurements are needed to cancel the inductive voltages in terminal voltages across the coil. Transformer for cancelling is connected in series to the circuit as shown in Fig. 5. In order to cancel the inductive voltage from coil voltage, the voltage of secondary winding of the transformer for canceling and a lock-in-amplifier are used.

Measured data is shown by Fig. 6. The horizontal axis is RMS values, and vertical axis is ac losses per cycle. Measured ac losses don't depend on frequency. This indicates that measured losses are mainly hysteresis losses. In range of low ac currents, ac losses depend on frequency due to eddy current losses in Cu. In order to show the validity of the tape, theoretical values of ac losses are shown by two lines in this figure, solid and dashed lines represent ac losses in a coil wound by a round wire and that of this test coil wound by a tape. It is found that our coil wound by a tape is low losses compared with a coil wound by a round wire. The reason of difference between theoretical values and

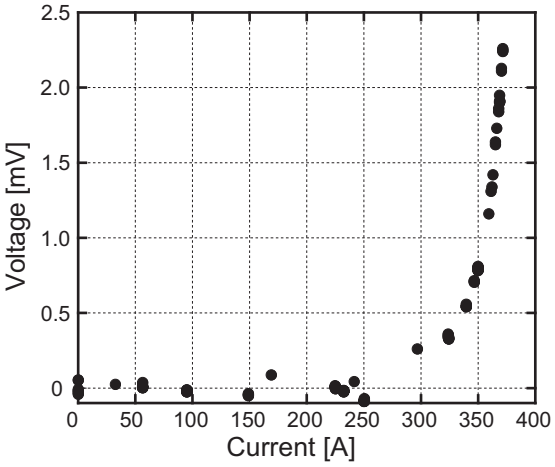

Fig. 4 I-V curve on the test coil

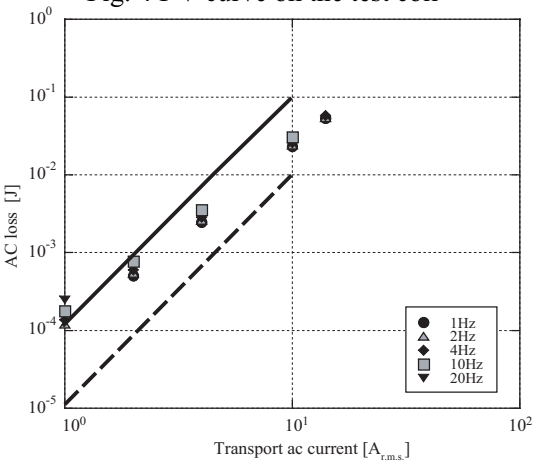

Fig. 6. Results of ac loss measurements

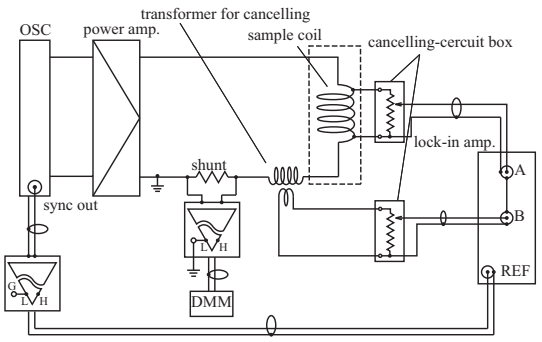

Fig. 5 Experimental circuit to measure ac losses in the test coil

experimental values might be J_c distributions in the filaments or surface pinning of filaments. The reasons will be submitted elsewhere.

5. Conclusions

In order to improve the electromagnetic properties of MgB_2 wires, we have proposed MgB_2 tapes. As an example of a superconducting conductor with large capacity of transport currents using our tapes, a parallel conductor composed of insulated tapes has been proposed. In order to validity of the conductor, the test coil has been designed, fabricated and tested. The test coil is composed of two coils arranged coaxially and connected in series. The two tapes in the winding conductor are transposed at joint point between the two coils. The measured critical current of the test coil was 360A, which is close to the designed value. AC losses measurements were carried out. In case that bias current was flowed, frequency dependence of the losses was not observed. This shows that hysteresis losses are dominant and lower than that of a coil wound by a round wire. Consequently, it has been shown that our MgB_2 tapes have value to develop high performance conductor or coil.

Acknowledgements

This work is performed with the support and under the auspices of the NIFS Collaboration Research Program.（NIFS07KOBA019）and the Grant-in-Aid for Young Scientists (B) (20760186).

Reference

[1] H. Kumakura, et. al., Physica C, **456** (2007) pp. 196-202.
[2] M. D. Sumption, et. al., IEEE Trans. on Appl. Supecond., **17** (2007), pp. 2838-2841,.
[3] K. Tanaka, et. al., Physica C, **382** (2002) pp. 203-206.
[4] M. D. Sumption, et. al., Physica C, **458** (2007) pp. 12-20.
[5] M. Razeti, et al., IEEE Trans. on Appl. Supecond., **18** (2008) pp. 882-886.
[6] W. J. Yao, et. al., IEEE Trans. on Appl. Supecond., **18**, (2008) pp. 912-915.
[7] A. Kawagoe, IEEE Trans. Appl. Supercond., **19** (2009) pp. 2686-2689.
[8] A. Kawagoe, et. al., IEEE Trans. Appl. Supercond., **20** (2010) pp. 1601-1604.

Test Facility for ITER CC Conductor

H.J. Liu, Y. Wu, Y. Shi, Zh.B. Ren, F. Long, J.L. Chen
Academy of Science Institute of Plasma Physics, P.O.Box 1126, Hefei, Anhui, China 230031
Contact of the main author: liuhj@ipp.ac.cn

Abstract: To meet the specifications of ITER CC conductor, a test facility had been set up to measure the conductor. This facility featured a DC background field up to 7T/4.2K in a 338mm useful bore diameter. A 50kA superconducting transformer was manufactured to provide the sample current. A 500W/4.5K refrigerator was used to provide the facility cooling. This paper presents the results of cooling of the test facility. The background magnet and the primary coil of the superconducting transformer were immersed in liquid helium. The test sample and the secondary coil were cooled by supercritical helium. The time constant of the secondary loop was about 1000s.

The Design of 100kV High Voltage Power Supply

Jiang Li
Academy of Science Institute of Plasma Physics, P.O.Box 1126, Hefei, Anhui, China 230031
Contact of the main author: jiangli@ipp.ac.cn

Abstract: A new high voltage power supply (HVPS) which is applied to drive the auxiliary heating system in EAST has been recently built. The HVPS is composed of a series connection of switched mode power supplies (SMPS), which provides the required voltage and current, up to 100kV and 100A in continuous operation. The specifications impose high accuracy on the voltage and the required voltage insulation. The HVPS includes two oil transformers which provide the main insulation 120kV DC from primary side to secondary side, four dry transformers which provide the insulation 35kV DC from primary side to secondary side. Each of oil transformer connect to two dry transformers which required 900V at the secondary side, each of dry transformer can connect to 26 SMPS which required output voltage 1200VDC. The connection in series of the 104 SMPS provides the required 100kV DC at the output. In addition, the SMPS can be switched off in the several microseconds, so a commonly used crowbar system in case of accelerator grid of the positive Ion Neutral Beam Injector arcing is not necessary. At last, the HVPS has been subjected to extensive tests, all tests performed on full power dummy load, were passed successfully.

The Development of Model Coil for 40T Hybrid Magnet

Zhihong Liu
Academy of Science Institute of Plasma Physics, P.O.Box 1126, Hefei, Anhui, China 230031
Contact of the main author: zhliu@ipp.ac.cn

Abstract: The construction of a 40-T hybrid magnet system is in progress at the Chinese High Magnetic Field Laboratory (CHMFL) of the Chinese Academy of Sciences. The magnet system consists of a superconducting outsert magnet and a resistive insert magnet. The outsert magnet with a bore diameter of 800 mm at room temperature is expected to provide 12 T. It is composed of four coils: the coil is made of Nb3Sn cable-in-conduit-conductor (CICC). The insert magnet, which will be a 20 MW Florida-Bitter-type resistive magnet with a clear bore diameter of 32 mm, will produce 28 T. The construction of the hybrid magnet is scheduled to be completed in 2014.

Design and Analysis of EAST 4.6G Hz LHCD Antenna Cooling System

Bo Li
Academy of Science Institute of Plasma Physics, P.O.Box 1126, Hefei, Anhui, China 230031
Contact of the main author: lib@ipp.ac.cn

Abstract: An actively cooled lower hybrid current drive (LHCD) launcher will be installed in EAST. It is not only the heat flux from plasma, but also the ratio frequency loss which heat up the antenna. Several sets of water cooling structure have been designed and compared by using thermal and structure analysis. Taking account of structural stability and machinability, a kind of composite structure had been adopted.

Subcooling System for LHD Helical Coils and Its Operation

S. Hamaguchi

National Institute for Fusion Science
322-6 Oroshi, Toki, Gifu 509-5292 JAPAN
hamaguchi@LHD.nifs.ac.jp

The Large Helical Device (LHD) is an experimental devise for heliotron plasma. The helical coils, which are large scale superconducting magnets, had been cooled with saturated helium at 4.4 K until 2005. However, normal zone propagations were observed 17 times at the innermost block of lower portion of the coils, where the cryogenic stability was degraded by geometric factor. Thus, the cooling system of the coils was upgraded in 2006 to improve the cryogenic stability of the coils by using subcooled helium as the coolant. A nominal mass flow rate and temperature of the subcooled helium at the inlet of the coils are 50 g/s and 3.2 K, respectively. The supplied helium is subcooled at a heat exchanger in a saturated helium bath. The bath pressure and temperature are reduced by a series of two centrifugal cold compressors with gas foil bearing. The helium flow through the compressors is automatically regulated by a heater in the bath to stabilize amount of the evaporated helium. In the present study, performance of the upgraded cooling system was investigated and optimization of the operating method was performed. Consequently, the designed mass flow rate and temperature of subcooled helium could be supplied to the coils and stable long-term operations have been achieved. The improvement of the cryogenic stability was also confirmed and the maximum average current of 3 blocks of the coils reached up to 11.833 kA.

1. Introduction

The Large Helical Device (LHD) is an experimental device for fusion plasmas and plasma experiments have been conducted successfully [1-2]. The LHD helical coils are a pair of large scale superconducting magnets to provide heliotron magnetic fields and had been cooled by saturated helium at 4.4 K from 1998 to 2005. However, normal zone was propagated at 17 times from the innermost block of lower portion of the helical coils because of the degradation of cryogenic stability by accumulation of helium bubbles due to the geometric factors. That is why the operating current of the coils was limited to about 90 % of the nominal critical current [3]. Thus, the cooling system of the coils was upgraded in 2006 to improve the cryogenic stability of the coils by using subcooled helium as the coolant [4-6].
In order to estimate the effect of subcooled helium on cryogenic stability, R&D tests were carried out in subcooled helium with a model coil, representative of the helical coils. It was confirmed that the cryogenic stability of the superconductor for the helical coils was improved thanks to disappearance of helium bubbles and reduction of the coil temperature. Test results showed that the operating current of the helical coils would be improved by about 7 % if the coil temperature is lowered to 3.6 K by subcooled helium [7]. In the present study, performance of the upgraded cooling system has been investigated and optimization of the operating method has been performed for the stable operation. The improvement of the cryogenic stability of the helical coils has also been confirmed in the actual system.

2. Description of Subcooling System

Figure 1 is a schematic of the subcooling system for the LHD helical coils. A cryostat was installed at the helical valve box to subcool supplied helium. Since the existing return line is only gaseous line, ten heaters were attached at outlet pipes of the helical coils in order to evaporate surplus supplied helium. The cryostat consists of a saturated helium bath with both a heat exchanger to subcool the supplied helium to the coils and a heater to regulate amount of vaporized helium gas, a series of two centrifugal cold compressors with gas foil bearing [8],

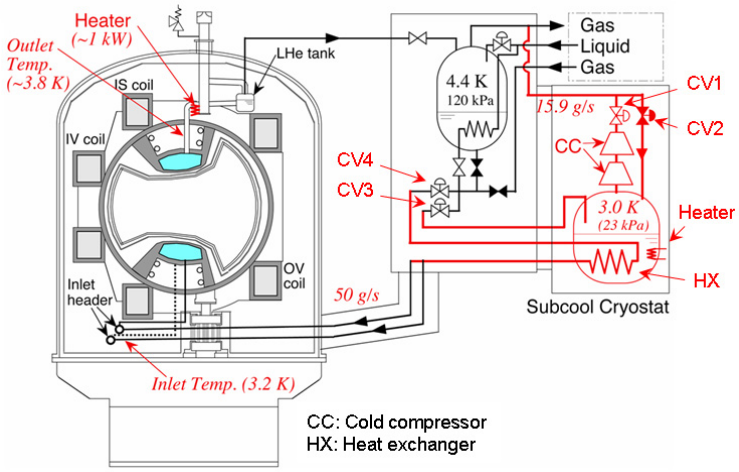

Figure 1: Schematics of the subcooling system for the LHD helical coils.

an outlet valve of the compressors (CV1) and a bypass valve (CV2) for pre-cooling operation and emergency protection. The bypass valve can also change the mass flow rate of the compressors. Liquid helium level in the saturated helium bath is automatically controlled by an inlet valve (CV3) in the helical valve box.

The saturated helium bath is evacuated by the cold compressors from 120 kPa (4.4 K) to 23 kPa (2.97 K). The supplied helium to the helical coils is subcooled in the heat exchanger. The mass flow rate of the supplied helium is adjusted by a supply valve (CV4) before the heat exchanger. The nominal mass flow rate and temperature of the supplied helium at the heat exchanger are 50 g/s and 3.0 K, respectively. In this case, the inlet and outlet temperature of the helical coils were expected to be 3.2 K and 3.8 K, respectively, due to steady heat load [9]. The upgrade of the cooling system for the helical coils was designed within the surplus cooling capacity of the existing LHD helium refrigerator/liquefier of 2 kW [4].

3. Performance Evaluation

The performance of the subcooling system was investigated to develop the stable operating method.

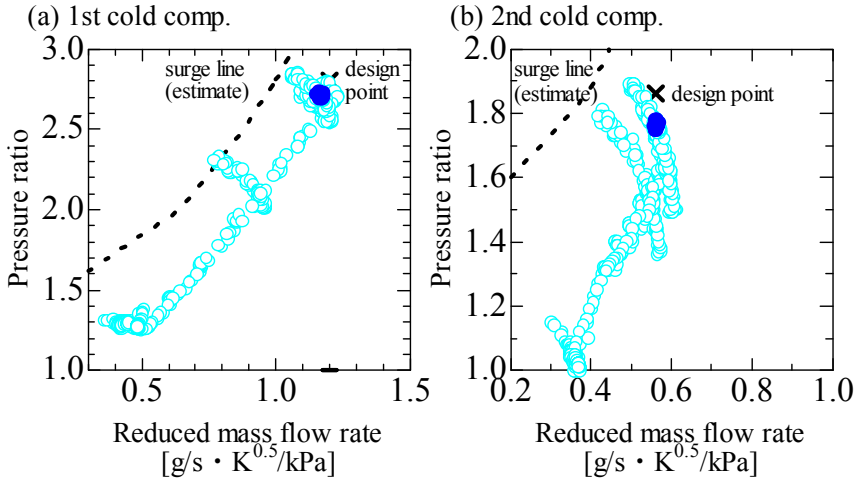

Figure 2: Performance curves of the cold compressors while helium flow was regulated by the heater in the saturated helium bath. (a); performance curve of first stage cold compressor, (b); performance curve of second stage cold compressor.

Table I: Performance of the cold compressors.

	Measured	Designed
Inlet pressure [kPa]	23.8	23.0
Outlet pressure [kPa]	112	120
Inlet temperature [K]	3.0	3.0
Outlet temperature [K]	7.25	7.5
Mass flow rate [g/s]	15.8	15.9
Heat input [W]	349	360
Efficiency [%]	66 (1st) 63 (2nd)	>55 >63
Cooling capacity [W]	288	300

Figure 2 shows performance curves of both compressors while helium flow through the compressors was regulated by the heater in the saturated helium bath. The left figure shows the performance of 1st stage cold compressor and the right one shows that of the 2nd stage cold compressor. Open marks express working points of the compressors and solid marks show the rated operating points. Dashed lines are surge lines estimated from preliminary examinations with air at room temperature. We can see from the figures that the cold compressors in the LHD subcooling system show similar characteristics to those obtained from the R&D tests with the model coil [10]. It was also confirmed that rated operating points were also close to the design and the compressors stably worked in the range of the helium flow from 16 g/s to 20 g/s. The measured performance of the cold compressors is listed in Table I, compared with the designed one.

Figure 3 displays the temperature and mass flow rate profiles of the supplied helium to the helical coils after the subcooling operation started. Solid lines show the temperature profiles at the each point of the helical coil line and a dashed line shows mass flow rate of the supplied helium. In this case, the supply valve (CV4) was kept 60 % open and the mass flow rate of supplied helium was approximately 50 g/s. The inlet temperature of the helical coils was kept to be 3.2 K, while the outlet temperature gradually decreased and finally reached to 3.8 K. It was proven that the subcooling system satisfies the requirements. The coil temperature was estimated to be 3.6 K by calculations using a simple 1D model [11]. At steady state, heat inputs from ten heaters at outlet of the helical coils were 1,128 W. The other additional heat

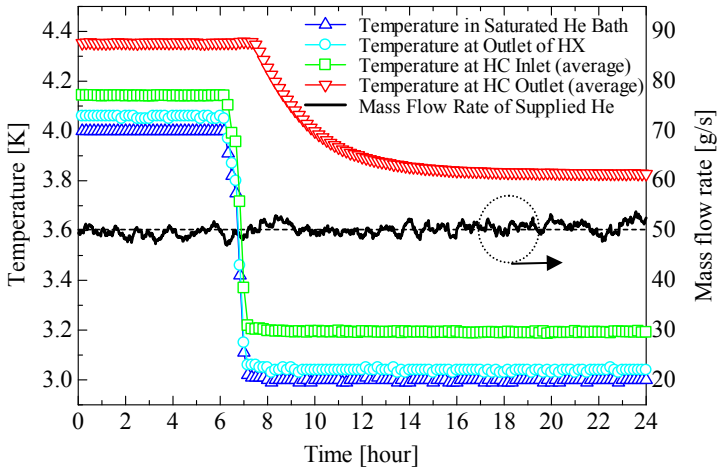

Figure 3: Temperature and mass flow rate profiles of the supplied helium after the subcooling operation started. HC; helical coil, HX; heat exchanger.

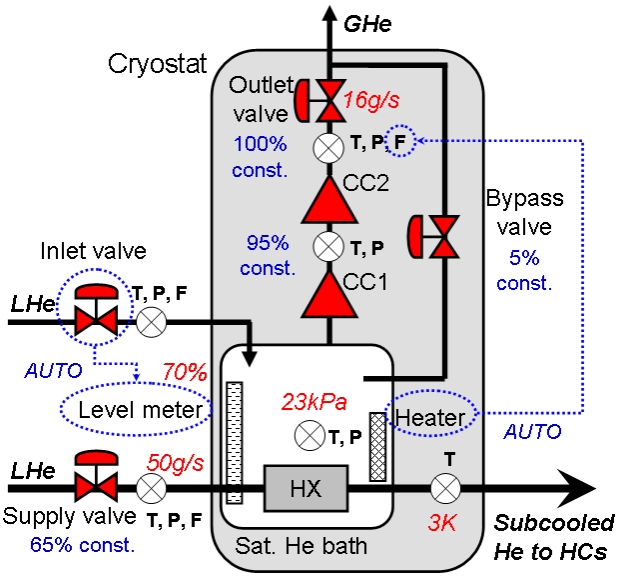

Figure 4: Operating values for the steady state subcooling operation.

load was 637 W (349 W + 288 W) from Table I. Thus, the sum of the additional heat loads to the existing LHD helium refrigerator/liquefier was about 1.76 kW less than the surplus cooling capacity of 2 kW. It was also confirmed that the cryogenic stability of the coils were improved in the subcooling operation. Consequently, the maximum average current of 3 blocks of the coils has reached up to 11.833 kA thanks to the revised excitation method and it corresponds to the operating current of the coils of 11.6 kA for the LHD plasma experiments [12].

4. Steady State Subcooling Operation

An operating method for the stable supply of subcooled helium to the LHD helical coils has been developed. *Figure 4* shows the subcool cryostat with some representative values for the steady state subcooling operation. Helium pressure, temperature, mass flow rate and level are measured for the operation at each position as shown in the *Figure 4*. The supply valve was manually adjusted to keep the mass flow rate of the supplied helium of 50 g/s. The outlet valve of the cold compressors kept fully open, while the bypass valve slightly open for prevention of temperature increase in the bypass line. The liquid helium level of the saturated helium bath was automatically controlled to be 70 % by the inlet valve of the bath. The set value of the rotational speed of the compressors was 95 %, corresponding to the rated rotational speed. The helium flow through the compressors was automatically controlled by

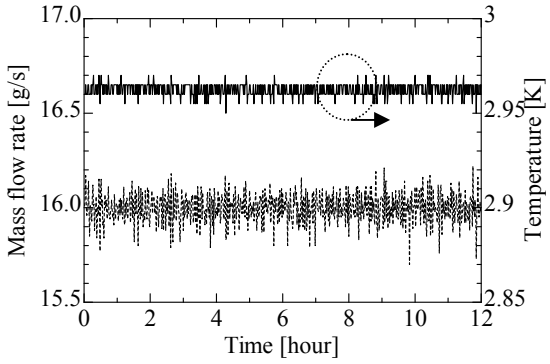

Figure 5: Helium mass flow rate of the cold compressors and bath temperature profiles in the steady state subcooling operation.

the heater in the bath. In the steady state subcooling operation, the helium mass flow rate was set to 16 g/s so that the compressors could work at the rated operating point. *Figure 5* shows the helium mass flow rate of the compressors and the bath temperature profiles. Dashed line shows the mass flow rate of the compressors and solid line shows the bath temperature. It was understood that they were remarkably stabilized thanks to the automatic flow control. The helium mass flow rate was controlled with the accuracy of 0.3 g/s and the bath temperature was stabilized within 0.02 K (peak-to-peak). Consequently, designed mass flow rate of subcooled helium of 50 g/s at 3.2 K could be stably supplied to the coils. So far, the steady state subcooling operations were achieved about 8,000 hours without interruption of the LHD plasma experiments and also the maximum time of the continuous subcooling operation has exceeded 2,000 hours by the optimization of the operating method.

5. Conclusion

The cooling system for LHD helical coils was upgraded in order to lower the coil temperature and improve the cryogenic stability of the coils. The performance of the system was investigated in detail and it was verified that requirements was satisfied, as follows: (1) the nominal performance of the cold compressors was confirmed, (2) designed temperature and mass flow rate of supplied helium were stably obtained, (3) the total additional heat loads were less than the surplus cooling capacity of the existing LHD helium refrigerator/liquefier, (4) the maximum average current of the coils increased up to 11.833 kA. Based on the obtained performance of the system, the operating method of the system has been optimized with adopting the automatic flow control of the compressors by the heater in the saturated helium bath. Consequently, the temperature of supplied helium could be stabilized within the range of 0.02 K and stable long-term operations have been demonstrated.

Acknowledgment
The present work was carried out by the NIFS budget, ULAA119, ULAA508 and KLAA004 and was partly supported by the JSPS-CAS Core-University Program in the field of "Plasma and Nuclear Fusion".

Reference

[1] IIYOSHI, A., et al., “Overview of the Large Helical Device project”, Nuclear Fusion 39 (1999) 1245–1256.

[2] MOTOJIMA, O., et al., “Recent development of LHD experiment”, Journal of Plasma and Fusion Research SERIES 5 (2003) 22–27.

[3] IMAGAWA, S., et al., “Excitation Properties and Cryogenic Stability of Helical Coils for the LHD”, IEEE Transactions on Applied Superconductivity 11 (2001) 1889–1892.

[4] HAMAGUCHI, S., et al., “Performance of upgraded cooling system for LHD helical coils”, Advances in Cryogenic Engineering 53 (2008) 1724–1730.

[5] CASPI, S., “Heat Transfer to Subcooled He I”, Advances in Cryogenic Engineering 29 (1984) 281–287.

[6] SAKURAI, A., et al., “Effect of System Pressure and Liquid Subcooling on Quasi-steady Nucleate Boiling and its Life for Liquid Helium I”, Advances in Cryogenic Engineering 35 (1990) 377–385.

[7] IMAGAWA, S., et al., “Upgrading program for improving the cryogenic stability of LHD helical coils by lowering the operating temperature”, Fusion Engineering and Design 81 (2006) 2583–2588.
[8] MILLET, F., et al., “Performance assessment of 35 Cold Hydrodynamic Compressor for the 1.8 K refrigeration unit of the LHC”, AIP Conference Proceedings 823 (2006) 1837–1844.
[9] IMAGAWA, S., et al., “Achievement of High Availability in Long-term Operation and Upgrading Plan of the LHD Superconducting System”, Nuclear Fusion 47 (2007) 353–360.
[10] HAMAGUCHI, S., et al., “Performance of cold compressors in a cooling system of an R&D superconducting coil cooled with subcooled helium”, Fusion Engineering and Design 81 (2006) 2617–2621.
[11] OBANA, T., et al., “Performance tests of the subcooling system for the LHD helical coils”, IEEE Transactions on Applied Superconductivity 18 (2008) 1475–1478.
[12] HAMAGUCHI, S., et al., “Helium Subcooling System for LHD Helical Coils”, Fusion Science and Technology 58 (2010) 581–585.

Superconducting Magnets with Built-in Oscillating Heat Pipes

T. Mito

National Institute for Fusion Science, Toki, Gifu, 509-5292, Japan

mito@LHD.nifs.ac.jp

Abstract

We are developing cryogenic oscillating heat pipes (OHP) built into the windings aiming to improve the heat removal characteristics of high-Tc superconducting (HTS) magnets. It is actually difficult for HTS magnets to take out the heat generated in the windings, because the thermal diffusivity of each component materials of the magnet such as copper, aluminum alloy, epoxy resin, GFRP, etc., decrease with an increase of the operating temperature. Therefore, a local hot spot can be easily generated in the magnet, and there are possibilities of degradation of superconducting properties and/or mechanical damage by thermal stresses. As a new cooling technology which can enhance the heat removal characteristics of the magnets, the OHP is proposed to be imbedded in the magnet windings. As proof of the feasibility of the cryogenic OHP, the stable operation has been confirmed by using hydrogen, neon, and nitrogen as the working fluid of the OHP. In addition, it has been shown to be able to achieve high thermal conductivity that surpassed high purity metals. The characteristics of the cryogenic OHP have been summarized, such as the measured effective thermal conductivities, the effect of a kind of working fluid, the effect in the orientation of the installation, etc.

1. Introduction

It has been expected that the superconductivity application would be dramatically accelerated by the discovery of the high-temperature superconductors (HTS). Though there have been tremendous developments in the application of HTS, such as for power transmission cables, transformers and motors, intense efforts are still needed for large-scale applications, such as superconducting magnetic energy storage (SMES) and fusion devices. In HTS magnets, the stability of winding conductors are assured by the rise of operating temperatures. However, when a part of the windings turns into the normal-conducting state, the protection of magnets becomes much more difficult than the case for low-temperature superconductors (LTS), and it is one of the most important issues for developing HTS magnets [1]. For example, the total magnetic storage energy of a 100 MW-class load-fluctuation compensating SMES using YBCO conductors will reach 2.4 GJ, and a fast protection is required for high reliability [2].It is generally difficult to remove the heat generated in HTS magnets, because the thermal diffusivities of component materials decrease with an increase of the operating temperature. Therefore, a local hot-spot can be rather easily generated in HTS magnets, and there are possibilities of observing degradation of superconducting properties and/or mechanical damages by thermal stresses.In this respect, a novel imbedded-type cryogenic oscillating heat pipe (OHP) is proposed, which can enhance the heat removal characteristics in HTS magnets.

2. Concept of Cooling with Heat Pipes

We have selected a type of heat pipes known as the OHP considering especially the following two merits for applying to magnets: A thin-panel OHP can be made, unlike the wick type with only cylindrical shapes. The degree of freedom of the installation orientation is high compared to that of thermo-siphons whose orientation is limited.

The OHP has a long capillary which is bent into many turns and a working fluid with two-phase mixture is filled inside the capillary as shown in Fig. 1 [3]. The OHP is a highly efficient two-phase heat transporting device which can transport the amount of heat several orders of magnitude greater than that by thermal conduction in solid metals. The OHP utilizes the pressure change in volumetric expansion and contraction during phase changes, which excites oscillation motions with liquid plugs and vapor bubbles between the evaporator and condenser. Fig 2 shows a conceptual design configuration of OHPs imbedded in a HTS magnet.

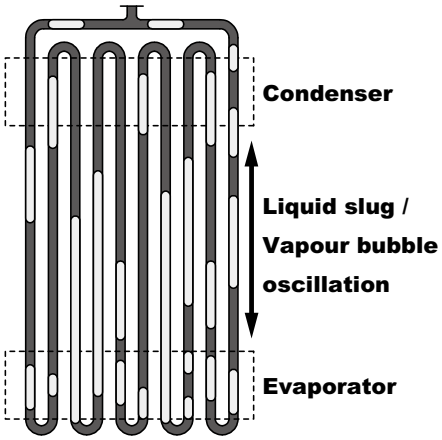

Fig. 1. Schematic illustration for showing the principle of OHP operation.

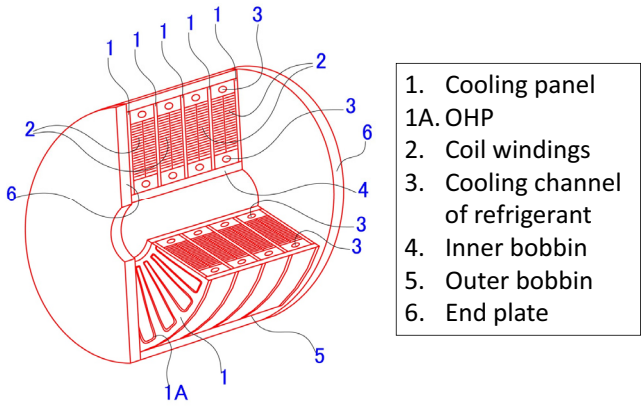

Fig. 2. Conceptual design of OHPs imbedded in a HTS magnet.

3. Performances of Cryogenic OHP

In order to investigate the feasibility of applying cryogenic OHPs in HTS magnets, we fabricated proto-type OHPs. As shown in Fig. 3, an OHP consists of an evaporator section and a condenser section both made of copper blocks, and stainless-steel pipes bent into 10 turns connect these sections. The outer diameter of the pipe is 1.59 mm (1/16 inch) and/or 3.18 mm (1/8 inch), and the inner diameter is 0.78 mm and/or 1.58 mm.Fig. 4 shows the experimental setup for the proof-of-principle experiment of the cryogenic OHP. Resistive thermometers are attached on the copper blocks to investigate the heat transport characteristics of the OHP. A heater is attached to the evaporator which is placed at the bottom. The condenser is at the top where it is connected to the cold head of the GM cryocooler using a copper bus-bar. The inlet of the working fluid is connected to the buffer tank through an isolation valve. The pressure gauges are installed in the buffer tank and the filling pipe, which are used to control the amount of working fluid to the OHP and to monitor the self-oscillation of the OHP. The working fluid of the OHP can be changeable among H_2, Ne and N_2 according to the operation temperature.

The heat transport characteristics of the OHP were investigated by observing the temperature difference between the evaporator and condenser by changing the heater power, the initial temperature of the condenser, the liquid filling ratio of the working fluid, and the kind of working fluid. Stable operations of the cryogenic OHP within the wide operational ranges has been confirmed [4, 5]. In addition, it has been shown to have high heat transport characteristics which surpass high-purity metals. Table 1 summarizes the measured effective thermal conductivity for the 1.59 mm OHP experiments.We here define the effective thermal conductivity k as

$$k = \frac{\text{heat input}}{\text{temperature difference}} \times \frac{\text{distance}}{\text{cross-sectional area}}$$

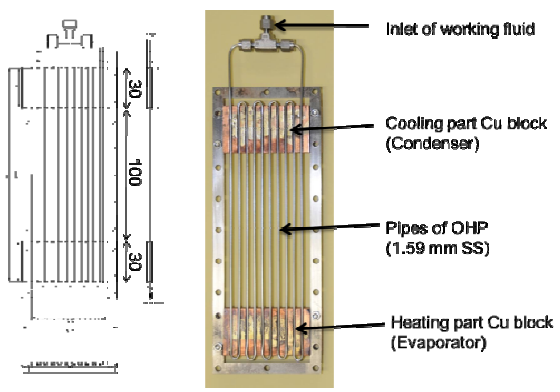

Fig. 3. Cryogenic OHP for the proofofprinciple experiments.

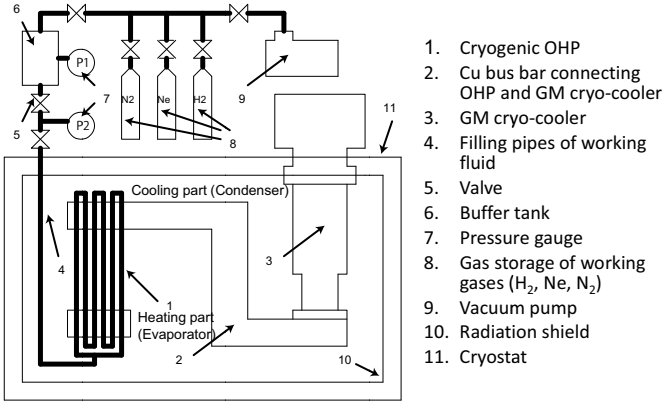

Fig. 4.Experimental setup of a cryogenic OHP for the proof-of-principle experiment.

Table 1. Heat transport characteristics of a 1.59 mm OHP

Work-ing fluid	Liquid filling ratio [%]	Heater input [W]	Condenser Temp. [K]	Evaporator Temp. [K]	Effective thermal conductivity [$Wm^{-1}K^{-1}$]
H_2	31 - 80	0 - 1.2	17 - 18	19 - 27	500 - 3,000
Ne	16 - 95	0 - 1.5	26 - 27	28 - 34	1,000 - 8,000
N_2	17 - 70	0 - 7	67 - 69	67 - 91	5,000 - 18,000

Table 2. Heat transport characteristics of a 3.18 mm OHP with different orientations.

Work-ing fluid	Orientation [degree]	Liquid filling ratio [%]	Heat flux [W/mm^2]	Effective thermal conductivity [$Wm^{-1}K^{-1}$]
H_2	+90	50.9 – 70.0	0.03 – 0.46	8,500 – 11,480
H_2	+45	50.0 – 70.4	0.05 – 0.82	2,220 – 10,330
H_2	0	51.1 – 72.2	0.05 – 0.30	2,830 – 6,380
H_2	-45 and -90	-	-	Did not work
Ne	+90	53.2 – 75.0	0.03 – 0.46	5,100 – 19,440
Ne	+45	50.6 – 70.1	0.10 – 0.82	6,000 – 17,000
Ne	0	69.8 – 86.1	0.03 – 0.82	6,000 – 8,500
Ne	-45 and -90	-	-	Did not work

In order to effectively cool HTS magnets, it is required that cryogenic OHPs can operate in a variety of installation orientations. In this respect, the operating characteristics of the proto-type OHPs were examined by changing the installation orientation [6]. The same type of cryogenic OHP was used with the outer diameter of the SS pipe 3.18 mm and the inner diameter 1.58 mm. The installation orientation was set at the following four angles: horizontal (0°), vertical with the evaporator located at the bottom (+90°), diagonal with the evaporator at the bottom (+45°), vertical with the evaporator at the top (-90°) and diagonal with the evaporator at the top (-45°). The measured effective thermal conductivities are summarized in Table 2.

For the orientations with the evaporator located at the bottom (+90° and +45°) and for the horizontal orientation (0°), the OHP operated stably with an effective thermal conductivity observed at 2,200–11,480 $Wm^{-1}K^{-1}$ (for H_2) and 5,100–19,440 $Wm^{-1}K^{-1}$ (for Ne). In these cases, the temperature of

the condenser was at 17–19 K (for H_2) and 26–28 K (for Ne), whereas the evaporator was at 19–30 K (for H_2) and 27–39 K (for Ne). For the orientations with the evaporator located at the top (–90° and –45°), however, the OHP did not work stably. There have been many reports that OHPs can work also with these orientations at room temperature. Further optimization is necessary in order to operate cryogenic OHPs in various configurations.

In order to mitigate the problem of installation orientation, here we propose a modified-type OHP, with both ends cooled (condenser) and the center heated (evaporator), such as shown in Fig. 5. We consider that the central heating is adequate for OHPs imbedded in magnet windings, such as shown in Fig. 2. The heat generated in the magnet windings can be transported toward the inner and outer bobbins by OHP-imbedded cooling panels. The heat is then removed by the cryogen flowing in the inner and outer cooling channels supplied from the refrigerator. For the proto-type OHP of Fig. 5, the cooling pipe is made of copper with an outer diameter 3 mm and inner diameter 2 mm.

Fig. 6 shows the measured effective thermal conductivity of the modified-type OHP using Ne as the working fluid. Stable operations have been confirmed experimentally. However, the measured effective thermal conductivity was much smaller than that observed in the conventional type OHP. We consider that the effective thermal conductivity can be further improved by incorporating an optimized configuration for the OHP structure.

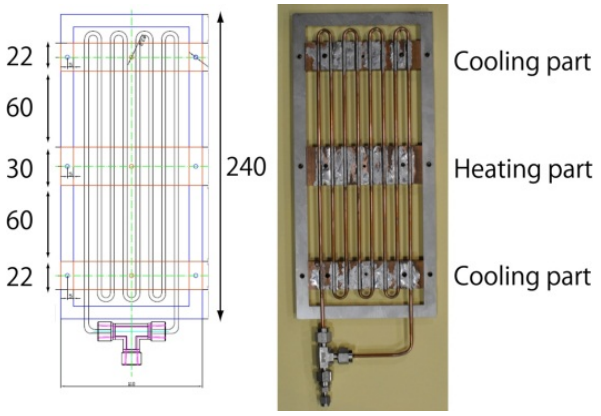

Fig. 5. Modified-type OHP with both ends cooled and the center heated.

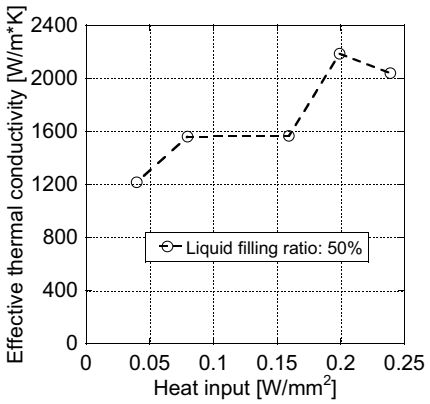

Fig. 6. Effective thermal conductivity of the improved-type OHP.

4. Conclusions

High heat transport properties of cryogenic OHPs have been experimentally confirmed at the operating temperature ranges of 17–30 K (for H_2), 26–39 K (for Ne) and 67–91 K (for N_2). A modified-type OHP, with both ends cooled and the center heated, mitigates the effect of installation orientation. We consider that it is possible to dramatically improve the performance of HTS magnets by using cryogenic OHPs.

Reference

[1] Y. Iwasa, “Case Studies in Superconducting Magnets: Design and Operational Issues”, Springer, 2009.

[2] K. Shikimachi, N. Hirano, et al., “System Coordination of 2 GJ Class YBCO SMES for Power System Control,”, IEEE Transactions on Applied Superconductivity, vol. 19, 2009, pp. 2012-2018.

[3] H. Akachi, US Patent No. 4,921041, 1990.

[4] T. Mito, K. Natsume, et al., “Development of Highly Effective Cooling Technology for a Superconducting Magnet Using Cryogenic OHP,” IEEE Transactions on Applied Superconductivity, vol. 20, 2010, pp. 2023-2026.
[5] K. Natsume, T. Mito, et al., “Heat transfer characteristics of cryogenic oscillating heat pipes for high temperature superconducting magnets,” Cryogenics (to be published.).
[6] K. Natsume, T. Mito, et al., “Heat transfer characteristics of cryogenic oscillating heat pipes for high temperature superconducting magnets”, presented at ICEC23-ICMC 2010, July 19 – 23, 2010, Wroclaw, Poland.
[7] T. Mito, K. Natsume, et al., “Achievement of High Heat Removal Characteristics of Superconducting Magnets with Imbedded Oscillating Heat Pipes”, presented at ASC 2010, August 1-6, 2010, Washington D. C., USA.

The History of 60 Years Development on Cryogenics in China

Laifeng Li
Key Laboratory of Cryogenics, TIPC, CAS, P.O.Box 2711, Beijing 100190, P.R.China
Contact of the main author: lfli@mail.ipc.ac.cn

Abstract: In this talk, a brief history of cryogenics in China is reviewed. Cryogenics in China was started since 1952 when Prof. Chaosheng HONG came back China from the Netherlands. He organized most of the R&D in cryology in China. Some important contributions in low temperature physics, gas separation technology, space cryogenics, helium cryogenics and applied superconductivity are described in this talk, such as the building of the first hydrogen and helium liquefiers and establishment of the low temperature physics laboratory at the institute of physics where experimental research began in late 1950s, .the applied superconductivity research in the 1960s, the satellite simulation in 1970s, the cold neutron source device and the break-through of 77K HTS in 1980s, small scale cryocollers and novel cryogenic materials in 1990s, and EAST, BEPC-II, ITER in 2000s. Some valuable photos are also presented in this talk.

Considerations on the Evaluation of Electrical Insulation for Superconducting System

Lijian Ding
North China electric Power University
Contact of the main author: dinglj@nsfc.gov.cn

Abstract: Electrical insulation of superconducting system is one of key issues for the safety of power supply system in ITER. Because the working conditions of superconducting system are so severe, which requires for low temperature (liquid nitrogen or Helium) and also for vacuum/low pressure, the electrical insulation structure in it is more complex than that of normal one. The failures of electrical insulation might be like as breakdown in the dielectrics, flashover on the surface of dielectrics, breakdown in Helium, and so on. In order to understanding the actual electrical insulation performance of superconducting system, it is worth to investigate the methods to evaluate the electrical insulation performance.

Usually, breakdown strength, partial discharge, surface flashover voltage are widely used as the parameters for the electrical insulation performance in normal conditions. However, how to get these parameters in a superconducting system? It was necessary that the working conditions must be considered when the test was taken. Therefore, how to simulate the electrical insulation structures in superconducting system is very important. In this topic, we are mainly concerned on the electrode systems and test conditions for the investigation. Some typical electrode systems (simulating the electrical insulation structure) are analyzed and compared, and the test conditions will be discussed. Finally a future test system has been proposed.

Giga Watt Class Hybrid Energy Transfer Line of Hydrogen and Electricity

S. Yamada, Y. Hishinuma, T. Uede*, K. Schippl**, N. Yanagi and T. Mito

National Institute for Fusion Science, Toki, Gifu, 509-5292, Japan

*** Nexans Deutschland Industries GmbH, Yokohama 232-0041 Japan*

*** Nexans Deutschland Industries GmbH, 30179 Hannover, Germany*

yamadas@LHD.nifs.ac.jp

Abstract

Applicability of 1 GW class hybrid energy transfer line (HETL) of hydrogen and electricity is investigated in this report. The rated current is 10 kA, and operation voltage is 100 kV (+ 50 kV and -50 kV for ground). Delivery capacity of the liquid hydrogen is 100 tons per day. Re-cooling station of the liquid hydrogen is placed on every 10 km of the unit section. High J_c performance under high temperature region around 20 K requires for the SC wire. The special multi-filamentary magnesium diboride (MgB_2) wire was developed to suppress the I_c degradation against bending strain. Structure of a coaxial stranded cable is proposed for the design of 10 kA MgB_2 cable. Pressure of liquid hydrogen from 0.4 to 0.6 MPa was chosen, in order to keep the liquid phase up to 25 K. It was confirmed that this HETL is one of the attractive energy transportation system which combines hydrogen fuel and SC power transmission.

1. Introduction

Thermo-nuclear fusion is recognized to be a clean and unexhausted energy resource because the fuel can be extracted from sea water unlimitedly. It also has a big advantage of less CO_2 emission, of which character would contribute to avoiding green house effect on the earth. Integrated energy transportation system will be necessary for the hydrogen society in near future. The force-free helical-type fusion reactor, FFHR, can produce the current-less steady-state plasma with no dangerous disruptions [1]. These are great advantages for the D-T reactors. To assess flexibility in operation of the FFHR, co-generation system of electricity and hydrogen is investigated. In this system, hydrogen is made from the steam electrolysis, in which thermal energy of the steam can be obtained from the waste heat of the divertor and the radiation shield components outside of the breeder blanket [2].

Hydrogen has to be packaged by compression or liquefaction, transported by trailer or pipeline, stored, and transferred to the end users. The Energy Supergrid that delivers electricity and hydrogen in the integrated energy pipelines in the USA was proposed [3]. World Energy Transmission System is also discussed to assess the global network of the SC power cables and fuel pipelines [4]. These reports deal the qualitative analysis and/or principle proposals.

One GW class hybrid energy transfer line (HETL) of hydrogen and electricity is proposed, and pressure loss and temperature rise of the 10 km long HETL are investigated on the basis of experiences of the SC bus-lines of the LHD [5]. Design of 10 kA class HTS cable and development of high Jc MgB_2 wire are also described in this paper.

2. Hybrid Energy Transfer Line of Hydrogen and Electricity

The characteristics of the HETL are, 1) low energy consumption system for long transportation, 2) low-voltage high-current power line system, and 3) integrated energy transportation system. It is desired for the new needs which combine hydrogen fuel and SC power transmission. The total

Table 1 Design parameters of hybrid energy transfer line.

Items	Target values
Target distance	
total length to end user	100 km
length between the cooling stations	10 km
unit length of a HETL	500 m
Power Transmission	
operation voltage between the lines	100 kV (+50 kV and -50 kV)
maximum operation current	dc 10 kA
Hydrogen Transportation	
Transportation capacity	100 tons/day (1.16 kg/s)
Operation temperature	17 – 24 K
Pressure of liquid hydrogen	0.4 – 0.6 MPa

length of 100 km is selected to assess the engineering potential of the HETL [6].

The HETL system requires high reliability and safety as well as the conventional power grid and natural-gas pipe line. The major concepts for the HETL are as follows. (1) Unit length of a HETL is 500 m. (2) The hydrogen re-cooling station is placed on every 10 km. (3) Delivery capacity of the liquid hydrogen is 100 tons per day. (4) Transmission capacity of the superconducting (SC) cable is 1 GW, and available current is 10 kA. Operation voltage between the lines is 100 kV, and operation voltage between the line and ground is +50 kV and -50 kV. Schematic illustration of HETL is shown in Figure 1. Design parameter of the HETL is summarized in Table 1.

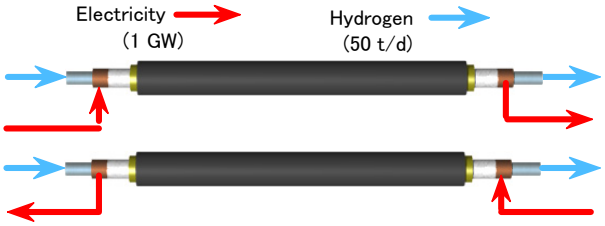

Fig. 1 Schematic drawing of the HETL.

2.1 Structure of the HETL

The HETL system should be flexible and robust, because of the transportation by cable drums and installation on site. The SC cable should have the large margins for the operation current in the limited area. Magnesium diboride (MgB_2) wire is one of the potential candidates for 10 kA class cable, since the core Jc of more than 1000 A/mm2 under the liquid helium was observed in various MgB_2 wires [7-9]. The 10 kA class SC cable for the HETL was designed on the basis data of the MgB_2 wires with a diameter of 1.3 mm [8]. Operation current of an MgB_2 strand at liquid hydrogen temperature was determined to 20 A (core Jc=100 A/mm2). Cross-sectional view of the MgB_2 is shown in Fig. 2 (a), and schematic drawing of the HETL is shown in Fig. 2 (b).

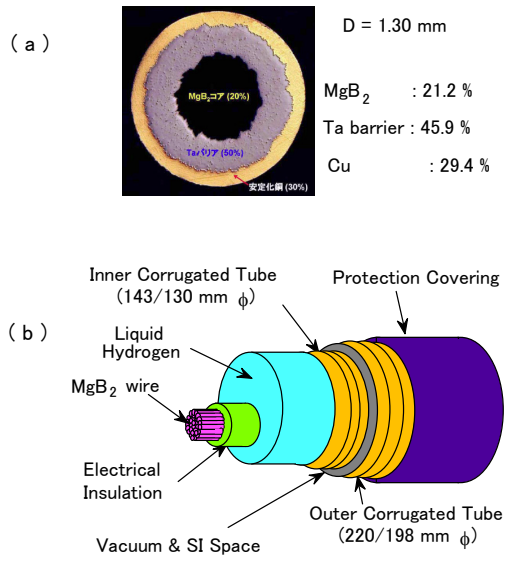

Fig. 2 Cross-sectional view of MgB_2 (a) and structure of the HETL (b)

2.2 Pressure loss of 10 km HETL

Transfer line consists of the SC cable, space

for liquid hydrogen, electrical insulation layer, inner corrugated tube, vacuum space for thermal insulation, outer corrugated tube and so forth. Area of liquid hydrogen is 103 cm^2 (equivalent diameter of 114 mm). We assume the inlet temperature for 17 K, and flow rate of each channel for 50 tons/day. Friction factor in large flow rate regime, λ was estimated by Nikuradse's equation. Pressure loss ΔP is expressed by following Fanning's equation.

$$\Delta P = 4\lambda\rho\frac{v^2}{2}\frac{L}{D} \qquad (1)$$

Where, ρ is density of the fluid, and v is velocity. The calculation result of the pressure loss as a function of pressurized hydrogen temperature is shown in Fig. 3. When the pressure of liquid hydrogen increases, boiling temperature becomes high. Density of liquid hydrogen is 0.071 g/cm^3 which is more than one order smaller than that of liquid nitrogen. Pressurization of liquid hydrogen enables to expand operation temperature region of the MgB_2 cable, and to absorb the head loss of the installation route. In order to obtain the operation temperature of MgB_2 cable from 17 K to 25 K, the pressure of liquid hydrogen from 0.4 to 0.6 MPa was chosen [6].

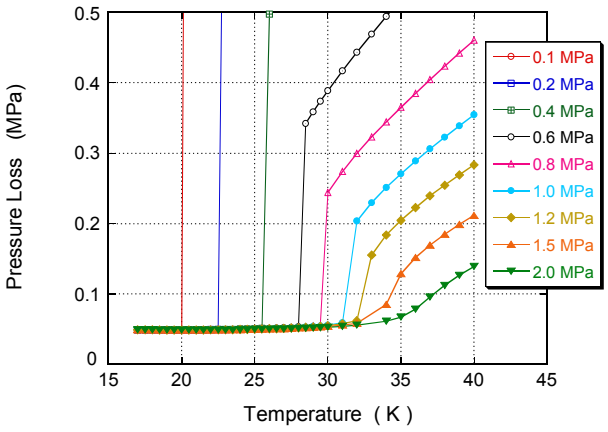

Fig. 3 Pressure loss of 10 km long HETL as a function of hydrogen temperature.

2.3 Heat load and required refrigerator

Reduction of the heat load into the transfer line is one of the important subjects to realize the low-loss HETL system. Following are effective methods to reduce the heat leak; 1) high vacuum degree (for convection), 2) increase in number of super-insulation sheet (for radiation), and 3) slender and long spacer (for conduction) [10]. Purging with clean and dry gas before evacuation is also important to obtain a high vacuum degree for the long cryogenic tube. Taking into consideration of the above mentioned methods, the heat load of 1.0 W/m is realizable. Temperature rise of liquid hydrogen after 10 km transportation is calculated as a function of heat load. When a heat load is 1 W/m, the temperature rise is 2 K. Even if the heat load is 2 W/m, the temperature rise is 4 K. Cryostable condition can be sustained, when the inlet temperature is less than 20 K.

When the heat load is 1 W/m per one-way, refrigeration capacity of 20 kW @17 K is necessary. Cryogenic refrigeration is a complex process involving Carnot cycles and physical effects that do not obey the theoretical law. Nevertheless, the Carnot function is used as a reference for the process analysis. Power consumption of the refrigerator, P, can be estimated as shown in the following equation.

$$P = W_L\frac{T_H - T_L}{T_L}\frac{1}{\eta} \qquad (2)$$

The refrigerator operates between T_H (=300 K) and T_L (=17 K). W_L is the refrigeration capacity, and η is efficiency of the Carnot cycle. Here, 0.25 was assumed as a value of η. Required power of the 20 kW refrigerators is estimated to 1.32 MW. The total power consumption for the energy transfer system of 100 km long becomes 13.2 MW. This value is equivalent to 1.32 % to the transport capacity of 1GW.

3. 10 kA MgB_2 Cable

3.1 Bending Property of MgB_2 Wire

It is important to understand the mechanical performance of the MgB_2 wire. To suppress the I_c degradation for bending strain, multi-filamentary MgB_2 wires have been investigated. The bending property of 19 filamentary MgB_2 wire was made, and it was tested in comparison with the mono-core MgB_2 wire. Diameter of both wires is 1.04 mm, and area ratio of Cu, Ta and MgB_2 of both wires is nearly same (Cu: Ta: $MgB_2 \cong$ 60: 35: 5).

A relationship between the normalized I_c and bending strain for mono-core wire and multi-filamentary wire is shown in Figure 4. The bending strain ε is defined as,

$$\varepsilon \equiv d / D \times 100 \quad (\%). \qquad (3)$$

Where the d is diameter of the wire, and D is diameter of the bend. The I_c degradation of both wires was observed. However, about 50 % of I_{c0} is remained in the multi-filamentary MgB_2 wire, even if the bending strain exceeds 2 %. This is that about half of the filaments of inside keep the I_{c0} value, whenever the filaments of outside are damaged by the large bending stress [6].

3.2 High Jc MgB_2 multi-filamentary Wire

In cable application of MgB_2, I_c improvement is important factor compared with high magnetic field property. The copper addition MgB_2 via low temperature diffusion process leads to higher J_c property in low magnetic field regime. Reduction ratio of area in drawing process affects strongly on the Jc property. High J_c trial has been conducted not only heat treatment study but also drawing process and configurations as shown in Fig. 5.

Figure 6 shows the I_c - B performance of 19-filamentary MgB_2 wire with a diameter of 1.04 mm, showing the load point of 10 kA MgB_2 cable. Temperature was changed from 4.2 K to 30 K in this test. It was confirmed that this MgB_2 wire has the large I_c margin and

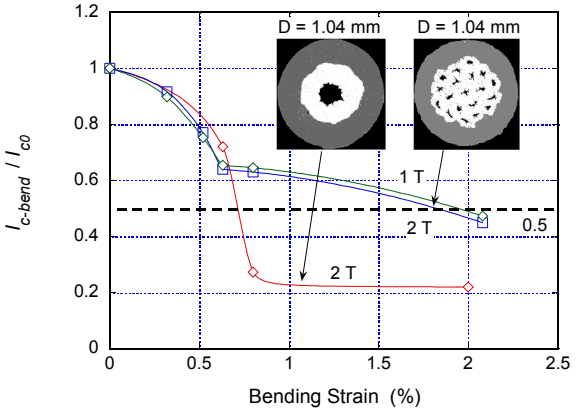

Fig. 4 Relationship between the normalized I_c and bending strain at 20 K.

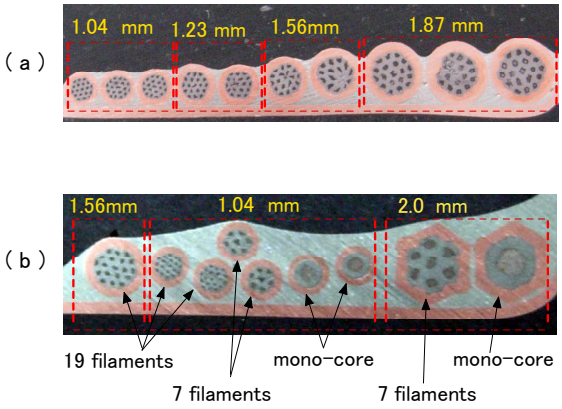

Fig. 5 Samples of the MgB_2 wire trial for drawing process (a), and configurations (b).

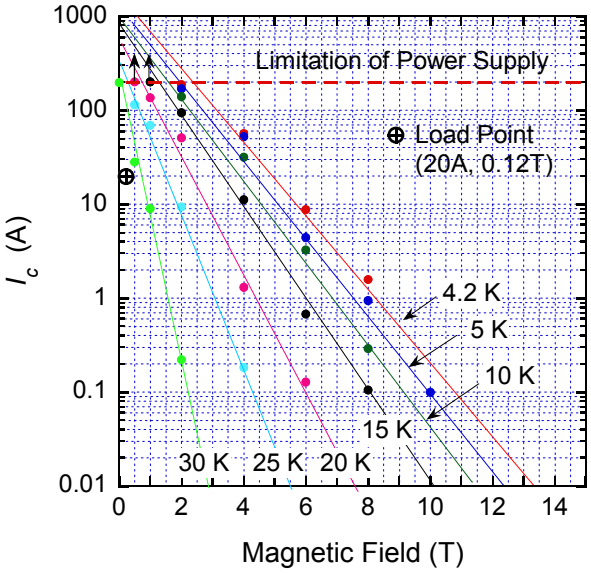

Fig. 6 I_c - B performance as a function of temperature.

Table 2 Design parameters of 10 kA MgB_2 cable.

Items	Target values
Number of the MgB_2 wire	507
Current of a MgB_2 wire	20 A
Diameter of SC cable	36.8 mm□ϕ
Thickness of electrical insulation	12 mm
Maximum magnetic field strength in SC cable	0.12 T
The value of P_c/d_c	30 (=1035 mm / 34.5mm)

temperature margin.

3.3 10 kA class MgB_2 Cable

The MgB_2 cable should be robust for the repetition of the bend and stretch of following manufacture process of; the heat treatment, transfer to the reel, twist and bundle, transportation by cable drums and installation on site. Since diameter of the cable dram has the restriction of the surface transportation, it is determined to 3 m. When the cable is wounded to the cable dram, tensile stress and compressive stress are induced to the outside and inside of the bend, as shown in Figure 7. Structure of a coaxial stranded cable is suitable to relieve the bending stress for the large bore cable. The bending strain of the tight-twisted cable can be explained by the Eq. (3). In the loose-twisted cable, bending strain will decrease, because the slip among the strands to the axial direction will compensate the outside tensile stress with inside compressive stress. To decrease the bending strain, twisting pitch (P_c) should be larger than cable diameter (d_c). The value of P_c/d_c is determined to be 30. Main parameters of 10 kA class MgB_2 cable are summarized in Table 2.

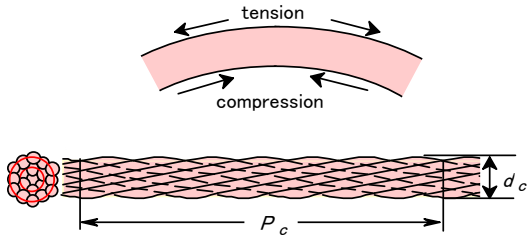

Fig. 7 Schematic drawing of coaxial twisted MgB_2 cable.

4. Conclusions

Design studies of 1 GW class hybrid energy transfer line of hydrogen and electricity is performed. The results are concluded as follows; (1) Power transmission capacity of the dc power line is 1 GW, and capacity of the liquid hydrogen transportation is 100 tons per day. (2) The special multi-filamentary MgB_2 wire was developed to improve the Ic performance against bending strain. (3) Coaxial stranded cable is suitable to relieve the bending stress for the large bore cable. It was confirmed that this HETL is one of the attractive energy transportation system which combines hydrogen fuel and SC power transmission

Acknowledgements

This work is supported by a grant from NIFS with ULAA005 and by the collaboration of JSPS-CAS Core University Program on Plasma and Nuclear Fusion. The authors would express their appreciation to Prof. A. Sagara and Prof. S. Imagawa in NIFS, and Prof. Y. Song in ASIPP for their kind advices.

Reference

[1] Sagara A et al, Nuclear Fusion **45** (2005) pp. 258-263.
[2] Yamada S. et al, Fusion Engineering and Design **82** (2007) pp. 2817-2823.
[3] Overbye T. J. et al, National Energy Supergrid Workshop Rept., Palo Alto, California, USA, Nov. 6-8, 2002
[4] Grant P M et al., WETS`03 Workshop Report, Meudon, France June, 2003.
[5] Yamada S. et al., IEEE Transactions on Applied Superconductivity (2002) pp. 1328-1331.
[6] Yamada S. et al., to be published in Journal of Physics: Conference Series (Proc. of 9th EUCAS) .
[7] Hishinuma Y. et al, Fusion Engineering and Design **81** (2006) pp.2467-2471.
[8] Hishinuma Y. et al, Superconductor Science and Technology **19** (2006) pp. 1269-1273.
[9] Hishinuma Y. et al, Superconductor Science and Technology **20** (2007) pp. 1178-1183.

Development of Superconducting Magnet System for Alpha Magnetic Spectrometer AMS

Qiuliang Wang,
Institute of Electrical Engineering, CAS, and AMS Team
P.O.Box 2703, Beijing 100190, P.R.China
Contact of the main author: Email:qiuliang@mail.iee.ac.cn
Tel: 0086-10-82547162, Fax:0086-10-82547161

Abstract: The Alpha Magnetic Spectrometer, AMS, is a particle physics detector designed to search for anti-matter, dark matter and the origin of cosmic rays in space. The detector will be installed on the International Space Station (ISS). The planned duration of the experiment is 3 years. An important feature of the detector is a strong superconducting magnet which generates a magnetic dipole field of 0.87 T in the center of the detector with a bending power of 0.78 Tm2. The magnet consists of a pair of large Helmholtz coils and two sets of six racetrack coils, circumferentially distributed between them. This special arrangement was chosen mainly to suppress the stray field outside of the magnet. All coils are superconducting and will be operated at 1.8 K. They are wound from a high purity aluminium-stabilized Niobium-Titanium conductor with a rectangular shape of 1.55 mm x 2.00 mm. The magnet is thermally connected to a 2500 l vessel of superfluid helium at 1.8 K which serves as a cold reservoir. Since the magnet design is optimized with respect to very low heat losses the magnet is expected to be operated for 3 year without refilling. This report describes the main features of the AMS superconducting magnet system including coil production and the principle concept of the cryogenic system. The development of some special cryogenic equipment required to operate a large subgravity conditions is presented.

Analysis of Mechanical Behavior of the Superconducting Magnet System for LHD-type Fusion Reactor

H. Tamura, K. Takahata, T. Mito, S. Imagawa, A. Sagara
National Institute for Fusion Science, 322-6 Oroshi-cho, Toki 509-5292, Gifu, Japan
tamura@nifs.ac.jp

Abstract

The large helical device (LHD) type fusion power reactor has many advantages in operations such as steady state and no active plasma current. The magnet system of the LHD-type fusion reactor consists of superconducting helical coils and superconducting poloidal coils. Clarifying the mechanical behavior of the magnet during coil excitation is very important for a design of the magnet system. The mechanical behavior for components in the helical coil can be estimated using a two dimensional axisymmetric model which has a mean radius of curvature of the actual helical coil. The stress distribution of a helical coil of a candidate design of LHD-type helical reactor, which was consists of an aluminum-alloy jacketed Nb_3Sn superconductor and indirect cooling using cooling panels within the coil, was estimated by using the model and the result showed that the stress level were within the reasonable range for composed materials. In parallel with the analysis, sub-scale superconductors for use in the indirect-cooled magnet have been developed. The results of performance tests of the sub-scale superconductor showed good feasibility for application in the helical coil.

1. Introduction

Experimental results with the large helical device (LHD) have shown that a LHD-type fusion power reactor has many advantages, a steady-state operation, no need for active plasma current, constant current coil excitation, for example[1]. Aiming for a demonstration device of a fusion power reactor, the LHD-type force free helical reactor (FFHR) is being studied at the National Institute for Fusion Science with universities [2]. Figure 1 shows schematics of the FFHR. Several design parameters has been candidates thus far, here we focus on FFHR2m1, which has a major radius of 14 m, a magnetic energy of 120 GJ with the coil current of 43.3 MA and a maximum field of 13 T [2, 3].

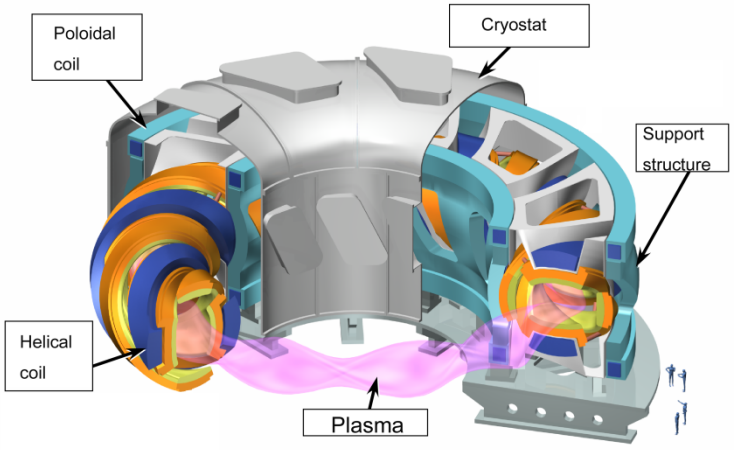

Figure 1. Schematics of the FFHR.

An aluminum-alloy-jacketed Nb_3Sn superconductor and indirect cooling using cooling panels within the coil was proposed as a magnet system for the helical coil [4]. Forced flow cooling is usually used for large-scale fusion experimental devices since a cable-in-conduit conductor (CICC) has the advantage in thermal and mechanical points of view. Indirect cooling is an alternative approach, which uses a superconducting magnet that solves the limitation of the winding length due to the pressure drops in CICC.

The helical coil has a complicated three-dimensional structure and it is difficult to describe the mechanical behavior of the coil. Clarifying the mechanical behavior and rigidity is very important to optimize the coil design and integrity assessment of the materials. The mechanical behavior of the helical coil can be analyzed using a two-dimensional (2-D) axisymmetric model [5]. The 2-D model is useful because it is easier to modify the model according to the geometrical and conditional changes than the three dimensional (3-D) modeling. The rigidity evaluation using the 2-D axisymmetric model for the helical coil, which is indirectly cooled, is introduced.

In parallel with this analysis, we have been developing Nb_3Sn superconductor jacketed by an aluminum alloy for use in the magnet. The results of performance tests for the sub-scale superconductor are also briefly introduced.

2. Structure of the Coil

Figure 2 shows a conceptual design of the cross section of the indirectly cooled helical coil, which is a rectangle 1.8 m wide and 0.9 m high. There are 432 superconductors (36 turns, 12 layers) made of Nb_3Sn and a jacketing material. An aluminum alloy was chosen as the jacketing material because it offers high thermal conductivity and mechanical strength. The cooling panels were placed at every two or four turns of the winding. Each cooling panel consists of two parts: a cooling module and a case section. The cooling module is connected to coolant plumbing outside the coil cross section. The case section has to be built continuously with the superconductor so it will be a strength member, whereas the cooling module can be divided into several parts along the winding direction. The coil is wound along the stainless steel (SS) coil case and covered with a lid. The indirect-cooled superconductor has a 50-mm-square shape and a 32 mm square Nb_3Sn superconducting region filled with

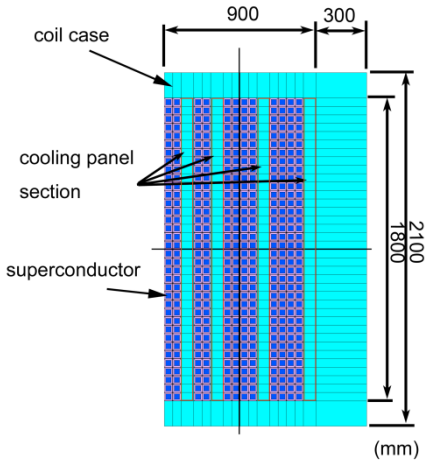

Figure 2. Cross-sectional view of the conceptual design of the indirect-cooled helical coil.

conductive material. The superconductor includes an 18-mm-thick aluminum alloy (6061 T6) and 1-mm-thick insulation. The material properties of the components at a cryogenic temperature [6–8] were used in the analytical model. The longitudinal rigidity of the indirect-cooled superconductors was estimated at 82 GPa, while a CICC type superconductor with a same electrical capacity was estimated 109 GPa [9]. However, the cooling panel also contributes to coil rigidity and if the cooling panel has a longitudinal rigidity of 163 GPa, the indirect-cooled coil can provide reasonable overall rigidity compared with the CICC coil. Assuming that the case section in the cooling panel is made of SS316 and no stress concentration occurs, 20% of the total cooling panel area can be used for the cooling module. The transverse rigidity of the indirect-cooled and CICC types were 79 and 56 GPa, respectively.

3. Coil Rigidity Evaluation

The helical coil has a complex three-dimensional structure. The curvature of the coil winding changes with the toroidal angle. It is believed that a circular coil that has a mean radius of curvature similar to that of an actual helical coil can sufficiently estimate the mechanical behavior of the coil. The average radius of curvature of the helical coil in FFHR2m1 is 5.5 m at the center of the cross-section of the coil. The cross-sectional structure of the helical coil introduced in previous section was used for creating the analytic model. The radius from the central axis to the center of the coil cross-section was set as 5.5 m. An electromagnetic force was applied as the body force by multiplying the current density and the magnetic field in the superconducting region, considering the actual magnetic field distribution. Here we took into account only the radial electromagnetic force since it generated a hoop stress which was more effective for a stress and a deformation of the coil. The magnetic field was applied to every single superconducting region to ensure that the electromagnetic force was precisely applied to the coil. ANSYS 10.0 was used for calculation, and the axisymmetric solid element was adopted. Although the magnetic field intensity was different in every cross-section, an averaged magnetic field was applied at every single superconductor position along the circumference. Furthermore, a constant value was added to the averaged magnetic field so that the total hoop force in the cross-section was equal to the maximum overall hoop force. The cooling panel was assumed to have 80% of Young's modulus for SS316. Figure 3 shows

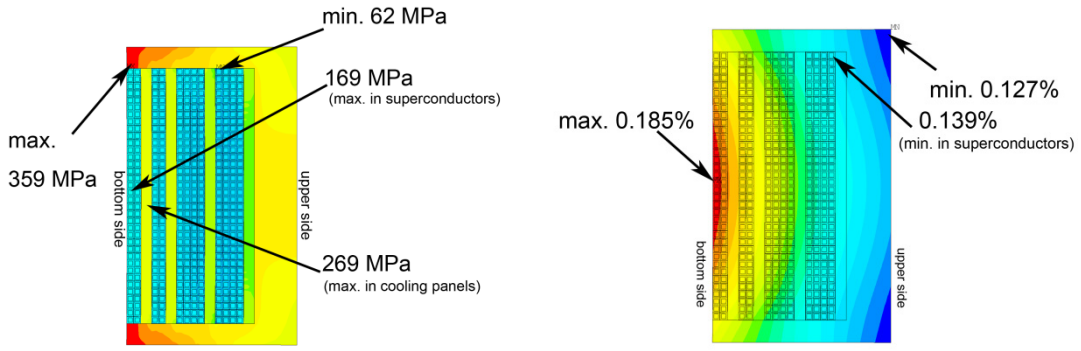

Figure 3 Hoop stress (left) and strain (right) distribution by the radial electromagnetic force.

the results of analysis with respect to the hoop stress and strain distribution. A maximum hoop stress of 359 MPa appeared in the side wall of the coil case. In the coil winding and cooling panel sections, the maximum stress was 169 and 269 MPa, respectively. The strain from the hoop force was 0.185% at the bottom center of the superconductor. The components in the coil were subjected to compressive stress toward the coil center region. The maximum in-plane shear stress in the insulation was 32 MPa. All stress and strain levels for each component were within the permissible range.

4. R&D of an Aluminum Alloy Jacketed Superconductor

The fundamental geometry of the superconductor is a 50 mm square, including insulation. Since the maximum magnetic field at the coil region is around 13 T, Nb_3Sn wires can be used. The operating current is 100 kA, and the overall current density is 40 A/mm^2. Since the melting point of aluminum alloy is lower than the heat treatment temperature of the Nb_3Sn wires, jacketing must be done after heat treatment of the wires. We developed a conductor fabrication process, using a friction stir welding (FSW) technique to avoid a temperature increase in the welding region. The superconducting wire is embedded in the aluminum alloy jacket with a solder material, and the lid is welded by FSW. A prototype 10-kA-class 17-mm-square superconductor was made to demonstrate the fabrication process and the performance of the conductor. It showed a 19 kA transport current at 8 T and confirmed that although some degradation occurred in the critical current, it was not due to the fabrication process, but the difference in thermal contraction between Nb_3Sn and aluminum alloy under a change from room temperature to 4 K.

To confirm the thermal influence of the FSW and examine an instance of bending deformation, 4.7-kA-class superconductors, made of Nb_3Sn cable and aluminum alloy jackets using the same production process as the 10-kA-class sample, were manufactured. Figure 4 shows a cross-sectional view of the sample conductor and its dimensions. The following two samples were tested: (1) without bending and (2) bent once along a ring with a radius of 150 mm and then bent back to the original straight shape (R150SA; bent to lid direction, SB;

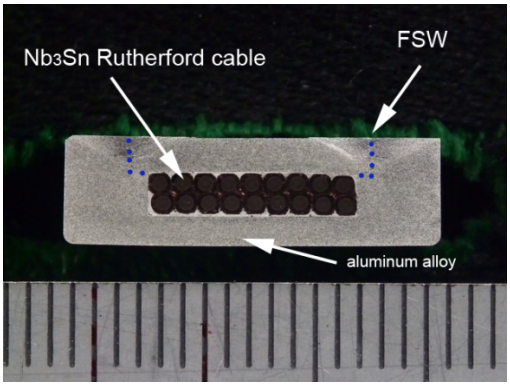

Figure 4. Photo of the cross-section of reduced- size 4.7- kA- class sample superconductor.

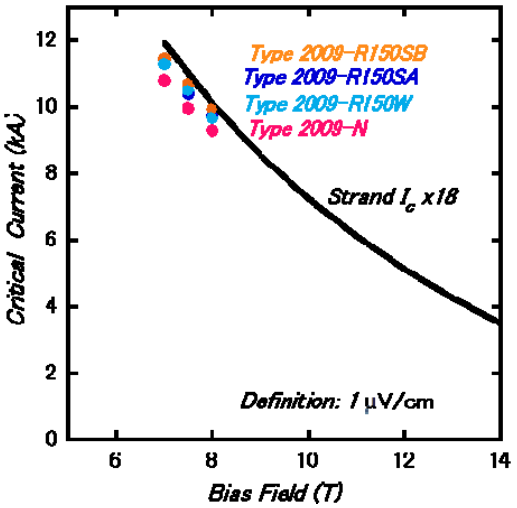

Figure 5. Critical current of the sub-scale superconductor with and without bending.

opposite to SA, W; both direction). Figure 5 shows the experimental results of current-carrying capacity tests. Open symbols indicate the critical current (definition; 1 μV/cm) of the test conductor at 4.4 K. The solid line indicates the critical current of each strand multiplied by 18 (the number of strands). We succeeded in carrying a current of 10 kA at 8 T with the sample R150SB. This confirms that the critical current was not affected by bending deformation.

4. Summary

In conceptual design studies of the LHD-type fusion reactor FFHR, indirect-cooled superconducting helical coils have been proposed. Stress and strain distributions in the helical coil were investigated by the FEM model. As the result, aluminum-alloy-jacketed Nb_3Sn superconductors with a cooling panel can prove the feasibility of this approach.

Sub-scale sample of the aluminum-alloy-jacketed Nb_3Sn superconductor, which has been developed for a candidate superconductor for the FFHR, showed good performance. It also showed that the critical current did not degrade by the jacketing process and by experience of bending.

Acknowledgements

The authors wish to express their thanks to Mr. M. Sugimoto of the Furukawa Electric Co., Ltd. for his efforts to develop a superconductor for the candidate system. This work was partly supported by the JSPS-CAS Core-University Program in the field of “Plasma and Nuclear Fusion” and by the NIFS (09ULAA117).

References

[1] Motojima, O., et al., “Progress of plasma experiments and superconducting technology in LHD”, Fusion Eng. Des. 81 (2006) 2277.

[2] Sagara, A., et al., “Optimization activities on design studies of LHD-type reactor FFHR”, Fusion Eng. Des. 83 (2008) 1690.

[3] Imagawa S., et al., “Concept of magnet systems for LHD-type reactor”, Nucl. Fusion 49 (2009) 075017.

[4] Takahata, K., et al., “Conceptual design of an indirect-cooled superconducting magnet for the LHD-type fusion reactor FFHR”, Fusion Eng. Des. 82 (2007) 1487.

[5] Tamura, H., et al., “Mechanical behaviour analysis of superconducting magnet in LHD-type reactor FFHR”, J. Phys.: Conf. Ser. 97 (2008) 012139.

[6] Cryocomp software (Eckels Engineering and Cryodata Inc., 1997).

[7] Mann, D., LNG Materials and Fluids (National Bureau of Standards, 1977).

[8] Mitchell, N., “Finite element simulations of elasto-plastic processes in Nb_3Sn strands”, Cryogenics 45 (2005) 501.

[9] Tamura, H., et al. “Conceptual design and development of an indirect-cooled superconducting helical coil in the FFHR”, Plasma and Fusion Research 5 (2010) S1035.

Investigation of the coupling current loops in CIC conductors based on 3-dimensional measurement of strand traces

T. Yagai[1], S. Teshima[2], S. Nakazawa[2], M. Tsuda[2], T. Hamajima[2]
1. Sophia University, 7-1, Kioi-cho, Chiyoda, Tokyo, Japan. 102-8554.
2. Tohoku University. 6-6-05, Aoba, Aramaki Aoba, Sendai, Japan. 980-8579.
e-mail: tsuyoshi-yagai@sophia.ac.jp

[abstract]
While the CIC conductor is the most promising one for fusion apparatuses, inherent disadvantages such as current imbalance or critical current degradation have not been overcome. As for the full size conductor, the current imbalance would not be estimated quantitatively before fabricating the one. The imbalance comes from the strand displacements due to the compaction of the conductor. For this reason, our group have been measured the 3-dimensional strand traces in the real conductor (1m in length for 81-strand cable or 500mm in length for 486-strands cable) in order to calculate the coupling current distributions as a function of time along the loops. The strand -traces analysis indicates that there are so many loops with various loop lengths. Before calculating the current distributions, number of loops and loop length distributions in full size conductor should be obtained. We proposed the newly developed calculation of the distributions based on the measured strand traces. The calculated distributions showed good agreement with the ones obtained from the real strand traces.

1. Introduction

The AC loss observed in large scale magnets for fusion magnets and superconducting magnetic energy storage (SMES) is the sum of the hysteresis and the coupling loss. In particular, the latter is bothersome because it depends on the operating conditions and the cable specifications. According to the theoretical approach, the loss is proportional to the coupling time constant $n\tau_c$ [1]. The constant is expressed as follows,[2]

$$n\tau_c = \mu_0 \sigma \left(\frac{l_p}{2\pi} \right)^2, \quad (1)$$

where n is a shape factor, μ_0 is a permeability, σ is an effective electric transverse conductivity, l_p is a twist pitch, respectively. In order to reduce the loss, the simplest way which is controlled by a manufacturing technique is to decrease the conductivity. Actually, the surface coating by the high-resistance material is recommended in [3] and the reduction of the loss was confirmed.

As for the quantitative analysis of the constant for the experimental results of AC loss measurement, substitution of the twist pitch is not sufficient to fit the constant observed in experiment[3][4]. The experimental work has be done for deriving scaling law of the constant by using various cable pattern [5].

The coupling currents especially with long time constants which have strong impact on the increment of the loss at low frequencies can be explained as local loops corresponding to cyclic changes of non-uniform current distributions in the conductor[4]. In fact, huge number

of loops are identified by measuring strand traces [6]. Equation (1) is not adequate to estimate the loss because it is related to the completely symmetrical twisting configuration.

At this moment, computation of the loss before fabricating large scale conductor is still complex and seems almost impossible. Theoretical work has be done by K. Seo who used the electrical circuit model of sub-scale twisted cable to compute the loss and pointed out the effect of asymmetric strand displacement would play a critical role on the increment of the loss at low frequencies [7].

In our approach for computing the loss, we use the statistic way where the lengths of the loops determine individual time constant are considered to have statistic distribution. For the purpose of getting statistic distributions of the lengths, we have been measured the 3-dimensional strand traces of two CICCs without splitting up into each strand. This makes possible to get the asymmetric strand traces and actual loops inside the conduit. In this paper, we show the stochastic technique to obtain the distributions of the lengths of the CICCs based on the experimentally obtained statistic distributions. By using these results, it is indicated that the distribution might be computed even in large scale CICC.

2. Specifications of CICCs

We use two CICCs for measuring 3-dimensional strand traces. The specifications of two conductors, identical for cable pattern until 4th sub cable, strand material and surface coating, but differ in number of strands, void fraction, twist pitches, shape of conduit, are described in Table I.

As for the 81strands conductor, the cable is not inserted into the conduit, but wrapped by stainless tape in order to compact the cable diameter and the void fraction is 42%, slightly higher than that of typical CICCs. The 486 strands CICC is used for the OV coil in LHD[8]. The void fraction of 38% is typical value and the shape of conduit is rectangular. It is considered that the asymmetric strand traces and sub-cable deformation in the CICCs are quite different from each other, which is suitable for comparison of the distribution of the loop-lengths in terms of sub-cable deformation.

TABLE 1 Specifications of two CICCs

	Circular	Rectangular
Strand material	NbTi	NbTi
Strand diameter	0.823mm	0.889mm
Surface	Bare copper	Bare copper
Void franction	42%(average)	38%
Cabling pattern	$3^4 = 81$	$3^4 \times 6 = 486$
twist pitches[mm]	65/90/150/270	70/120/170/250/400

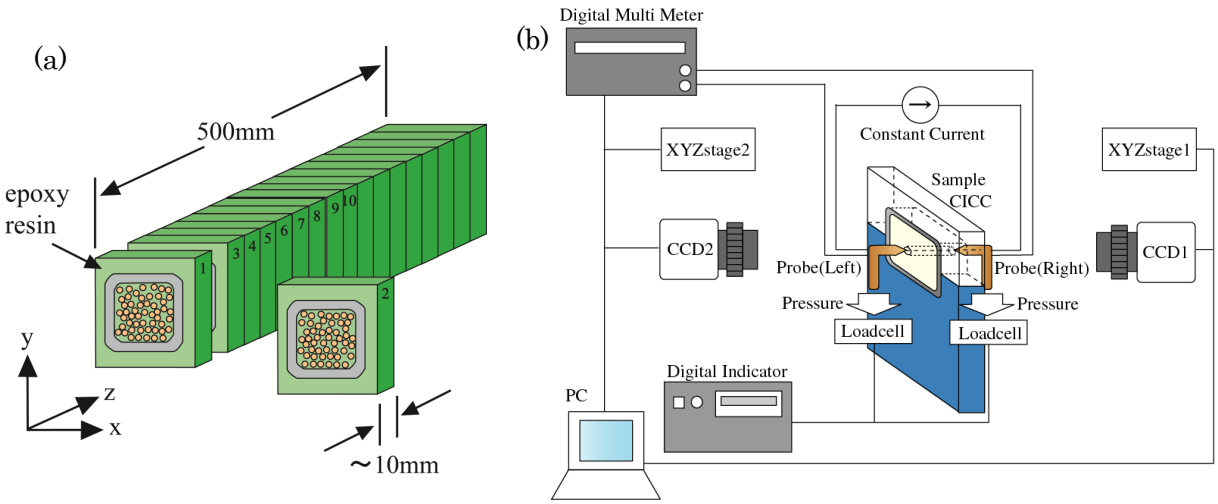

Figure. 1 Schematic views of (a) slicing of the CICCs and (b) resistance measurement system.

3. Measurement system of strand traces

Figure 1 shows the schematic views of (a) slicing of the CICCs and (b) measurement system of strand resistance in order to identify the strand positions on the cross section which provides the strand traces by connecting those in order from the edge. First of all, the CICCs are hardened by epoxy resin to prevent the strand motion during the slicing process. After slicing, with about 10 mm in thickness, the strand positions on both sides of the pieces by measuring the resistance between cross sections.

We newly developed semi-automatic measurement system of strand traces along CICC axis. The probes which are used for the 4-terminal method and mounted on the 3-dimensional manipulators are set in front of both cross sections. The CCD cameras are used for taking picture of cross sections. The pictures are sent to the personal computer for controlling the manipulator. By using the control software, only we have to do in the process of measurement is selecting the strand cross sections showed on the screen. After that, the probes are automatically moved to the selected positions then the resistance is measured and stored. The corresponding strand cross sections on both sliced surfaces are obtained when the measured resistance between the surfaces is the minimum value. We can easily determine the strand traces by connecting the positions along the conductor length.

4. Experimental results -Formed coupling current loops

The coupling current loop is formed by a pair of strands which contact and apart from each other frequently along the length. The frequency of the contact would be determined by the divisor of twist pitches. Therefore, we can categorize the loops by introducing the sub-cable boundary. The strand contact occurs not only on the strand surface but also on the sub-cable boundary. Figure 2 shows the numbers of the loops as a function of loop length. The loop "in n^{th} sub-cable" means the one formed over the boundary of $(n-1)^{th}$ sub-cable. In Fig.2, the distributions of numbers of loops have some peaks. This indicates that the contact frequencies

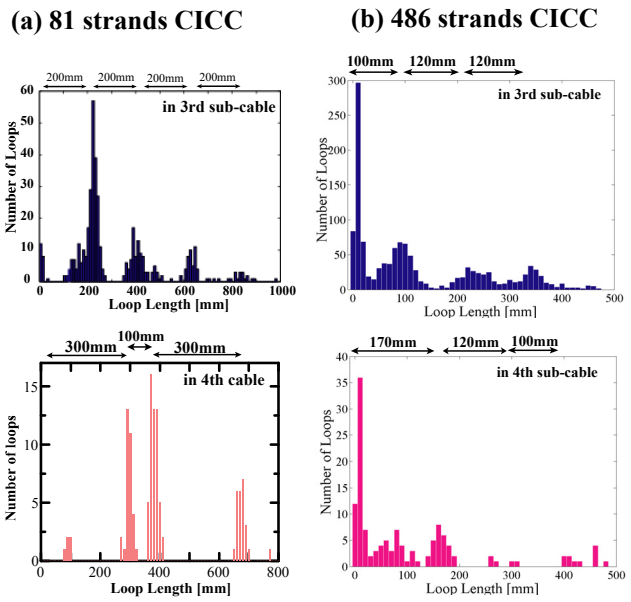

Figure 2 The number of loops as a function of loop length obtained from measured traces

are not random. According to our former work, the loop length should be determined by the function of twist pitches

$$l_{ct} = \left(\frac{1}{l_{n-1}} - \frac{1}{l_n} \right)^{-1} \tag{2}$$

where l_n means twist pitch of nth sub-cable. As for the 81 strand CICC case, the frequencies are 220mm and 337.5mm for 3rd sub-cable and 4th sub-cable, respectively. Those seem good agreement with the values calculated by equation (2). On the other hand, the periods of 486 CICC are 408 mm and 531 mm in 3rd and 4th sub-cables, respectively, which cannot explain the lengths observed less than 400 mm in Fig. 2 (b) Figure 3 describes that schematic of the difference of contact conditions between high and low void fraction cables. In the high void fraction case (left side of Fig. 3), sub-cables are not deformed without compaction. Then the sub-cables are round cable. The strands and sub-cables are rotating around the barycenters. In this case, the contact condition is just “point” in which the distance between strands is exactly its diameter. Unlikely the previous case, in the low void fraction, the sub-cables are deformed

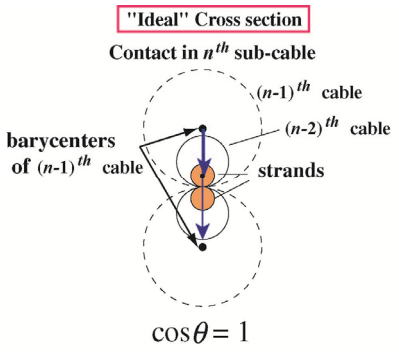

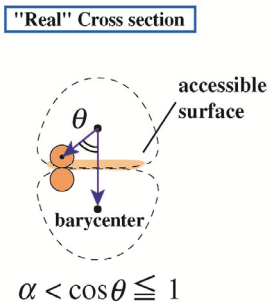

Figure 3 Schematic of difference of contact conditions between high and low void fraction cables.

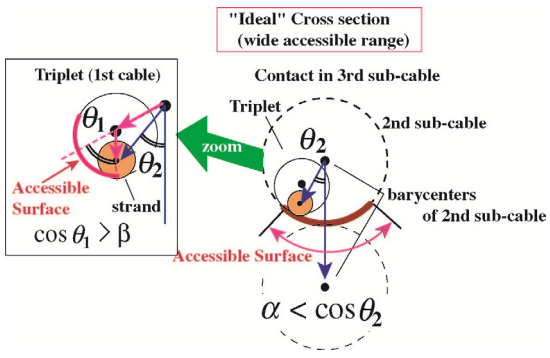

Figure 4 The concept of applying cosθ for calculating loop length distribution

due to the compaction of the cable. In this case, the contact condition is not “point” but “surface”. In order to simulate this deformation effect of the sub-cables, we introduce the angle θ which is the angle between two vectors, the basic one starts at one barycenter of a sub-cable and heads for the other barycenter, the other one starts at the same barycenter of basic one but heads for strand core. The averages over the lengths of the $\cos\theta$ are 0.65 and 0.8 for 486 and 81 strands CICCs for 2nd sub-cable contact in 3rd sub-cable loops. By using experimentally obtained angles, we can calculate the loop length distributions.

Figure 4 describes the concept of applying the angle in order to calculate the loop length distribution. For calculating the loop length distributions, we introduce very simple assumptions, such as, (i) strands and sub-cables rotate around its barycenters with angular velocities depend on the twist pitches, (ii) the strand encounter on the accessible surface. For example of accessible surface, there are two angles for strand contact in 3rd sub-cables.

Figure 5 shows the examples of two angle distributions along the length and schematic view of forming the loops by using stochastic method. The strand contact on the calculation is determined by random numbers. We produce the random numbers on the accessible surface at an interval of 1mm in length. When the number exceeds 0.9 (probability is 1/10), the point is considered to be the contact point. That means the contact length becomes 10mm, which is consistent with the average contact length estimated by using measured traces. In Fig.5, the accessible surface is described by the three shaded region and each region has one contact point. In this case, the lengths of the loops are 100mm, 220mm, and 350mm. We repeated the procedure up to the number of strand combinations.

Figure 6 shows the comparison between experimentally obtained loop length distributions and calculated ones. The left side (a) shows the results in the case of 3rd sub-cables, and (b) shows in the case of 4th sub-cables. As for the 486 strands CICC, the lengths around 100 mm, 240 mm, 350 mm are well simulated by the method proposed above. With respect to the 81 strands, the masses of the lengths are simulated at an interval of 200mm.

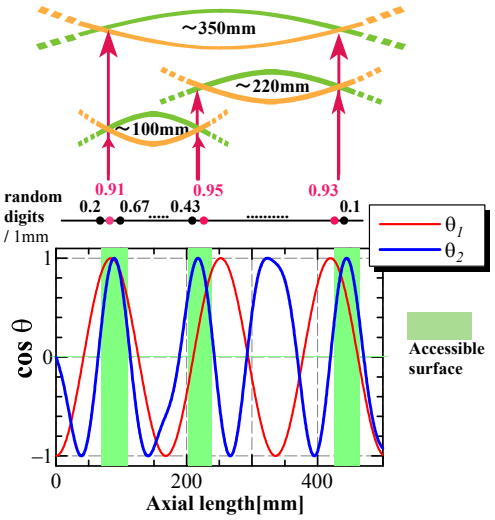

Figure 5 Example of two angle distributions and calculation procedure of the lengths of the loops by using stochastic method

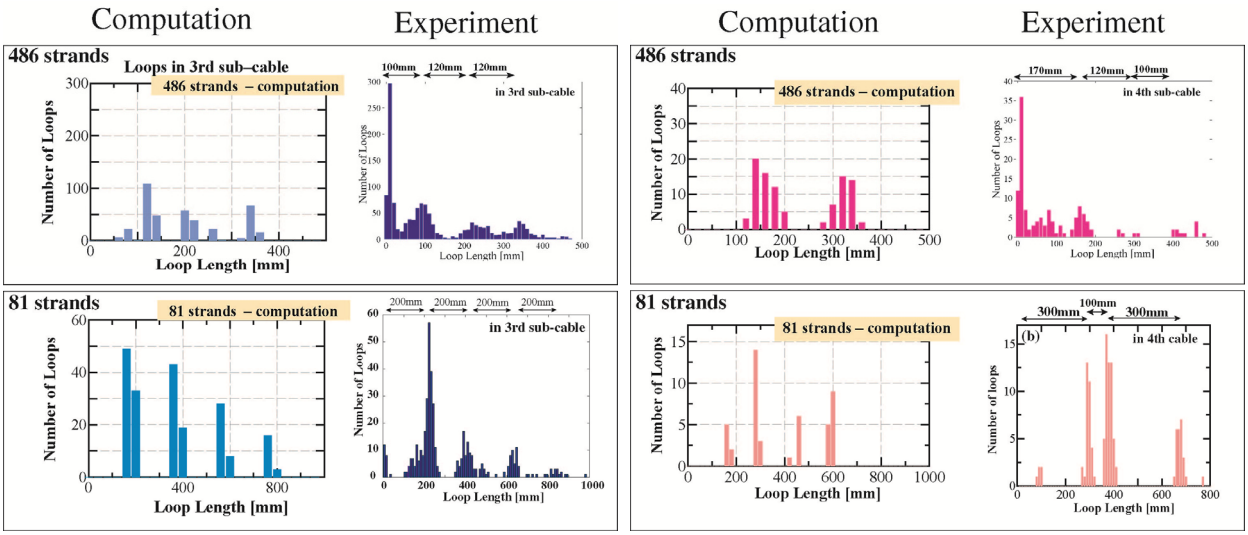

Figure 6 Comparison between experimentally obtained loop length distributions and calculated ones. (a) is the loops in 3rd sub-cables, and (b) is in 4th sub-cables, respectively.

It is indicated that the contacting period, in other words, loop length would be determined by the combination of twist pitches, deformation of sub-cables which depends on void fraction of conductors.

As for the distributions of the lengths in 4th sub-cables, it seems to be consistent with the experimental results, however, partly inconsistent with the results. The strand rotation around the barycenters in 4th sub-cable is considered to be complex. Farther investigation of computing the length in 4th sub-cable would be considered.

It is indicated that the method proposed above would be useful for computation of loop length distributions in full size CICCs. This leads to the production of simulation code for loss calculation and stability analysis of CICCs.

References:

[1] A. M. Campbell, “A general treatment of losses in multifilamentary superconductor,” *Cryogenics.* vol. 22, 1982, pp. 3–16.

[2] G. Ries, “AC-Losses in Multifilamentary superconductors at Technical Frequencies”. *IEEE Trans. Magn.* vol. 13, 1977, pp. 524–526.

[3] T. Hamajima, et al, “AC Loss Performance of the 100kWh SMES Model Coil,” *IEEE Trans. Appl. Supercond.* vol. 10, no. 10 , 2000, pp. 812–815.

[4] T. Mito, et al, “Extra AC losses for a CICC coil due to the non-uniform current distribution in the cable”. *Cryogenics* vol. 38, 1998, pp. 551–558.

[5] A. Nijhuis, Herman H. J. ten Kate, P. Bruzzone and L. Bottura, “Parametric Study on Coupling Loss in Subsize ITER Nb_3Sn Cabled Specimen,” *IEEE Trans. Magn.*, vol. 32, no. 4, 1996, pp2743-2746.

[6] T. Yagai, et al, “Investigation of a Mechanism Forming Irregular Loops in Large CIC Conductor,” *IEEE Trans. Appl. Supercond.*, vol. 18, no. 2 (2008), pp.1123-1126.

[7] K. Seo, K. Fukuhara and M. Hasegawa, “Analysis for inter-strand couling loss in multi-strand superconducting cable with distributed contact resistance between strands,”, Cryogenics, vol.40, 2001, pp.131-137.

[8] K. Takahata, et al, “Coupling losses in cable-in-conduit conductors for LHD poloidal coils,” *Fusion Eng. Design*, vol. 65, 2003, pp. 39–45.

[9] T. Yagai, et al, “Investigation of a Mechanism Forming Irregular Loops in Large CIC Conductor,” *IEEE Trans. Appl. Supercond.*,vol. 18, no.2, 2008, pp. 1123-1126.

Status of R&D on Fabricating for ITER Correction Coils

Weiyue Wu, Jing Wei, Shiqiang Han , Liping Liu, Shuangsong Du, Xufeng Liu, Xiaowu Yu
Academy of Science Institute of Plasma Physics, P.O.Box 1126, Hefei, Anhui, China 230031
Contact of the main author: wuwy@ipp.ac.cn

Abstract—The Correction Coils (CC) in ITER consist of 18 individual coils arranged in 3 groups around the toroidal field coils(TF), those are 6 on top(TCC), 6 on side(SCC) and 6 on bottom(BCC) by out of the TF. The correction coils are placed and sized can correct the most significant error on poloidal (PF), TF and feeders that come from manufacturing and assembly tolerances. These opposite pairs of coils are connected in 9 independent circuits. The coils have been designed using a cable-in-conduit NbTi conductor (CICC) with a 10kA operating current. They are pancake wound with a vacuum pressure impregnated (VPI) with glass-kapton-epoxy insulating system. The winding pack is contained in a case which is mounted onto the TF coil cases as support. The ITER Organization (IO) and the Institute of Plasma Physics at the Chinese Academy of Sciences (ASIPP) are jointly preparing the definition of the technical specifications and the upcoming qualification program for the Correction Coils. The development of major items such as terminal joints, casing manufacture, and vacuum impregnation system, is an essential phase before the series production which will take place at the premises of the supplier. This paper was shown the status on key technologies for fabricating of CC coils.

1. Introduction

The correction coils (CC) system of International Thermonuclear Experimental Reactor (ITER) is designed with NbTi cable-in-conduit conductors (CICC). Outside the TF coils are located three independent sets of the system, each consisting of six coils arranged around the tokamak machine. The Correction coils are grouped as six top CC (TCC), six side CC (SCC), and six bottom CC (BCC) as shown in Figure 1 . They are powered by 10kA current rated power converters per pair of coils diametrically opposed in the tokamak and connected through dedicated SC feeder busbars. The Correction Coil system is designed to correct particularly toroidal asymmetries and reduce error magnetic fields detrimental for physical processes in the plasma.

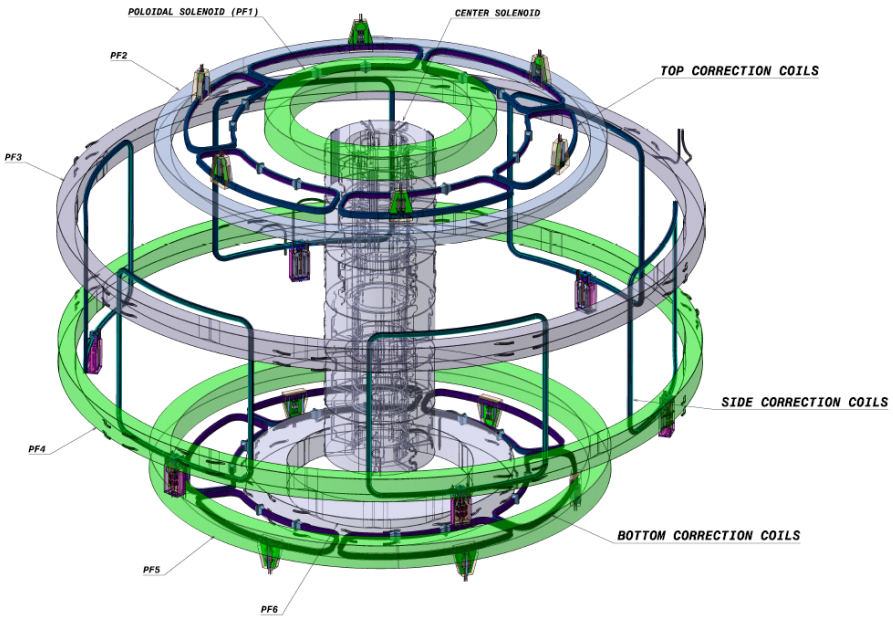

Fig. 1 Layout of Correction coils system and SC, PF systems

The effect of coil positioning errors is defined always as an error in the coil current centerlines from the CS, PF and TF Coils. The field asymmetry is due to various

misalignments and deviations that can occur in the manufacture and assembly of the coils and also due to the presence of winding joggles, coil joints and terminals. The coils have been designed using a cable-in-conduit NbTi conductor with a 10kA operating current. They are pancake wound with a vacuum impregnated glass-kapton-epoxy insulating system. The winding pack is contained in a case which is mounted onto the TF coil cases.

2. Bending Dummy CICC for CC Winding Test

The winding manufacturing line of the Correction coils (Figure 2) has been designed in ASIPP in such a way to wind both correction coil types. The continuous one-in-hand winding scheme without internal joint is adopted to reduce losses. The winding line is equipped with the pay off spool, straightening units, calendaring unit rolls to correct dimensions of jacket during bending on CICC conductor.

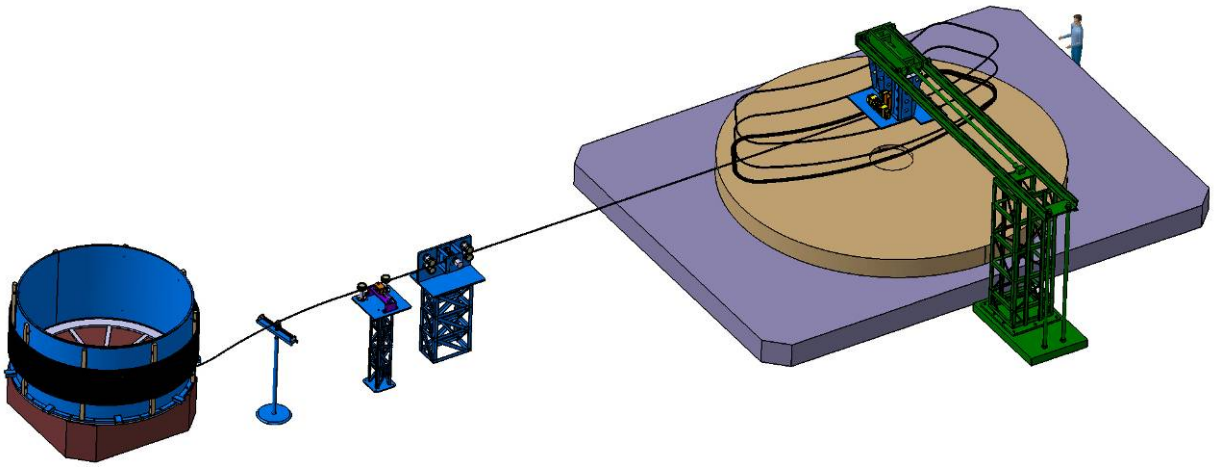

Fig. 2 Axonometric View of Winding Line

The difficulty lies first in the high precision required in their final dimensions, because the CC must fit into a narrow, predetermined space. Secondly, their unusual shape which is non-planar for side CC and planar but banana shaped for the top and bottom CC. For this reason, the manufacture process must be carefully developed to ensure the manufacturability of these coils within specified tolerances, before advancing to the actual manufacturing stage.

Worked performed included winding trials using dummy conductor to wind a test coil with T/BCC shown in Figure 3.

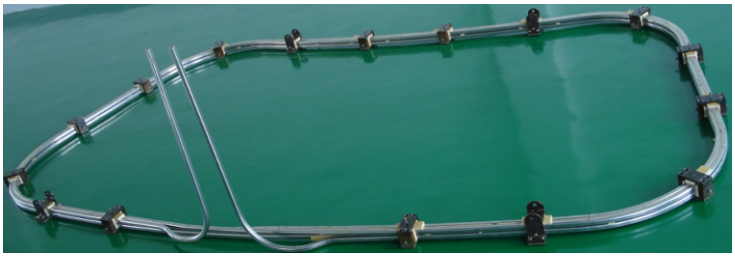

Fig. 3 Four turns T/BCC test coil

3. Vacuum Pressure Impregnation Test

The insulating tapes in CC winding pack are wrapped in dry conditions and shall be impregnated with a qualified resin by a multi-step procedure consisting of drying by heating and evacuation, filling all voids with low viscosity resin at elevated temperature, out gassing by vacuum-pressure cycling, and finally curing of the resin under gas pressure above the

filling level of the resin and at an elevated polymerization temperature. This is referred to as the vacuum pressure impregnation(VPI) process.

The VPI of insulation mock-ups (Figure 4 and Figure 5) has been done two times. The results from these trials and mock-ups will help significantly in the preparation of the manufacturing development plan, the equipments for next step in the execution of coils. It was tested in high voltage on the insulation of turne and ground that results show the quaulity is quite well.

Fig. 4 Vacuum Presure Impregnation Sample

Fig. 5 Cross-section of the obtained the second test sample

For evacuating the winding pack the coil has to be placed into a vacuum chamber to avoid any air entrance during impregnation and into a tight mould for resin hydraulic tightness. Two moulding techniques are best candidates for VPI implementation on CC coils. It is to use the final case structure as a mould for the secondly VPI stage.

4. Case Fabrication and Enclosure Welding Test

This section summarizes the main steps in the manufacture of the CC stainless steel cases and the procedure of encasing of CC winding pack based on 20 mm thick SS316LN base material. It also contains descriptions of equipment which may be used on the manufacturing of the CC case. One of the most critical items in the manufacturing procedure is the management of tolerances. Tolerance control is required throughout the following manufacturing stages to ensure that subcomponents interface correctly during connecting welding of subcomponents to form the half case, the inserting of winding pack into the case, and the closure welding of the two half cases.

The case manufacturing route investigation as the “U” shape for T/BCC and “L” shape for SCC. A test sample for extrusion of the “L” shape case has started and the figure 6 is shown the piece of sub-case has just finished the extrusion.

Fig. 6 Sub-case pieces with "L" shape have been extruded

5. Conclusion

China will contribute to fabricate eighteen correction coils for ITER. There are sieris of test have done that including the winding for CICC on sample, two VPI samples and subcase "L" shape of 316LN pieces. The equipmets have started to design and preparing to fabricate.

ACKNOWLEDGMENT

The authors would like to thank IO Magnet division and China International Nuclear Fusion Energy Program Execution Center (CNDA) for their active contribution to the definition of CC technical specifications, development of task packages and funds support.

REFERENCES

[1] N. Mitchell, A. Foussat, P. Libeyre, DDD11-5_Correction coils and supports_2N6NU_v1_13, ITER Design Documents, 7th September 2009

[2] A. Foussat, P. Libeyre, N. Mitchell, Y. Gribov, C.Jong, D. Bessette, R. Gallix, P. Bauer, A. Sahu, Overview of the ITER Correction Coils Design, *IEEE Trans. Appl. Supercond.* 20 (3) (2010), pp 402-406.

[3] J. Wei, W.G. Chen, Y.N. Pan, W.Y. Wu, D.M. Gao, S.T. Wu, Y. Wu, P.D. Weng, Y.X. Wan, The Superconducting Magnets for EAST Tokamak, IAEA 2010 conference in South Korea

Recent progress of NbTi and Nb_3Sn strands for ITER in China[1]

X.H. Liu [a,b], J.F. Li [a,b], G. Yan [a,b], J. W. Liu [a,b], K. Zhang [a,b], T.C. Wang [a,b], S.J.Du[a,b], Y. Feng [a,b], P.X. Zhang [a,b,c]

[a] *Western Superconducting Technologies Co., Ltd., Xi'an 710018, China*

[b] *State Engineering Laboratory for Superconducting Materials Preparation, Xi'an 710018, China*

[c] *Northwest Institute for Nonferrous Metal Research, P.O. Box 51, Xi'an 710016, China*

Abstract:

High-quality multifilament NbTi and Nb_3Sn strands for International Thermonuclear Experimental Reactor (ITER) have been manufactured by Western Superconducting Technologies Co., Ltd. (WST) for the fabrication of poloidal field (PF) coils and toroidal field (TF) coils. NbTi strands with a diameter of 0.73 mm and 2600 filaments have been obtained by a conventional process, which could be used for mass production of long strands with a unit length more than 5×10^4 m. The I_c and n-value of NbTi strands reach over 350 A @ 4.2 K, 5T and over 34 respectively. The hysteresis loss per unit NbTi strand is less than 45 mJ/cc @ 4.2 K, ±1.5 T. For internal-tin (IT) and bronze process, the multi-filamentary Nb_3Sn strands with a diameter of 0.82 mm and a unit length longer than 5×10^3 m have been successfully fabricated. The I_c @ 12 T, 4.2 K over 241 A with hysteresis loss less than 470 mJ/cc for internal tin process strand and I_c over 236 A with hysteresis loss less than 433 mJ/cc for bronze process strand have been obtained. The PFCN1, TFCN2 and TFCN3 SULTAN samples made by WST strands have passed the ITER qualification test in 2010. The results indicate that the properties of NbTi and Nb_3Sn strands have already met the specifications proposed by the ITER project.

1. Introduction

ITER device consists of six TF coils and six central solenoid (CS) coils both totally made by 400 tons Nb_3Sn strand, and six PF coils made by 240 tons NbTi strand [1-7]. China is responsible for the supply of 180 tons of NbTi and Nb_3Sn strand.

As the only one manufacturer of NbTi and Nb_3Sn strands in China, WST will produce all the strands as Chinese supply in the near future. How to achieve mass production of NbTi and Nb_3Sn strands is the key point due to the series of technical and physical specifications to strands by ITER project. WST aims at the improvement of performances of strands in the large-scale and low-cost production process and has achieved great progress in the manufacture and performances of the superconducting strands for ITER in recent year. So far, an advanced mass production line has been established and enabled to produce superconducting strands in large scale. The substantial technologies and experiences for the fabrication of high performance NbTi and Nb_3Sn strand have been obtained via the R&D and manufacture process in these years [6-14]. All the performances of both NbTi and Nb_3Sn strand satisfy the ITER specifications now. As a sequence, the PFCN1 SULTAN sample made by WST NbTi strand, TFCN2 SULTAN sample made by WST internal-tin (IT) Nb_3Sn strand and TFCN3 SULTAN sample made by WST bronze Nb_3Sn strand have passed the test in 2010. The industrial production of superconducting strands for the next phase has been qualified. In this paper, we report the recent progress on the performances of superconducting strands for ITER in China.

[1] Corresponding author: X. H. Liu. E-mail: xhliu@c-wst.com.

2. Preparation and Characterization of long multifilamentary NbTi and Nb_3Sn strands

The NbTi strand with 2600 filaments was fabricated by the conventional composite process, by which the multifilamentary billet, assembled by thousands of NbTi monofilamentary rods, was extruded, drawn and heat treated to the final strand. Nb Barrier was used to prevent Cu–Ti compound formation at the interfaces between NbTi filaments and Cu matrix.

The IT and bronze process Nb_3Sn strand was fabricated mainly by two steps. First, subelements were obtained through the assembly, extrusion, drawing and shaping of Cu-Nb-Sn composite. Second, final billet was assembled by subelements, barrier and Cu stabilizer followed by extrusion (only for bronze Nb_3Sn strand), drawing, twisting and final drawing process to the final strand. Ta and Nb barriers were inserted into the final billet of IT and bronze Nb_3Sn strand to prohibit Sn from diffusing into the Cu stabilizer, respectively.

The Ic of the strands was determined by a criterion of 0.1μV/cm in varied magnetic fields. The n value was calculated according to the slope of the log V – log I plot between 0.1 and 1.0 μ V/cm using a least mean square fit. The hysteresis loss was calculated by the magnetization hysteresis loop @ 4.2 K, ±1.5 T cycle for NbTi strand and ±3 T cycle for Nb_3Sn strand. The micro-graphs of strands were investigated by a JEOL JSM-6460 scanning electron microscope (SEM). The tests of current sharing temperature (T_{cs}) of SULTAN samples made by WST NbTi and Nb_3Sn strands were carried out at CRPP, Switzerland.

The typical parameters of NbTi and Nb_3Sn strands are shown in Table.1. The cross section views of as-drawn NbTi stand, internal tin and bronze Nb_3Sn stand are shown in Fig. 1(a), Fig. 1(b) and Fig. 1(c), respectively.

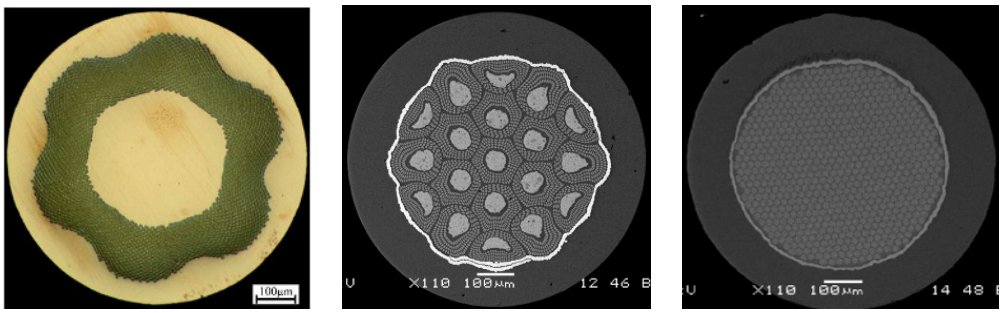

Fig. 1 (a) Cross-sectional SEM images of NbTi strand, (b) internal tin Nb_3Sn stand and (c) bronze Nb_3Sn stand.

Table.1 The characteristics of NbTi and Nb_3Sn strands

Strand type	NbTi strand	Internal tin Nb_3Sn	Bronze Nb_3Sn
Number of filaments	2600	3040	12787
Filaments diameter (μm)	≤7.8	5.8	2.8
Barrier material	Nb	Ta	Nb
Twisting pitch (mm)	13.2-16.8	15.62-16.15	15.80-16.30
Cu/non Cu ratio	2.28-2.34	0.91-1.05	0.91-1.02

I_c (A)	⩾350 @4.2K, 5T	241-260 @4.2K, 12T	236-260 @4.2K, 12T
Jcn @4.2K,12T (A/mm^2)	⩾2826 @4.2K, 5T	913-985 @4.2K, 12T	894-985 @4.2K, 12T
AC loss (mJ/cm^3)	<45 @4.2K, ±1.5T	375-470 @4.2K, ±3T	380-433 @4.2K, ±3T

3. Test results of CHINA ITER SULTAN samples

3.1 NbTi SULTAN sample

Fig.2 show the I_c measurement of PFCN1 Sultan sample at different temperature and background field fabricated by WST NbTi strands and tested in May 2010. It is worthy to note that the T_{cs} of NbTi strand for PF 2-4 under 5 T and operating current of 69 A is 6.31 K, meeting the ITER specification of 6.1 K and above, and that the T_{cs} of NbTi strand for PF 5 under 5.7 T and operating current of 45 A is 6.23 K, also The SULTAN sample made by WST NbTi superconducting strand has exhibited a T_{cs} of 6.33 K under operating current of 50 kA and background field of 4.2 T after circulation, meeting the ITER specification of larger than 6.2 K. This is the first SULTAN sample for PF coil passes the qualification test in the world.

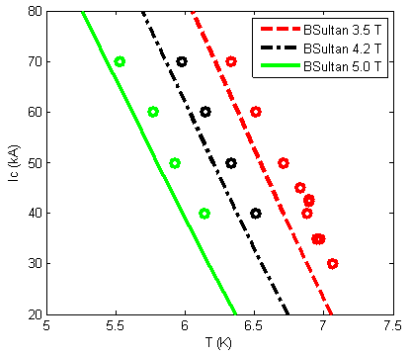

Fig. 2 The measurement result of PFCN1 NbTi Sultan sample.

3.2 IT Nb_3Sn SULTAN sample

One of the most important characteristics of the CICC is its ability to withstand cyclic loads. The IT Nb_3Sn strand made in WST has been cabled and jacketed for SULTAN sample, named TFCN2, which was measured in October 2010. Fig.3 shows evolution of the current sharing temperature T_{cs} as a result after 1000 cycling and warm up and cooling down loads. The T_{cs} for both legs of the sample are 6.35 K and 6.37 K after circulation, satisfying the ITER specification of more than 5.7 K. No relevant performance degradation is observed with cyclic load in TFCN2 conductor. This is the first SULTAN sample made by Chinese IT Nb_3Sn strand that passes the qualification test.

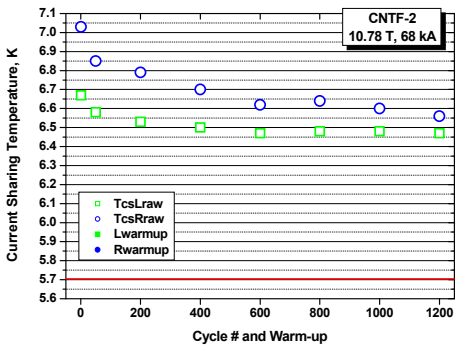

Fig. 3 The measurement result of TFCN2 IT Nb_3Sn Sultan sample.

3.3 Bronze Nb_3Sn SULTAN sample

As an only substitute for IT Nb_3Sn stand, bronze Nb_3Sn stand is also important for ITER TF coil fabrication. Fig.4 shows evolution of the current sharing temperature T_{cs} as a result of cycling. The bronze Nb_3Sn strand made in WST has been cabled and jacketed for SULTAN sample, named TFCN3, which was measured in December 2010. The T_{cs} for both legs of the sample are 6.08 K and 5.93 K after after 1000 cycling and warm up and cooling down loads, satisfying the ITER specification of more than 5.7 K. This is the first SULTAN sample made by Chinese bronze Nb_3Sn strand that passes the qualification test.

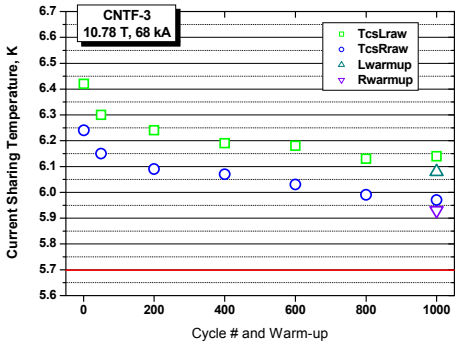

Fig. 4 The measurement result of TFCN3 bronze Nb_3Sn Sultan sample.

4. Summary

NbTi and Nb_3Sn superconducting strands have been successfully fabricated in WST. All the strand performances can meet the ITER specifications and display homogeneous distribution in a small range. The PFCN1, TFCN2 and TFCN3 SULTAN samples made with WST strands have passed the ITER qualification test. WST has been qualified by ITER to produce both NbTi and Nb_3Sn superconducting strand for the next phase.

Acknowledgements

This work is supported by the National Basic Research Program (973 Program) with No. 2008CB717903, ITER Program in The Ministry of Science and Technology of People's

Republic of China (973 Program) with No. 2008GB101001, the international cooperation program with No. 2007DFA50700, and National High-tech R&D Program (863 Program) with No. 2009AA03Z227. The authors are also grateful for the measurement assistance of ASIPP.

References

[1] CIAZYNSKI D., "Electrical and Thermal Designs and Analyses of Joints for the ITER PF Coils", IEEE Trans. Appl. Supercond., 12 (2002) 538.
[2] SBORCHIA C., "Status of ITER Magnet Design and Model Coils", IEEE Trans. Appl. Supercond., 10 (2000) 554.
[3] SALPIETRO E., "Status of the ITER Magnets", Supercon. Sci. Technol., 19 (2006) S84.
[4] MAIXR K., "Completion of the ITER Toroidal Field Model Coil", Fusion Eng. Design, 58-59 (2001) 159.
[5] CIAZYNSKI D., "Current Distribution Measurement in the Busbars of ITER TFMC", Appl. Supercond. Conf., Houston, (2002).
[6] ZHOU Lian, et al., "Development of Multifilamentary Niobium-Titanium and Niobium-Tin Strands for the International Thermo-nuclear Experimental Reactor Project", J. Nucl. Mater. 362 (2007) 208.
[7] ZHANG Pingxiang, et al., "Investigation of Multifilamentary Nb_3Sn Strand for ITER by Internal Sn Process", Physica C, 445-448 (2006) 819.
[8] ZHANG Pingxiang, et al., "Effect of twist process on critical current and hysteresis loss of Nb3Sn strands", Physica C, 463-465 (2006) 817.
[9] Zhang Ke, et al., "Investigation of Nb_3Sn strand for ITER by bronze route", IEEE Trans. Appl. Supercond., 20 (2010) 1440.
[10] LI Chunguang, et al., "Investigation of superconducting properties of Nb_3Sn strands by internal tin process for ITER", IEEE Trans. Appl. Supercond., 20 (2010) 1487.
[11] LIU Jianwei, et al, "The Effect and Introduction of Ti in Nb_3Sn Superconducting Strand", Chinese J. Low Temp. Phys., 5 (2010) 322.
[12] LI Jianfeng et al., "The microstructure of NbTi superconducting composite wire for ITER project", Physica C, 468 (2008) 1840.
[13] ZHANG Pingxiang, et al., "Fabrication and characterization of internal Sn and bronze-processed Nb_3Sn strands for ITER", Supercond. Sci. Technol., 23 (2010) 034013.
[14] LIU Weitao et al., "Development of Fine Filament NbTi Superconducting Strands for ITER", IEEE Trans. Appl. Supercond., 20 (2010) 1504.

Magnetic field and structure analysis of joggle region for CC of ITER

S.S.Du 1), W.Y.Wu 1),J. Wei 1), X.F.Liu 1), L.P.Liu 1), S.Q.Han 1), X.W.Yu 1),A.Foussat 2), N.Dolgetta 2), P.Libeyre 2)
1) Institute of Plasma Physics, CAS, P.R. China（ASIPP）
2) ITER Organization, CS 90 046, 13067 St Paul Lez Durance Cedex, France

E-mail contact of main author: ssdu@ipp.ac.cn

Abstract: The Correction Coils system (CC) within ITER, is intended to reduce the range of magnetic error fields created by assembly or geometrical imperfections of the other coils used to confine, heat, and shape the plasma. The proposed magnet system consists of three sets of 6 coils each, located at the top (TCC), side (SCC) and bottom (BCC), arranged toroidally around the machine inside the PF coils and mounted on the TF coils and uses a NbTi cable-in-conduit superconducting conductor (CICC) operating at 4.2 K.

The structure for the CC joggle region is very complicated including terminal joints, the transition from pancake to pancake for the cable. For the casing, it included the inlet and outlet for the superconductor and the cooling pipe, which can cause the stress very higher for the structure is discontinuous. So it is necessary to do analysis for the CC joggle region. The electromagnetic loads reacts the CC joggle region mainly. So, magnetic field was done and basing on the calculated electromagnetic force, static structure analysis and fatigue analysis were done. This paper is focusing on the magnetic field analysis, static structure and fatigue analysis, the results show that it not exceeds the allowable scope and the CC joggle region can satisfy the physical requirements.

1. Introduction

The ITER magnet system is made up of four main sub-systems: the 18 Toroidal Field coils, referred to as TF coils; the Central Solenoid, referred to as CS; the 6 Poloidal Field coils, referred to as PF coils; and the 18 Error Field Correction Coils, referred to as CC. Pairs of diametrically opposite CCs are connected in anti series inside the cryostat. The top and bottom coil sets are essentially planar while the side coils assume a saddle shape developing on a cylindrical surface[1]， The CC system (see Fig. 1) has been designed to reduce possible error fields complying with the '3-mode' criterion. The CC consists of three sets of superconducting coils (top, side and bottom) placed poloidally in the machine. Each pair of toroidally facing coils are connected in anti-series to produce a n=1 asymmetric mode and to avoid coupling with the axi-symmetrical magnetic fields[2]. Three independent power supplies are used for each CC set to provide toroidal rotation of the correcting field. The CC current capacity limits, based on the physics requirements and the design considerations, are 320 kAt for the top coils and the bottom coils, 200 kAt for the side coils [3].

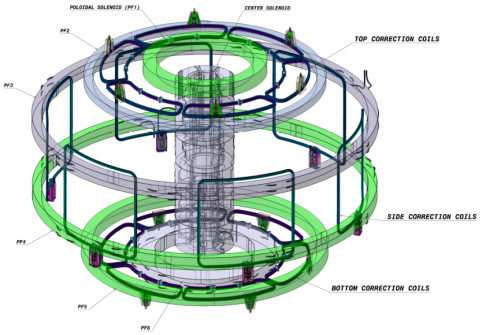

Fig.1. Layout of correction coils system

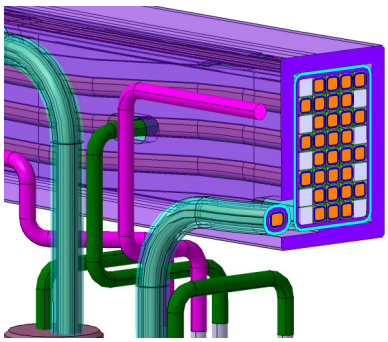

Fig 2 CC cable arrangements in transitions region

When the ITER is on operate,it will be changed for the scenario of PF,CS, so the magnetic load appling on the CC is also changed, which would be danger for the CC, especially for the BCC joggle region, because not only it has much higher magnetic load, but also has the complicated structure,see Fig 2 ,basing on these condition, the magnetic and structure analysis were done for BCC joggle region in this paper.

2. The FE analysis for the CCs

The electromagnetic loading distribution onto the CC coils for tokamak reference scenarios is determined by running the global magnet ANSYS FE-model. Electromagnetic resultant nodal force distributions on the CCs are then transferred to the CC coils stress analysis. The creation of a detailed local stress CC coil FE-model enables to determine the stress levels into the casing and insulation material system. All the results are provided for the BCC joggle region which include the electromagnetic analysis and structure analysis.

2.1 Electromagnetic analysis for BCC joggle region

Element Solid5 was used to calculate the electromagnetic analysis.The model are included PF,TF,CS,plasma and BCC joggle regjon. The FE models and the result for electromagnetic analysis are shown in fig.3. The maximum magnetic flux of the BCC joggle region is 3.8T.

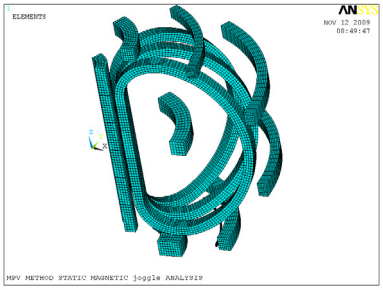

a) FE model for magnetic analysis

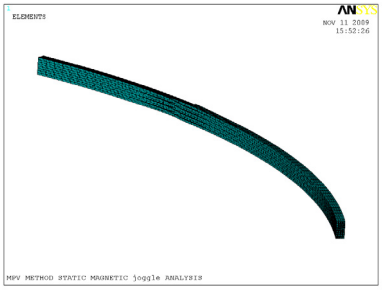

b) FE model for BCC joggle region

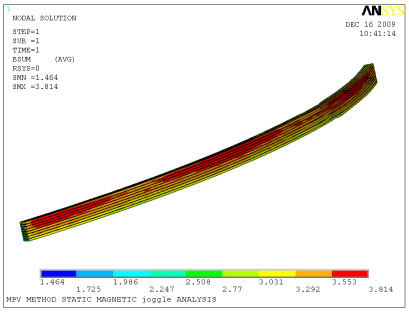

c) Magnetic field for joggle region (T)

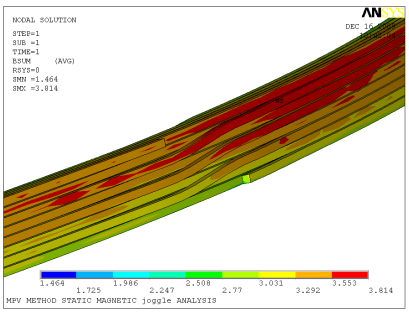

d) Detailed magnetic field for the joggle region (T)

Fig.3. Magnetic analysis for BCC joggle region

2.2 Structure analysis for BCC joggle region

The elements used in ANSYS to perform the 3D mesh of the BCC joggle region FE-model are solid45 and solid 187. Moreover, additional element types have been defined for creating contact elements between the supports and the casing using the contact element CONTA174 and the target element TARGET170 and the contact element placed on casing, target element placed on the clamps. In order to make sure the magnetic load apply correctly, it must make sure the nodes are correspond from EM model to structure model for the cable.

The BCC joggle region was analyzed in detail for the FE structural analysis as it is subject to the maximum magnetic load for the correction coils. The FE models and the result shows the intensity stress results of the BCC joggle region in Fig 4 and Table.1 lists the Pm and Pm plus Pb result.

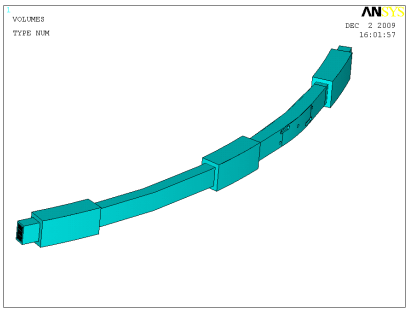

a) BCC joggle region model for structure analysis

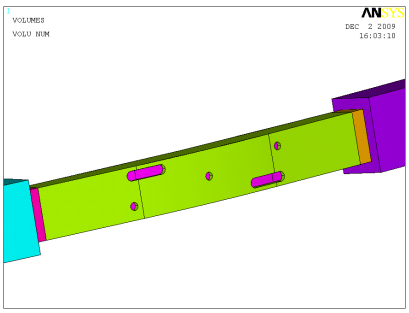

b) detailed model for joggle region casing

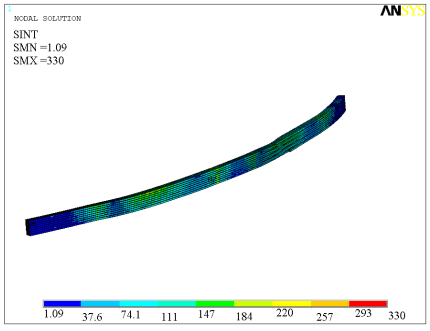

c) intensity stress of joggle region(Mpa)

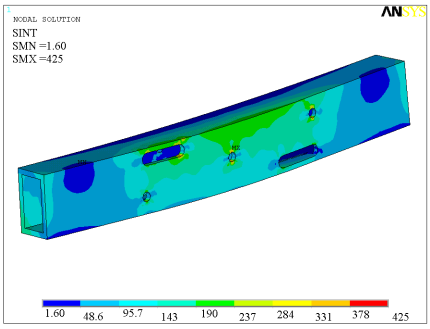

d) Intensity stress of casing for joggle egion(MPa)

Fig.4. Structure analysis for BCC joggle region

Table1 Membrane and membrane + bending stress of BCC joggle region

Maximum stress in	Stress type	stress[MPa]	Allowable stress[MPa]
Path1 in BCC joggle region casing	Pm	362	466.7
	Pm+Pb	392	700
Path1 in BCC joggle region jacket	Pm	219	466.7
	Pm+Pb	248	700

The result for insulation is showed in Fig 5 and Table 2.

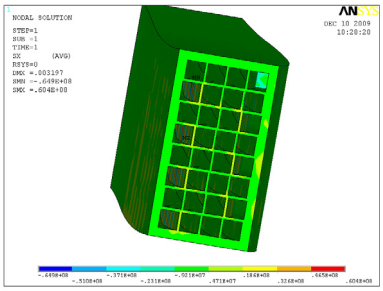

Fig 5 σx stress of insulation for joggle egion(MPa)

Table 2 Stress components on insulation for BCC joggle region

Stress components	*σx*	*σy*	*σz*	τxy	τyz	τxz
	[MPa]	[MPa]	[MPa]	[MPa]	[MPa]	[MPa]
Primary stress	-64.9/60.4	-89.1/77.9	-49.7/45.7	-21.4/22.9	-14.9/15.9	-12.4/15.6

The allowable stress for shear stress is 42.5MPa

2.3 Fatigue analysis for BCC joggle region

For fatigue assessment, it should make sure the minimum of lorentz force resultant and the maximum of lorentz forces resultant, then get the stress range and mean stress, and then get the stress amplitude basing on the GOODMAN law.And it get at the Initial Magnetization(IM) time having the minimum lorentz force resultant, End of Burn + PD (EOB+PD) time having the maximum lorentz force resultant,it shows the result at table 3 for the casing fatigue analysis.

Table 3 The stress range for the casing

Node	IM	EOB+PD	Stress range
	S1 (total)	S1 (total)	S1 (total)
	[MPa]	[MPa]	[MPa]
515643	56.26	328.92	272.7

It shows the S-N curves for the 316LN at 4.5K in Fig 6,see Fig 6

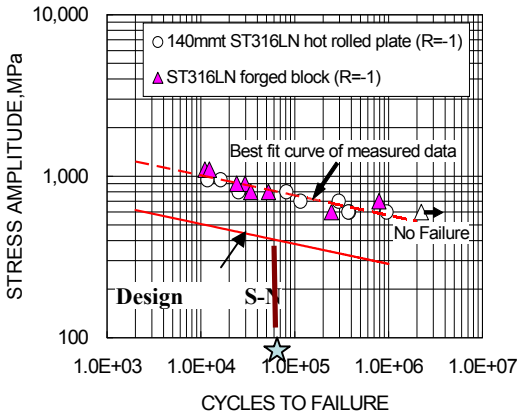

Fig 6 S-N curve for 316LN at 4.5K

Basing on IO requirment, BCC will cycle 30000 times, and give 2 safty factor, so the allowable cycle would be 60000 times,And then the allowable stress amplitude is 410Mpa[4].Basing on GOOGMAN law, it can be known the stress amplitude is 171MPa for the joggle region casing, so it is within the allowable.

3. Conclusion

It has performed on the detailed analysis for the BCC joggle region, and the results show that all are within the allowable limit, So the structure for the BCC joggle region is satisfied the requirment.

Referances

[1] Technical specification ANNEX B to Procurement Arrangement 1.1.P3C.CN.01

[2] A. Foussat et al., Overview of the ITER CC design, MT 21 Hefei Proceedings

[3] J. Knaster et al. The magnet system of ITER and the error fields

[4] Structural_analysis_of_standard_CC_coils_2XW2EG_v1_0

Low temperature thermal expansion and mechanical properties of epoxy composites filled with negative thermal expansion particles

Xinxin Chu,[a,b] Rongjin Huang,[a] Huihui Yang,[a,b] Zhixiong Wu,[a,b] Junfeng Lu,[a] Yuan Zhou,[a] and Laifeng Li [a,]*

The Key Laboratory of Cryogenics, Technical Institute of Physics and Chemistry, Chinese Academy of Sciences, Beijing, 100190, P.R. China

Graduate University of Chinese Academy of Sciences, Beijing, 100039, P.R. China

Abstract

In this paper, epoxy resin reinforced by negative thermal expansion material, ZrW_2O_8, was fabricated. The surface modification of ZrW_2O_8 particles was performed via plasma enhanced chemical vapor deposition (PECVD) process. As a result, a thin film was uniformly deposited on the surfaces of the ZrW_2O_8 particles, leading to an improvement of compatibility and dispersion of ZrW_2O_8 fillers inside epoxy matrix. Moreover, the coefficients of thermal expansion (CTEs) of the composite material containing 0~40 vol. % fillers were studied under cryogenic temperatures. The results showed that a significant reduction in thermal expansion with increasing ZrW_2O_8 content. The cryogenic mechanical properties of ZrW_2O_8/epoxy composites were also investigated, showing the properties were improved by adding ZrW_2O_8 to certain content. In addition, the mechanical strength and modulus of the composite were observed significantly higher at cryogenic temperature than that at room temperature because of the thermal shrink effect and the frozen of epoxy matrix.

Keywords: plasma coating; ZrW_2O_8; epoxy composites; thermal expansion properties

1. Introduction

Epoxy resins have been widely used as the matrix of composites because of their good displayed properties in electric insulation, chemical resistance, and of their cost-effective production. Binding with the rapid developments in spacecraft and super conducting technologies, as well as large national and international cryogenic engineering projects (such as the International Thermonuclear Experimental Reactor (ITER)), epoxy resins have been increasingly employed in cryogenic engineering applications. They were extensively used as structural materials (such as for cryogenic tank), impregnating materials, adhesives, and support matrix material for advanced composites [1-4]. However, comparing with other alloy structural materials, epoxy matrix has a relatively larger CTE, which is about 40-80×10^{-6}/K. Thus, when the temperature slides down to cryogenic area, the internal stress due to the thermal contraction is generated by the epoxy matrix. This will result in two crashes: 1) micro-cracks inside the matrix arise from the volumetric shrinkage due to the large CTE; and 2) the interfaces between the fillers and the matrix will be damaged because of the mismatch in thermal expansion of different materials in the substrate. Therefore, epoxy composites with greatly reduced CTE are urgently desired.

In the plastics industry, the addition of filler materials to a polymer is a common method to obtain a material with desired mechanical and thermal properties. To reduce the CTE of polymers,

* Corresponding author: Tel.:+86 10 82543698; Fax.: +86 10 82543699.

E-mail address: laifengli@mail.ipc.ac.cn

the glass fabrics, carbon fibers or some low CTE inorganic particles were used as fillers in some of previous research works [5, 6]. However, carbon fiber reinforced polymer composites are anisotropic, as a result, the CTE of the material varies in different directions. The most commonly used inorganic particles are nanotubes [6], SiO_2 [7], clay [8-10] or graphite [11, 12] etc. However, the reduction in CTE of the polymer filled by these particles is limited because of the positive CTE of the fillers.

In contrast to most materials that exhibit positive thermal expansion as the temperature increases, zirconium tungstate (ZrW_2O_8) displays relatively large isotropic negative thermal expansion (NTE) over a wide temperature range (from 0.3 to 1050K) [13-17]. Therefore, ZrW_2O_8 is considered as an attractive candidate of filler material to significantly reduce the CTE of a composite material with polymer matrix. Recently, admixture of ZrW_2O_8 with polymers such as polyester [18], polyimide [19], phenolic resin [20], or BECy [21, 22] assigned the polymer composites with reduced thermal expansion property. The CTEs of composites are reduced with the increased amount of ZrW_2O_8. Reported from above work**,** adding nano-particles with appropriate volume fraction into epoxy resin can improve the mechanical properties of composites. This hints us an idea to fabricate a novel strengthened cryogenic composite material with reduced CTE.

Settling phase separation can be a problem in preparing inorganic-organic hybrid composites because of the high density of filler and the low density of the polymer matrix. Therefore, when ZrW_2O_8, with the density of about 5.08 g/cm^3, is used as the filler of epoxy matrix, how to improve the dispersion of nanoparticles inside the epoxy matrix is extremely important. Traditionally, surface modification process are performed to disperse particles because it can decrease the surface energy of these particles, thus further it suppresses agglomeration meanwhile improves dispersion. As an example to illustrate this process, Sullivan [19] ever used 3-aminopropyltriethoxysilane in surface derivatization of ZrW_2O_8 particles to enhance the dispersion properties in preparing ZrW_2O_8/polyimide nanocomposites. However, this kind of wetting chemical method is usually complicated and the chemical properties of substrate may be changed by organic solution. Plasma enhanced chemical vapor deposition (PECVD) is a method that is used to deposit an extremely thin film on the surfaces of nanofibers and nanoparticles [23, 24]. The main principle of the PECVD is that the ionized and excited monomer molecules created by the electrical field bombard and attach on the surface of the substrate. As a result, after the plasma is polymerized, a thin polymer film is deposited on the surfaces of nano-particles and the surface properties are modified. It was proved to be convenient and efficient in surface processing without affecting bulk properties of the substrate [23-25].

In this paper, plasma treated ZrW_2O_8 was added into epoxy to fabricate the well-dispersed ZrW_2O_8/epoxy composites. The thermal expansion behavior and mechanical properties of the composite material were also studied.

2. Experimental Section

2.1. Materials.

The base epoxy resin (Tri-glycidyl-p-aminophenol (TGPAP, AFG-90)) used in this study was a commercially supplied by Institute of Synthetic Resin, Shanghai. The flexible resin additive (IPBE) from Huntsman was a DGEBA type resin with the trade name of PY 4122. It was believed that this type of resin with substituted butoxy groups can create an internally flexable resin that is fully reacted into the structure when it is blended with the base epoxy. The hardener obtained from Huntsman was a liquid aromatic amine, diethyl toluene diamine (DETD), which is a mixture of 2, 4-isomer and 2, 6-isomer. The ZrW_2O_8 powder used for reinforcement was

synthesized by solid-state reaction using ZrO_2 and WO_3 as the raw materials. The acrylic acid monomer to coat on the ZrW_2O_8 particles was purchased from Sinopharm Chemical Reagent Beijing Co., Ltd.

2.2. Preparation of ZrW_2O_8 powder.

The synthesis of NTE material ZrW_2O_8 has been described in many literatures previously [13, 15-17]. To obtain micro ZrW_2O_8 powder, bulk ZrW_2O_8 composite was initially grinded in an agate mortar until the mean particle size is less than 100 um. After that the powder was wetted and milled with appropriate alcohol in a ball grinder at the rotation speed of 350 rpm for 24h. And then, the powder was dried inside a vacuum drying oven. The final size of ZrW_2O_8 particle was around 100 nm~20 um.

Surface modification of ZrW_2O_8 particles was achieved by a plasma polymerization process. The plasma reactor for thin film deposition mainly consists of a radio frequency (RF) source, a glass vacuum chamber, and a pressure gauge. The schematic diagram of reactor was shown in Fig. 1. The powder of ZrW_2O_8 was placed at the bottom of glass vacuum chamber. A RF power generator operating at 13.56 MHz was used to generate plasma, and a thermocouple pressure gauge was used to measure the system pressure. Since the basic pressure was pumped down to less than 40 Pa, the monomer vapor and carrier gas were introduced into the reactor chamber. A magnetic bar was used to stir the powder so that the surface of a ZrW_2O_8 particle can be continuously exposed to the plasma during the PECVD process. In our experiment, acrylic acid (AA) was used as the monomer for its low vaporization temperature and high saturation of vapor pressure. During the PECVD process, the input power of the system was 50W, and the pressure was about 50 Pa. After being plasma treated for 120 min, thin films were coated on the surface of ZrW_2O_8 particles.

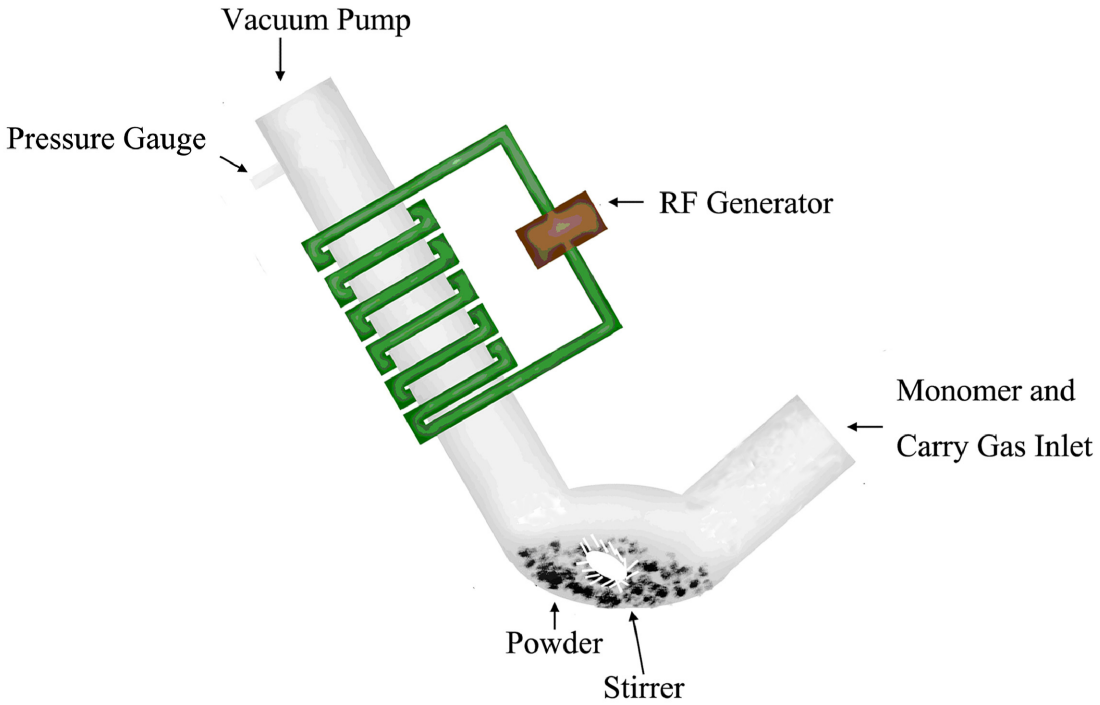

Figure 1. Schematic diagram of the reactor for PECVD on nanoparticles.

2.3. Preparation of ZrW_2O_8/epoxy composite.

ZrW_2O_8/epoxy composite was prepared by blend process via the following steps. Initially, 75% base epoxy resin (TGPAP) and 25% epoxy toughening agent (IPBE) were mixed in a two-neck 250ml round bottom glass flask. And then, ZrW_2O_8 powder and hardener (DETD) were added and mixed using a magnetic stirrer at approximately 45℃. Meanwhile, a mechanical pump was used to as vacuum de-aerating system for the mixture. After being treated for a while, the mixture is uniform. And then, the ZrW_2O_8/epoxy composites were impregnated into a preheated mould inside an oven. Then the sample was gelled at 80 ℃ for 12 h and post-cured at 120 ℃ for 12 h.

2.4. Characterization.

Transmission electron microscope (TEM) measurements of untreated and treated ZrW_2O_8 particles were performed with a JEOL JEM 4000EX TEM. To clarify the chemical bonding structures and functional groups of the PAA films deposited on ZrW_2O_8 particles by PECVD, the powder was analyzed by Fourier transform infrared spectroscopy (FT-IR). FT-IR spectra were acquired from Excalibur 3100 (Varian, American). The CTE of ZrW_2O_8 and epoxy composites were determined using a strain gauge technique. In our study, 120Ω strain gauge was bonded on the specimen surface using a ultrathin glue so that the strain gauge and the specimen had the same strain during temperature variation. It was well known that relative change in length ($\Delta L/L$) of strain gauge could be detected electrically by the relationship:

$$\frac{\Delta L}{L} = \frac{1}{K_S}\frac{\Delta R}{R} \qquad (1)$$

where $\Delta R/R$ is the relative change in the electrical resistance of strain gauge, Ks is the gauge factor which is 2.00 in our study. In our study, stain gauge readings were calibrated using low CTE quartz as a reference specimen to correct for the influence of temperature to the stain gauge. The specimens were cooled down from room temperature to liquid nitrogen temperature (77K). The strain gauges in sample and quartz were connected to form a half-bridge circuit to measure the ΔR/R, and the strain ΔL/L was collected by a computer. Consequently the mean CTE of specimens could be obtained by the following relation:

$$\alpha = \frac{1}{\Delta T}\frac{\Delta L}{L} \qquad (2)$$

where α was the mean CTE, ΔT was the temperature variation.

Tensile and flexural tests were carried out by using MTS-SANS CMT5504 system both at 77 K and at room temperature. The low temperature was achieved by dipping clamps and samples inside a liquid nitrogen cryostat. The cross-head speeds were 2 mm/min and 1 mm/min for tensile and flexural testing respectively. Five specimens were tested for each composite. The experiments for tensile and flexural tests as well as the calculation for their results were in accordance with the national standards GB/T 1447-2005 and GB/T 1449-2005 respectively. Scanning Electron Microscope (SEM) photographs of the fracture surfaces after tensile test were taken with a HITACHI S-4300 SEM. The fracture surfaces were gold coated prior to SEM investigation to avoid charging and were examined at 15 kV accelerating voltage.

3. Results and discussion

3.1. Surface features of plasma modified ZrW_2O_8.

Fig. 2 (a) shows the TEM image of the original, uncoated ZrW_2O_8 particles. As can be seen in this figure, the size of the particles ranges around several hundred nanometers. Besides, the shape of the particles is irregular. Fig. 2 (b) is the TEM image of the coated particles. In this image we

can clearly see that a polymer film is uniformly deposited on the surfaces of ZrW_2O_8 particles. The thickness of poly(acrylic acid) film is approximately 20 nm.

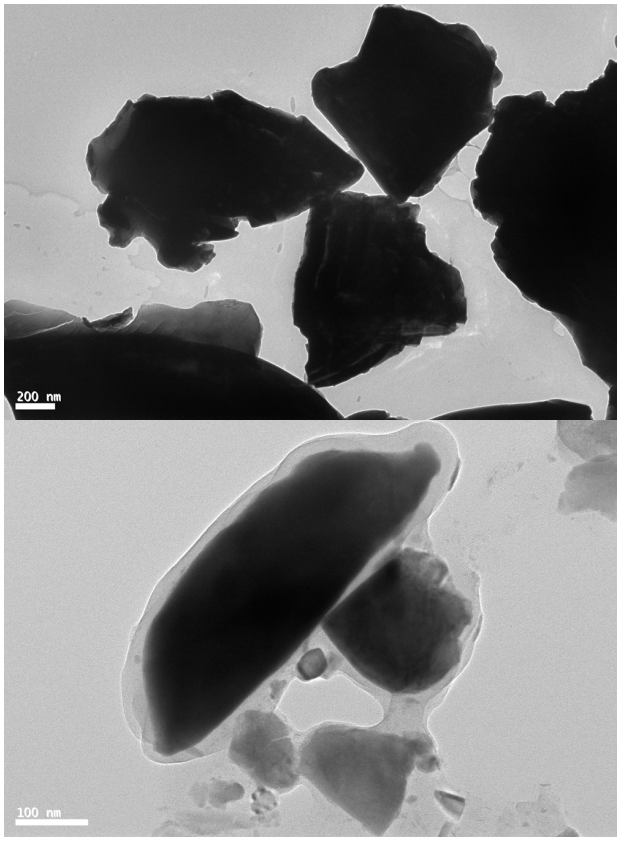

Figure 2. The HRTEM images of untreated ZrW_2O_8 and PEVCD treated ZrW_2O_8 particles.

Particularly, it should be noted that although the shape of particles is irregular, the coating remains almost the same thickness. This indicates a uniform distribution of active radicals inside the plasma chamber with a magnetic stirrer.

The main principle of the plasma polymerization technique is that: the ionized/excited molecules and radicals created by the electric field bombard and react with the surface of the substrate; as a result, the surface properties of ZrW_2O_8 particles are modified by the condensation of the monomer vapor on the surface of the particles. This mechanism naturally lowers the surface energy of the particle by forming an extremely thin film encapsulating the particle surface. As a result, the agglomeration of ZrW_2O_8 particles can be significantly reduced. On the other hand, the functional group of organic monomer anchored on the ZrW_2O_8 surface can also react with the epoxy matrix, thus the ZrW_2O_8 particles can be easily absorbed by the matrix. Therefore, the sedimentation process of the particles is suppressed and the dispersion process of ZrW_2O_8 fillers is improved.

To characterize the chemical bonding nature of the deposited films, the FTIR spectroscopy of untreated ZrW_2O_8 and plasma treated ZrW_2O_8 with acrylic acid are shown in Fig. 3. As can be seen in this figure, there are obvious peaks at 3420.0 cm^{-1}, 1716.6 cm^{-1} and 1385.2 cm^{-1} respectively. The wide peak around at 3420.0 cm^{-1} is the special absorption of the O-H stretching vibration. The peak at 1716.6 cm^{-1} is the special stretching vibration absorption of the C=O function group. At 1385.2 cm^{-1}, there is a small peak, which indicates the winding vibration of O-

H. However, the untreated ZrW_2O_8 particles don't exhibit such peaks. Thus, we can conclude that poly(acrylic acid) films are coated on the particles surface after plasma polymerization, which is in accordance with the previous TEM images in Fig. 2.

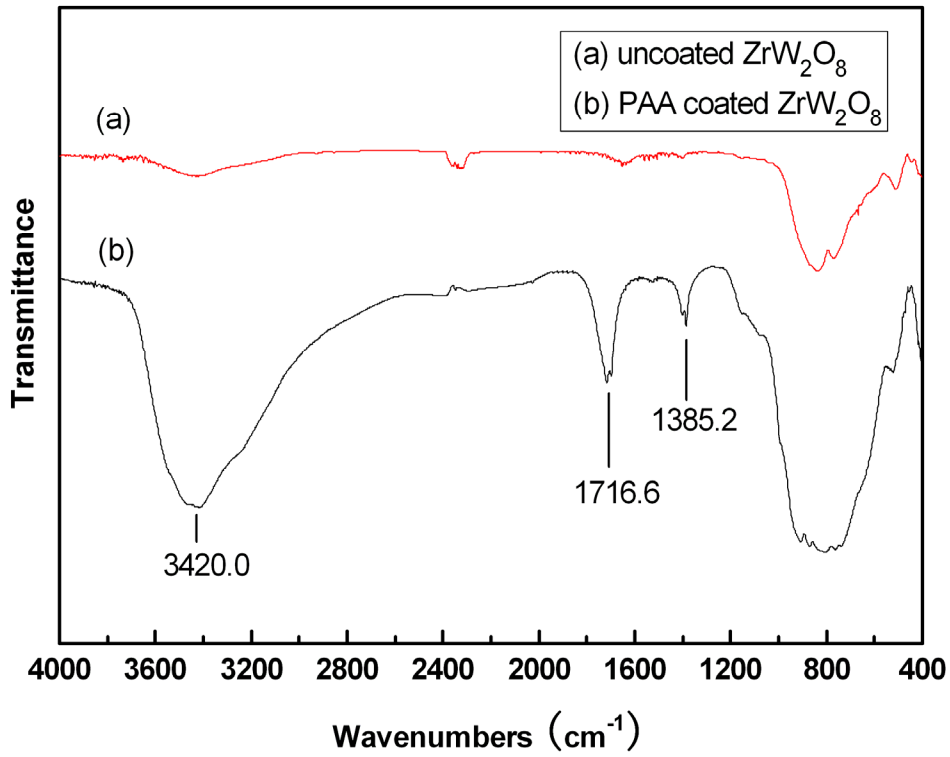

Figure 3. FTIR spectra of (a) uncoated ZrW_2O_8 and (b) PAA coated ZrW_2O_8.

3.2. Thermal expansion behavior of ZrW_2O_8/epoxy composites

The relationship curves of relative strains ($\Delta L/L$) of ZrW_2O_8 and pure epoxy resin vs. the temperature are drawn in Fig. 4. As shown in this figure, with the temperature increase, the linear thermal expansion, or $\Delta L/L$, of ZrW_2O_8 slides down. This indicates that ZrW_2O_8 is negative thermal expansion material, which is in accordance with the previous works [14, 15]. From the slope of this curve, we can easily obtain that the mean CTE of ZrW_2O_8 is about -10.5×10^{-6}/K. In contrast to ZrW_2O_8, the pure epoxy exhibits a positive thermal expansion and its mean CTE is about 45.5×10^{-6}/K, which is extremely large. Besides, one can also find from the figure that the relative strain $\Delta L/L$ is nearly linearly responded to the temperature variation. This also indicates that there is no phase change or crystallinity during temperature variation. As the thermal expansion behaviors of ZrW_2O_8 and epoxy are contrary, the complex of these two materials can significantly reduce volume deformation.

To reduce the CTE of ZrW_2O_8/epoxy composite, more ZrW_2O_8 content should be added into the composite. Fig. 5 exhibits the linear thermal expansion $\Delta L/L_{(300K)}$ curves according to the content change of ZrW_2O_8 reinforced epoxy. From this figure, as can be expected, when the content of ZrW_2O_8 increases, the linear thermal expansion $\Delta L/L_{(300K)}$ of ZrW_2O_8/epoxy

composite decreases steadily. Relatively, the thermal expansion of ZrW_2O_8/epoxy composite at 5, 10, 20, 30, and 40 vol. % ZrW_2O_8 reaches to about 9300 ppm, 8280 ppm, 7200 ppm, 6120 ppm and 3870 ppm, respectively. The mean value of CTE of ZrW_2O_8/epoxy composite can be determined from the slope of the experimental curve. When the ZrW_2O_8 content reaches to 40%, the CTE of composite reduces to 17.6×10^{-6}/K. Compared to 45.5×10^{-6}/K of pure epoxy, the value is reduced by 60%, which is considerable on controlling the CTE of epoxy composite. In a word, the experiment results indicate that ZrW_2O_8 fillers contribute to the decrease in the thermal expansion; and the CTE of ZrW_2O_8/epoxy composite decreases with an increase of ZrW_2O_8 content.

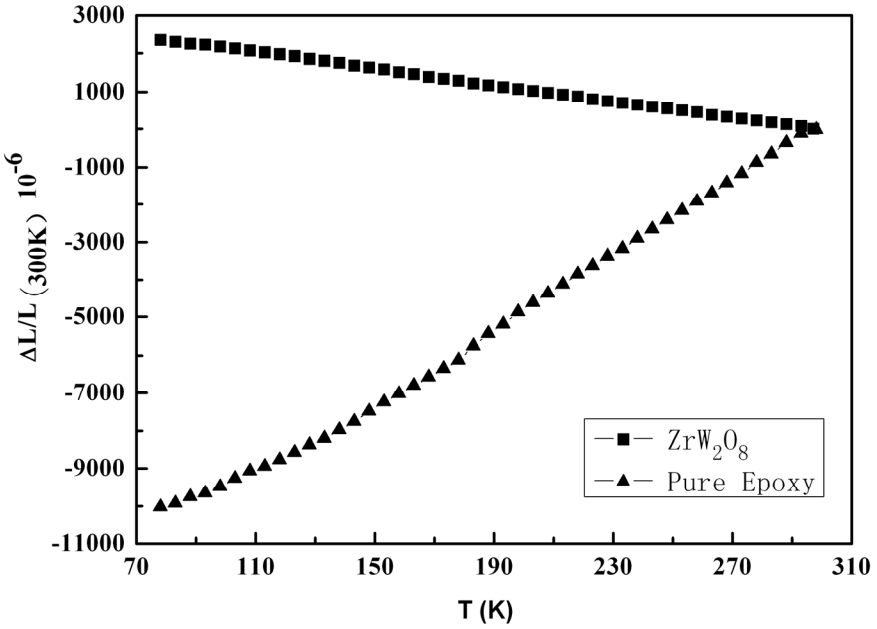

Figure 4. The linear thermal expansion of ZrW_2O_8 and pure epoxy

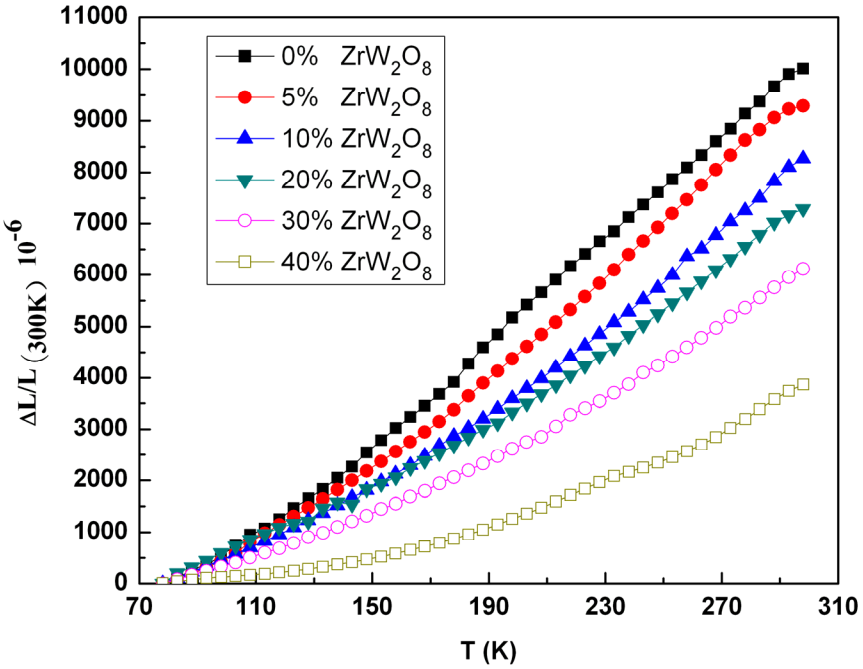

Figure 5. The near linear thermal expansion of ZrW_2O_8/epoxy composite

Figure 6 shows a plot of CTE experimental values as a function of the volume loading for ZrW_2O_8 fillers, and the calculated curves by adopting ROM [26], Turner [27, 28] and Schapery's models [29].

The ROM model serves as the first-order approximation to the overall calculation of the CTE of the composite.

$$\alpha_c = \alpha_f \phi + \alpha_m (1-\phi) \qquad (3)$$

where α_c, α_m and α_f represent the CTE values of the composite, the matrix, and the filler, respectively; ϕ represents the volume fraction of the filler.

In Turner's model, the mechanical interaction between the different materials inside the composite is taken into account. Based on the assumption that all phases in the composite have the same dimension change with temperature, Turner's equation is given as follows:

$$\alpha_c = \frac{\alpha_m K_m (1-\phi) + \alpha_f K_f \phi}{K_m (1-\phi) + K_f \phi} \qquad (4)$$

where K_m and K_f represent the bulk moduli of the matrix and of filler, respectively.

Based on thermoelastic principles, Schapery developed a model to predict the upper and lower bounds of the CTE of a composite. The two bounds are given by:

$$\alpha_c^u = \alpha_m + \frac{K_f}{K_c^l} \frac{(K_m - K_c^l)(\alpha_f - \alpha_m)}{(K_m - K_f)} \qquad (5)$$

$$\alpha_c^l = \alpha_m + \frac{K_f}{K_c^u}\frac{(K_m - K_c^u)(\alpha_f - \alpha_m)}{(K_m - K_f)} \qquad (6)$$

where subscripts "u" and "l" refer to the upper and lower bounds, respectively. K_c^l and K_c^u are the lower and upper bounds of the bulk modulus of the composite, respectively, which can be calculated from the Hashin-Shtrikman model [30, 31] as shown below:

$$K_c^l = K_m + \frac{1}{\frac{1}{K_f - K_m} + \frac{3(1-\phi)}{3K_m + 4G_m}} \qquad (7)$$

$$K_c^u = K_f + \frac{1-\phi}{\frac{1}{K_m - K_f} + \frac{3\phi}{3K_f + 4G_f}} \qquad (8)$$

where the K_m and K_f are the bulk moduli of the matrix and the filler, as well, G_m and G_f represent the shear moduli of the epoxy matrix and of the filler, respectively. The bulk and shear modulus are related to the elastic modulus E and the Poisson ratio ν in isotropic media by means of:

$$K = \frac{E}{3(1-2\nu)} \qquad (9)$$

$$G = \frac{E}{2(1+\nu)} \qquad (10)$$

The bulk and shear moduli values of ZrW_2O_8 used in our studies are 74.5 GPa and 33.9 GPa,[32] respectively. Considering the influence of temperature to the properties of epoxy matrix, the elastic modulus and the Poisson ratio of matrix corresponding to 3 GPa and 0.35, respectively, have been used. Relatively, the K_m and G_m are calculated to be 3.3 GPa and 1.1 GPa, respectively.

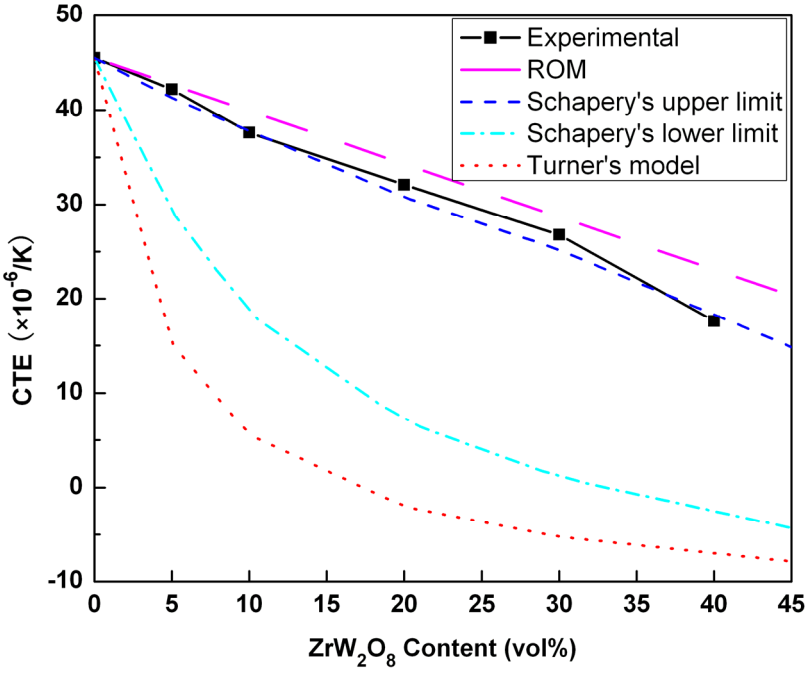

Figure 6. CTE experimental values versus ZrW_2O_8 loading (vol. %) for ZrW_2O_8/epoxy composite along with curves representing CTE values calculated by adopting ROM, Turner's model and Schapery's model.

From figure 6, one can see that the Schapery's upper limit provides the best estimate for the CTEs of the ZrW_2O_8/epoxy composite. The ROM model also provides an approximate prediction but the estimated curve is a little bit higher than the experimental curve. The Turner's model presents the lowest values, which deviate from the experimental results a lot. The ROM model is the simplest one because it only considers the volume fraction variation of each component of the composite. Since it does not include the interface interaction between the polymer and the NTE filler, the prediction of CTE is always higher than the experimental observation. In contrast, the Turner's model estimates the CTE of composite base on the bulk modulus of filler and matrix as well as the volume fraction, but the bulk modulus of ZrW_2O_8 is much larger than the epoxy matrix. As a result, the CTE of the composite is closer to that of the filler and the prediction of CTE is much smaller than the experimental values. The Schapery's model is more complex. The model initially assumes a homogeneous and isotropic reference material in which the constituents are dispersed. The Schapery's upper and lower bounds are depended on whether the stiffness of the reference materials is more or less than that of the reinforcement. Compared to the Schapery's lower limit, the upper limit is more rely on the bulk modulus and shear modulus of the matrix, and the composite modulus is also proximate to that of matrix. As a result, the Schapery's upper limit provides the better estimate for the composites.

3.3. Mechanical properties

The strength and modulus after tensile and flexural tests of 0, 3, 5, 8 and 10 wt. % ZrW_2O_8 content reinforced epoxy composites are illustrated in Fig. 7 and Fig. 8. It is seen that, both at room temperature and 77K, the tensile and flexural strengths increase initially up to the maximum at 5% ZrW_2O_8 content and then decrease with further increasing of fillers. The tensile modulus and flexural modulus have the similar tendency. However, when the tensile strength of ZrW_2O_8/epoxy composite exhibits a tiny decrease with ZrW_2O_8 loading up to 8%, the modulus is still increasing. It can be assumed that the increase concentration of ZrW_2O_8 powder made the composite more brittle and reduced its failure strain. This phenomenon is closely related to most other reinforced polymer composites. Asma Yasmin et al. reported that the addition of low graphite platelet content (2.5%) in epoxy matrix increased the tensile strength and modulus. However, the higher graphite content (5%) decreased the tensile strength [12]. Chen et al. reported a monotonic increase in the tensile modulus with loading up of nanosilica to epoxy resins to 20 wt. %. At 20 wt. %, the sample was more brittle with a slightly decreased strength but increased modulus [33]. In our study, increasing ZrW_2O_8 to a proper content will increase the mechanical performance because of the high strength and high modulus of ZrW_2O_8 particles and the well interfacial bonding between plasma coated particles and epoxy matrices. It can be assumed that PECVD with organic monomer on the outer surface of ZrW_2O_8 can make a low contact angle and high surface energies. As a result, it creates a strong interface interaction between the matrices and fillers and induces efficient load transfer from the polymer to the fillers. However, at higher ZrW_2O_8 content ($\geqslant$8 wt. %), the mechanical properties decreased with filler loading can be attributed to the following three major reasons: 1) the dispersion of ZrW_2O_8 is more homogeneous in the 5 wt. % composite. However, at high concentration the aggregation of particles is inevitable. Therefore, when the composite are under load, the ZrW_2O_8 in the cluster may produce a high stress concentration and cause premature failure; 2) as ZrW_2O_8 content increased, the plastic range of composites decreased considerably. Therefore, it causes a decrease in ductility and an increase in brittleness, which leads a reduction of mechanical properties; and 3) the voids in the composites may be another effect for the decrease of the mechanical properties. Although we degassed the mixture of epoxy matrix and fillers before curing, in fact, we observed that few voids were produced during the curing process and the voids increased with the increase of ZrW_2O_8 content. These voids could be the influence of mechanical properties.

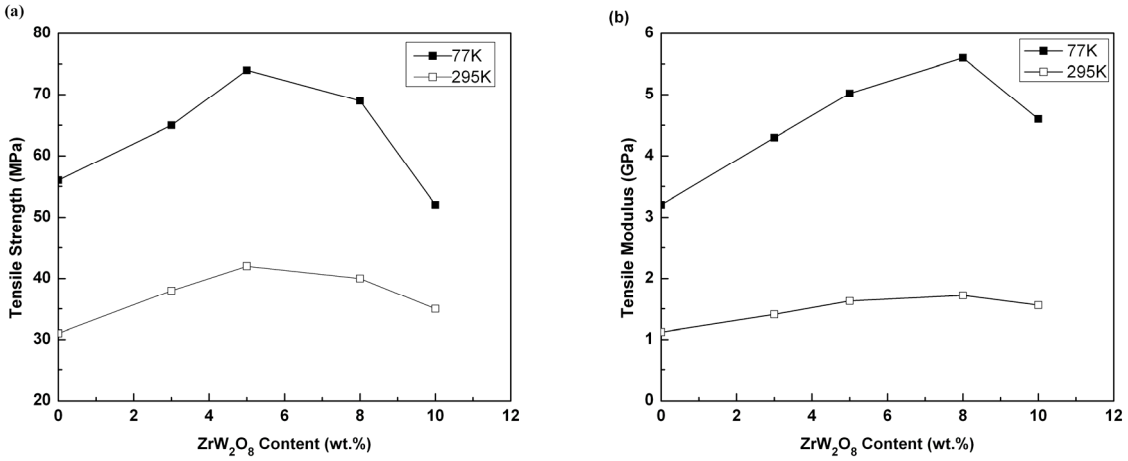

Figure 7. Effect of ZrW2O8 content on the tensile properties of ZrW2O8/epoxy composite at room and cryogenic temperature, (a) tensile strength and (b) tensile modulus

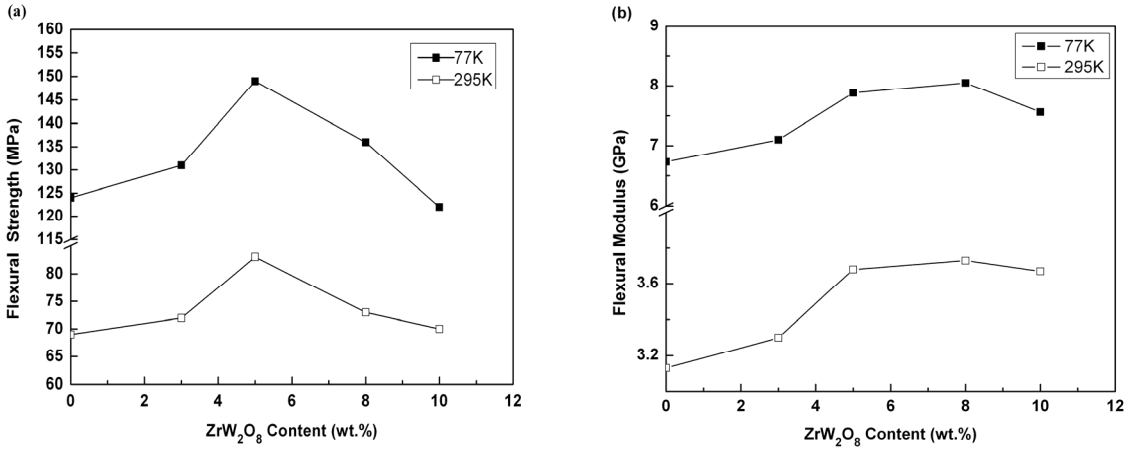

Figure 8. Effect of ZrW_2O_8 content on the flexural properties of ZrW_2O_8/epoxy composite at room and cryogenic temperature, (a) flexural strength and (b) flexural modulus

Moreover, as expected, the mechanical strength and modulus at cryogenic temperature are much higher than those at ambient temperature as illustrated in Fig. 7 and Fig. 8. On the one hand, the interface adhesion between ZrW_2O_8 fillers and epoxy becomes stronger because of the thermal shrinkage of epoxy matrix and tight clamping of the fillers by the epoxy matrix at cryogenic temperature. On the other hand, when the temperature decreases from room temperature to 77K, the chemical bond and molecules of epoxy matrix will shrink and the binding forces between molecules will become stronger. Thus, it can be imagined that molecules are more compacted and the binding forces between molecules are high at cryogenic temperature which makes the positive contributions to the mechanical strength and Young's modulus.

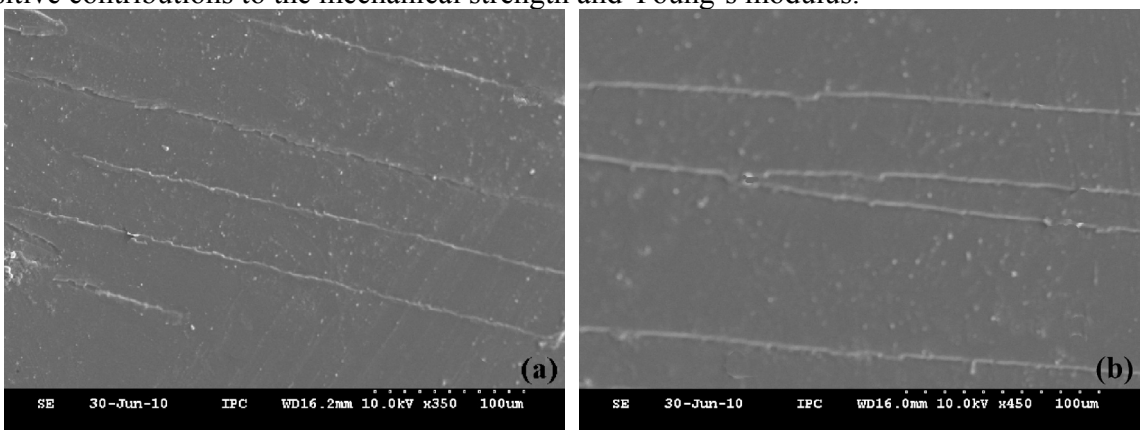

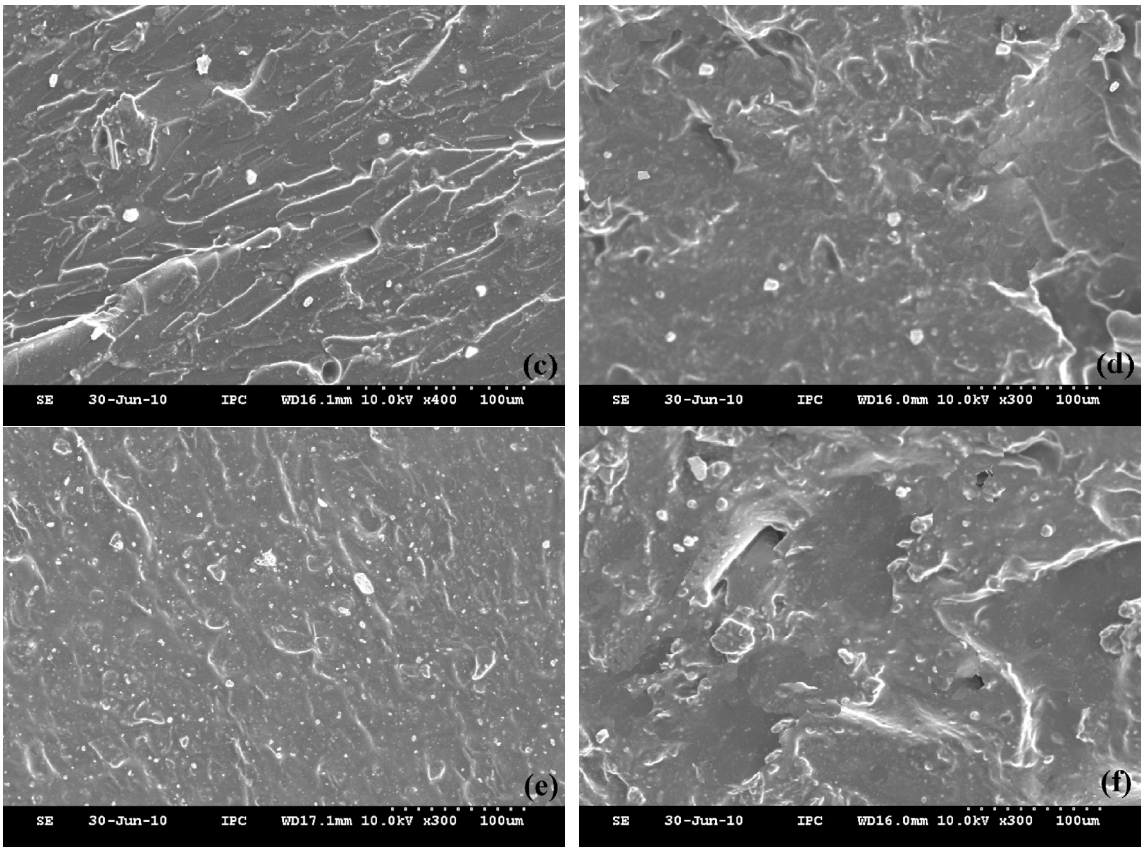

Figure 9. SEM micrographs of tensile fracture surfaces of the ZrW_2O_8/epoxy composites. (a) pure epoxy at room temperature, (b) pure epoxy at 77K, (c) 5 wt. % ZrW_2O_8 reinforced epoxy at room temperature, (d) 5 wt. % ZrW_2O_8 reinforced epoxy at 77K, (e) 10 wt. % ZrW_2O_8 reinforced epoxy at room temperature and (f) 10 wt. % ZrW_2O_8 reinforced epoxy at 77K.

The tensile fracture surfaces of ZrW_2O_8/epoxy composites observed by SEM are illustrated in Fig. 9. The fracture surfaces of the pure epoxy resin in Fig. 9 (a) and (b) show river lines which are the characteristics of brittle fracture behavior of homogenous materials. The fracture surface between the river lines is relatively smooth. This observation is consistent with the brittle failure mechanisms of epoxy materials as mentioned elsewhere [2, 34]. Fig. 9 (c) to (f) show the tensile fracture surfaces of the ZrW_2O_8/epoxy composites with the 5 wt. % plasma treated ZrW_2O_8 content at room temperature and 10 wt. % at 77K, respectively. The fracture surfaces show substantial increase in the surface roughness, which indicates the reinforcement of ZrW_2O_8 fillers in the epoxy matrix. The rough fracture surface indicates deflection of crack path, i.e. the crack deviation from its original plane, increasing the area of the crack. Hence, the required energy for the propagation of the cracks on the fracture surfaces increases. However, the improved toughness and strength by the rough fracture surfaces for the case of 10 wt. % would be overwhelmed by the effect of aggregation of ZrW_2O_8 particles. As a result, micro-cracks would relatively easily initiate at the micro-sized aggregated ZrW_2O_8 particles, resulting in a reduced macroscopic toughness as shown in Fig. 9 (e). Relatively, the fracture surfaces of samples at 77K showed in Fig. 9 (b), (d) and (f) are smoother than those at room temperatures with the same contents of ZrW_2O_8. This indicates more brittle fracture of the composites at cryogenic temperatures.

4. Conclusion

In this study, epoxy resin reinforced with NTE material ZrW_2O_8 particles was fabricated with different fillers contents. The ZrW_2O_8 powder was home-made by solid-state reaction. And then, plasma enhanced chemical vapor deposition (PECVD) was carried out on the surfaces of ZrW_2O_8 to improve their dispersion in epoxy matrix. HRTEM images showed that there was a thin film (about 10nm) coated on the surface of ZrW_2O_8 particles after plasma surface modification. The comparison results of before and after plasma treated ZrW_2O_8 particles from FTIR spectroscopy also indicated that the surfaces of the particles were well modified. The CTEs of ZrW_2O_8/epoxy composites with 0-40 vol. % ZrW_2O_8 were measured by a strain gauge technique. The results showed that: 1) as ZrW_2O_8 increases, the CTEs of composites decrease significantly; 2) when the volume of ZrW_2O_8 reaches 40%, the CTE of composite reduces by almost 60%, which is considerable on controlling the CTE of epoxy composites. Three theoretical models, the rule of mixtures (ROM), Turner's model and Schapery's model were used to analyze the thermal expansion mechanism of ZrW_2O_8/epoxy composites. The results showed that the Schapery's upper limit provides the better estimate for the composite material because it considers the modulus and interfacial performance between the filler and the matrix.

The mechanical properties of epoxy reinforced by ZrW_2O_8 with 0-10 wt. % were studied by tensile and flexural tests at both 77K and room temperature. It was shown that the tensile strength and flexural strength reached the maximum at 5 wt. % ZrW_2O_8 content, and then decreased by adding more ZrW_2O_8 fillers. The modulus had the similar tendency but the maximum existed at 8 wt. % ZrW_2O_8 because ZrW_2O_8 had a much higher modulus than epoxy matrix. Moreover, both the mechanical strength and modulus at 77K were much higher than those at room temperature. SEM micrographs of tensile fracture surfaces showed that a brittle rupture at 77K leads to a lower elongation at break and a higher modulus at cryogenic temperature.

Acknowledgments

The research work is sponsored by the National Science Foundation of China (grant No. 10904153, 50776095, 50936006, and 50676101).

References

[1] P.E. Fabian, J.B. Schutz, C.S. Hazelton, R.P. Reed, Adv. Cryog. Eng. Mater., 40 (1994) 1007-1014.
[2] G. Yang, S.Y. Fu, J.P. Yang, Polymer, 48 (2007) 302-310.
[3] Y. Shindo, S. Takano, K. Horiguchi, T. Sato, Cryogenics, 46 (2006) 794-798.
[4] Y. Shindo, S. Takano, F. Narita, K. Horiguchi, Fusion Eng. Des., 81 (2006) 2479-2483.
[5] J.I. Meijerink, S. Eguchi, M. Ogata, T. Ishii, S. Amagi, S. Numata, H. Sashima, Polymer, 35 (1994) 179-186.
[6] L.M. McGrath, R.S. Parnas, S.H. King, J.L. Schroeder, D.A. Fischer, J.L. Lenhart, Polymer, 49 (2008) 999-1014.
[7] C.J. Huang, S.Y. Fu, Y.H. Zhang, B. Lauke, L.F. Li, L. Ye, Cryogenics, 45 (2005) 450-454.
[8] I.N. Jan, T.M. Lee, K.C. Chiou, J.J. Lin, Ind. Eng. Chem. Res., 44 (2005) 2086-2090.
[9] N. Karak, J. Polym. Mater., 23 (2006) 1-20.
[10] T. Lan, T.J. Pinnavaia, Chem. Mater., 6 (1994) 2216-2219.
[11] A.A. Fahmy, A.N. Ragai, J. Appl. Phys., 41 (1970) 5112-5115.
[12] A. Yasmin, I.M. Daniel, Polymer, 45 (2004) 8211-8219.
[13] C.A. Perottoni, J.A.H. da Jornada, Science, 280 (1998) 886-889.
[14] T.A. Mary, J.S.O. Evans, T. Vogt, A.W. Sleight, Science, 272 (1996) 90-92.
[15] J.S.O. Evans, T.A. Mary, T. Vogt, M.A. Subramanian, A.W. Sleight, Chem. Mater. , 8 (1996) 2809-2823.

[16] M.N. Mancheva, R.S. Iordanova, Y.B. Dimitriev, K.P. Petrov, G.V. Avdeev, J. Phys. Chem. C, 111 (2007) 14945-14947.
[17] A.P. Wilkinson, C. Lind, S. Pattanaik, Chem. Mater. , 11 (1999) 101-108.
[18] J.D. Shi, Z.J. Pu, K.H. Wu, G. Larkins, Mater. Res. Soc. Symp. Proc., 445 (1997) 229-234.
[19] L.M. Sullivan, C.M. Lukehart, Chem. Mater. , 17 (2005) 2136-2141.
[20] J. Tani, H. Kimura, K. Hirota, H. Kido, J. Appl. Polym. Sci., 106 (2007) 3343-3347.
[21] K. Haman, P. Badrinarayanan, M.R. Kessler, Appl. Mater. Inter., 1 (2009) 1190-1195.
[22] W.K. Goertzen, M.R. Kessler, J. Therm. Anal. Calorim., 93 (2008) 87-93.
[23] D.L. Shi, S.X. Wang, W.J.v. Ooij, L.M. Wang, J.G. Zhao, Z. Yu, Appl. Phys. Lett., 73 (2001) 1243-1245.
[24] D.L. Shi, J. Lian, P. He, L.M. Wang, W.J.v. Ooij, M.J. Schulz, Y.J. Liu, D.B. Mast, Appl. Phys. Lett., 81 (2002) 5216-5218.
[25] H. Cho, D.L. Shi, Y. Guo, J. Lian, Z.F. Ren, B. Poudel, Y. Song, J.L. Abot, D. Singh, J. Routbort, L.M. Wang, R.C. Ewing, J. Appl. Phys. , 104 (2008) 074302.
[26] M. Orrhede, R. Tolani, K. Salama, Res. Nondestr. Eval., 8 (1996) 23-37.
[27] H.T. Vo, M. Todd, F.G. Shi, A.A. Shapiro, M. Edwards, Microelectron. J., 32 (2001) 331-338.
[28] X.X. Chu, Z.X. Wu, R.J. Huang, Y. Zhou, L.F. Li, Cryogenics, 50 (2010) 84-88.
[29] R.A. Schapery, J. Compos. Mater., 2 (1968) 380-404.
[30] Z. Hashin, J. Appl. Mech.-Trans. ASME, 50 (1983) 481-505.
[31] Z. Hashin, S. Shtrikman, J. Mech. Phys. Solids., 11 (1963) 127-140.
[32] F.R. Drymiotis, H. Ledbetter, J.B. Betts, T. Kimura, J.C. Lashley, A. Migliori, A.P. Ramirez, G.R. Kowach, J. Van Duijn, Phys. Rev. Lett., 93 (2004) 059903.
[33] C.G. Chen, R.S. Justice, D.W. Schaefer, J.W. Baur, Polymer, 49 (2008) 3805-3815.
[34] J. Kathi, K.Y. Rhee, J.H. Lee, Composites Part A, 40 (2009) 800-809.

Electromagnetic and Structural Analysis of EAST Passive Stabilizers Loop

X. Ji, Y.T. Song, S.T. Wu, Z.B. Wang, G.. Shen, L. Cao, Z.B. Zhou, X.B. Peng, C.H. Wang
Institute of Plasma Physics, Chinese Academy of Sciences
P.O.BOX 1126, Hefei Anhui, China, 230031
jixiang@ipp.ac.cn

Abstract: The passive stabilizers loop (PSL) is part of the plasma stabilizing system built in the EAST. Its purpose is to provide passive feedback control of the plasma vertical instability on short time scales. To accommodate with the new stage for high performance plasma and enhance the control of vertical stabilization in EAST, the project of PSL has been carried out.

The eddy currents are induced by the vertical displacement events (VDEs) and disruption. The distribution of the eddy currents depend on the structure of the PSL and the formation of the induction. The FE model is created and meshed by the ANSYS software. Base on the simulation of plasma VDEs and disruption, the distribution and decay curve of the eddy currents on the PSL are obtained. The stress and the strain caused by the eddy currents and the magnetic fields are calculated.

Keywords: Passive stabilizers loop (PSL), Electromagnetic analysis, Structural analysis, VDEs, Disruption

1. Introduction

The Experimental Advanced Superconducting Tokamak (EAST), that is an advanced steady-state plasma physics experimental device which has been built in ASIPP, has Plasma Facing Components (PFCs) to protect the vacuum vessel, heating systems and diagnostic components from the plasma particles and heat loads. (**Figure.1**)[1-3]The passive stabilizers are part of the plasma stabilizing system built in the EAST (Fig.2). Its purpose is to provide passive feedback control of the plasma vertical instability on short time scales.[4-7] To accommodate with the new stage for high performance plasma and enhance the control of vertical stabilization in EAST, the project of Passive stabilizers Loop (PSL), connect all the independent passive stabilizers together as a loop, has been carried out.

Two copper toroidal rings, each with an electric break and connecting bridge, form a saddle connection. The current bridges are designed coaxial and symmetrical in order to counterpoise the electromagnetic forces. The passive plate with a saddle connection can produce a radial magnetic field in the plasma region due to the eddy currents in the plates induced by vertical plasma motion. (**Figure.2, Figure.3**)

The purpose of the passive stabilizers loop is to reduce the growth rates of vertical instability and make the active control of the plasma possible. The passive plate with a time constant of 100 ms will be provided for the plasma vertical position control on fast time scales, then the currents in the active control coil will immediately compensate for the decay of the currents in the passive plate and restrain the plasma vertical displacement. [8]

2. Theory of eddy current

Lenz' law says that if a current moves, a magnetic field is induced that creates other currents in order to keep the centre of the total current at the same location. The eddy currents in the passive plates are induced by the varying magnetic field due to the plasma vertical displacement. The distribution of the eddy currents depends on inducing magnetic field configuration, i.e. the form of the plasma vertical motion. The plasma current is considered as

a rigid current ring and the plasma vertical drifts can be shown as an exponential function:

$$Z = Z_0 \exp(\gamma t)$$

Where Z_0 is an initial change of the plasma position caused by some disturbance and the growth time ($1/\gamma$) is about 20 ms in EAST. [9]

The eddy currents satisfy the continuity condition:

$$\nabla \cdot \mathbf{J} = 0$$

The electrical vector potential **T** can be applied to describe the eddy currents:

$$\mathbf{J} = \nabla \times \mathbf{T}$$

Maxwell's equation can be written as:

$$\nabla \times \mathbf{E} = -\partial \mathbf{B} / \partial t$$

When the vertical displacement events (VDEs) of plasma happened, there are eddy currents induced in the passive stabilizers loop (PSL). Especially when the displacement of VDEs of plasma is large and plasma disruption happened, the eddy currents in the PSL are very large. The eddy current can be obtained by the following equation:

$$M_P \frac{di_P}{dt} = L_U \frac{di}{dt} + L_D \frac{di}{dt} - 2M \frac{di}{dt} + iR$$

In the equation, the M_P is the mutual inductance between passive stabilizers and plasma current. The Ip is the plasma current. The L_U and L_D are the self-inductance of upper and bottom passive stabilizers. The M is the mutual inductance between upper and bottom passive stabilizers. The R is the resistance of passive stabilizers. The i is the eddy current in the PSL.

3. Finite Element Analysis

3.1. FE Model

A 3D finite element model with ANSYS code has been created to simulate the transient behavior. (**Figure.4**) The element used for the air and PSL is SOLID96 whose DOF is magnetic scalar potential, and the coils are modeled by SOURC36 which is actually not a finite element but a primitive representing the distribution of magnetic field that are used to calculate. To minimize the element number in the model, the infinite surface is applied to the open boundary of the model by means of INFIN47 elements.

Furthermore, taking into account the particular geometrical features of the PSL, special care should be taken to build the model. In order to insert adequate number of finite elements within the thickness of the PSL, without prohibitive increase in the total elements number, a particular modeling approach has been developed. Moreover this technique made it possible that only structured meshes are used which are much more accurate than the tetrahedral elements that are instead needed when free meshing technique is used.

3.2. Electromagnetic Analysis

The Electromagnetic Analysis will focus on the plasma disruption, which could induce the largest eddy currents in the PSL. [10-13]

The magnetic fields on the PSL are provided by all currents, which include TF coils, PF coils, plasma and the eddy currents. To identify the worst case, several plasma scenarios have been analyzed using 3D FE model by ANSYS code.

As shown in **Figure.5**, the eddy currents with different plasma currents have been obtained. In the simulation, the vertical displacement of plasma is 200mm, and the time constant of plasma decay is 3ms. The largest eddy currents disappear at time 11ms and they are directly proportional to the plasma currents.

As shown in **Figure.6**, the eddy currents with different vertical displacement of plasma have been obtained. In the simulation, the plasma current is 1MA, and the time constant of plasma decay is 3ms. The eddy currents they are directly proportional to the plasma currents. The directions of eddy currents are decided by the direction of plasma movement. There is no eddy currents in the PSL when plasma disruption without vertical displacement.

From the simulations, it is found that the largest eddy currents in the PSL are 200MA, which will interact with the magnetic fields and produce tremendous electromagnetic force. The distribution of the largest eddy current is shown as **Figure.7**.

3.3.Structural analysis

The current bridges provide the electrical connection between the two PSLs. As they are Perpendicular to the toroidal field which produce the largest magnetic field 3.5T, they could be the weakest point of the PSL structures. The material of the current bridges is CuCrZr which could provide high strength to against the electromagnetic force.

As shown in **Figure.8**, the largest stress and deformation are 68MPa and 0.31mm, which appear at the shell of the current bridge.

4. Conclusions

The eddy currents in the PSL are induced by the VDEs and disruption. The distribution of the eddy currents depend on the structure of the PSL and the formation of the induction. Owing to the character of geometric structure and current distribution, the electrical parameters of the PSL cannot be expressed as a simple form, so the FE model is used to simulation.

The FE model is created and meshed by the ANSYS software. Base on the simulation of plasma VDEs and disruption, the distribution of the eddy currents on the PSL are obtained. The stress and the strain caused by the eddy current and the magnetic field are calculated.

It could be useful to go ahead with these analyses considering different influences from coming from the vacuum vessel. But, maybe at first, the model should be validated with some experimental results, so that also the boundary condition for these analyses could be more precise.

Acknowledgements

This work is partly supported by JSPS-CAS Core University Program in the field of “Plasma and Nuclear Fusion”. The authors acknowledge the Shuichi Yamada of the NIFS who have contributed to the project.

References

[1] Y.T. Song X. Ji, X. Liu, etc. 2010, J. Plasma Fusion Res. SERIES, Vol.9, 131-135

[2] YAO Damao, BAO Liman, LI Jiangang, etc. 2008, Plasma Science and Technology, Vol.10, No.3,368-372.

[3] Y.T.Song, D.M.Yao, S.T.Wu, P.D.Weng. 2005, Fusion Engineering and Design 75-79,

499-503.
[4] V.S.MUKHOVATOV, V.D.SHAFRANOV, I.V.Kurchatov. 1971, NUCLEAR FUSION, 11, 605-633.
[5] W.Suttrop, O.Gruber, S.Gunter, etc. 2009, Fusion Engineering and Design, 84, 290-294
[6] T.Vierle, B.Streibl, M.Rott, etc. 2009, Fusion Engineering and Design, 84, 1928-1932
[7] M.Rott, U.Seidel, B.Streibl, etc. 2009, Fusion Engineering and Design, 84, 1653-1657
[8] D.M.Yao, J.G.Li, Y.T.Song, etc. 2005, Fusion Engineering and Design, 75-79, 491-494
[9] Shijun Du, Liheng Wang, Xufeng Liu, Damao Yao. 2006, Fusion Engineering and Design. 81, 2267-2273
[10] M.Ferrari, L.Anzidei, V.Cristini, G.Simbolotti. 1995, Fusion Engineering and Design, 27, 507-514
[11] R.Albanese, G.Ambrosino, M,Ariola, etc. 2009, Fusion Engineering and Design, 84, 394-397
[12] Y.T.Song, Y.H.Peng. 2007, Nuclear Fusion and Plasma Physics. Vol.27, No.3,222-226
[13] T.Jordan, D.Schneider. 1996, Fusion Engineering and Design, 31, 313-321.

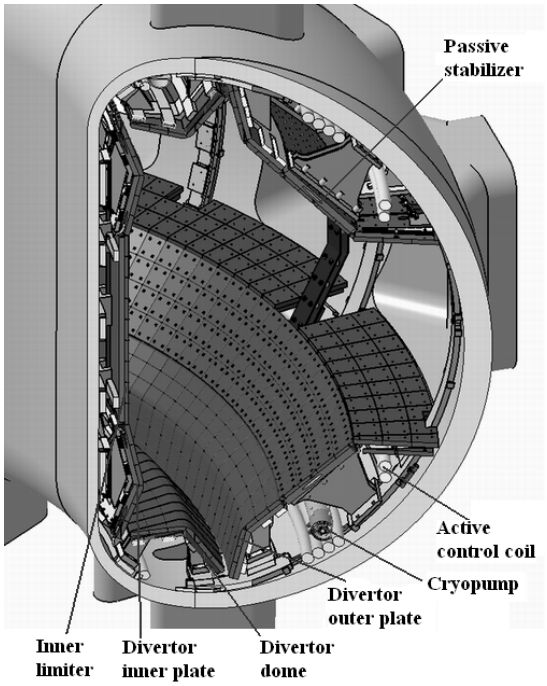

Figure.1: Elevation view of EAST PFCs

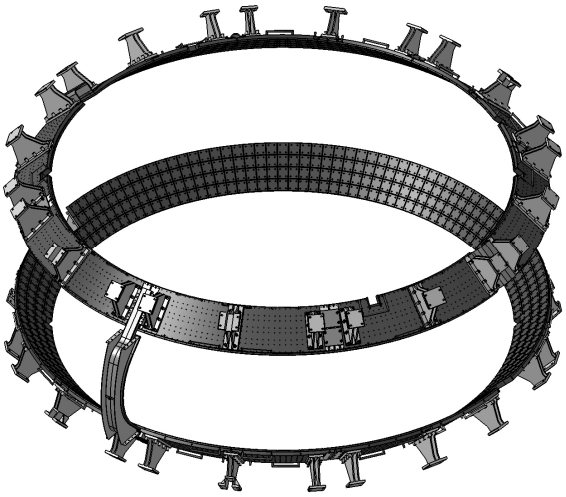

Figure.2: The structure of passive stabilizers loop

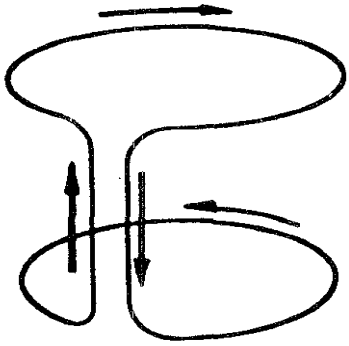

Figure.3: The eddy current in PSL saddle coil

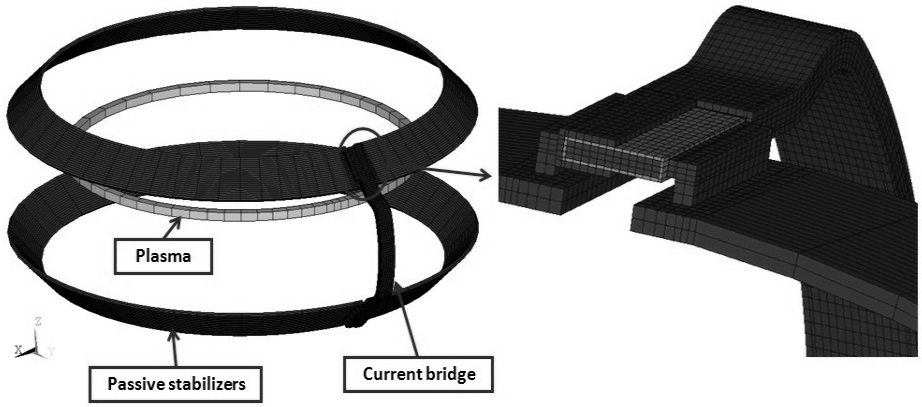

Figure.4: Finite element model of PSL

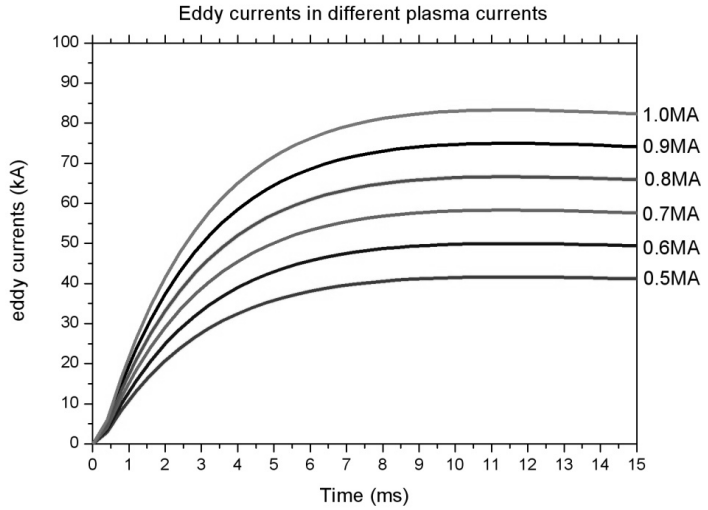

Figure.5: The eddy currents with different plasma currents

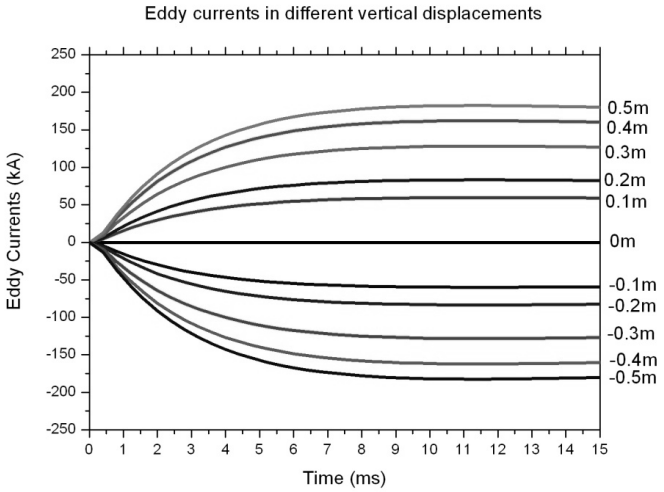

Figure.6: The eddy currents with different vertical displacement of plasma.

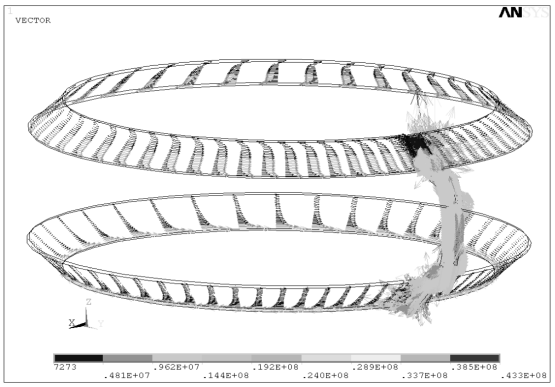

Figure.7: The distribution of the largest eddy currents

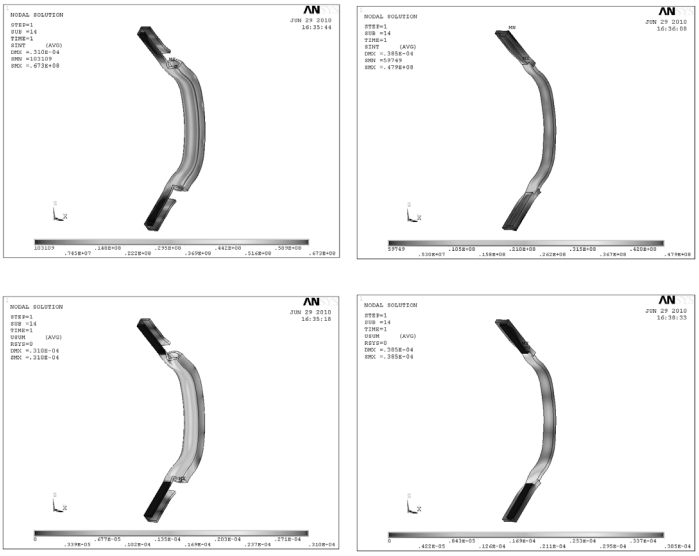

Figure.8: The stress and deformation of current bridges.

Numerical simulation of subcooled flow boiling and application to the EAST plasma facing components

Q.L.Kang, Y.T.Song, S.H.Huang, Z.W.Wang, X.Ji
Institute of Plasma Physics, Chinese Academy of Science,
P.O.BOX 1126, Hefei Anhui, China, 230031
qlkang@ipp.ac.cn

Abstract

The paper describes numerical simulation approaches to subcooled boiling and investigates their application to EAST plasma facing components(PFC). A two-fluid model implemented with a wall boiling model based on a wall heat flux partition algorithm was used to solve control equations for mass, momentum and energy, which coupled with additional closure relations describing the exchange of two phases at the interface. A user-defined function(UDF) was written to define the source terms of phase exchange and specify the customized parameters of the multiphase. And the proposed two-fluid model was verified by experimental data of Lee et al. Also the simulation of the EAST plasma facing components was done with subcooled flow boiling method.
Keywords: Plasma facing components; subcooled flow boiling; Two-fluid model; *UDF*

1. Introduction

Subcooled flow boiling means the process of evaporation of liquid flowing near the heated surface while the bulk flowing temperature is lower than the local saturation temperature and the liquid temperature exceeds the saturation temperature. Lots of experiment have proven that subcooled flow boiling has higher heat transfer efficiency and critical heat transfer performance compared to saturated flow boiling, so the subcooled flow boiling has gained more and more attention where high heat removal is required, such as the cooling of neutron accelerator targets and the first wall cooling of fusion reactors.

The Experimental Advanced Superconducting Tokamak(EAST) is an advanced plasma physics experimental device to be built in PR China. The plasma facing components(PFC) are designed to protect the injection power system, diagnostic components and vacuum vessel from plasma particles and heat loads, in which the peak heat flux is $3.6\,Mw/m^2$ in first phase of double null plasma operation[1]. And this value may become larger with application of commercial nuclear power reactors in the future. Under such high levels of heat flux, the hypervapotron which actually engineering application of theory of subcooled flow boiling was chosen as one of major methods of heat transfer enhancement.

2. Physical model

Currently the most conventional CFD method to modelling two-phase flow is the Eulerian two-fluid model which consists of a dispersed phase (vapour bubbles) and a

continuous phase (liquid). And each phase is treated as a continuum that fills up the entire control volume and is described by its own control equations for mass, momentum and energy. Averaged equations for both phases are coupled with additional closure relations describing the exchange of mass, momentum and energy at the interface.

2.1 Modeling of heat transfer at a heated wall

Numerous investigation demonstrated that the total heat flux Q per unit area of heating surface is partitioned into three components[2].

$$Q_W = Q_c + Q_e + Q_q \tag{1}$$

Where Q_c is the heat flux component due to single-phase convection, which can be calculated as:

$$Q_c = h_c A_l (T_W - T_l) \tag{2}$$

Here h_c is single phase convection heat transfer coefficient, A_l is the area fractions of the convection controlled region, T_W is the local wall temperature and T_l is the liquid temperature of the near-wall cell.

Q_e is the heat flux component due to evaporation which is obtained via the evaporation mass flux on the wall.

$$Q_e = \dot{m}_w H_{\lg} \tag{3}$$

Where $\dot{m}_w$ and $H_{\lg}$ are the evaporation rate and latent heat respectively.

Q_q represents heat flux due to quenching which can be calculated as:

$$Q_q = A_g h_q (T_W - T_{lW}) \tag{4}$$

Where $A_g = 1 - A_l$ is the the area fractions of the "bubble influence region", h_q and T_{lW} is the quenching heat transfer coefficient and liquid temperature immediately next to the heating surface respectively.

To describing bubble nucleation and departure, some other parameters like bubble departure diameter d_{bW} ,the active site density n and the bubble waiting time t_w will be discussed in the following.

The active nucleation site density n depends on the wall surface roughness, on the wettability of the solid-liquid pair and on the wall superheat. In this paper only superheat was considered for the sake of simplifing[3]

$$n = \left[185 \Delta T_{\sup}\right]^{1.805} \tag{5}$$

Where $\Delta T_{\sup} = T_W - T_{sat}$ is the wall superheat above saturation. T_{sat} is the saturation temperature.

The bubble departure diameter d_{bW} is an important parameter in modeling subcooled

boiling and the following correlation was applied to obtain it:

$$d_{bW} = \min\left[0.6mm \cdot \exp\left(\frac{-\Delta T_{sub}}{45}\right), 1.4mm\right] \quad (6)$$

Where $\Delta T_{sub} = T_{sat} - T_{lW}$ is the liquid subcooling below saturation.
The bubble departure frequency was simply estimated as the terminal rise velocity divided by the bubble departure diameter:

$$f = \sqrt{\frac{4g(\rho_l - \rho_g)}{3d_{bW}\rho_l}} \quad (7)$$

Where g and ρ are gravity acceleration and density of working fluid . The subscripts l and g represent liquid phase and vapour phase respectively.
The bubble waiting time t_w takes 80% of bubble departure period from assumption by Kurul and Podowski[4]:

$$t_w = \frac{0.8}{f} \quad (8)$$

From above parameters, the evaporation rate, area fraction and quenching heat transfer coefficient can be obtained.

$$\dot{m}_w = \rho_g \frac{\pi d_w^3}{6} nf \quad (9)$$

$$A_g = \min\left[\pi \frac{(ad_w)^2}{4}, 1\right] \quad (10)$$

$$h_q = \frac{2}{\sqrt{\pi}} f \sqrt{t_w \lambda_l \rho_l C_{pl}} \quad (11)$$

Where a is the bubble influence factor and 2 is taken for its value. λ is the thermal conductivity and C_p is the specific heat. Then heat transfer from the wall can be calculated by model each mechanism in terms of above parameters.

2.2 Phase exchange in bulk flow

In the present model of subcooled flow boiling, mass transfer in bulk flow between the phase are described by superheated liquid evaporating and subcooled liquid condensing. The evaporation rate Γ_w per unit volume can be calculated as:

$$\Gamma_w = \frac{h_{\lg} A_l (T_l - T_{sat})}{H_{\lg}} \quad (12)$$

The condensation rate of saturation steam in subcooling liquid can is calculated as:

$$\Gamma_{cond} = \frac{h_{\lg} A_g (T_{sat} - T_l)}{H_{\lg}} \quad (13)$$

Where $H_{\lg}$ is the interphase heat transfer coefficient, defined by the bubble Nusselt number Nu_b :

$$h_{\lg} = \frac{\lambda_l Nu_b}{d_{bW}} \tag{14}$$

Where Nu_b is calculated from Ranz-Marshall correlation[5]. Here the detailed information was not provided.

The energy transfer between phase are described by heat conduction formula as following:

$$Q_{\lg} = A_{\lg} h_{\lg} (T_g - T_l) \tag{15}$$

Where $A_{\lg}$ is the interfacial area per unit volume, which expressed as $6\alpha / d_{bW}$, α is the vapour volume fraction..

The interphase momentum transfer in subcooled boiling flow is usually modeled with the following interfacial forces[6]: drag force and non-drag force such as lift force, turbulent dispersion force and wall lubrication force. The detailed description can be seen in numerous published literature. Here no longer to repeat.

3.Validation of the model

3.1 numerical simulation method

In present work, the general-purpose CFD code Fluent 6.3 was used for solving the generic two-fluid model with additional relevant closure relations, which describe the mechanisms of phase change and lateral transport of mass, momentum and energy. The discretization of transport equations in the Fluent 6.3 code is based on a conservative finite-volume method. A user-defined function(UDF) written in C program language was used to define the source terms of phase exchange and specify the customized parameters of the multiphase. The mass transfer rate specified using a DEFINE_MASS_TRANSFER Macro is used to compute mass, momentum and energy for the two phase based on the above mentioned formula about bubble parameters.

3.2 Comparison between experimental and numerical results

The proposed two-fluid model of subcooled flow boiling was validated against the experimental data from the literature published by Lee et al.[7]. The experimental was carried out in a vertical annulus with a heated inner tube. The 1.67m inner tube with a outer diameter of 19mm is composed of a heated section with copper electrodes at the both ends. The outer tube was a stainless steel tube with a inner diameter of 37.5mm. In the work of Lee et al, only radial profiles of fluid parameters at a single axial location, 1.61m downstream of the beginning of the heated section are reported. The

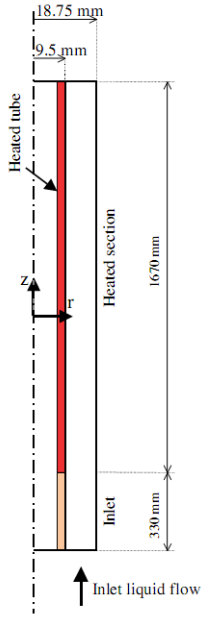

Figure 1 Simulation domains of test section

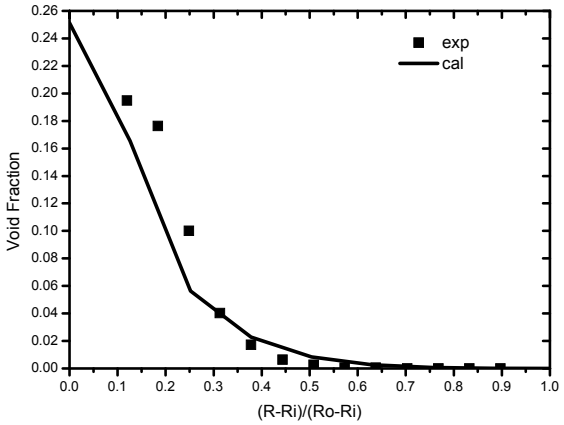

Figure 2 radial distribution of volume fraction

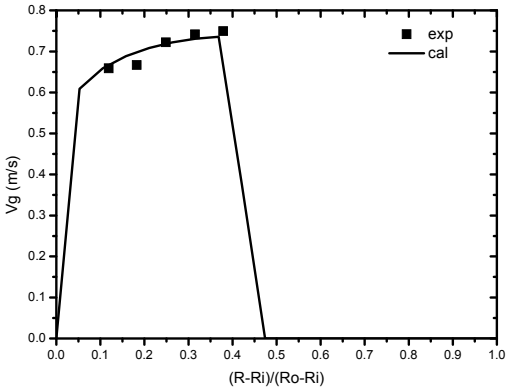

Figure3 radial profiles of vapour velocity

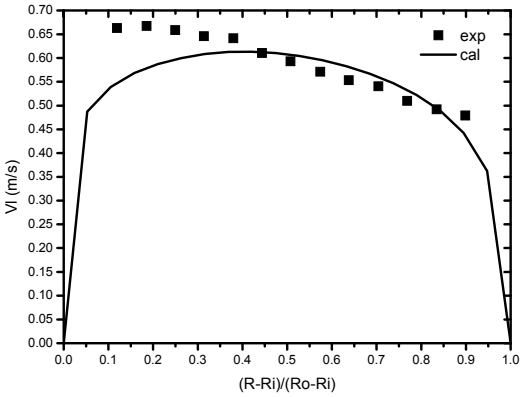

figure 4 radial profiles of liquid velocity

calculation was carried out on a two-dimensional computational domain in cylindrical coordinates(Figure 1). The simulation domains were divided into 20 radial and 2000 axial cells. The heat flux was 169.76 kw/m^2 and the mass flow of the water at the pressure of 0.115MPa amounted to 478.14 $kg/(m \cdot s)$. And the temperature of inlet water was 83.9℃。Figure 2-4 show comparisons of radial profiles between measured and calculated results of void fraction, vapour velocity and liquid velocity. From the picture, Both the volume fraction and fluid velocity along the radial direction show good agreement with the experimental data. A conclusion can be drawn that the proposed two-fluid model is reasonable and the UDF in my work was written properly.

4. Subcooled flow boiling applied to EAST PFC

The EAST PFC consists of divertors, baffles, passive stabilizers and limiter[8]. Each part has a plasma facing surface, which is affixed to a cooled support plate. Among these parts, the baffle plates of the divertor will endure the maximum peak heat flux.

So the thermal analysis was done for the divertor baffle plate system[9]. Figure 5 shows the recommended structure of PFC. The graphite tiles bolted to the copper plates, which brazing on a water-cooled tube. The heat flux on the surface was given to $4 Mw/m^2$. The temperature of the inlet water is room temperature ~20℃ and velocity of the cooling water is 7m/s with 0.3MPa. Figure 6 shows the temperature distribution in a cross fraction of the PFC structure. The maximum temperature of the graphite tiles is 711℃ which are lower the 829℃ that without subcooled boiling and also lower than 850℃ which limited by the graphite material properties. The distribution of vapour volume fraction in the channel cross section shows the maximum vapour generation at the tube wall that has a smaller distance with the heat flux wall(Figure 7).

5. Conclusion

A two-fluid model of subcooled boiling flow was proposed and a user defined function was written to supplement the model in numerical simulation. A good overall agreement between calculated and experimental data from Lee et al's literature was obtained. The model was used in EAST PFC cooling system and improve the safety and applicability of the system. An experimental about subcooled boiling flow will be carried out for further study.

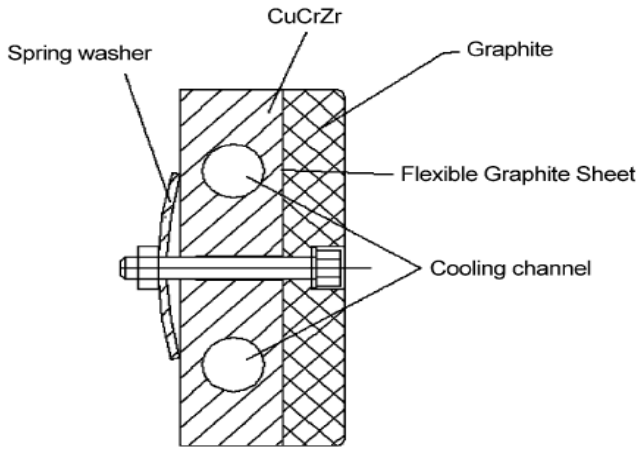

Figure 5 Recommended structure of PFCs

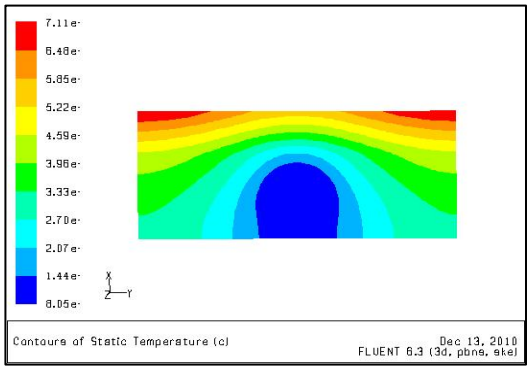

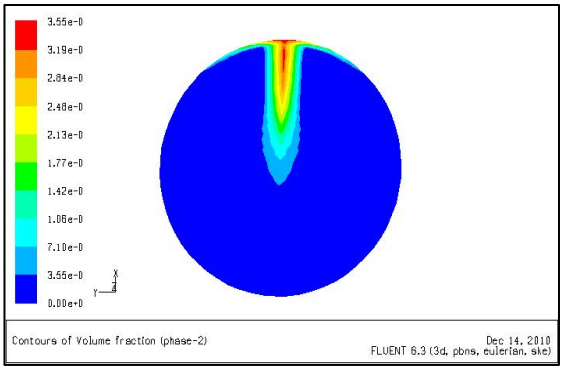

Figure 6 Temperature distribution of PFCs figure 7 Volume fraction distribution of PFCs

References

[1] Y.T.Song, D.M.Yao, S.T.Wu,P.D.Weng, Thermal and mechanical analysis of the EAST plasma facing components, Fusion Eng. Des. 75-79(2005)(499-503)

[2] Joseph Milnes, Dimitris Drikakis, Qualitative assessment of RANS models for Hypervapotron flow and heat transfer, Fusion engineering and design, 2009

[3] E. Krepper et al., CFD modeling of subcooled boiling-concept,validation and application to fuel assembly design, Nuclear Engineering and Design 237 (7) (2007) (716–731).

[4] Kurul,N.,Podowski,M.Z., On the modeling of multidimensional effects in boiling channels, Heat Transfer,1991

[5] Bostjan Koncar et al.,Modelling of local two-phase flow parameters in upward subcooled flow boiling at low temperature, Heat and Mass Transfer 47 (2004) (1499-1513)

[6] Joseph Milnes, Dimitris Drikakis, Qualitative assessment of RANS models for Hypervapotron flow and heat transfer, Fusion engineering and design, 84（2009）(1305-1312)

[7] T.H.Lee, G.C.Park, D.J.Lee, Local flow characteristics of subcooled boiling flow of water in a vertical concentric annulus, Multiphase Flow 28(2002)(1351-1368)

[8] J.Reimann et al, Conceptual design of an evaporation-cooled liquid metal divertor for fusion power plants, Fusion Engineering and Design 56–57 (2001) (369–373)

[9] R.E. Nygren, Actively cooled plasma facing components for long pulse high power operation, Fusion Engineering and Design 60 (2002) (547–564)

Tests of JT-60SA EF conductors in the NIFD superconducting test facility

T. Obana
National Institute for Fusion Science, 322-6 Oroshi, Toki, Gifu 509-5292 Japan
obana.tetsuhiro@LHD.nifs.ac.jp

Abstract

A collaborative project between the National Institute for Fusion Science (NIFS) and Japan Atomic Energy Agency (JAEA) has been carried out since 2007 for the purpose of evaluating the performance of the cable-in-conduit (CIC) conductors for Equilibrium Field (EF) coils of JT-60 Super Advanced (JT-60SA), which is a part of the ITER-BA project. In the project, the CIC conductors have been tested by using the upgraded test facility of NIFS. As a result, the performance of the CIC conductors filled successfully the design requirements.

1. Introduction

A collaborative project between the National Institute for Fusion Science (NIFS) and Japan Atomic Energy Agency (JAEA) has been carried out since 2007 in order to evaluate the performance of the superconductors for Equilibrium Field (EF) coils of JT-60 Super Advanced (JT-60SA), which is a part of the ITER-BA project. In the collaborative project, the test facility of the NIFS is utilized to measure the current sharing temperature (Tcs) and stability margin of the superconductors [1]. The superconductors are cable-in-conduit (CIC) conductors consisting of a NbTi multi-strand cable surrounded by a SUS316L conduit, in which supercritical helium (SHe) flows [2]. The test facility was upgraded to deal with the CIC conductor [3]. In the upgrade, SHe cooling lines were set up with transfer tubes and a heat exchanger [4]. The cooling line on the supply side was equipped with film heaters to control the SHe temperature. Additionally, a thermal insulation vessel for the CIC conductor was installed in the facility so that the CIC conductor could be tested in gas helium. In the paper, the details of the upgraded test facility and the test results of JT-60SA EF coil conductors are described.

2. Experimental setup

As an experimental setup for this study, the superconducting test facility at the National Institute for Fusion Science (NIFS) was utilized. The test facility can deal with testing of the CICC cooled by supercritical helium (SHe) and generate an external magnetic field with a superconducting split coil [4, 5]. Fig.1 illustrates the test facility including the short conductor sample, the configuration of which is a racket shape of 300 mm in diameter at the circular part. The short conductor sample was installed into the gap of the split coil. The external magnetic field is homogeneous at the circular part of the short conductor sample. Fig.2 shows the

schematic view of the short conductor sample equipped with Hall sensors and a CERNOX thermometer. Film resistance heaters were attached to the inlet pipe to control the conductor temperature. Details of the test facility are described in References 4, 5.

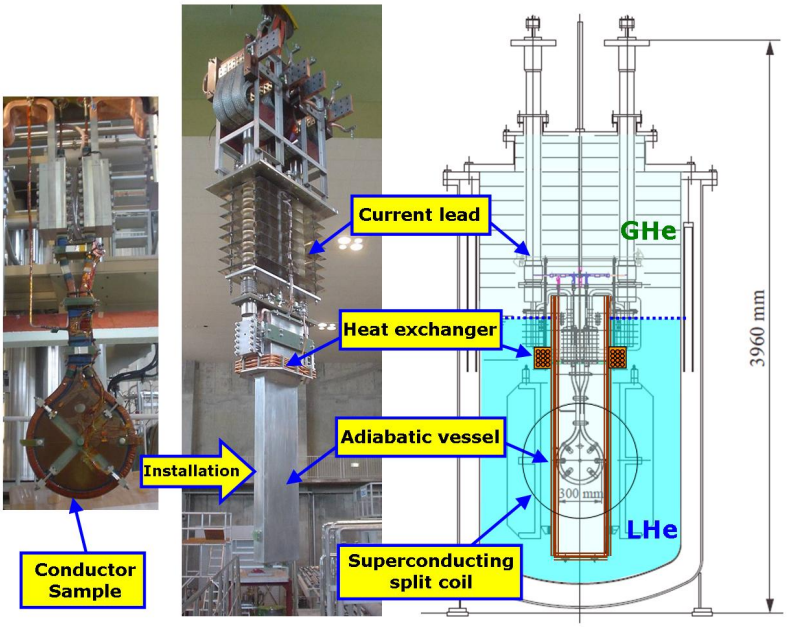

Fig.1 Schematic view of the test facility

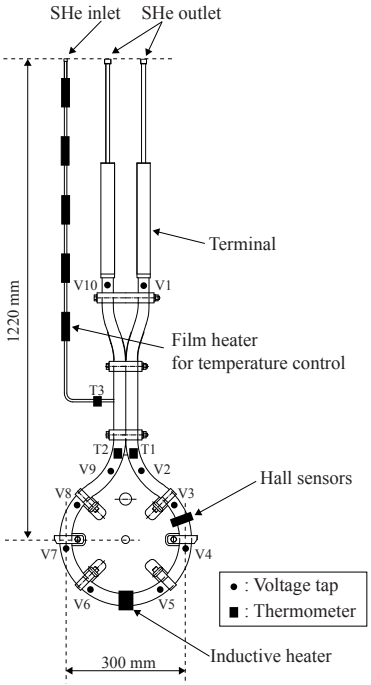

Fig.2 Schematic view of the short conductor sample

3. EF coil conductors

There are two types of conductors which are EF-H conductor and EF-L conductor [1-3]. The EF-H and EF-L conductors were optimized for the magnetic field of 6.2 T and 4.8 T, respectively. Nickel coating on strand was utilized to reduce AC loss. The jackets consisting SUS316L were compacted and formed from circular tubes. In the both conductors, cables were not wrapped with stainless steel tape. Specifications of the CICC are described in table 1.

Table I Parameters of EF-H and EF-L conductors

	EF-H	EF-L
	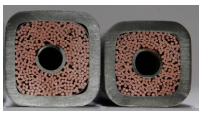	
Strand diameter (mm)	0.829	0.829
Cu/non - Cu ratio	2.3	2.3
Number of SC strands	450	216
Cabling pattern	3x5x5x6	(2+1)x3x6x6
Final twist pitch	160	160
Sub wrap tape	No	No
Jacket inner size (mm)	21.8x21.8	19.1x19.1
Jacket outer size (mm)	27.7x27.7	25.0x25.0
Void fraction	34%	34%

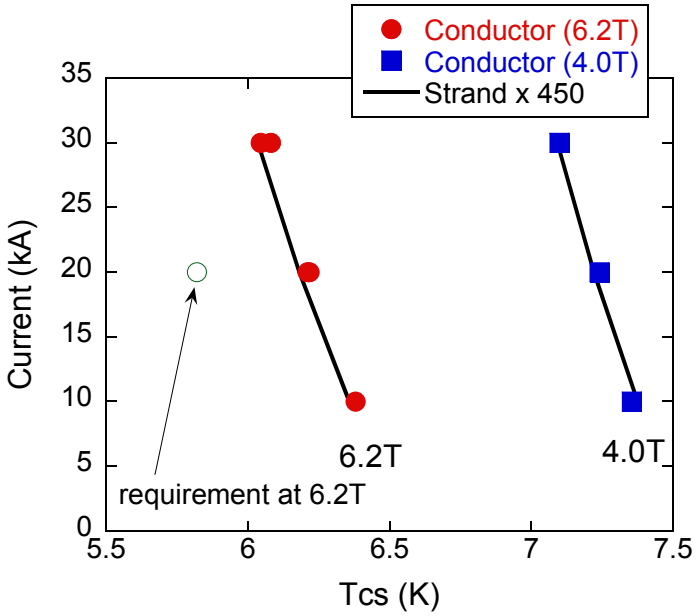

Fig.3 Schematic view of the short conductor sample

4. Test results of the EF coil conductors

In order to confirm the performance of the EF coil conductors, the current sharing temperature

(Tcs) of the conductors have been measured. Fig. 3 shows the measurement result of the EF-H conductor. In the measurement, the magnetic field includes background field by split coil and self field by the conductor. As a result, Tcs measurement results fulfilled the design requirements under the magnetic field. The details of the measurement result are described in Reference 3, 6 and 7.

5. Conclusion

The collaborative project between NIFS and JAEA started in 2007 for the purpose of evaluating CIC conductors for EF coils of JT-60SA. In order to test the CIC conductors, the NIFS superconductor test facility was upgraded. EF coil conductor tests were successful, and CS coil conductor tests are going to be carried out soon.

References

[1] K. Yoshida, K. Tsuchiya, K. Kizu, H. Murakami, K. Kamiya, T. Obana, K. Takahata, M. Peyrot, P. Barabaschi, "Development of JT-60SA superconducting magnet system," Physica C, vol. 470, pp. 1727-1733, 2010.

[2] Kaname Kizu, Katsuhiko Tsuchiya, Tetsuhiro Obana, Kazuya Takahata, Ryo Hoshi, Shinji Hamaguchi, Yoshihiko Nunoya, Kiyoshi Yoshida, Makoto Matsukawa, Nagato Yanagi, Shinsaku Imagawa and Toshiyuki Mito, "Critical current measurement of prototype NbTi cable-in-conduit conductor for JT-60SA," Fusion Eng. Des., vol. 84, pp. 1058-1062, Jun. 2009.

[3] Kaname Kizu, Yoshitoshi Kasiwa, Haruyuki. Murakami, Tetsuhiro Obana, Kazuya Takahata, et al, "Fabrication and tests of EF conductors for JT-60SA," Fusion Eng. Des., 2011, to be published.

[4] Tetsuhiro Obana, Kazuya Takahata, Shinji Hamaguchi, Nagato Yanagi, Toshiyuki Mito, Shinsaku Imagawa, Kaname Kizu, Katsuhiko Tsuchiya, Ryo Hoshi and Kiyoshi Yoshida, " Upgrading the NIFS superconductor test facility for JT-60SA cable-in-conduit conductors," Fusion Eng. Des., vol. 84, pp. 1442-1445, Jun. 2009.

[5] J. Yamamoto, T. Mito, K. Takahata, et al., "Superconducting test facility of NIFS for the Large Helical Device", Fusion Engineering and Design, Vol. 20, pp. 147–151, 1993.

[6] Murakami, H.; Ichige, T.; Kizu, K.; Tsuchiya, K.; Yoshida, K.; Obana, T.; Hamaguchi, S.; Takahata, K.; Mito, T.; Imagawa, S., "Stability and Quench Test for NbTi CIC Conductor of JT-60SA Equilibrium Field Coil", IEEE Transactions on Applied Superconductivity, vol. 20, pp. 512-516, Jun. 2010.

[7] H. Murakami, T. Ichige, K. Kizu, K. Tsuchiya, K. Yoshida, T. Obana, S. Hamaguchi, K. Takahata, N. Yanagi, T. Mito, S. Imagawa, "Stability margin of NbTi CIC conductor for JT-60SA equilibrium field coil", IEEE Transactions on Applied Superconductivity, 2011, to be published.

The Design, Analysis and Progress of ITER Converter Power Supply System

Z. Q. Song, P. Fu, G. Gao, L. W. Xu, P. Chen
ITER Chinese Participant Team,
Institute of Plasma Physics, Chinese Academy of Sciences (ASIPP), Hefei, China, 230031,
zhquansong@ipp.ac.cn

Abstract: In this paper, firstly, a general introduction of the current ITER power supply system is given. Then a detailed analysis on ac/dc converters of the ITER FDR2001 baseline design has been given, especially some important design criteria of 2001 design such as fault suppression capability (FSC) and internal bypass are studied, some proposes to reduce the risk of the FDR2001 design and fabrication challenges have been presented, and those proposes have been validated and supported by two independent expert groups organized by ITER Organization (IO). Lastly, the main technical challenges and the current progress of research and development (R&D) of the ITER converter power supply are presented.

Keywords: AC/DC Converter, FSC, Bypass, Progress

1. Introduction

The International thermonuclear experimental reactor (ITER) power supply system is to receive power from the high voltage (HV) grid and distribute it to the pulsed loads of the coil power supply system (CPSS), heating and current drive (H&CD) power supplies. The CPSS shown in Figure ***1*** comprises a 400kV/500MW HV substation, 66kV/750MVar reactive power compensation & harmonic filtering (RPC&HF) system, 2.2GVA AC/DC conversion system, switching network unit for plasma initiation and fast discharge units as quench protection.

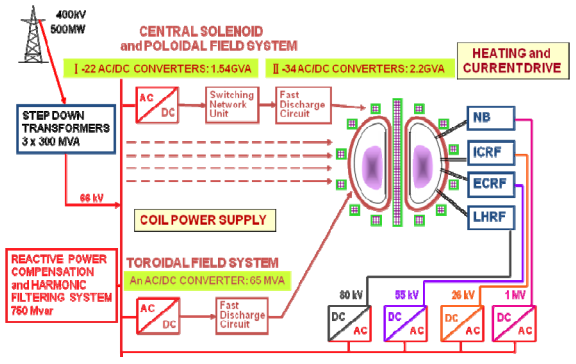

Figure 1 Configuration of ITER Power Supply

The CPSS is supplied by a double circuit incoming 400kV line, and connected to three identical 3-winding, step-down transformers, which provide two levels of voltage, i.e. 66 kV and 22 kV. The RPC & HF systems are connected on each 66 kV busbar to regulate the line voltage. The H&CD are connected to both 66kV and 22kV lines.

ITER AC/DC converters provide controlled DC voltage/current to the superconducting magnets for plasma initiation, current, shape and position control as well as error field correction. The thyristor-based converter is selected according to the requirements of current/voltage rating and response.

According to the IO current design solution, there are two stages for AC/DC conversion system. The total installation power of AC/DC converters is about 1.6GVA in the first stage, and the final total installation power will be up to 2.2 GVA.

The current design configuration of AC/DC converter circuits shown in Figure ***2*** includes:

- 1 circuit for the 18 series connected Toroidal Field (TF) coils;
- 1 circuit for the Central Solenoid (CS) CS1 upper and CS1 lower modules connected in series;
- 4 circuits for the CS2 upper, CS2 lower, CS3 upper and CS3 lower modules;
- 1 common system for the four outer Poloidal Field (PF) coils, i.e. PF2, PF3,

PF4 and PF5, used for plasma vertical stabilisation;
- 2 circuits for individual supply of the PF1 and PF6 coils;
- 9 independent circuits for the error field Correction Coils (CCs).

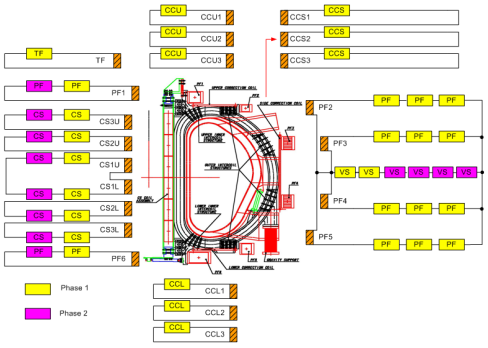

Figure 2 Configuration of AC/DC Converter Plant

The current design solution of ITER AC/DC Main Converter unit (MC) is different from FDR2001 baseline design. This paper will present the reasons and results of the design changes.

2. The FDR2001 Baseline Analysis of AC/DC Converter Design[1][2][3]

According to FDR2001 baseline of converter design, the typical circuit topology of the main converter (MC) unit can be shown in Figure 3.

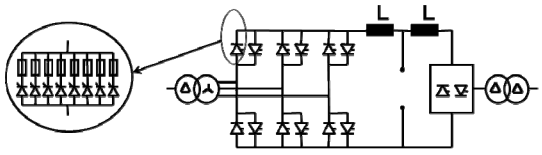

Figure 3 Circuit Topology of the MC Unit

The main design criteria and features of the FDR2001 design are:
- Back to back thyristor configuration (except the TF and Booster Converter);
- 12-pulse, 4-quadrant operation;
- 45kA, 2kV (no load) main converter unit;
- Internal bypass in case of fault conditions;
- FSC (Fault Suppression Capability) criteria.

FSC and internal bypass are two important design criteria in FDR2001 baseline of converter design.

FSC is the capability of the converter to clear the over-currents, due to the most frequent faults, by gate pulse suppression and backup ac breaker opening without melting of the fuses. That is to say it allows fuse melting only in the case of thyristor failure. The fault shall be cleared in the first AC cycle by the electronic protection and if it fails, the fuses and thyristors can't be damaged during 4 AC cycles (additional 3 cycles for AC breaker opening).

Internal bypass is that in case of fault, the current path is formed by the thyristor arms connected to the same phase of converter transformer inside the bridge.

The basic main circuit structure of MC and its PSCAD/EMTDC simulation model can be shown in Figure 4 according to the circuit topology of MC designed in FDR 2001.

In order to make the simulation results close to the real condition, the stray parameters of DC busbar is considered, and the superconducting coil (SC) is instead of a fixed dc current source in fault analysis. In addition, assuming the current unbalance factor is 1.4 in fault analysis.

The following detailed analysis focused on FSC and internal bypass criteria of FDR2001 design is based on above model and hypothesis condition.

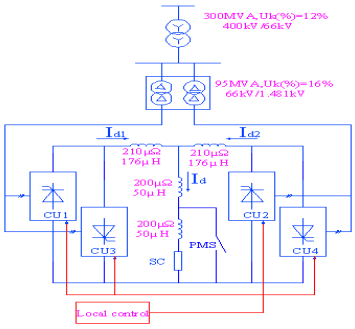

(a) Main circuit structure

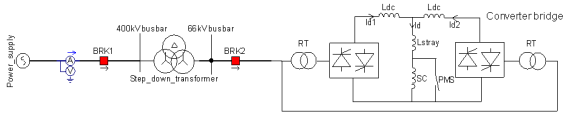

(b) Schematic of the PSCAD simulation model

Figure 4 Main circuit and PSCAD model of the MC

2.1. FSC Analysis[2][4][5][6]

Generally junction temperature is the key parameter to judge thyristor good or bad. In addition, it is another important factor for the thyristor whether there is the direct or reverse voltage could be applied to it after the fault.

All possible faults are performed by using above model. As a conclusion, the worst fault is the misfiring reverse parallel thyristor fault, and its peak fault current is up to 350kA, the second worse fault is short circuit upstream the DC reactor with the maximum fault current at 265kA.

In the following analysis, the junction temperature of thyristor and the voltage could be applied to the thyristor will be detailed analyzed and computed in two worse faults, in order to check whether the FDR2001 design can meet the FSC requirement.

According to the thyristor parameters required in FDR design, ABB thyristor 5STP 52U5200 could be the closest to the parameters, its data is:

$T_{inlet}=40°C, T_{outlet}=47°C, Q_{total}=9L/s, K_{umbAC}=1.4, K_{umbDC}=1.1,$
$N_P=7+1(\textbf{redundant}), V_{drm,rrm}=5200V(T_j\le 110°C), V_{T0}=1.03V,$
$r_T=0.110m\Omega, I_{tsm}=82kA, T_{vj\,max}=125°C, R_{thjhsDC}=5K/kW$

According thermal model analysis and relevant data provided by ABB products, we can get the thermal model of 52U5200 thyristor junction to case as below figure.

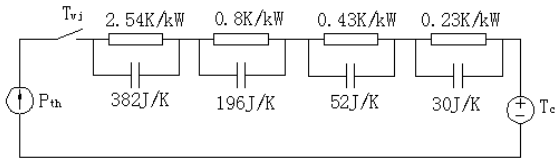

Figure 5 Thermal Network of 52U5200 Thyristor

(Junction to case)

Where, T_c: Case temperature; T_{vj}: Virtual junction temperature; P_{th}: Total power loss of thyristor.

Using above thyristor data and the transient thermal impedance model of the thyristor, the junction temperature variation curve of thyristor in the worst case can be calculated for two worse faults above.

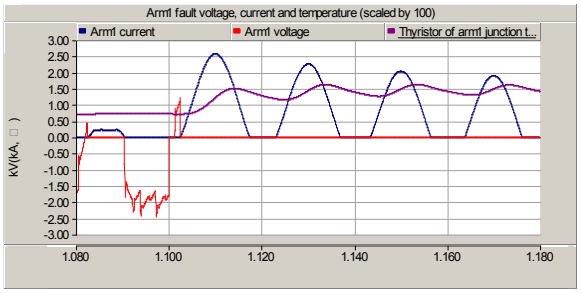

(a) Current, voltage and junction temperature curve of the most overloaded thyristor in dc terminals short circuit fault

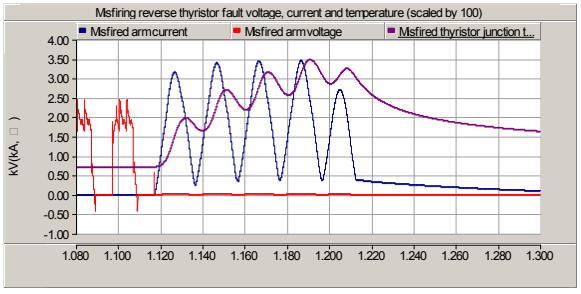

(b) Current, voltage and junction temperature of the most overloaded thyristor in misfiring fault

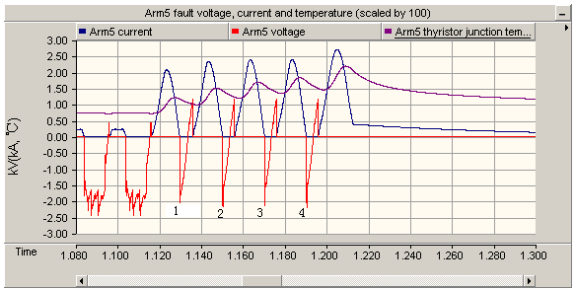

(c) Current, voltage and junction temperature of the most overloaded thyristor among non-misfired thyristors

Figre 6 Fault current, voltage and junction temperature in two worse faults if electronic protection fails (N_P=7)

In Figre 6, it is to be noted that the red curve represents the direct and reverse voltage applied to the thyristor, the blue and purple curves represent the fault current and junction temperature respectively, and their values are scaled by 100.

From Figre 6 it can be seen that the thyristors with maximum fault current are not subjected to reapplied reverse voltage or direct voltage. But the junction temperature of the most overload thyristor is very high. While in misfiring fault, some non-misfired thyristors are subjected to reapplied direct and reverse voltage after overloaded. This requires that the junction temperature of those thyristors should be "sufficiently" low when reverse voltage is reapplied.

Table 1 lists the maximum junction temperature values when the reverse voltage is reapplied to the non-misfired thyristors in different parallel number.

Table 1 Simulation Results of Non-Misfired Thyristor

5STP 52U5200 thyristor (Misfiring reverse parallel arm fault and ac breaker open in 80ms)				
Fault arm	Non-misfired thyristor			
key	**1**	**2**	**3**	**4**
point				
The max reverse voltage(V)	**2040**	**2173**	**2155**	**2215**
N_P=7	**116**	**142**	**159**	**171**
N_P=8	**105**	**126**	**140**	**149**
N_P=9	**94**	**112**	**123**	**131**
N_P=10	**89**	**103**	**113**	**120**

(T_{vj} (℃))

Table *2* shows the relation between thyristor junction temperature and different parallel thyristor number of each arm at different fault cases.

Table 2 Simulation Results of Junction Temperature

Parallel number	**5STP 52U5200 thyristor**			
	DC terminals short fault		Misfiring fault	
	$T_{vj\max}$(°C)			
	Electronic protection	AC breaker open in 80ms	Electronic protection	AC breaker open in 80ms
N_P=7	**100**	**163**	**144**	**348**
N_P=8		**143**	**127**	**289**
N_P=9		**127**	**118**	**246**
N_P=10		**115**		**215**

According to above analysis and tables, it can be concluded as follows:

- Misfiring fault is the worst fault, if the converter is compliant with the FSC criterion in the misfiring case, and it is also well verified in other faults.
- The FDR2001 design couldn't meet the FSC requirement.
- If the electronic protection fails, although the maximum fault current arms of two worse faults are not subjected to

reapplied direct or reverse voltage, but their junction temperature is very high. While in misfiring fault the non-misfired thyristors are subjected to reapplied reverse voltage, this requires that the junction temperature of them should be "sufficiently" low when reverse voltage is reapplied.

Due to the converter configuration in FDR2001 design can't meet the FSC requirement. Some solutions should be implemented:

- Back to back bridges instead of back to back thyristor, the parallel thyristor number in each arm can keep as in the original design.
- Increasing the parallel thyristor number, however this solution will cause higher cost and space.

2.2. Internal Bypass Analysis[2][4][6][7]

Bypass is the important device to protect superconducting coils when ac/dc converter power supply occur fault or superconducting coils quench. In case of the converter fault, the converter should switch to freewheeling in order to conduct the discharge decay current in the superconductive magnets and avoid the over-voltage due to the current blocking. So freewheeling of the converter is very important to protect the magnet and the converter power supply from being damaged by over-current and over-voltage.

Internal non-cyclic bypass is the FDR2001 baseline design shown as below figure.

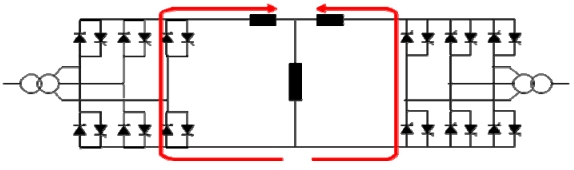

Figure 7 Internal non-Cyclic Bypass

But by analysis the internal non-cyclic bypass, there are some fatal disadvantages to use it. The main reasons are as follows.

- The complicated control much downgrade the reliability;

There could be problem on the selection of the right bypass pair in case of some faults.

For example, in dc short circuit upstream dc reactor, the bridge arm fault current of one converter unit is shown in Figure 8.

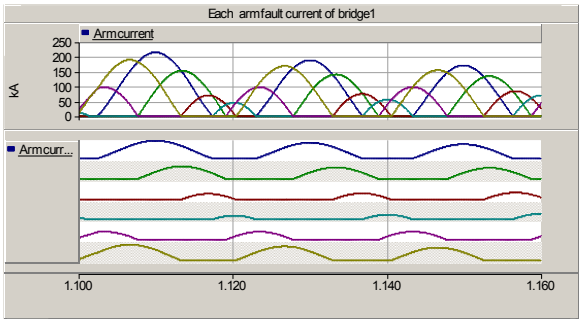

Figure 8 Bridge Arm Fault Current of One Converter Unit

From the figure, it can be seen before the fault clearance, the T1, T2 and T6 could sustain an over-current, so there is no suitable bypass pair can be selected. It is only by increasing the parallel number to satisfy this condition.

In misfiring fault, if misfiring happens during the commutation from T3 and T1, the reversed thyristor T1' is misfired, the T3 and T5 will flow an over-current, the only possibility to set the bypass pair is the using T1 and T4, however, it is difficult to give a judgement to have the right selection through the detecting of AC or DC current.

- It exist the pre-fault junction temperature and the pre-freewheeling junction temperature in the thyristor of the converter bridge. Therefore to assess the parallel number of the thyristor shall start from that temperature, and it will need to increase the parallel number to satisfy the FSC requirement.

- The current balance in two bypass pairs formed by two parallel bridges is difficult, so half rated DC current will not a design criterion for the internal bypass.

- In case of the internal fault, it is not reliable to using a bridge which has potential fault to form the bypass.

According to above analysis on the internal bypass, it can be concluded that the internal bypass isn't suitable to the converter power supply. Therefore an external bypass connected at the converter terminal is suggested as in Figure 9.

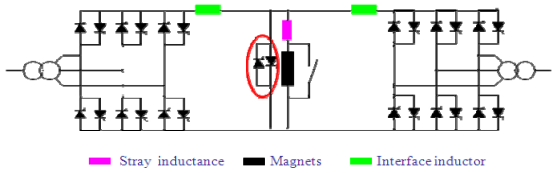

Figure 9 Circuit Topology of External Bypass

3. Current New Baseline Design[8][9]

By above analysis, in order to reduce the risk of the FDR2001 design and fabrication challenges. The new baseline design changes of main converter from the FDR2001 baseline are:

- To adopt back to back bridge instead of back to back thyristors. This change is to reduce the possible fault current level due to the misfiring fault;
- To adopt two 1kV converter units in series with sequential control for the main CS and PF converters, instead of 2kV main converter unit; This change would bring the range of the converter rating into standard industrial practice, using commercially available thyristors, and also bring benefit of the Q reduction, which can enhance the system stabilization;
- To adopt external bypass instead of internal bypass. However, to limit the cost increase, the external thyristor bypass for the MC will be designed for pulse duty and with closing function only. This change is intended to enhance the reliability of main converter.

The main circuit topology of the new baseline is shown as below Figure 10.

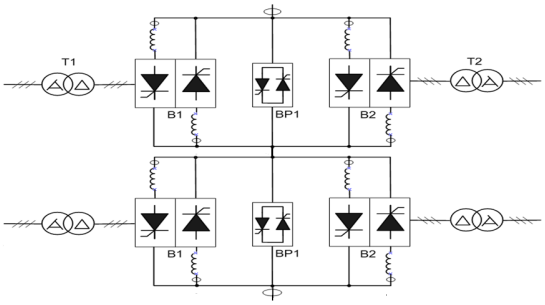

Figure 10 Topology of New Baseline Design

The contrast of two baseline design is presented as below Table 3.

Table 3 FDR2001 Baseline vs. New Baseline Design

Name	FDR2001 Design	New Baseline Design
Peak Fault Current for MC	350kA	265kA
FSC	No	Yes
Component Selection	Difficult	Easy
Bypass Control	Complicated	Simply
Reliability	Low	High
Cost	Less	More

From Table 3, it can be seen that compared with the FDR2001 baseline design, the current design solution can reduce the risk of the past design and fabrication challenges, and it can bring the range of the converter rating into standard industrial practice using commercial available devices.

The new baseline design is in accordance with the two independent external Expert

Groups conclusions and has been approved by IO finally in Project Change Request (PCR)-0187.

4. R&D Work and Progress

Since 2005, ITER Chinese Participant team has performed a lot of R&D activities for ITER power supply system, such as fault analysis of power supply system, R&D of ac/dc converter configuration and mechanical structure considering electromagnetic and mechanical stability, local control system of ac/dc converter, design of power supply test platform for completing power supply procurement in China.

Last year we have completed the review of FDR2001 design and some improvement proposals have been accepted by IO.

Until now we have completed the R&D of local control and concept design for AC/DC converter. All the test facilities of ITER power supply test platform in ASIPP are under construction, it is supposed to be completed before the first half of the next year.

The following Figure 11 shows the conceptual design of AC/DC converter unit structure. Figure 12 shows the two prototypes of DC inductor with aluminium material, the square inductor have been fabricated to be tested. The cylinder inductor is under fabrication. The final structure of DC inductor will be determined after completing the tests of two inductors.

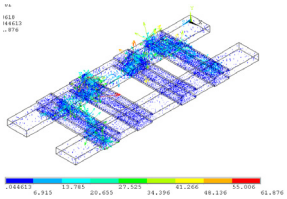

Magnetic field distribution

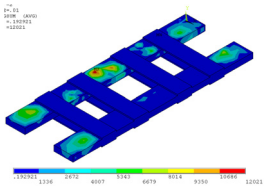

Electro-dynamic force distribution

(a) Simulation Results of Bridge Arm in Converter Unit

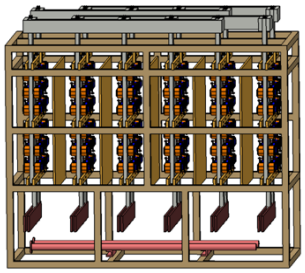

(b) MC Structure

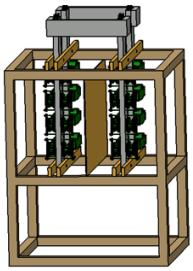

(c) External Bypass Structure

Figure 11 Conceptual Design of Converter Unit

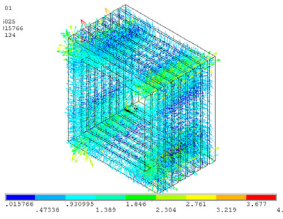

Magnetic field distribution

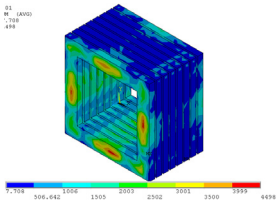

Electro-dynamic force distribution

(a) Simulation Results of DC Inductor with square structure

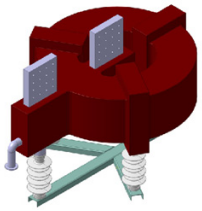

(b) Square Inductor

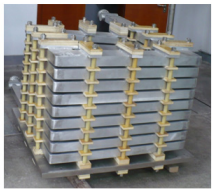

(c) Cylinder Inductor

Figure 12 Prototype of Aluminum Inductor (30kA/50μH)

The circuit configuration of ITER power supply test platform is shown in Figure 13.

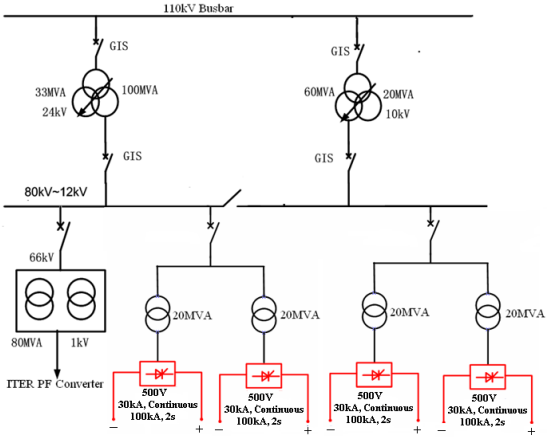

Figure 13 Configuration of ITER Test Platform in ASIPP

5. Technical Challenges

Due to the special requirements of the ITER AC/DC Power Converter Systems, the main technical challenges for the converter power supply design are foreseen as follows:

- High unit power (up to 80MVA/unit, continuous duty, 4 quadrants with circulation current operation);
- Strong magnetically coupled superconducting coil loads;
- Fast dynamic operation conditions due to the requirements of plasma control and interference between converters;
- Huge fault current (up to 350kA for PF), requiring strong electro-mechanical restraint;
- Huge installed power (2.2GVA in total) compared with the short circuit capacity (10GVA) and interference between converters, requiring large capacity RPC&HF system.
- Current sharing between many parallel devices both in steady and transient state.

6. Summary

This paper presents the current new baseline and FDR2001 baseline design of the ITER AC/DC converter power supply.

Some important design criteria of FDR2001 design such as FSC and internal bypass are detailed analyzed. Some proposals to improve the FDR2001 design have been presented, and the current new baseline design is given based on those proposals.

The R&D work and progress on ITER converter power supply done by our Chinese ITER participant team are described.

Lastly, the main technical challenges for the converter power supply design are given.

7. Acknowledgement

The authors would like to thank first the Chinese ITER participant team members for their kindly help and information and then two Expert Groups for the helpful discussions and suggestions, also thank the IO power supply division for providing a lot of beneficial and necessary information and discussion. And thank the ITER executive center of China for the financial assistance.

#

8. Disclaimer

The views and opinions expressed herein do not necessarily reflect those of the ITER Organization.

References:

[1] I. Benfatto et al., "AC/DC Converters for the ITER poloidal system" in Proc. of the 16th SOFE, 1995. Champaign, IL, USA, pp658-661.
[2] IO team, "Design description document (DDD 4.1), ITER pulsed power supply", ITER report, 2001.
[3] P. L. Mondino, et al., "ITER R&D: Auxiliary Systems: Coil Power Supply components," Fusion Engineering and Design, 55 (2001), p.325-330.
[4] "PSCAD/EMTDC", Version 4.2, 2007.
[5] P. Fu, et al, "Quench protection of poloidal field superconducting coil system for the EAST tokamak ", Nuclear Fusion, 46 (2006) S85-S89, February, 2006.
[6] P. Fu, et al., "Review and analysis of the AC/DC Converter of ITER Coil Power Supply" in Proc. of the 25th APEC, USA(2010), pp1810-1816.
[7] P. Fu, et al., "Design and test results for the PF power supply system of EAST", Fusion Science and Technology, vol.54, pp1003-1009, Nov. 2008.
[8] Expert Group 1, "Final report, ITER Coil Power Supply & Distribution System", ITER assessment report, Dec. 12, 2008
[9] Expert Group 2, "Final report, ITER Coil Power Supply & Distribution System", ITER assessment report, Mar. 26, 2009.

EAST Cryogenic System and Its Operation

Zhang Qiyong Fu Bao and EAST Cryogenics Group
Institute of Plasma Physics, Chinese Academy of Sciences, P.O. Box 1126, Hefei, Anhui 230031, China
Email: zhangqy@ipp.ac.cn

Abstracts:

The cryogenic system of EAST Tokamak consists of a 2 kW/4.5K helium refrigerator, cryogenic transfer lines, helium distribution valve box, the cooling loops of PF and TF coils, structures, thermal shields and the HTS current leads. The 2kW/4.5K helium refrigerator assembling was finished in the end of 2004 and the refrigerator has been commissioned successfully in July of 2005. The installation of the cryogenic distribution system has been completed in January of 2006. On Feb. 18, the Tokamak began to cool-down. It took 18 days to cool-down all of the superconducting magnets, buslines and HTS current leads to the certainly temperature. EAST Tokamak has been cool-down for seven times until Oct. 2010. Every time it was duration more than 80 days. This paper presents the design of the cryogenic system, the operation and optimization of the cryogenic system.

Key words: EAST Cryogenic System, Operation, optimization

1. Introduction

EAST cryogenic system consists of compressor system, cold box, Helium management system, distribution valve box, and so on. The components of EAST Cryogenics system is in Fig.1, Schematic flow sheet of the helium refrigerator is shown in Fig.2 as follows.

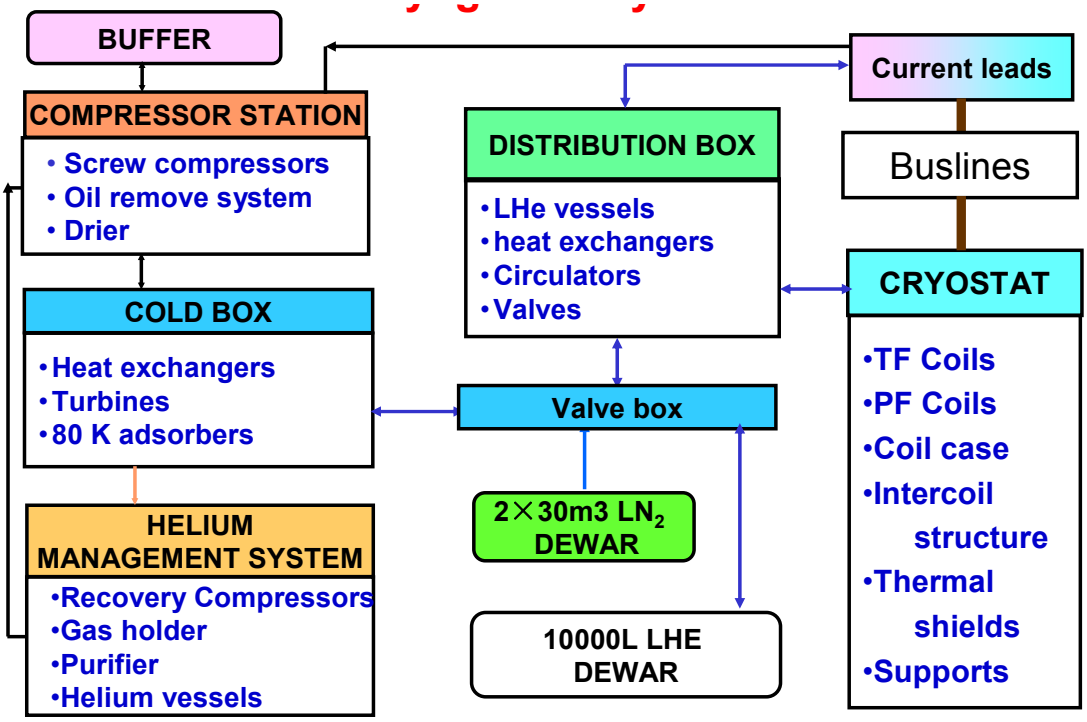

Fig.1 the components of EAST Cryogenics system

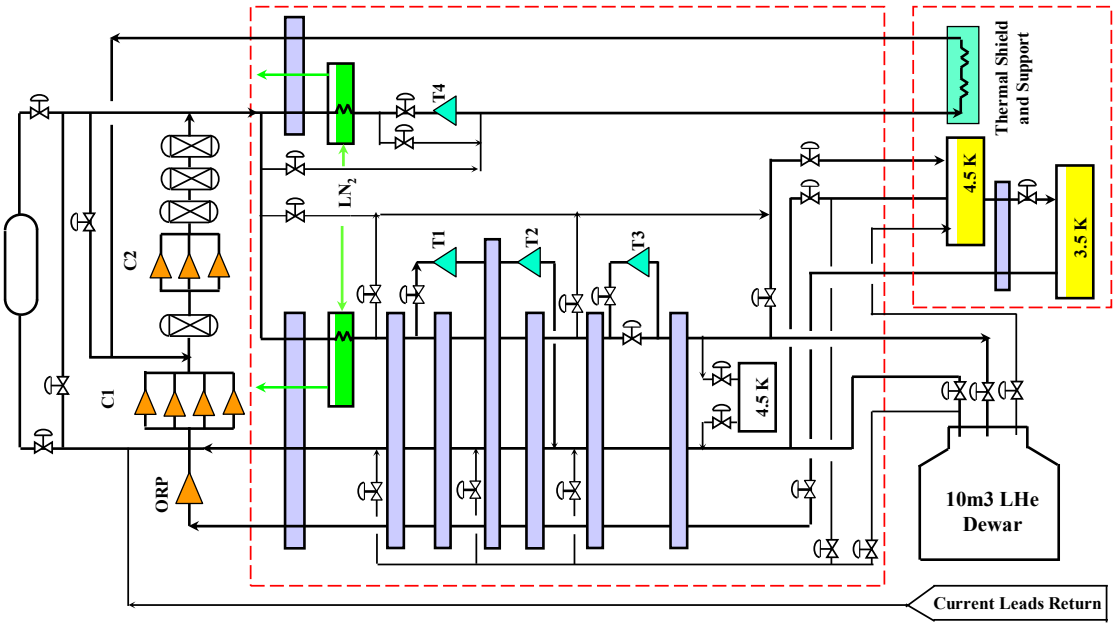

Fig.2 Schematic flow sheet of the helium refrigerator

2. Compressor station

Screw compressors are used to supply compressed helium to the cold-box Compressor system which consists of 7 oil injected screw compressors and 1 oil ring pump. The compressor system has two stages: 4 compressors composed the low-pressure stage, the operating flow rate is 250 g/s and the pressure is 5bara ,3 compressors composed high-pressure stage the operating flow rate is 360 g/s and the pressure is 20bara .The suction pressure of the Oil ring pump is about 0.40bara , the flow rate of it is about 3000 Nm3/h.

The oil of the compressed helium is removed by a four-stage oil removal system: three coalescers of super-fine glass fiber in series followed by an oil vapor adsorber of active charcoal. It can reduces the oil-residuals down to 0.01 ppm(w). The oil removal system is followed by a molecular sieve (13X) dryer to remove water vapor in the helium flow. Finally a dust filter of less than 5 micrometers is installed.

To store the required pure helium for the running of the refrigerator and the cooling of the cold mass, Two He buffers of 100 m^3 are used. The pressure of the buffer is kept between 0.5 MPa and 1.5 MPa. They can be switched to supply and recover helium between the suction side of the low-pressure stage compressors and the discharge side of the high-pressure stage compressors. Control valves are used to control the pressure of the compressor

After almost ten years used the isothermal efficiency of screw compressors becomes lower and lower. The reasons may be the screws have been frayed and the screw compressor inner pressure ratio and the exterior pressure ratio not matched. So the compressors needed to be improved.

3. Cryogenic control system

The structure of the cryogenic control network is shown in Figure 3. The design is based on an Emerson process management DeltaV automation system[4], which is a Distribution Control System(DCS) that ensures the expandability for the future developments. The

cryogenic system employs a 3-layer communication network structure. The layers are the process level, the control level, and the operator and engineering level. The process level includes all the equipments, actuators, sensors and transducers. All the process variables and status information are converted to manipulable and supervisory data by the control level. The control level also transfers manipulated information to actuators. Analog/Data conversion, operation of control algorithm and disposal of input/output variables are realized inside the control level. The operator and engineering level is the interface between operators and the control system. In this level, engineers can configurate program and operate for the cryogenic system.

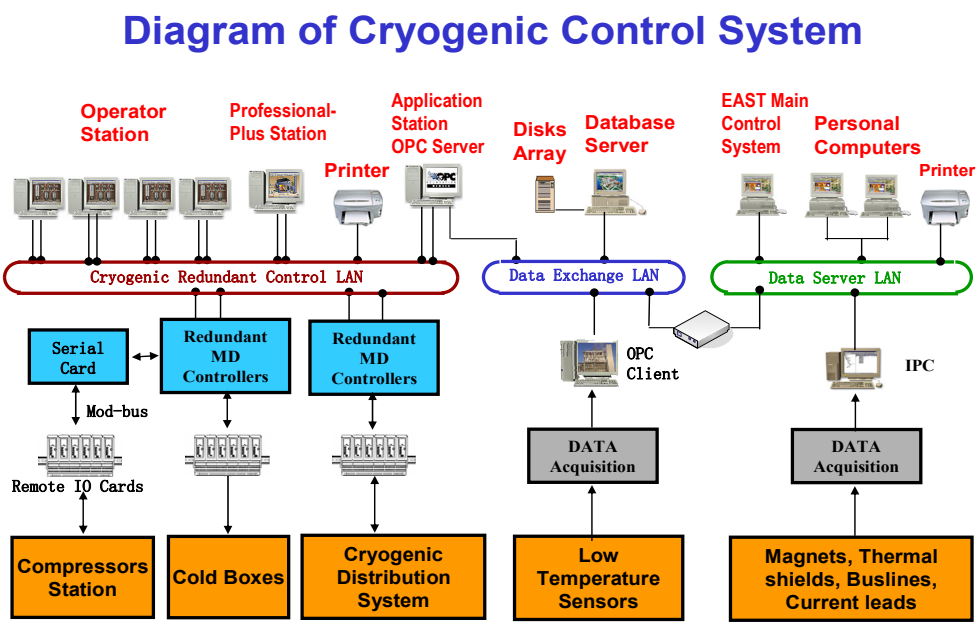

Fig 3 diagram of cryogenic control system

The Delta-V DCS offers the software to be used in all components. These include configuration software, control software, operation software and advanced process control software. The I/O numbers are shown in table 2. There are 1200 I/O numbers in the control system, which is an about 20% margin.

4. Research project of helium turbine

Helium turbine is the core part of helium cryogenic system. EAST cryogenic system helium turbines are imported from Russia. Which are the static gas bearing combine with the static oil bearing .There are four type helium turbines in EAST refrigerator, the turbine A(TA) gets the 13 kW/80 K, to cool down the thermal shield of the EAST tokamak , The TB&C gets about 5.6 kW/20 K to cool down the main flow. The TD is to expand the main flow to get the supercritical helium to cool down the magnets, busline and other components of EAST.

There are something wrong with the imported turbines during its operation. So we designed and manufactured the turbines by ourselves. The final product is showed in fig.4 and the starting up process is showed in Fig.5. This turbine(TD) has been started for 4^{th} times. And it is being used for more than 90 days. The capacity is suitable. But the speed of it is not operating at the designed value and this need to be test after this experiment.

Fig.4 Static Gas bearing & oil bearing helium turbine

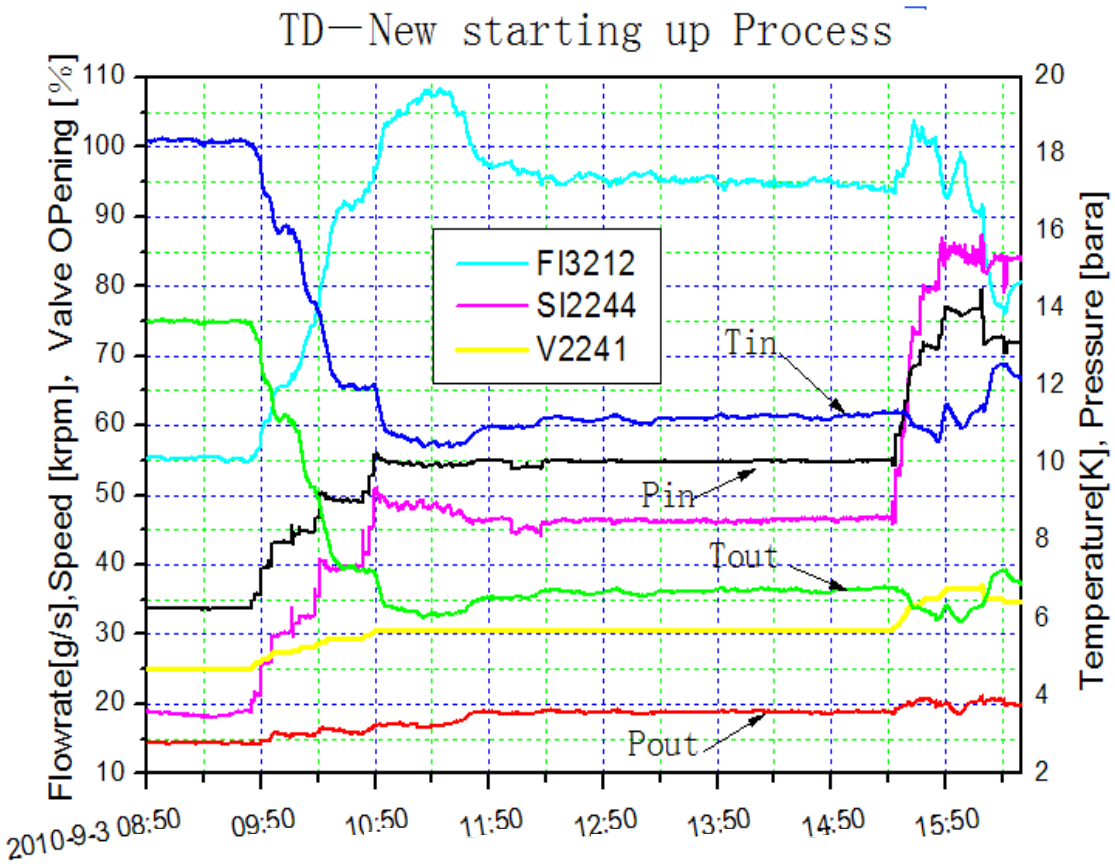

Fig.5 Starting up of new TD helium turbine

5. Conclusions

The EAST cryogenic system has been designed and constructed in ASIPP. The refrigerator was commissioned semi-automatically. The power of the refrigerator is more than 2 kW/4.5K,The EAST superconducting tokamak has been cooled down for 7 times till Sep. 2010.09 It takes about 15 days to cool down all of the cold components of EAST,3.8 K cooling of the superconducting magnets have also been achieved. The cryogenic system has run more than 450 days in total. Another cooldown mode was also tested which is the magnets was cooled down by turbine B&C and JT valve and the capacity is about 1800 W/4.5 K.

References

[1] Yuanxi Wan, HT-7 Team, HT-7U Team, Overview of steady state operation of HT-7 and present status of the EAST project, Nuclear Fusion, 40 (2000), 1057-1068.

[2] P. D. Weng & HT-7U Team, The engineering design of the HT-7U tokamak, SOFT 21, Vol.58-59(2001), 827-831.

[3] H. Bai, Y. Bi, J. Wang, M. Zhuang, P. Zhu, Q. Zhang, Design of 2kW/4K helium refrigerator for HT-7U, Proceedings of the 19th ICEC, 2002, pp.183-186.

[4] Y. Jin, X. Shao, M. Zhuang, H. Bai, EAST cryogenic supervisory and control system based on DeltaV DCS, Plasma Physics and Technology, No. 5(2005), 3013-3016

Development of "Low activation superconducting wire" for an advanced fusion reactor

Y. Hishinuma[1)], A. Kikuchi[2)], T. Takeuchi[2)], K. Matsuda[3)], S. Yamada[1)], H. Taniguchi[4)] and A. Sagara[1)]

1) National Institute for Fusion Science, 322-6 Oroshi-cho, Toki, Gifu
2) National Institute for Materials Science, 1-2-1 Sengen, Tsukuba, Ibaraki
3) University of Toyama, 3190, Gofuku, Toyama
4) Osaka Alloying Works Co.,Ltd, 45-5-9, Shirakata, Fukui

E-mail of corresponding author: hishihnuma.yoshimitsu@nifs.ac.jp

Abstract

In the D-T burning plasma reactor beyond ITER such as DEMO and fusion power plants assuming the steady-state and long time operation, it will be necessary to consider carefully induced radioactivity and neutron irradiation properties on the all components for fusion reactors. The decay time of the induced radioactivity can control the schedule and scenarios of the maintenance and shutdown on the fusion reactor. V_3Ga and MgB_2 compound have shorter decay time within 1 years and they will be desirable as a candidate material to realize "low activation and high magnetic field superconducting magnet" for advanced fusion reactor. However, it is well known that J_c-B properties of V_3Ga and MgB_2 wires are lower than that of the Nb-based A15 compound wires, so the J_c-B enhancements on the V_3Ga and MgB_2 wires are required in order to apply for an advanced fusion reactor. We approached and succeeded to developing the new process in order to improve J_c properties of V_3Ga and MgB_2 wires. In this paper, the recent activities for the J_c improvements and detailed new process in V_3Ga and MgB_2 wires are investigated.

1. Introduction

The International Thermonuclear Experimental Reactor (ITER) project was started to realize deuterium (D)–tritium (T) fusion energy generation. A magnetic confinement typed D-T fusion reactors, ITER and DEMO etc, require a higher magnetic field property to confine the burning plasma and maintain the fusion reaction for longer operation times, so that the superconducting magnet system is one of the most important components in the fusion reactor system. Burning plasma is sure to generate many 14 MeV fusion neutrons during the D-T reaction, and they stream and penetrate the superconducting magnet through plasma heating and/or diagnostic ports. In the future, both the radio-activation and degradation of superconducting properties by the streaming and penetration of neutron irradiation will have to be considered.

A simulation result for the decay time of induced radioactivity of various superconducting wires in the Toroidal magnetic Field (TF) coils of an ITER design is

shown in fig. 1 [1]. The superconducting magnets of an advanced fusion reactor will be fabricated by the Nb-based superconductors such as Nb-Ti, Nb_3Sn and Nb_3Al due to the excellent high magnetic field property. However, Nb-based superconductors require a longer cooling time than ten of thousand years, if the 10 mSv/h for the remote-handling recycling level is satisfied. The activity that is maintained during a long time cooling is caused by the formation of long-lived nuclides such as ^{94}Nb ($t_{1/2}$=2.0×10^4 years), produced by $^{93}Nb(n,\gamma)^{94}Nb$ reaction, and ^{26}Al ($t_{1/2}$=7.2×10^5 years), produced by $^{27}Al(n,2n)^{26}Al$ reaction. A dose rate of around 10 mSv/h–100 mSv/h is kept at the magnet near the vacuum wall for a long time. This means that thicker shielding is necessary in front of the magnet if Nb-based superconductors are used for the long operation. On the other hands, V-based and MgB_2 superconductors show remarkably shorter decay times compared with the Nb-based superconductors. The dose rates of V-based and MgB_2 superconductors are reduced to 10μSv/h for the hands-on maintenance level below 1 year. This suggests that the hands-on maintenance of these materials is possible because of their short-time cooling. We thought that the V-based and MgB_2 compounds could be suitable as candidate materials for a 'low activation superconducting magnet' for a fusion reactor application.

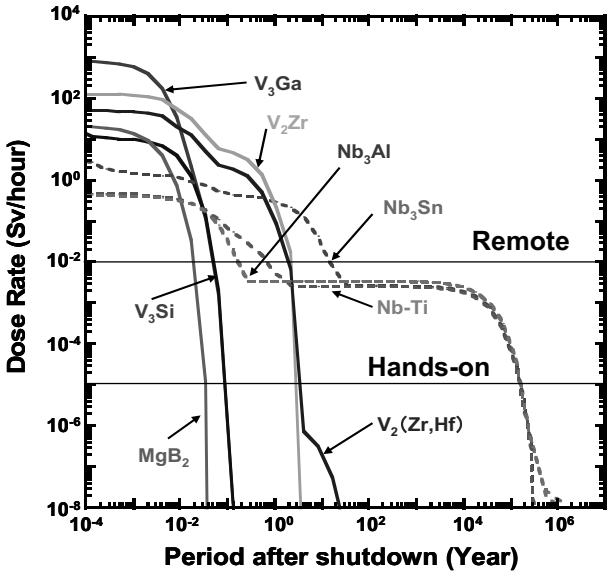

Fig. 1 The decay time of the induced radioactivity on various superconducting wires in the toroidal magnetic field (TF) coils of the ITER design [1].

Recently, we approached to investigate the further J_c enhancements of V_3Ga and MgB_2 wires for applying an advanced fusion reactor and succeeded to developing the new process in order to improve superconducting properties of V_3Ga and MgB_2 wires. In this paper, the recent activities for the J_c improvements and detailed new process in V_3Ga and MgB_2 wires are investigated.

2. Recent activity for the J_c improvement of V_3Ga wire

V_3Ga is one of the V-based superconducting compounds and it is attractive in the several V-based compounds as high magnetic field and low activation superconducting wire materials. V_3Ga compound has high upper critical magnetic fields (H_{c2}) above 20 T. In addition, V_3Ga has lower strain sensitivity of J_c degradation compared with Nb_3Sn compound. Furthermore, V_3Ga compound was historically origin material to succeed the development of "Bronzed process" on commercial Nb_3Sn wire

[2], its J_c property was higher than that of Nb_3Sn wire at the time. After that, the bronzed processed V_3Ga tape was applied to 18.1 T generation superconducting magnet and this generated magnetic field was world record at the time [3]. We thought that V_3Ga was one of the candidate strand materials for the low activation high magnetic field and electromagnetic force superconducting magnet such as TF and Helical coils of advanced fusion reactor. Therefore, we reconsidered superconducting properties and wire process on V_3Ga compound for fusion reactor. In the previous study, the wire process of V_3Ga compound was mainly investigated "Bronzed process" between Cu-Ga solid solution within 20 at%Ga composition and V filament shown in Fig. 2 (a). We approached the new route V_3Ga wire process for the aim of the J_c enhancement by the increase of V_3Ga volume fraction and investigated the new PIT process using high Ga content Cu-Ga compound powder above 20 at%Ga shown in Fig.2 (b). The Ga content dependence of the thickness of diffusion reaction layer in V_3Ga mono-cored wire using high Ga content Cu-Ga compounds is shown in Fig.3. The thickness of diffusion layer when is used various Ga content below 20 at% Cu-Ga solid solution through "Bronzed process" is also shown for the comparisons. The thickness of diffusion layer was corresponded to that of V_3Ga

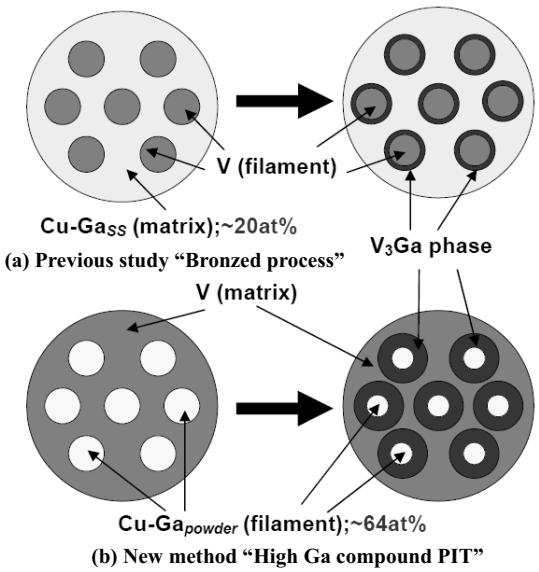

Fig. 2 The concept of new PIT processed V_3Ga wire using high Ga content Cu-Ga compound.

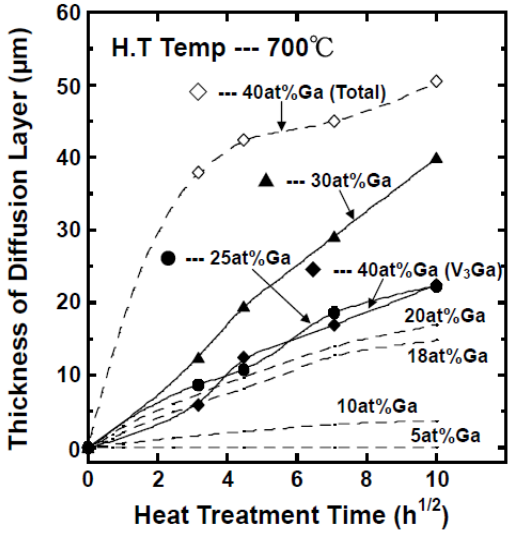

Fig.3 The relationship between thickness of diffusion layer and heat treatment time on the several Ga content samples reacted at 700℃

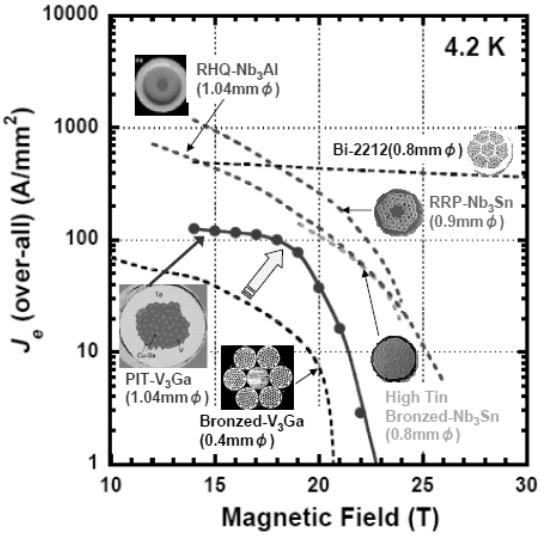

Fig.4 The recent J_c-B performance of V_3Ga multifilamentary wires using high Ga content compound.

phase in 25 at% and 30 at%Ga composition due to forming V_3Ga single phase. The total diffusion layer was remarkably increased with increasing of Ga content. The high Ga content into Cu-Ga compound was effective to promote diffusion reaction and to increase V_3Ga phase layer. It suggested that the volume fraction of V_3Ga phase was increased remarkably by using high Ga content compound as Ga source during diffusion reaction.

We also fabricated successfully V_3Ga multifilamentary precursor wire using Cu-Ga/V mono-cored billets. The recent J_c-B performance of V_3Ga multifilamentary wire via new PIT process using high Ga content and the comparison of J_c-B property between the other superconducting wires are shown in Fig.4. For the V_3Ga wire, it was clear that J_c property of new PIT process sample was three times higher than that of "Bronzed process" sample. It suggested that high Ga content compound was effective to improve J_c-B performance and it also was suitable material as Ga source material. The upper critical magnetic field (H_{c2}) was also increased 2 T compared with the conventional processed sample. However, the J_c-B performance of new processed V_3Ga wire was lower than that of Internal Tin processed Nb_3Sn and RHQT processed Nb_3Al. In the future, the further J_c and H_{c2} enhancements of V_3Ga are required for the applying fusion reactor. We thought that the optimum wire cross-section configuration and impurity addition like Ti and/or Ta additions into Nb_3Sn would be significant method for the further J_c enhancement of the new processed V_3Ga wire.

3. J_c enhancement of MgB_2 wire by Cu addition using Mg_2Cu compound

In the concept of a low activation superconducting coil system for a fusion reactor, MgB_2 superconducting wire was an alternative material for Nb-Ti alloy wire for the PF and feedback coils if the critical current density (J_c) around lower magnetic field region could be improved. We investigate Cu addition using Mg_2Cu compound in the MgB_2 phase synthesized by conventional processes with the purpose of improving J_c without lowering critical temperature (T_c). The Mg_2Cu compound is an intermetallic brittle material, so it is easy to fabricate fine particle powders by mechanical grinding. The Mg_2Cu compound is promoted the diffusion reaction in order to form higher T_c MgB_2 phase at lower temperatures due to no-oxidation and a lower melting point than metal Mg [4,5]. Precursor mixture powders were made by metal Mg powder (99.9%), Mg_2Cu compound and amorphous B powder

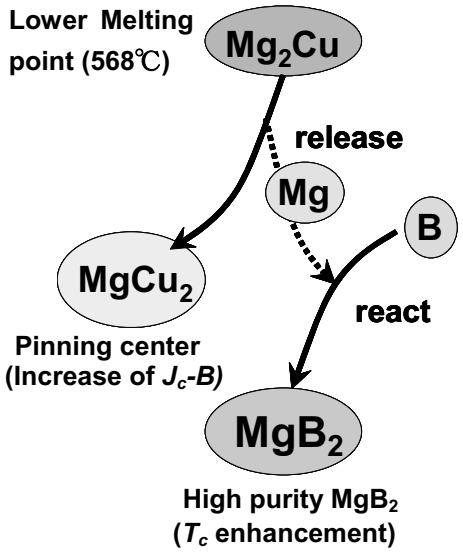

Fig.5 The principle of new route synthesis of MgB_2 phase.

(99.9%). The mixture powders were tightly packed into metal Ta tubes (99.99%) with 10 mm outer diameter and 6 mm inner diameter. The precursor wires had a final diameter of about 1.04 mm. The prepared short sample wires were heat treated using a low temperature diffusion process which used various temperatures for long time in Ar atmosphere. The typical J_c–B performances of Ta sheathed samples when heat treated at 450℃ were shown in fig. 6. The core J_c property under the magnetic field of the Ta sheathed sample was increased by extending the treatment time: the optimum treatment time was defined as 200 h in the case of a heating temperature of 450℃. Typical present high J_c–B performances of SiC doped and undoped MgB_2/Fe tapes using metal Mg and MgH_2 as Mg source material through PIT processes are also shown for comparison [6]. The J_c–B performance of the Cu addition MgB_2/Ta wire which was heat treated at 450℃ for 200 h was higher compared with that of undoped SiC Fe sheathed samples using MgH_2. It is noteworthy that the core J_c value which was heat treated at 450℃ for 200 h in a lower magnetic field than 6 T was improved remarkably in comparison with the SiC doped Fe sheathed sample. This was why the high purity MgB_2 phase having a high T_c value of 35 K was promoted to form the core for the low-temperature diffusion process. It was also noticed that the core J_c property of MgB_2 wire by the low-temperature diffusion process was almost equivalent to the conventional Nb-Ti wire in the low magnetic field region and then the MgB_2 wire was able to be an alternative material for Nb-Ti wires for a low activation superconducting magnet system in the low magnetic field region of an advanced fusion application. For practical applications in advanced fusion reactor, we succeeded to fabricate 100 m long length class new processed MgB_2/Ta/Cu mono-cored wire shown in Fig. 7 [7]. Wire deformation was carried out using only drawing dies, and the precursor wire finally was about 1.04 mm in diameter. This wire has stabilized Cu to prevent the thermal running and quench. We made the small solenoid coil

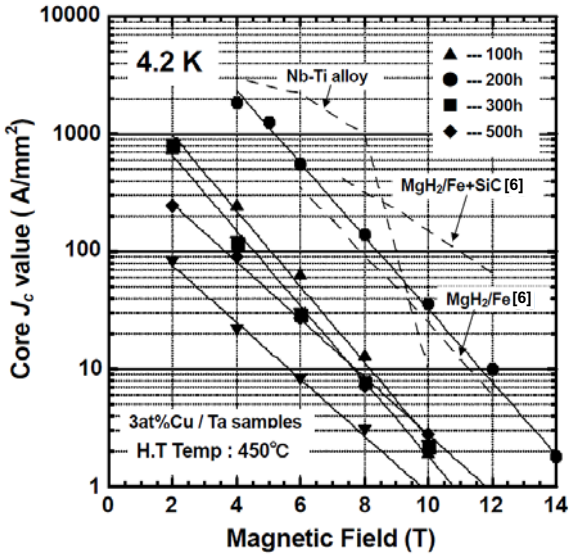

Fig. 6 Typical J_c–B performances of Ta sheathed wires when heat treated at 450℃ for long time.

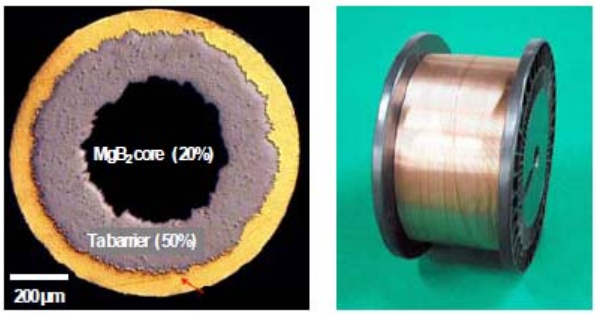

Fig. 7 Typical photographs of the 100 m length class Cu addition MgB_2 mono-cored wire. (a) Cross-section, (b) 100 m length wire.

using long MgB_2 mono-cored wire to investigate the reliability of the long wire deformation. The photograph of the small solenoid coil using MgB_2/Ta Cu long wire and the result of the coil excitation test is shown in Fig. 8. The 2.62 T of the central magnetic field (B_0) and 88 % of the load factor were shown in the solenoid test coil. We found that MgB_2 superconducting materials have the large potential as "Low activation superconductor" to applying for advanced fusion reactor.

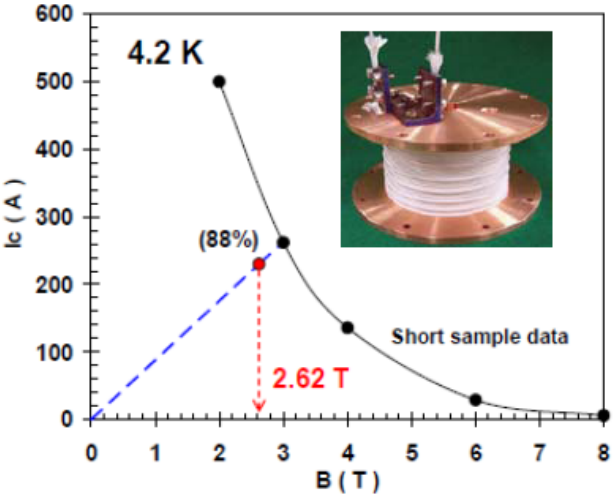

Fig. 8 The photograph of solenoid coil using Cu addition MgB_2/Ta/Cu mono-cored wire and the result of the excitation test at 4.2K.

4. Summary

V_3Ga and MgB_2 wires are candidate materials of Nb-based superconducting wires as the "low activation superconducting magnet". We approached to investigate the J_c enhancements of V_3Ga and MgB_2 wires for applying an advanced fusion reactor and succeeded to developing the new process in order to improve superconducting properties of V_3Ga and MgB_2 wires.

Reference

[1] NODA, T., et al., "Induced activity of several candidate superconductor materials in a tokamak-type fusion reactor", J. Nucl. Mater. **329–333** (2004) 1590.

[2] TACHIKAWA, K., et al., "Superconducting critical currents of V_3Ga wires made by a new diffusion process", Jpn. Journal of Applied Physics, vol. 6, (1967), pp. 782.

[3] MARKIEWICZ, W., et al., "A 17.5 Tesla superconducting concentric Nb_3Sn and V_3Ga magnet system", IEEE Trans. Magnetics, vol. **13**, (1977), pp.35-37.

[4] KIKUCHI, A., et al., "The synthesis of MgB_2 superconductor using Mg_2Cu as a starting material", Supercond. Sci. Technol., vol.**17,** (2004) 781.

[5] HISHINUMA, Y., et al., "Microstructure and superconductivity of Cu addition MgB_2 wires using Mg_2Cucompound as additional source material", Supercond. Sci. Technol., vol. **19** (2006) 1269

[6] MATSUMOTO, A., et al., "Effect of SiO2 and SiC doping on the powder-in-tube processed MgB_2 tapes", Supercond. Sci. Technol., vol. **17** (2004) S319.

[7] HISHINUMA, Y., et al., "Superconducting properties and microstructure of MgB_2 wires synthesized with a low-temperature diffusion process", Supercond. Sci. Technol., vol. **20** (2007) 1178.

The First Benchmarking of ITER BR Nb3Sn Strand of CNDA

Long Feng, Liu Fang, Wu Yu, Ni Zhipeng
Institute of Plasma Physics, Chinese Academy of Sciences, P.O. Box 1126, Hefei, Anhui 230031, China
Email: longf@ipp.ac.cn

Abstract

According to the International Thermonuclear Experimental Reactor (ITER) Procurement Arrangement (PA) of Cable-In-Conduit Conductor (CICC) unit lengths for the Toroidal Field (TF) and Poloidal Field (PF) magnet systems of ITER, at the start of process qualification, the Domestic Agency (DA) shall be required to conduct a benchmarking of the room and low temperature acceptance tests carried out at the Strand Suppliers and/or at its Reference Laboratories designated by the ITER Organization (IO). The first benchmarking was carried out successfully in 2009. Nineteen participants from six DAs (China, EU, Japan, South Korea, Russia, and the United States) have participated in the first benchmarking. Bronze-route (BR) Nb3Sn strand and samples prepared by ITER reference lab (CERN) were sent out to each participant by CERN. In this paper, the test facility and test results of the first benchmarking of Chinese DA was presented.

Keywords: benchmarking, BR Nb3Sn, CNDA

1. ITER benchmarking

The CICC of Toroidal Field (TF) [1] and Central Solenoid (CS) [2] magnet systems of ITER are cabled and jacked by Nb3Sn superconducting strands. Six of the seven ITER DAs (China, European Union, Japan, South Korea, Russia, and the United States) will participate in supplying Nb3sSn-based conductor to the ITER project. Each superconducting strand supplier is required to carry out acceptance test and each DA is required to establish one or more reference lab, which will verify the acceptance tests independently.

To ensure uniform production quality at all the suppliers and Das, according to the ITER PA, at the start of process qualification, the DA shall be required to conduct a benchmarking of the room and low temperature acceptance tests carried out at the strand suppliers and/or at its reference laboratories designated by the IO.

The benchmarking shall be carried out under the DA responsibility and is within the scope of the PA. The benchmarking of the critical current and hysteresis loss measurements shall be performed on reference strand samples and according to procedures defined by the IO.

Once benchmarking is successfully completed, the DA shall be required to conduct a yearly cross-check of acceptance tests with respect to the reference laboratories. The yearly cross-check of the critical current and hysteresis loss measurement shall be carried out on reference strand samples and according to procedures defined by the IO.

2. Test facility

The test department of Chinese ITER conductor package in Institute of Plasma Physics Chinese Academy of Sciences (ASIPP) is the Chinese DA reference laboratory. The superconducting strand test facility was set up in 2006. The aim is to study on the critical

performance of the superconducting strand. Up to now, hundreds of critical current samples and RRR samples were tested. The test results were used to improve the processing technique of Nb3Sn and NbTi superconducting strands potential supplier in China.
The SMS superconducting magnet system of CRYOGENIC LTD is to produce the background magnet field. Nominal specifications of the magnet system are shown in Table 1.

Table 1 Nominal specifications of the magnet system

Magnet model	16t-70-H3
Guarantee fields at 4.2K	14.0T
Guarantee fields at 2K	16.0T
Design fields at 4.2K	14.8T
Design fields at 2K	16.5T
Maximum operating current for Bmax	<120A
Homogeneity over 32mm diameter and ±17.5mm axially about field centre	0.5%
Central homogeneity over 10mm dsv	0.1%
Clear central bore	70mm
Overall diameter	260mm
Overall length	450mm

A vacuum heat treatment furnace is used for the heat treatment of the Nb3Sn strand. The main specifications of the furnace are shown in Table 2.

Table 2 Main specifications of the vacuum heat treatment furnace

Model	L4510 II-6/ZM
Maximum operating temperature	950℃
Inner diameter	120mm
Length of constant temperature zone	450mm
Temperature accuracy	±2℃ (≥600℃, ≤900℃) ±3℃ (≥200℃, <600℃)
Heating rate	≥5℃/min
Ultimate vacuum	5×10^{-4}Pa
Operating condition	Vacuum Ar protection

The reference heat treatment cycle for the ITER BR Nb3Sn strand is cycle B as required in the Procurement Arrangement (PA) [3]. The heat treatment cycle is shown in Fig. 1. It is specified in Table 3.

Fig.1. Heat treatment cycle B for BR Nb3Sn strand

Split time(h)	Duration(h)	T(℃)
0	0	20
38	38	210
50	88	210
26	114	340
25	139	340
22	161	450
25	186	450
25	211	575
100	311	575
15	326	650
100	426	650
30	456	500
44	500	20

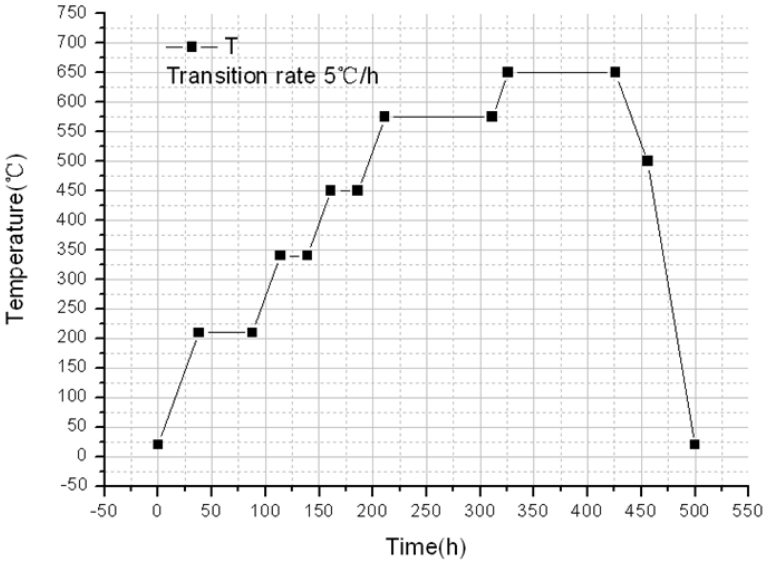

Table 3 Specifications of heat treatment cycle B

Heat treatment cycle for BR Nb3Sn strand	Cycle B
Reaction atmosphere	Vacuum
Temperature homogeneity	±3℃(Target)
Transition rate	5℃/hr
Plateaus	210℃/50hrs
	340℃/25hrs
	450℃/25hrs
	575℃/100hrs
	650℃/200hrs``
Cool down rate	5℃/hr to 500℃, then faster

Because significant temperature deviation will lead to obvious performance degradation, temperature and vacuum data should be recorded by acquisition system to monitor the whole heating process.

3. Benchmarking items

Totally 19 labs participated in the first benchmarking [4]. ASIPP took part in the benchmarking as the China DA reference lab.

Samples and benchmarking items are described as follows.

(1) IO-prepared samples:

Three samples prepared and heat-treated by IO reference lab (CERN) were sent to each DA for I_c and n value testing.

(2) Self-prepared samples:

Un-reacted BR Nb3Sn strand was distributed to each DA by IO reference lab. 30m strand was shipped to ASIPP directly to perform and manage the benchmarking.

Testing items for self-prepared samples include I_c, n value, residual resistance ratio (*RRR*), hysteretic losses (Q_{hys}), Cu:non-Cu ratio, strand diameter, Cr plating thickness, and twist pitch. Sample test conditions are listed in Table 4.

Table 4 Test conditions

Items	Conditions
I_c, n value	12 T (no self-field correction), 4.22 K (with correction if necessary), ITER barrel
RRR	Ratio of electrical resistance at 273 K and 20 K
Q_{hys}	±3 T magnetization loop at 4.22 K

ITER standard Ti-6Al-4V barrel shall be used for the critical current measurement. The electric field criterion is 10 μV/m. The n value is determined from a power law fit in the range of 10 μV/m to 100 μV/m. The measurement is performed in liquid helium and the temperature is corrected to 4.22 K using the following equation:

$$I_c / I_m = 1 + 0.11834(T_m - 4.22) \quad (1)$$

Where I_c is the critical current at 4.22 K, and I_m is the measured critical current at measurement temperature T_m, where 4.0K< T_m <4.4K [5]. This equation is valid only at 12 T.

4. Results

The IO-prepared samples were prepared, heat treated at the University of Geneva, and measured by CERN. The average I_c of all the 18 samples is 188.7A, with a standard deviation of 1.8A, or 1.0% of the mean. The average I_c of all participants is 189.1A, with a standard deviation of 2.1A. The average n-value was 41.4 with a standard deviation of 1.4 measured by CERN and 43.5 with a standard deviation of 3.5 measured by all participants. The maximum deviation of the average I_c and n-value measured at ASIPP are 2.4A and 3.2, respectively.

The ITER standard barrel was used for the self-prepared samples. Heat treatment was carried out by cycle B as required in the PA. The same barrel after teat treatment was used for I_c and n-value measurement. The average I_c and n-value of all the participants are 188.1A and 42.7. The maximum deviation of the average I_c and n-value measured at ASIPP are 4A with standard deviation of 3.5A and 2.9 with standard deviation of 1.92, respectively.

Statistical results showed that sample preparation technique such as wingding method, heat treatment, soldering, testing, signal processing, etc., are appropriate and consistent.

Despite of the highly consistent results of I_c and n-value measurement, significant deviation was found in the RRR measurement, which has a standard deviation equal to 15.9% of the mean value. Two possible reasons were estimated: (1) poor temperature/heat removal control at 20 K, and (2) significant local variation from very short samples. The RRR value measured at ASIPP was 37% deviation from the mean value. Because the result we measured was far blow the requirement of the PA, different methods, i.e. gaseous helium and refrigerator, were used to cross check the unbelievable result. But the same result was obtained. Local variation or damage during processing after heat treatment could be the reasons.

Two contributors were participated in the Q_{hys} measurements, which are Beijing University (SQUID) and Ningbo Institute of Material Technology & Engineering Chinese Academy of Sciences (VSM). The test results showed both well-controlled measurement.

There are no obviously difficulty for the room temperature measurements (Cu:non-Cu ratio, strand diameter, Cr plating thickness, and twist pitch). Most measurements are reasonably well-controlled, though plating thickness shows some significant variability due to the highly local nature of the metallographic measurement.

5. Conclusions

The first round BR Nb3Sn strand benchmarking was finished successfully. Test facilities and data processing of all the participants were verified and compared with the ITER reference lab (CERN) by IO-prepared samples. Small differences between test sample assembly, accuracy of the sensors and data processing methods may lead to the standard deviation increases from 1.8A measured by CERN to 2.1A measured by all participants. The standard deviation of self-prepared samples further increases to 3.5A due to the additional preparation processes.

Most measurement results were well-controlled by ASIPP, except *RRR* (37% deviation). Gaseous helium and refrigerator methods were used to verify the test results. The same result showed the correctness of the two methods. Local variation or damage during processing after heat treatment could be the reasons.

Beijing University and Ningbo Institute of Material Technology & Engineering Chinese Academy of Sciences are the participants for Q_{hys} measurement in the first round benchmarking. But because of the much larger Q_{hys} value of Internal-tin (IT) strand, Ningbo Institute of Material Technology & Engineering will be the only participant for the hysteresis losses measurement of IT strand.

Acknowledgment

The tests were carried out in ASIPP, the author would like to thank my colleagues gave great help especially in the room temperature measurement.

We also thank Matt Jewell at ITER, Sihua Zhu and Huixian Gao at Westren Superconducting Technologies company (WST) for many useful discussions.

References

[1] F. Savary et al., “Status report on the toroidal field coils for the ITER project” IEEE Trans. Applied Supercond., vol. 20, pp.381-384, Jun. 2010..

[2] P. Libeyre et al., “Detailed design of the ITER central solenoid,” Fusion Eng. Des., vol. 84, pp. 1188–1191, Jun. 2009.

[3] Kazutaka Seo, JAEA & ITER IO, “Procedure of Ic Sample Preparation and Test in the ITER Strand Benchmarking”, 11 Nov. 2008.

[4] Matthew C. Jewell et al, “World-Wide Benchmarking of ITER Nb3Sn Strand Test Facilities”, IEEE Trans. Appl. Supercond., vol. 20, pp.1500-1503, Jun. 2010

[5] T. Boutboul, “Temperature critical current correction for ITER samples,” unpublished memo, Dec. 2008.

Agenda

JSPS-CAS Core University Program Seminar on Superconducting Technology of Nuclear Fusion Reactor
18-21 October, 2010, Xi'an, China

AM 17 October, Sunday, 2010					
Time:	Title	Address	Place	Contact	Remarks
8:30-18:00	Registration	No.45 Xingqing Road, Xincheng District, Xi'an, China	Xi'an Empress Hotel	Phone: +86-029-88136666 Fax: +86-029-88136999	
6:00- Supper					

AM 18 October, Monday, 2010 (Day 1)			
Chairman: Peng Fu			
No	Time	Speaker	Title
	8:30-8:45	Peng Fu T. Mito	Opening Ceremony
1	8:45-9:10	T. Hamajima	Coaxial Multilayer CIC Conductor for Large-Scale Superconducting Magnet
2	9:10-9:35	T. Takeuchi	Development of Rapid-Heating, Quenching and Transformation Processed Nb_3Al Superconducting Wires for Nuclear Fusion Devices
3	9:35-10:00	Yanfang Bi	R&D on HTS current leads for Fusion Magnet
10:00-11:00 Coffee Break and Group Photo			
Chairman: T. Mito			
4	11:00-11:25	K. Matsui	Manufacturing Progress of ITER TF Coil in Japan
5	11:25-11:50	Zhixiong Wu	Mechanical and Thermal Properties of Radiation Stable Epoxy Composite
6	11:50-12:15	S. Nomura	Force-Balanced Helical Coil for Superconducting Magnetic Energy Storage
12:15-14:00 Lunch Break			

PM 18 October, Monday, 2010 (Day 1)			
Chairman: S. Yamada			
No	Time	Speaker	Title
1	14:00-14:25	Yuntao Song	Status of ITER Feeder System
2	14:25-14:50	A.Kawagoe	Development of MgB_2 Tapes with High Aspect Ratios
3	14:50-15:15	Huajun Liu	Test facility for ITER CC conductor
4	15:15-15:40	Li Jiang	The Design of 100KV High Voltage Power Supply
15:40-16:00 Coffee Break			
Chairman: Weiyue Wu			
5	16:00-16:25	Zhihong Liu	The Development of Model Coil for 40T Mixed Magnet
6	16:25-16:50	Bo Li	Design and analysis of EAST 4.6G Hz LHCD antenna cooling system
7	16:50-17:15	S. Hamaguchi	Subcooling System for LHD Helical Coils and Its Operation
6:00- Supper			

AM 19 October, Tuesday, 2010 (Day 2)			
Chairman: Qiuliang Wang			
No	Time	Speaker	Title
1	8:30-8:55	T. Mito	Superconducting Magnets with Built-in Oscillating Heat Pipes
2	8:55-9:20	Laifeng Li	The History of 60 Years Development on Cryogenics in China
3	9:20-9:45	Lijian Ding	Considerations on the evaluation of electrical insulation for superconducting system
4	9:45-10:10	S. Yamada	GW Class Hybrid Energy Transfer Line of H_2 and Electricity
10:10-10:30 Coffee Break			
Chairman: Takao TAKEUCHI			
5	10:30-10:55	Qiuliang Wang	Development of Superconducting Magnet System for Alpha Magnetic Spectrometer AMS
6	10:55-11:20	H. Tamura	Analysis of mechanical behavior of the superconducting magnet system for LHD-type fusion reactor.
7	11:20-11:45	T. Yagai	Investigation of the coupling current loops in CIC conductors based on 3-dimensional measurement of strand traces.
8	11:45-12:10	Weiyue Wu	Status of R&D on Manufacture of ITER Correction Coils
12:10-14:00 Lunch Break			

PM 19 October, Tuesday, 2010 (Day 2)			
Chairman: Takatarou HAMAJIMA			
No	Time	Speaker	Title
1	14:00-14:25	Xianghong Liu	New progress of superconducting strands for ITER in China
2	14:25-14:50	Shuangsong Du	Design and Analysis of ITER CC coils
3	14:50-15:15	Rongjin Huang	Cryogenic Thermal Expansion and Mechanical Properties of Epoxy Composites Filled With Negative Thermal Expansion Particles
4	15:15-15:40	Xiang Ji	Electromagnetic and Structural Analysis of EAST Passive Stabilizers Loop
15:40-16:00 Coffee Break			
Chairman: Xianghong Liu			
5	16:00-16:25	T. Obana	Tests of JT-60SA EF conductors in the NIFS superconductor test facility
6	16:25-16:50	Zhiquan Song	The Design and Analysis of ITER Magnet Power Supply System
7	16:50-17:15	Peng Cheng	Study of W7-X Superconducting Magnet
6:00- Supper			

20 October, Wednesday, 2010 (Day 3)			
Chairman: H. Tamura			
No	Time	Speaker	Title
1	8:30-8:55	Qiyong Zhang	EAST Cryogenic System and Its Operation
2	8:55-9:20	Y. Hishinuma	Development of "Low activation superconducting wire" for an advanced fusion reactor
3	9:20-9:45	Feng Long	The First Benchmarking of ITER Nb_3Sn Strand of CNDA
	9:45-10:00	Yuntao Song S. Yamada	Closing Activity
10:00-10:20 Coffee Break			
10:20-12:00 **Discussion on CPU Cooperation** -Summary of 20D collaboration Activities of previous six years-			
12:00-14:00 Lunch Break			
14:00-18:00 Technical Visit of Western Superconducting Technologies Co.,Ltd			
18:30- Supper			

21 October, Thursday, 2010 (Day 4)
Discussion on New Collaboration - Structure and Framework -Collaboration Themes -Future Works and Plans
(Visit of Emperor Qin Shihuang's Mausoleum in Xi'an)

Appendix：Author Index

Name	Organization	Professional title	E-mail
Toshiyuki MITO	核融合科学研究所	Professor	mito@LHD.nifs.ac.jp
Shuichi YAMADA	核融合科学研究所	Associate Professor	yamadas@LHD.nifs.ac.jp
Takatarou HAMAJIMA	東北大学大学院	Professor	hamajima@ecei.tohoku.ac.jp
Takao TAKEUCHI	物質・材料研究機構	Professor	TAKEUCHI.Takao@nims.go.jp
Shin-ichi NOMURA	明治大学	Associate Professor	nomuras@meiji.ac.jp
Tsuyoshi YAGAI	上智大学	Associate Professor	tsuyoshi-yagai@sophia.ac.jp
Kunihiro MATSUI	日本原子力研究開発機構	Professor	matsui.kunihiro@jaea.go.jp
Akifumi KAWAGOE	鹿児島大学	Assistant Professor	kawagoe@eee.kagoshima-u.ac.jp
Hitoshi TAMURA	核融合科学研究所	Associate Professor	tamura@nifs.ac.jp
Shinji HAMAGUCHI	核融合科学研究所	Assistant Professor	hamaguchi@LHD.nifs.ac.jp
Yoshimitsu HISHINUMA	核融合科学研究所	Assistant Professor	hishinuma.yoshimitsu@nifs.ac.jp
Tetsuhiro OBANA	核融合科学研究所	Assistant Professor	obana.tetsuhiro@LHD.nifs.ac.jp
Xianghong Liu	Western Superconducting Technologies Co.,Ltd	Professor	Xhliu@c-nin.com
Laifeng Li	Technical Institute of Physics and Chemistry	Professor	lfli@mail.ipc.ac.cn
Rongjin Huang	Technical Institute of Physics and Chemistry	Assistant Professor	huangrongjin@mail.ipc.ac.cn
Zhixiong Wu	Technical Institute of Physics and Chemistry	PHD	wzx513@163.com
Lijian Ding	National Nature Science Foundation of China	Professor	dinglj@nsfc.gov.cn
Qiuliang Wang	Institute of Electrical Engineering, CAS	Professor	qiuliang@mail.iee.ac.cn
Cheng Peng	Institute of Electrical Engineering, CAS		
Youping Tu	North China Electric Power University	Professor	typ@ncepu.edu.cn

Name	Organization	Professional title	E-mail
Yanfang Bi	Institute of Plasma Physics	Professor	yfbi@ipp.ac.cn
Weiyue Wu	Institute of Plasma Physics	Professor	wuwy@ipp.ac.cn
Yuntao Song	Institute of Plasma Physics	Professor	songyt@ipp.ac.cn
Qiyong Zhang	Institute of Plasma Physics	Professor	zhangqy@ipp.ac.cn
Huajun Liu	Institute of Plasma Physics		liuhj@ipp.ac.cn
Zhiquan Song	Institute of Plasma Physics	Engineer	zhquansong@ipp.ac.cn
Feng Long	Institute of Plasma Physics	Engineer	longf@ipp.ac.cn
Zhihong Liu	Institute of Plasma Physics	Engineer	zhliu@ipp.ac.cn
Tingzhi Zhou	Institute of Plasma Physics	Engineer	tingszhou@ipp.ac.cn
Shuangsong Du	Institute of Plasma Physics		ssdu@ipp.ac.cn
Li Jiang	Institute of Plasma Physics		jiangli@ipp.ac.cn
Bo Li	Institute of Plasma Physics		lib@ipp.ac.cn
Bao Fu	Institute of Plasma Physics		fubao@ipp.ac.cn
Xiang Ji	Institute of Plasma Physics		jixiang@ipp.ac.cn
Yixiang Xing	Institute of Plasma Physics		xingyx@ipp.ac.cn
Li Wang	Institute of Plasma Physics		wangli@ipp.ac.cn